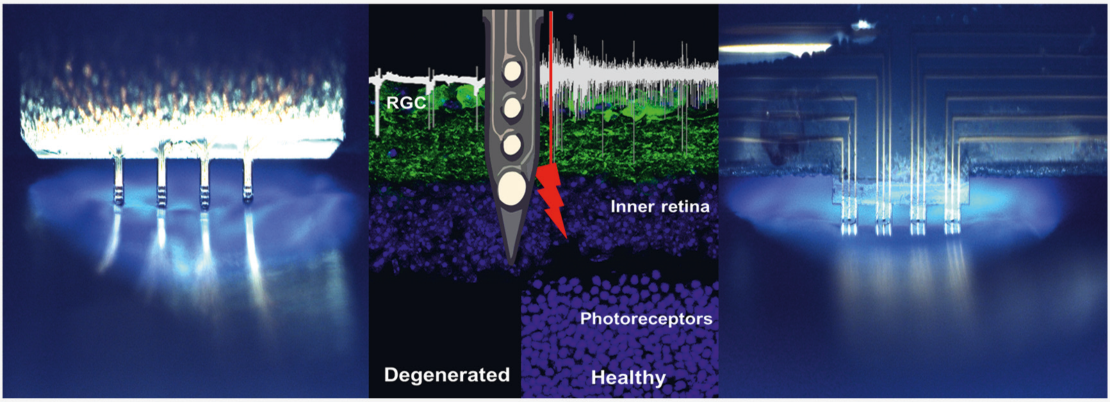

Development, characterization, and application of intraretinal implants

Viviana Rincón Montes

Information
Band / Volume 67
ISBN 978-3-95806-553-6

Mitglied der Helmholtz-Gemeinschaft

JÜLICH
Forschungszentrum

Schriften des Forschungszentrums Jülich
Reihe Information / Information Band / Volume 67

Forschungszentrum Jülich GmbH
Institute of Biological Information Processing
Bioelectronics (IBI-3)

Development, characterization, and application of intraretinal implants

Viviana Rincón Montes

Schriften des Forschungszentrums Jülich
Reihe Information / Information Band / Volume 67

ISSN 1866-1777 ISBN 978-3-95806-553-6

Bibliografische Information der Deutschen Nationalbibliothek.
Die Deutsche Nationalbibliothek verzeichnet diese Publikation in der Deutschen Nationalbibliografie; detaillierte Bibliografische Daten sind im Internet über http://dnb.d-nb.de abrufbar.

Herausgeber und Vertrieb: Forschungszentrum Jülich GmbH
Zentralbibliothek, Verlag
52425 Jülich
Tel.: +49 2461 61-5368
Fax: +49 2461 61-6103
zb-publikation@fz-juelich.de
www.fz-juelich.de/zb

Umschlaggestaltung: Grafische Medien, Forschungszentrum Jülich GmbH

Druck: Grafische Medien, Forschungszentrum Jülich GmbH

Schriften des Forschungszentrums Jülich
Reihe Information / Information, Band / Volume 67

D 82 (Diss. RWTH Aachen University, 2021)

ISSN 1866-1777
ISBN 978-3-95806-553-6

Eidesstattliche Erklärung

Ich, Viviana Rincón Montes, erklärt hiermit, dass diese Dissertation und die darin dargelegten Inhalte die eigenen sind und selbstständig, als Ergebnis der eigenen originären Forschung, generiert wurden.

Hiermit erkläre ich an Eides statt

1. Diese Arbeit wurde vollständig oder größtenteils in der Phase als Doktorand dieser Fakultät und Universität angefertigt;

2. Sofern irgendein Bestandteil dieser Dissertation zuvor für einen akademischen Abschluss oder eine andere Qualifikation an dieser oder einer anderen Institution verwendet wurde, wurde dies klar angezeigt;

3. Wenn immer andere eigene- oder Veröffentlichungen Dritter herangezogen wurden, wurden diese klar benannt;

4. Wenn aus anderen eigenen- oder Veröffentlichungen Dritter zitiert wurde, wurde stets die Quelle hierfür angegeben. Diese Dissertation ist vollständig meine eigene Arbeit, mit der Ausnahme solcher Zitate;

5. Alle wesentlichen Quellen von Unterstützung wurden benannt;

6. Wenn immer ein Teil dieser Dissertation auf der Zusammenarbeit mit anderen basiert, wurde von mir klar gekennzeichnet, was von anderen und was von mir selbst erarbeitet wurde;

7. Teile dieser Arbeit wurden zuvor veröffentlicht, siehe: „*List of publications and contributions in conferences*".

25. April 2021

Viviana Rincón Montes.

Abstract

With the ultimate goal to restore vision in blind patients, visual prostheses have been developed to interface and modulate the electrical activity of different neuronal structures along the visual pathway, targeting mainly the visual cortex, the optic nerve, and the retina. Thus, prosthetic devices that stimulate electrically the retina have been employed to treat blind patients with retinal degenerative diseases such as age-related macular degeneration and retinitis pigmentosa, which comprise the third leading cause of blindness worldwide. In the last decades, the development of retinal implants with commercial approval and those used in clinical trials has shown meaningful progress towards the restoration of useful vision. Nonetheless, the recent withdrawal of current retinal implants from the market exhorts the scientific community to join and enhance efforts to improve the technology and the efficiency of such devices to achieve further steps in the restoration of vision.

Aiming at a new generation of retinal implants, the BiMEA consortium has proposed the development of a bidirectional microelectrode array (BiMEA) to enable a bidirectional communication with the retina. To this end, penetrating neural probes were proposed to allow access to the intraretinal space and to modulate and record simultaneously the electrical activity of the retina. To further develop the BiMEA strategy, this work exposes the development and *in vitro* validation of BiMEA probes, setting in turn the groundwork for the future development of novel intraretinal implants.

First, the BiMEA concept was validated in healthy and degenerated ex-planted mouse retinas using silicon-based devices, thereby demonstrating the feasibility of a bidirectional communication between the retina and a prosthetic device. Thus, the stimulation of the inner retina with safe electrical stimuli while recording the neuronal activity of the output neurons of the retina, the ganglion cells, was achieved. Going a step further, intraretinal devices based on flexible materials were developed and optimized to better match the anatomy and the mechanical properties of the retina while fulfilling the insertion requirements of such devices. Hence, flexible intraretinal probes with miniaturized shanks 7 µm thick and 145 µm long were successfully inserted into the thin retina. As a result, local field potentials and the spiking activity of both, healthy and degenerated retinas, were recorded. Moreover, electrically evoked potentials were captured after applying charge densities as low as 81.5 $\mu C/cm^2$.

Furthermore, a systematic study to validate the acute performance of both silicon and flexible BiMEAs was conducted. This study revealed that flexible penetrating probes based on parylene-C with a shank width as narrow as 50 µm diminished the acute insertion footprint of intraretinal probes, inducing lesions nearly 2.5 times the cross-section of the probe. Moreover, electrical recordings had a maximum signal-to-noise ratio of 12.37 and a success rate of insertion of 93%. Consequently, the development of intraretinal devices open the door for closed loop feedback systems, offering the possibility to track and acknowledge *in situ* the electrical activity of the retina and the success of the stimulation while adjusting accordingly the stimuli. Even more, aiming future *in vivo* applications, flexible BiMEA probes showed the potential for the development of intraretinal implants.

Zusammenfassung

Mit dem letztendlichen Ziel der Wiederherstellung des Sehvermögens bei blinden Patienten sind Sehprothesen entwickelt worden, um eine Schnittstelle zur elektrischen Aktivität verschiedener neuronaler Strukturen entlang der Sehbahn zu bilden und diese Strukturen zu modulieren, allen voran die Sehrinde, den Sehnerv und die Netzhaut. Solche Sehprothesen zur elektrischen Stimulation der Netzhaut wurden eingesetzt, um blinde Patienten mit degenerativen Netzhauterkrankungen wie der altersbedingten Makuladegeneration und Retinitis pigmentosa, die die weltweit dritthäufigste Ursache für Blindheit darstellen, zu behandeln. In den letzten Jahrzehnten hat die Entwicklung im Bereich von Retinaimplantaten mit kommerzieller Zulassung und solchen mit Einsatz in klinischen Studien bedeutende Fortschritte in Richtung der Wiederherstellung nützlichen Sehvermögens gemacht. Nichtsdestotrotz mahnt der kürzliche Rückzug aktueller Retinaimplantate vom Markt die wissenschaftliche Gemeinschaft, zusammen die Bemühungen zur Verbesserung der Technologie und damit der Effizienz solcher Implantate zu verstärken, um weitere Schritte zur Wiederherstellung des Sehvermögens zu unternehmen.

Zum Zwecke einer neuen Generation von Retinaimplantaten hat das BiMEA-Konsortium die Entwicklung eines bidirektionalen Mikroelektroden-Arrays (BiMEAs) vorgeschlagen, um eine bidirektionale Kommunikation mit der Netzhaut zu ermöglichen. Dazu wurden penetrierende neuronale Sonden vorgeschlagen, um den Zugang zum intraretinalen Raum zu ermöglichen und gleichzeitig die elektrische Aktivität der Netzhaut zu modulieren und abzuleiten. Zur Weiterentwicklung der BiMEA-Strategie befasst sich diese Arbeit mit der Entwicklung und *In-vitro*-Validierung von BiMEA-Sonden und legt damit den Grundstein für die zukünftige Entwicklung von neuartigen intraretinalen Implantaten.

Zu diesem Zweck wurde das BiMEA-Konzept zunächst an gesunden und degenerierten explantierten Mäusenetzhäuten unter Verwendung von Sonden auf Siliziumbasis validiert. Damit wurde die Machbarkeit einer bidirektionalen Kommunikation zwischen der Netzhaut und einer potentiellen Sehprothese demonstriert. Auf diese Weise wurde die Stimulation der inneren Netzhaut mit sicheren elektrischen Stimuli bei gleichzeitiger Ableitung der neuronalen Aktivität von den Output-Neuronen der Netzhaut, den Ganglienzellen, erreicht. Darüber hinaus wurden intraretinale Vorrichtungen aus flexiblen Materialien entwickelt und optimiert, bei denen die Sonden besser an die Anatomie und die mechanischen Eigenschaften der Netzhaut angepasst sind und gleichzeitig die Insertionsanforderungen solcher Vorrichtungen erfüllen. So wurden flexible intraretinale Sonden mit 7 µm breiten und 145 µm langen miniaturisierten Schäften erfolgreich in die dünne Netzhaut eingeführt. Als Ergebnis wurden die lokalen Feldpotentiale und die Aktionspotentiale sowohl gesunder als auch degenerierter Netzhäute abgeleitet. Ferner wurden elektrisch evozierte Potentiale nach Anwendung von Ladungsdichten von nur 81,5 µC/cm2 erfasst.

Darüber hinaus wurde eine systematische Studie zur Validierung der akuten Leistung sowohl von Silizium- als auch von flexiblen BiMEAs durchgeführt. Diese ergab, dass flexible penetrierende Sonden auf der Basis von Parylene-C mit einer Schaftbreite von nur 50 µm die akute Einführungsfläche von BiMEA-Sonden verringerten und Läsionen mit einem Durchmesser von fast bis zum 2,5fachen des Sondenquerschnitts induzierten. Des Weiteren ermöglichten sie Ableitungen mit einem maximalen Signal-Rausch-Verhältnis von 12,37 und einer

Insertionserfolgsrate von 93%. Somit ebnet die Entwicklung intraretinaler Sonden den Weg für geschlossene Rückkopplungsschleifen und bietet die Möglichkeit, die elektrische Aktivität der Netzhaut und den Erfolg der Stimulation *in situ* zu verfolgen und zu bestätigen, während die Stimuli entsprechend angepasst werden können. Ferner zeigten flexible BiMEA-Sonden das Potenzial für die Entwicklung von intraretinalen Implantaten für zukünftige *In-vivo*-Anwendungen.

Contents

Abbreviations

ADC	Analog-to-digital converter
AMD	Age-related macular degeneration
AP	Action potential
Au	Gold
BiMEA	Bidirectional microelectrode array
BioMAS	Bioelectronic Multifunctional Amplifier System
BMI	Brain-machine interface
Ca^{2+}	Calcium ion
CCS	Current-controlled stimulation/stimulator
C_{dl}	Double layer capacitance
CIC	Charge injection capacity
Cl^-	Chloride ion
CMB	Current measurement board
CNS	Central nervous system
Cr	Chromium
CSC	Charge storage capacity
CSC_c	Cathodic charge storage capacity
CV	Cyclic voltammetry
CVD	Chemical vapor deposition
DBS	Deep-brain stimulation
DTE	Distance from the tip to the first electrode of a shank
E	Young’s modulus
E_c	Cathodic polarization voltage
ECF	Extracellular fluid
EIS	Electrochemical impedance spectroscopy
E_{ma}	Maximum anodic polarization voltage
E_{mc}	Maximum cathodic polarization voltage
EPSP	Excitatory postsynaptic potential
ERG	Electroretinogram
ES	Electrical stimulation
ESA	Electrochemical surface area
ESE	Electrical stimulation efficiency
FBR	Foreign body reaction
FIB	Focused ion beam
FR	Firing rate
GCL	Ganglion cell layer
GHK	Goldman-Hodgkin-Katz
GSA	Geometric surface area
$I_{del,\ ph}$	Delivered current per stimulation phase
IHP	Inner Helmholtz plane
$I_{inj,\ ph}$	Current injection per stimulation phase
INL	Inner nuclear layer
IPL	Inner plexiform layer
IPSP	Inhibitory postsynaptic potential
IrO_x	Iridium oxide
K^+	Potassium ion
LED	Light-emitting diode
LFP	Local field potential
LGN	Lateral geniculate nucleus
MEA	Microelectrode array
NFL	Nerve fiber layer
OHP	Outer Helmholtz plane
OPL	Outer plexiform layer
PaC	Parylene-C

PBS	Phosphate buffered solution
PCB	Printed circuit board
PDMS	Polydimethylsiloxane
P_e	Euler's buckling load
PEDOT: PSS	Poly(3,4-ethylenedioxythiophene): poly(4-styrenesulfonate)
PI	Polyimide
PL	Photoreceptor layer
P_R	Rankine-Gordon's buckling load
Pre-amp	Pre-amplification stage
Pt	Platinum
$Q_{d,\,ph}$	Charge density per stimulation phase
$Q_{inj,\,ph}$	Charge injection per stimulation phase
R_{ct}	Charge transfer resistance
Rd10	Animal model for retinitis pigmentosa
RGC	Retinal ganglion cell
ROI	Region of interest
RP	Retinitis pigmentosa
RPE	Retinal pigment epithelium
SA	Spontaneous activity
SEM	Scanning electron microscope
Si	Silicon
SIROF	Sputtered iridium oxide film
SNR	Signal-to-noise ratio
Na^+	Sodium ion
Ti	Titanium
TN-L15	Genetically encoded Ca^{2+} sensor
T_{ph}	Phase duration of electrical stimulus
VCS	Voltage-controlled stimulation/stimulator
V_{in}	Insertion speed
WT	Wildtype mouse retina
Z	Impedance at 1 kHz
Z_{in}	Initial step of an intraretinal insertion
ΔZ	Steps after Z_{in}

Chapter 1

Introduction

The process of detecting, transforming, and interpreting light as images is what characterizes the special sense of vision. This complex task is carried out by neurons along the visual pathway, a neuronal network that starts in the eye and ends up in the brain. The retina is a multi-layered neural tissue at the back of the eye. Here, photoreceptors provide input to the network after sensing light and initiate a cascade of light-induced responses within the so called “inner retina”, a region where second and third order neurons fulfill the first processing phase of visual information. As an output, transduction of light stimuli into electrical impulses is performed by retinal ganglion cells (RGCs), whose axons form the optic nerve and convey the information to the visual cortex in the brain [1].

When diseases affect the anatomical structures of the visual pathway, visual impairment and blindness can occur. The third leading cause of blindness worldwide are retinal degenerative diseases caused by photoreceptors loss, such as age-related macular degeneration (AMD) and retinitis pigmentosa (RP) [2], [3]. While vision restoration is not yet possible, treatments for patients with AMD and RP comprise dietary regulations, vitamins, and experimental approaches like stem-cell based therapy, retinal tissue transplantation, or the implantation of visual prostheses [4]–[6].

In the last decades, the development of visual prostheses that stimulate the retina electrically has been of focus given the significant progress in the restoration of useful vision in blind patients with AMD and RP. Around 13 retinal prostheses have been tested in chronic human implantations, only three of them have been approved for commercial use, and approximately 500 patients have been implanted with commercially available devices or in a clinical trial phase. Retinal implants have offered meaningful but limited improvements to the daily life of patients, enabling mostly motion and contrast detection, and in the best cases, the reading of big letters upon good illumination. Results obtained by current retinal implants are limited, and even more, the two manufacturers with approved devices have stopped the commercialization of retinal prostheses since 2019 [7]–[10].

These recent events urge the scientific community for the development of a new generation of retinal implants. One of the main challenges that current retinal implants must overcome is the efficacy of the device while interacting with the diseased retina. Given the absence of photoreceptors input, the retina undergoes remodeling/rewiring processes that lead to a pathologic electrical behavior. The latter has proven to increase the current thresholds during stimulation, reducing in turn the efficiency of electrical stimulation (ES) protocols [10]–[13].

Efforts to improve the ES therapy offered by retinal prosthetic devices go from the optimization of protocols [14]–[17] to the implementation of different stimulation modalities [18], as well as the use of novel electrode materials and geometries [19]–[21]. One of the strategies that has been gaining momentum to reduce the charge density thresholds during ES aims to achieve a closer coupling with target neurons in the retina. Thus, the use of penetrating electrodes has been investigated by different research groups, which include approaches like silicon (Si)-nanoneedles [21] or protuberant 3D electrodes [20], [22], [23].

Moreover, comprising a new approach, the BiMEA consortium has proposed the use of penetrating multi-shank and multi-site neural probes for a bidirectional communication strategy to enable a feedback system that tracks and modulates simultaneously the electrical activity of the retina. Thus, penetrating probes containing multiple electrode sites could establish an intraretinal interface that performs ES of vital neurons in the inner retina while recording the electrical activity of RGCs (Figure 1.1) [10], [13], [24], [25]. A bidirectional communication strategy could offer beneficial features to retinal implants: i) a dual functionality for electrical recording and stimulation, ii) information about abnormal retinal activity, iii) feedback about ES, and iv) the system could in principle calibrate autonomously stimulation pulses if a closed loop feedback is established [10], [13]. Consequently, an intraretinal approach can open the door to not only improve the efficiency of current retinal implants, but to understand better the physiology of both healthy and degenerated retinas upon ES.

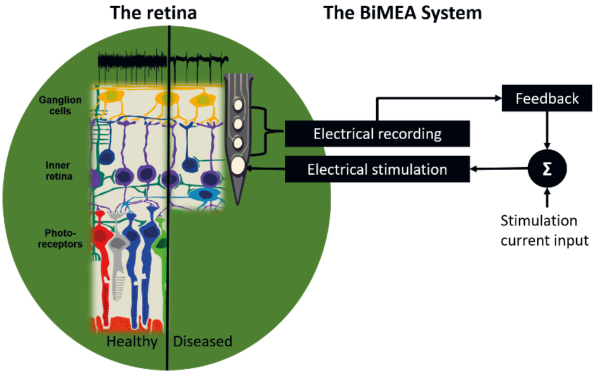

Figure 1.1. The BiMEA system. BiMEA stands for bidirectional microelectrode array, aiming a closed-loop feedback system in which a penetrating microelectrode array (MEA) performs simultaneously electrical stimulation and recordings of the electrical activity of the retina. Figure modified from [13].

While penetrating neural probes have been widely used in neuroscience for intracortical and interfascicular applications [26], the first use of such devices in the retina was reported by [25] using commercial Neuronexus chips. Here, access to the intraretinal space, as well as the feasibility of intraretinal recordings was demonstrated. However, retinal responses upon ES were mostly achieved when using high voltage stimuli and long pulse durations that caused the electrolysis of water and subsequent damage of the retina [25]. Hence, with the purpose to further develop the BiMEA strategy, the work exposed in this thesis comprises the development and *in vitro* validation of custom-made BiMEAs for intraretinal applications, establishing in turn the foundations of a future intraretinal implant.

To this end, the following thesis presents an introductory background (Chapter 2) on the main concepts that will be addressed along the text. The latter comprises topics such as the retina, the development of neural and visual prostheses, as well as the establishment of interfaces for neural recording and stimulation. Next, Chapter 3 describes the technology, the materials, and the techniques used to accomplish the objective of this thesis, followed by four chapters that will present the accomplishments and challenges of this work.

As a first step, Chapter 4 exposes a proof of concept to demonstrate the recording and the stimulation capabilities of the BiMEA proposal. To this effect, a first generation of custom-made BiMEAs based on Si, which were designed and fabricated by the Institute of Materials in Electrical Engineering 1 (IWE-1, RWTH Aachen University, Germany), as part of the BiMEA consortium, were used. Here, the feasibility of recording retinal activity while stimulating the retina within a safe window of stimuli was shown, though, inspection of the biological samples revealed the potential damages that Si-based devices can generate to the retina. To overcome the latter and thinking towards a future intraretinal implant that diminishes the insertion trauma of the tissue, BiMEAs based on flexible and tissue-like materials, such as polyimide (PI) and parylene-C (PaC) were proposed. Thus, Chapter 5 unveils the design and fabrication principles to customize the probes to better match the anatomy and the mechanical properties of our target tissue, the retina. Additionally, the characterization of flexible intraretinal probes was performed, assuring in turn the necessary features for recording and stimulation.

Likewise, Chapter 6 shows the intraretinal application of flexible BiMEAs, revealing an appropriate insertion protocol, the recording capabilities of such devices, and exploring the boundaries of intraretinal stimulation using a low range of charge injection. Furthermore, Chapter 7 exposes the acute performance of both Si and flexible BiMEA devices, establishing the biological impact induced to the retina, the quality of intraretinal recordings, and the success rate of insertion. Finally, an overview of the accomplishments and challenges is given in Chapter 8, disclosing in turn the next steps towards a flexible intraretinal implant for future *in vivo* applications.

Chapter 2

Background

2.1. The sense of vision and the retina

The capability of light perception, image formation, and object recognition and identification is enabled by the special sense of vision. The ability of seeing is accomplished by using more than half of the sensory receptors of the human body, which are mainly located in the eye. Thus, visual information is processed not only in the eye itself but in large cortical areas in the brain [1], [27].

2.1.1. The visual pathway

The neuronal circuit that detects, transmits, and processes visual information in the human body is referred to as the visual pathway (Figure 2.1). It all starts when light is projected onto the central (nasal) and peripheral (temporal) regions of the retina in the eye. Here, around 126.5 million photoreceptors detect light initiating a signal cascade of graded potentials that are transmitted by bipolar, horizontal, and amacrine cells to 1.2 million RGCs. The latter are third order neurons whose axons form the optic nerve and convey visual information in the form of action potentials (APs) into the brain.

The first structure in the brain reached by the optic nerve is the optic chiasm, a crossing point where fibers coming from the central retina cross over to the opposite hemisphere of the brain. Consequently, visual information that is projected onto the left and right central retina will be processed by the right and left hemisphere of the brain, respectively. Continuing the visual pathway, fibers of the optic nerve, now called optic tract, extend towards the lateral geniculate nucleus (LGN), a conveyance center of visual information located in the thalamus. At this point, optic radiations conformed by approximately 5 million axons generate a direct connection to the primary visual cortex in the occipital lobe in the brain, where 500 million neurons process visual stimuli allowing the human body to see [1], [6], [27].

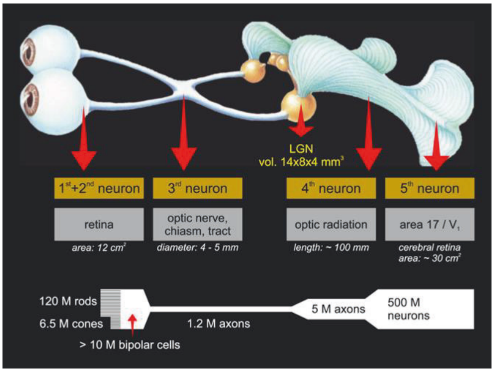

Figure 2.1. Overview of the visual pathway. Details given in text. Image from [6].

2.1.2. The retina

Being an extension of the central nervous system (CNS) [28], the retina is a neural tissue at the back of the eye (Figure 2.2a) that marks the starting point of the visual pathway. This structure is composed of a pigmented and a neural region as depicted in Figure 2.2b. Anterior to the choroid (the nourishment supply of the retina) lies the pigmented region or retinal pigment epithelium (RPE), which comprises a sheet of epithelial cells containing melanin granules that facilitate light absorption. Posterior to the vitreous body and anterior to the RPE is located the neural layer of the retina. This neural layer harbors a neuronal network organized in a multilayered structure with first, second, and third order neurons, which are mainly identified as five types of neurons: photoreceptors, bipolar cells, horizontal cells, amacrine cells, and RGCs.

Likewise, as exhibited in Figure 2.2b, six anatomical strata can be distinguished within the retina: the photoreceptor layer (PL), the outer plexiform layer (OPL), the inner nuclear layer (INL), the inner plexiform layer (IPL), the ganglion cell layer (GCL), and the nerve fiber layer (NFL). The PL spans from the outer and inner segments to the cell bodies of photoreceptors, followed by the OPL, which embraces the synaptic connections between photoreceptors, bipolar, and horizontal cells. The INL comprehends the cell bodies of bipolar, horizontal, and amacrine cells. Afterwards comes the IPL, where the synaptic connections between bipolar, amacrine, and RGCs can be found. Next is the GCL, which contains the cell bodies of RGCs, and the NFL, which comprises the output of the retina, the axons of RGCs that form the optic nerve [1], [29].

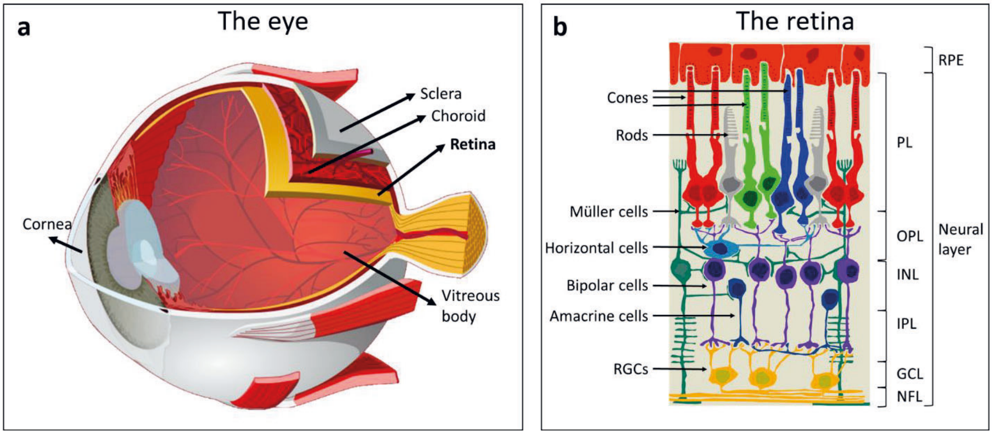

Figure 2.2. Anatomy of the eye and the retina. a) The eye. When light enters the eye through the cornea, it projects on the retina, a neural tissue between the vitreous body and the choroid. Imaged modified from [30]. b) Microstructure of the retina. Retinal layers are coded as follows: RPE = retinal pigment epithelium, PL = photoreceptors layer, OPL = outer plexiform layer, INL = inner nuclear layer, IPL = inner plexiform layer, GCL = ganglion cell layer, NFL = never fiber layer. Image modified from [31].

Retinal neurons

Photoreceptors

The visual pathway starts with the activity of photoreceptors, first order neurons whose main function is to detect and transduce light stimuli into electrical signals. There are two classes of photoreceptors: rods and cones. The former allow vision in dim light conditions and are usually found at the periphery of the retina. The latter provide color vision and are present all along the retina with a higher concentration at the fovea, a region in the center of the retina (macula lutea) where rods are not present and the sharpest acuity resolution is met. Moreover, there are three classes of cones that are each sensitive to long (red), middle (green), and short (blue) wavelengths [1], [29].

Thus, when a photon hits the retina, rhodopsin, a photopigment molecule at the outer segments of rods and cones, is activated. Consequently, a phototransduction process that reduces the influx of cations into the outer segments of photoreceptors is triggered. This induces in turn the hyperpolarization of photoreceptors and diminishes the release of glutamate at the synaptic terminals with bipolar and horizontal cells. With an opposite behavior, photoreceptors depolarize and release glutamate during dark conditions. In this way, a signaling cascade mediated by graded potentials is initiated within the retina [1], [32].

Bipolar cells

Once bright or dark conditions are detected by photoreceptors, visual information is transmitted to bipolar cells, second order neurons that convey information to amacrine and RGCs via non-spiking membrane potentials. Depending on the type of photoreceptor contacted, bipolar cells can be classified as rod or cone bipolar cells [33]. Cone bipolar cells enable a direct neural circuit between cones and RGCs, whereas rod bipolar cells follow an indirect pathway in which they reach first amacrine cells that interconnect with cone bipolar cells, which then transmit the information to RGCs [34].

In addition, according to their physiological response bipolar cells can be identified as ON or OFF bipolar cells, which hyperpolarize and depolarize under the release of glutamate, respectively. Hence, ON bipolar cells depolarize under light stimuli, when hyperpolarized photoreceptors diminish the release of glutamate at their synaptic terminal, while OFF bipolar cells depolarize under dark conditions [33], [34]. Moreover, according to the axonal termination of bipolar cells, the IPL is stratified into five sublayers, being the first close to the INL and the fifth to the GCL. In this manner, synapses of each OFF and ON bipolar cells lie in the first three (also called sublamina a) and last two stratifications (sublamina b) of the IPL [33].

Horizontal and amacrine cells

While bipolar cells offer a direct vertical pathway between photoreceptors and RGCs, horizontal and amacrine cells provide each lateral signaling circuits at the OPL and IPL. On one side horizontal cells contribute to contrast enhancement of neighboring bright and dark regions by conducting inhibitory feedback to the stimulated photoreceptor and its neighbors. Likewise, they play a role in the reduction of signal redundancy measuring the overall illumination of the exposed area and subtracting it from the system's response that is transmitted to the following layers of the retina. On the other side, amacrine cells carry out an inhibitory feedback of the synaptic output of bipolar cells, adjusting in turn the response of RGCs to specific stimuli, like for example the firing synchronicity of neighboring RGCs or spiking responses to direction selectivity [34].

Retinal ganglion cells

RGCs provide an output to the phototransduction pathway within the retina transducing visual stimuli into APs. At least 30 types of RGCs have been distinguished in the mammalian retina according to morphological, physiological, intraretinal layer distribution, and molecular characteristics. Thus, each one decodes specific features such as light intensity, color, and motion [35].

First classification of RGCs can be performed according to their electrophysiological responses under light stimuli: ON, OFF, and ON-OFF. ON cells correspond to those RGCs that react with a continuous discharge of APs during a light stimulus, OFF cells are characterized by a silent activity during light stimulation but a spiking activity at the offset of the stimulus, while ON-OFF responses are given by a burst of spikes at the onset and offset of the stimulus but a non-spiking behavior during the stimulus [36], [37]. Likewise, cells identified with each one of the former responses interconnect with bipolar cells at different strata of the IPL. While dendrites of ON cells extend to a region of the IPL close to the cell bodies of RGCs, the dendritic arbor of OFF cells spans along the first three sublayers of the IPL. With a bistratified branching, ON-OFF cells interconnect with intermediate neurons in both regions.

Moreover, RGCs have a receptive field that comprises two concentric regions (center and surround), which expand with the dendritic arbor of the cells and have an antagonistic interaction. Thus, a cell with an ON-center and OFF-surround field will react with a burst of spikes if light is directed to the ON-center of the field, while the spontaneous activity of an OFF-center and ON-surround cell will be inhibited by the same stimulus. As depicted in Figure 2.3, an opposite effect will be observed if the light is directed onto the ON or OFF surround of the cell [29], [37]. Consequently, according to the receptive fields exhibited by RGCs, they are classified as X or Y cells. X cells, also referred as midget cells have a small receptive field (~ 15 µm) that performs a linear summation of the receptive field response, thereby showing a sustained (tonic) spiking activity in the presence of a light stimulus. Whereas Y cells, also called parasol cells, have a large receptive field with non-linear responses that exhibit a transient (phasic) firing of APs during light stimulation [29], [34], [37].

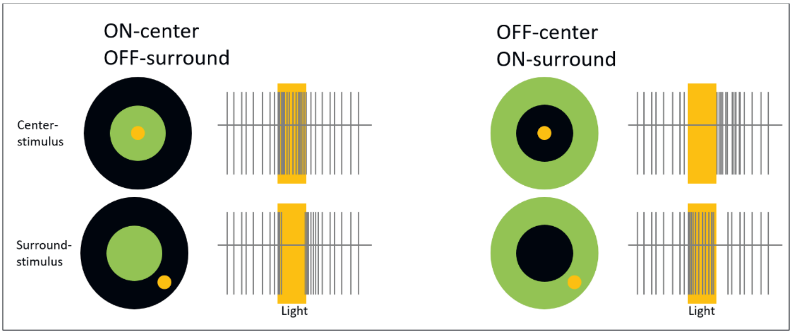

Figure 2.3. Receptive field responses of the retina. The electrical activity of an ON-center OFF surround cell is stimulated when a light stimulus is directed onto the center of the receptive field, while this effect is observed in an OFF-center ON-surround cell if the stimulus is on the periphery of the receptive field. An inhibitory effect is generated when the light is on the surround and on the center of the receptive field of an ON-center OFF-surround and OFF-center ON-surround cell, respectively.

Furthermore, the retina can be stimulated with artificial electrical impulses that will generate a direct or an indirect response of RGCs. A direct stimulation comprises somatic and axonal stimulations. The former refers to the activation of RGC somas or the initial segment of RGC axons, while the latter implies the activation of a bundle of peripheral RGC axons that are near the stimulation source. In the case of an indirect stimulation, retinal neurons in the inner retina, such as bipolar cells, are activated, modulating in turn the electrical activity of postsynaptic RGCs [38].

Electroretinogram

The electroretinogram (ERG) is a local field potential (LFP) that represents the summed response of all retinal neurons under a light stimulus, thereby becoming a tool to assess retinal function to diagnose and to characterize retinal diseases in both, the clinical setting and in research. ERG measurements are typically performed at the corneal surface (full-field ERG) or at the retina (local ERG) using microelectrodes at the surface of the retina or intraretinally. The ERG is originated from extracellular potassium ion (K^+) currents produced by the activation of retinal cells that are vertically directed (e.g.: photoreceptors and bipolar cells). Due to a process called spatial buffering, Müller cells (retinal glial cells) carry through the intraretinal space K^+ currents, creating in turn an inflow and outflow of ion currents according to the local changes of the concentration of K^+ in activated cells. In the mammalian retina, the ERG comprises a low frequency wave that has a negative crest called the a-wave and a positive peak referred as the b-wave. The a-wave reflects the diminished currents in the photoreceptors after hyperpolarization under a light stimulus, while the b-wave is attributed to the extracellular increase of K^+ after the depolarization of ON bipolar cells [39], [40].

ERG waveform differences are observed depending on whether the retina is dark or light adapted (Figure 2.4). Dark-adapted or scotopic ERG responses (Figure 2.4a) are composed not only of the a- and b-wave, but an extra component identified as oscillatory potentials, which are attributed to the interactions of neurons in the IPL. Likewise, while the a-wave response is initially driven by the activity of rod photoreceptors, a rod-cone response can be observed with an increase in the a-wave amplitude when the strength of the stimulus increases. On the other hand, the a-wave in light-adapted or photopic ERG responses (Figure 2.4b) is driven exclusively by cone photoreceptors, thereby leading to a reduced a-wave in amplitude [40], [41].

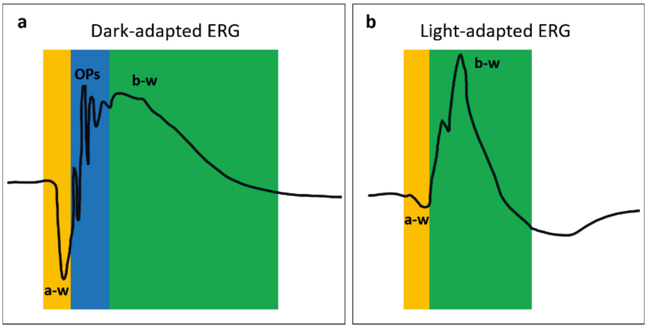

Figure 2.4. Full-field ERG responses in wildtype mouse. Typical ERG responses in C57BL/6J wildtype mouse after light stimulation of a dark-adapted (a) and a light-adapted (b) retina. Waveform components are depicted as follows: a-waveform (a-w) in yellow, oscillatory potentials (OPs) in blue, and b-waveform (b-w) in green. Image modified from [41].

2.1.3. Retinal degenerative diseases

Visual impairment and blindness can occur when the anatomical structures of the visual pathway are affected. In the world, the third leading cause of blindness is attributed to diseases related to photoreceptor degeneration, such as AMD and RP [2], [3]. Considering there is no cure for AMD or RP yet, current treatments focus on slowing down the progression of the disease through the regulation of nutritional diets and vitamins. Moreover, efforts to restore vision in blind patients have led to the development of novel experimental strategies, such as stem-cell based therapies, gene therapies, transplantation of lost retinal tissue, and visual prostheses [3], [5], [42], [43].

Age-related macular degeneration (AMD)

Around 10.37 million people suffer from AMD worldwide, of which 1.96 million are blind [2]. Caused by a combination of genetic and exogenous factors, AMD affects mainly elder individuals and is experienced as a progressive blurring, distortion, and darkening of the central vision. The latter is triggered by white-yellow deposits of protein, lipids, and cholesterol fragments called drusen, which appear between the RPE and the neural layer of the retina [42]. In advanced cases, AMD is distinguished as dry or wet. Dry AMD, also called geographic atrophy, is when drusen along with a gradual degeneration of RPE and photoreceptors occur. Wet or neovascular AMD is characterized by the emergence of fragile and abnormal blood vessels in the retina, which leak blood and fluids into the RPE and the PL [42].

Retinitis pigmentosa (RP)

RP has a prevalence of 1 in 4000, affecting more than one million people worldwide. RP is a hereditary degeneration of the retina that induces the progressive death of both rod and cone photoreceptors. The early phase of the disease, usually during adolescence, is experienced with night blindness, followed by mid-peripheral vision loss during adulthood due to the death of photoreceptors at the periphery of the retina. In this way, patients develop a tunnel vision, which is reduced until central vision loss occurs in an advanced phase around the age of 60 [3].

2.2. Neural interfaces

2.2.1. Overview of medical applications

Neural interfaces are electronic devices that interface the central and peripheral nervous system with the aim to treat neurodegenerative diseases, to restore lost sensorimotor functions, and to understand and map the complex neural networks of the human brain [44], [45]. Multiple clinical and empirical applications are displayed in Figure 2.5.

For example, cortical electrodes have been used from the laboratory to the clinical setting to enable applications such as cortical stimulation mapping to guide epilepsy and tumor surgeries [46] and the development of brain-machine interfaces (BMI) to restore motor functions in humans with quadriplegia [47]. Moreover, deep-brain stimulation (DBS) has been used to treat motor disorders such as Parkinson’s disease, essential tremor, and dystonia, as well as neurological and neuropsychiatric disorders such as epilepsy, obsessive-compulsive disorder, and depression [48], [49]. Likewise, vagal nerve stimulators have been also used to treat epilepsy and depression, and preclinical research aims to expand its use to treat chronic inflammatory disorders like rheumatoid arthritis [50].

One of the most widely used prothesis is the cochlear implant, which restores hearing and allow the acquisition of spoken language in deaf-born children [51]. In addition, sacral neuromodulation, known as SNN, has been used to treat incontinence [52], while spinal cord stimulators are used in the treatment of chronic pain or for the restoration of locomotion after paralysis in spinal cord injury [53], [54]. Furthermore, visual prostheses, such as retinal implants, have been employed to restore partial vision in blind patients with degenerative retinal diseases [55, Pt. II. Retinal Approaches].

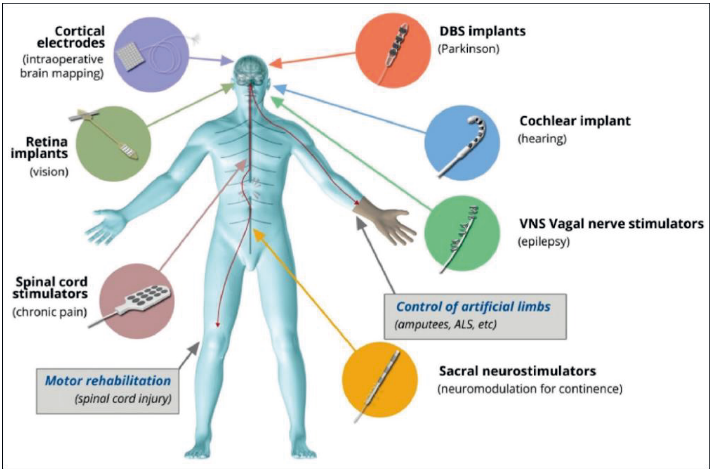

Figure 2.5. Applications of neural interfaces. Examples of neural prostheses interfacing the central and peripheral nervous system for the treatment of neurodegenerative diseases, restoration of lost sensorimotor functions, and mapping of the brain. Figure from [44].

2.2.2. Types of neural interfaces

Neural interfaces have been developed to interact and communicate with the nervous system through unidirectional (sensing) and bi-directional (sensing and stimulating) probes, thereby allowing to monitor and modulate neural activity. Most neural probes comprise mainly a single or an array of macro- or microelectrodes or transistors that record the electrical activity of neurons and/or perform electrical stimulation [56]–[58]. Moreover, next-generation interfaces integrate sensors, transducers, surface modifications, and new designs that comprise from micro light emitters and photodetectors to mesh designs and microfluidic channels to enable in turn electrical, optical, and chemical neuromodulation, as well as *in situ* drug delivery [58]. Thus, four main approaches are used to interface electrical devices with neural tissues, which can be identified as penetrating, conformal surface, circumvented, and sieve or regenerating neural probes (Figure 2.6).

Penetrating probes

Penetrating probes are devices that consist mainly of a single or multiple shank(s) that poke through different layers of a neural tissue. They are typically used to interface the brain in the intracortical space and peripheral nerves to reach within nerve fascicles. Penetrating devices can be distinguished as micromachined or microwire arrays. Standard micromachined designs include Si-based devices such as Michigan (Figure 2.6a-i) and Utah arrays (Figure 2.6a-i) [26]. The former is a probe with multiple shanks that has multiple electrode sites along each shank, allowing the implementation of 3D arrays with the assembly of multiple 2D arrays [59]. The latter, is an array of Si-needles with shafts that are encapsulated with a biocompatible polymer and tips that are coated with a metal-based material or a conductive polymer [26], [60], [61]. Likewise, CMOS (complementary-metal-oxide semiconductor) technology has been exploited to increase the spatiotemporal resolution of penetrating probes. As a cutting-edge example, the high-density array Neuropixels (Figure 2.6a-iii) offers up to 960 recording sites in a single Si-shank [62]. Moreover, microwire arrays consist of a bundle of fine metal wires or carbon fibers (Figure 2.6a-iv) that, akin to Utah arrays, are insulated except the tip [26], [61], [63].

Furthermore, penetrating probes based on flexible polymers are being developed to better match the mechanical properties of neural tissues. An example is depicted in Figure 2.6a-v, where devices with a Michigan-like design were fabricated out of SU-8 and a cross-sectional area below 10 μm^2 was achieved for each individual shank [64]. Due to the flexibility of such devices, insertion aids based on stiff shuttles or biodegradable coatings are employed to allow the insertion of flexible penetrating neural probes [65].

Conformal surface probes

Conformal surface probes are devices that fit their shape to the surface where they are placed on [58]. To this effect, flexible polymer materials are used as substrate and encapsulation layers. They can be used as electrocorticogram-electrode arrays, known as ECoGs (Figure 2.6b-i), to enable the measurement of LFPs over large brain areas [66]. Likewise, they are used to interface the spinal cord (Figure 2.6b-ii) to carry out electrochemical neuromodulations [54], or to contact anatomical structures such as damaged or missing sensory hair cells in the cochlea or the retina in the eye for the restoration of hearing [51] and vision [55, Pt. II. Retinal Approaches], respectively.

Circumvented probes

Circumvented probes are devices that surround the target tissue, mainly peripheral nerves. They are also sheet-like structures like conformal surface probes, however during fabrication and/or implantation they are subjected to a temper/wrapping step. Designs vary from cuff devices (Figure 2.6c-i-ii), which have a hollow-tube design with a predefined diameter, to ribbon-like structures (Figure 2.6c-iii), which adapt to the diameter of the target nerve. In both cases, the electrodes are facing the inner side of the implant [67]–[69].

Regenerative probes

Regenerative devices intend to regenerate nerve fibers through the holes of a sieve structure that is placed between the two cut ends of a nerve stump (Figure 2.6d). Likewise, guidance channels placed at each end of the sieve are used to direct and fix, while ring electrodes surrounding the sieve holes are used to stimulate and record the electrical activity of the nerve. Main applications of sieve probes comprise the reinnervation after amputation trauma and basic research concerning for example the control of artificial limbs [67], [69].

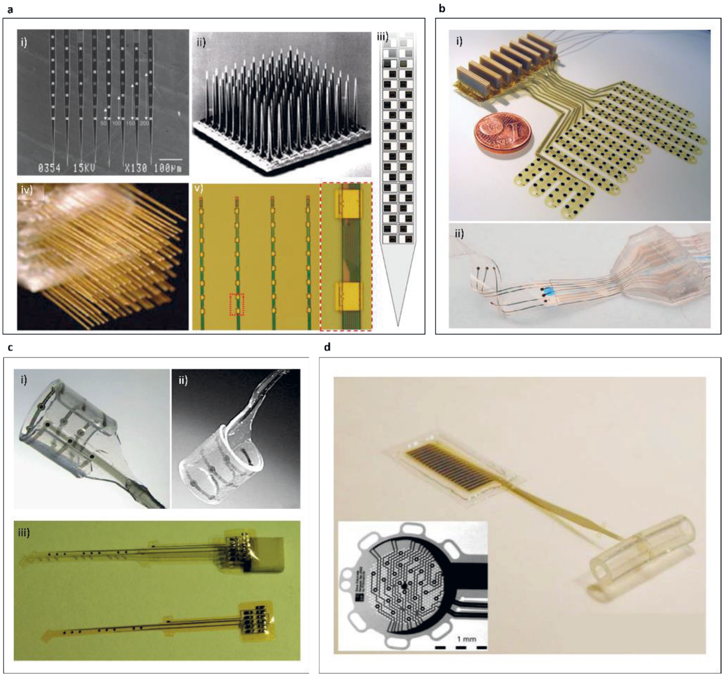

Figure 2.6. Types of neural interfaces. a) Penetrating probes: i) Michigan array [70], ii) Utah array [60], iii) Neuropixels probe [62], iv) iridium microwire array [61], and the v) flexible NET-e device [64]. b) Conformal surface probes: i) flexible ECoG-electrode array [66] and the ii) electronic dura implant. c) Circumvented interfaces: Cuff probes in i) [67] and ii) [69], and iii) ribbon probes [68]. d) Regenerative probe. The inset shows the sieve structure of the implant [67].

2.3. Visual prostheses

Visual prostheses are neural interfaces that aim to restore the lost sense of vision. To this end, efforts have been made to develop electronic devices that consist mainly of a light sensor connected to a microelectrode array (MEA). In this way, visual information is artificially transduced into electrical signals that stimulate electrically the remaining neurons at specific sites along the visual pathway (Figure 2.7). Thus, when photoreceptors of the retina are lost but the remaining neural network from the inner retina to the visual cortex is still intact, retinal implants are employed. If the visual pathway from the retina to higher order neurons in the brain is damaged, cortical implants have been pursued. Additionally, approaches to stimulate the axons of RGCs at the optic nerve or its extension at the LGN in the thalamus are being investigated [71], [72].

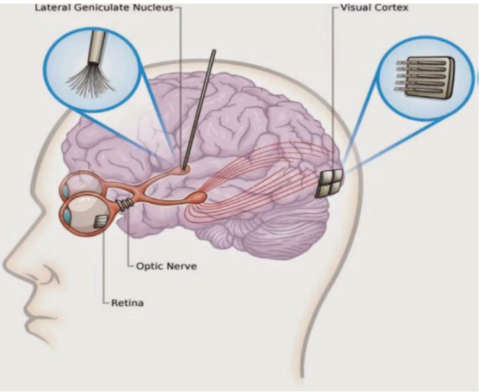

Figure 2.7. Targets of visual prostheses for electrical stimulation. Implants aiming to restore vision target different neurons along the visual pathway. Surface conformal implants are used to interface the retina, cuff-like and penetrating devices are used to stimulate the optic nerve, DBS electrodes or bundled microwires are used in the lateral geniculate nucleus (LGN), and both surface and penetrating prostheses are used to stimulate the visual cortex. Image from [73]

2.3.1. Retinal implants

Retinal implants have been developed to artificially replace the function of dead photoreceptors in blind patients with degenerative retinal diseases such as RP and AMD [7]. To this end, two main strategies have been established to detect light and perform electrical stimulation. The first one consists of an extraocular camera that detects visual information and a signal processor that translates such information intro electrical pulses, which are sent to individual electrodes of an intraocular MEA interfacing the retina. The second approach uses natural incident light or infrared light projected onto the retina, where an intraocular array of photodiodes measures local light intensity and/or transduce light into energy to trigger the stimulation of nearby neurons in the retina [7], [72].

Retinal implants have demonstrated significant progress in the restoration of useful vision in blind patients. Visual percepts experienced by patients comprehend mainly patterns of monochromatic light spots called phosphenes [7] that allow them to identify and localize objects, detect motion, detect letters, and in the best cases perform limited reading [6], [71]. However, half of the patients with implanted retinal devices have only experienced rudimentary improvements, such as dark and bright light perception [74].

Depending on the location where the prosthesis interface the tissue, retinal implants can be mainly distinguished as epiretinal, subretinal, and suprachoroidal (Figure 2.8):

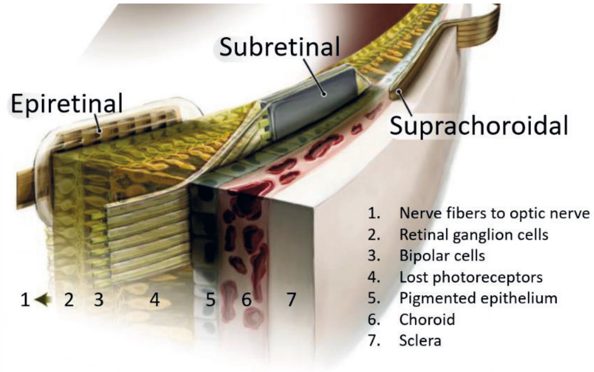

Figure 2.8. Location of retinal implants. While epiretinal implants are located at the surface of the nerve fibers of retinal ganglion cell, subretinal implants are located at the site where photoreceptors are lost. Additionally, suprachoroidal implants are placed between the choroid and the sclera of the eye. Image adapted from [71].

Epiretinal implants

Epiretinal implants are placed on the surface of the nerve fibers of RGCs (Figure 2.8). Their target is to carry out a direct stimulation of RGCs. However, collateral stimulation of RGC axons, as well as of bipolar cells, can lead to retinotopically incorrect phosphenes, thereby creating distorted visual percepts in patients [7], [71], [75]. While epiretinal approaches use mostly an extraocular camera in combination with an intraocular surface MEA implant [72], efforts to develop an epiretinal photovoltaic system [76] and a complete intraocular device with penetrating Si nanoneedles [77] are still under research.

To date, two epiretinal systems targeting patients with severe RP have been granted with approval for commercialization: the Argus II System (Second Sight Medical Products, USA), FDA and CE mark approved with 60 stimulating electrodes, and the IRIS II [7] (Pixium Vision, France), CE mark approved with 150 electrodes. Although the Argus II system has been widely implanted in ~ 300 patients worldwide, and both have shown visual improvements in blind patients, both products are no longer manufactured. In the case of Second Sight Medical Products, efforts will focus on the development of a cortical implant [7]. Additionally, initiatives like EPIRET (RWTH-Aachen University, Germany) finished a clinical trial with six patients [78], and NR600 (Nano Retina, Israel) is undertaking preclinical studies [77].

Subretinal implants

Subretinal implants are placed at the input region of the retina, between the residual layer of photoreceptors and the RPE (Figure 2.8) [71]. Given their close position to the degenerated region, the aim is to use the residual healthy network of the retina as early in the visual pathway as possible. Thus, stimulation of bipolar cells is mainly the target, albeit stimulation of RGCs is also expected [6], [7]. Unlike epiretinal implants, subretinal prostheses use the intraocular photodiode approach as the sensing element of light, allowing patients to exploit the natural movement of the eye when detecting visual information [6], [7], [71], [72].

Containing 1500/1600 photodiodes and aiming to treat blind patients with RP, the Alpha IMS/AMS implant (Retina Implant AG, Germany) is the only subretinal device with CE mark approval. However, the company that develops such devices dissolved in 2019 and research will be continued from the academy. Moreover, the PRIMA implant (Pixium, France) is under ongoing clinical trials in Europe and the USA, targeting patients with AMD [7], [71], [79]. Other initiatives with preclinical studies include the Boston Retinal Implant Project (Harvard University and MIT, USA), and the Liquid Crystal Polymer Prosthesis (Seoul National University, Korea).

Suprachoroidal implants

Suprachoroidal implants are placed between the choroid and the sclera or within the sclera (Figure 2.8), thereby simplifying surgery procedures but avoiding in turn the direct contact of the stimulating electrode with the neural retina. The latter implies that suprachoroidal devices require higher currents for stimulating retinal neurons, being bipolar cells the closest input of the retinal network [7]. Clinical trials with implants containing 33 (Bionic Vision Technologies, Australia) [80] and 49 stimulating electrodes (Osaka University, Japan) [81] have shown visual percepts in patients.

2.3.2. Optic nerve and thalamic implants

Cuff and penetrating neural interfaces have been used to stimulate electrically the optic nerve. Only two volunteer patients with RP have been implanted with cuff implants, who reported colored phosphenes with irregular shapes and locations [82], [83]. Moreover, *in vivo* experiments in cats have shown that the stimulation of the optic nerve with penetrating probes evoked electrical potentials whose position in the visual evoked cortical map shifted in accordance to the penetration depth within the nerve [84]. The latter results have served as proof of concept of the potential use of optic nerve stimulation.

Additionally, electrical stimulation to the LGN in the thalamus (Figure 2.7) has been tested in animal experiments using tetrodes (tungsten microwires). Results show visual percepts that were predictable when comparing fast eye movement responses in monkeys after electrical and optical stimuli. While the deep position of the LGN in the brain has hindered the early research of this approach, technology advancements available for DBS has enabled the use of neural interfaces for such target in the visual pathway. Moreover, considering that the LGN has a large projection of the fovea, neurons corresponding to the central visual fields are highly represented in the LGN. Hence, simple and focalized visual percepts should be possible when stimulating the LGN. This approach is still under development [85].

2.3.3. Cortical implants

Cortical implants aim to stimulate the primary visual cortex (V1) at the occipital lobe of the brain [73]. Early attempts were made in the 1960s, in which surface stimulating electrodes were placed at the occipital surface generating phosphenes with consistent locations at one or several spots in the visual field. Although the feasibility of a visual prosthesis targeting the surface of the visual cortex was shown, it required high stimulating currents that caused pain and light precepts were diffuse and did not last long enough to enable the formation of concrete images [86]. Furthermore, research using an intracortical microstimulation approach proved the use of lower current thresholds in the generation of phosphenes and the increased density of the electrodes yielded improvements in spatial resolution [87].

Cortical implants might offer advantages over the visual prostheses previously described: i) given the large surface area of the visual cortex (~ 1400-6300 mm^2), a larger number of electrodes could be implanted, what can potentially offer a higher spatial resolution, ii) the implantation of electrodes at the occipital lobe is easier than thalamic implants or subretinal implants, and iii) cortical implants can be used to treat a wider range of causes and diseases that lead to blindness [73].

Moreover, different initiatives pursuing a cortical visual prosthesis lead approaches that comprise the intracortical stimulation of the visual cortex using Utah- and Utah-slanted-like arrays to reach different layers in V1. Examples are given by the CORTIVIS project (Miguel Hernandez de Elche University, Spain) [55, Ch. 15], the intracortical visual prosthesis project ICVP (University of Illinois, USA) [55, Ch. 16], or the Gennaris vision system (Monash University, Australia) that proposes the use of tiles of Utah-like arrays [55, Ch. 17]. So far, no cortical visual prosthesis is approved for commercialization. While some projects are undergoing clinical trials, such as NeuroPace (University of California, USA), CORTIVIS (Miguel Hernandez de Elche University, Spain), and the Orion project (Second Sight Medical Products, USA), there are many other efforts that are under research and development [88].

2.4. Neural stimulation and recording

The principles behind neural interfaces that perform electrical recording and stimulation are given by the physiology that gives rise to nerve impulses, the modelling of the cell membrane as an electric circuit, the modelling of the interface between the electrodes and the target tissue, the charge transfer mechanisms during electrical stimulation, and the type of recording aimed.

2.4.1. Neurophysiology

In the nervous system, neurons communicate through electrical and chemical signals. On one side, electrical signals are mediated by concentration gradients and charge differences that are generated by the fluctuation of ions among the intra- and extracellular space of a neuron. On the other side, chemical signals are given by the release of neurotransmitters at the chemical synapse of two neurons (Figure 2.9). Additionally, although less common in the CNS, electrical synapses comprising gap junctions are present, providing a low resistance pathway to communicate and synchronize neurons [89].

In mammalian cells, the intracellular concentration of K^+ is higher than the extracellular concentration, whereas the concentration of sodium (Na^+), calcium (Ca^{2+}), and chloride (Cl^-) ions is lower inside and higher outside the cell. The latter generates a concentration gradient that drives the diffusion of ions from higher to lower concentration regions. Likewise, given the electric charges carried by ions, their movement is also influenced by electric fields. While it is true that the cell membrane has an insulating nature, the membrane is permeable to specific ions, which generates the separation of charges across the membrane that results in an electric potential. Thus, when the current flow of an ion *i* is zero or at equilibrium, the membrane potential is determined by the Nernst equation (Eq. 2.1):

$$E_i = \frac{RT}{z_i F} \cdot \ln\left(\frac{[i]_{out}}{[i]_{in}}\right) \tag{2.1}$$

In Eq.2.1, R is the gas constant (8.314 J/K mol), T is the temperature (°K), z_i is the valence of the ion, F is Faraday's constant ($9.6 \cdot 10^4$ C/mol), and $[i]_{out}$ and $[i]_{in}$ are the extracellular and intracellular concentrations of the ion [90, Ch. 2].

Furthermore, the concentration gradient and the ion distribution of a cell membrane is maintained by two main ion transport mechanisms. The first is product of the selective permeability of the membrane to ions such as K^+, which causes an efflux that produces a negative charge inside the cell. The second mechanism is driven by the active transport of ion pumps, such as the Na^{2+} - K^+ pump, which is a transmembrane protein that produces a negative net charge after pumping out three Na^{2+} for every two K^+ that are pumped in.

Under the assumption that a constant electric field is generated across the membrane, the membrane potential (E_m) can be described as a function of the membrane permeability for a specific ion (P_i) and the corresponding ionic concentrations. The latter is defined by the Goldman-Hodgkin-Katz (GHK) voltage equation [90, Ch. 2] (Eq. 2.2):

$$E_m = \frac{RT}{F} \cdot \ln\left(\frac{P_K[K^+]_{out} + P_{Na}[Na^+]_{out} + P_{Cl}[Cl^-]_{in}}{P_K[K^+]_{in} + P_{Na}[Na^+]_{in} + P_{Cl}[Cl^-]_{out}}\right) \tag{2.2}$$

In a resting state, the membrane potential of a neuron is ~ -70 mV. After a stimulus, neurotransmitters released at the synapse activate ligand-gated ion channels that enable the influx and efflux of ions across the membrane. This current flow generates graded potentials that can be distinguished as excitatory postsynaptic (EPSP) or inhibitory postsynaptic (IPSP) potentials, depending whether the local voltage change across the membrane is positive or negative. When the summation of these localized potentials induces a positive shift higher than the threshold potential (~ -55 mV), the neuron depolarizes and an AP, known as a nerve impulse, is generated.

During depolarization, Na^+ channels are opened and Na^+ enter the intracellular space. When the AP is reaching its maximum peak, K^+ channels are opened and Na^+ channels are closed, inducing then the repolarization of the neuron and further hyperpolarization due to the continuous outflow of K^+ outside the membrane. Once the ion channels are closed, the neuron recovers its resting potential, and the AP is then propagated along the axon of the neuron until it reaches the axonal terminal. Here, voltage-gated channels open and allow the inflow of Ca^{2+}, thereby triggering the release of neurotransmitters to convey the signal to the next postsynaptic neuron (Figure 2.9) [90, Ch. 2], [91], [92].

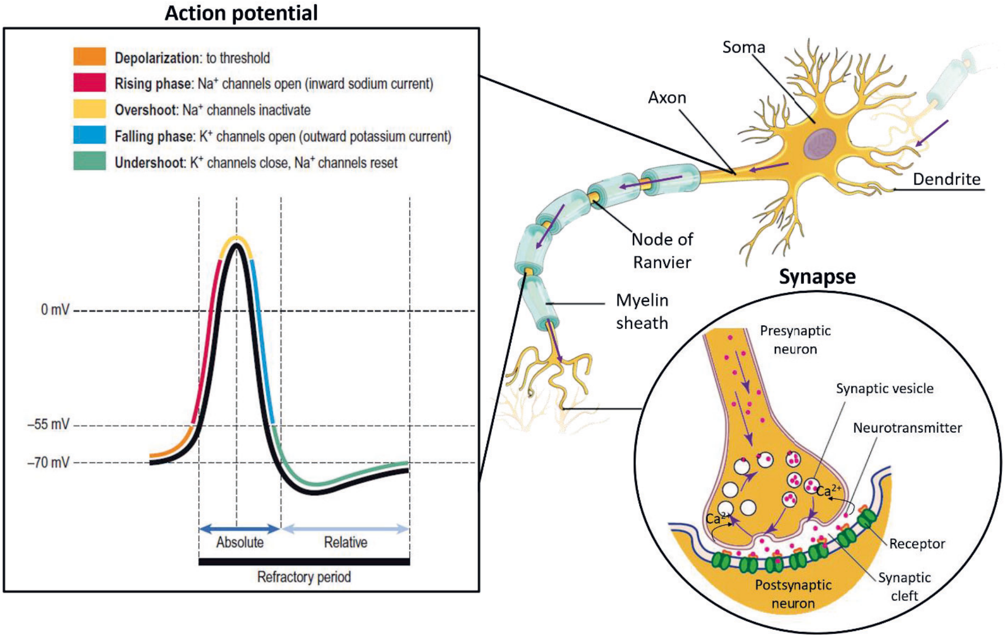

Figure 2.9. Neural signals. Schematic depicting the transmission of an electrical signal (action potential) that reaches first the dendrites of a neuron and is conveyed from the soma through the axon until it reaches the axon terminal, where a chemical signal (release of neurotransmitter) is triggered at the synapse with a postsynaptic neuron. Action potential: The resting membrane potential is increased towards the threshold at ~ -55 mV (orange). If the threshold is surpassed, the neuron depolarizes rapidly (red) forming an action potential (AP) (yellow). After the AP reaches its maximum peak, the neuron hyperpolarizes (blue) and the membrane potential becomes more negative. During this period, no other AP can be triggered (absolute refractory period). As the potassium (K^+) channels are close, the membrane voltage becomes mor negative (green) until the ion channels reset. During this (relative refractory period) another AP might occur if the stimulus strength is high enough to exceed the threshold. Synapse: The electrical signal propagates along the axon, arrives the axon terminal and voltage-gated calcium channels open, allowing the inflow of calcium ions (Ca^{2+}). The increase of Ca^{2+} triggers the release of neurotransmitters at the synaptic cleft, and the neurotransmitters bind the receptors at the postsynaptic membrane. Ligand-gated channels open allowing the inflow of ions, generating localized changes in the membrane potential, and shifting the resting potential to start the process of a new action potential. Images adapted from [90], [92]–[94].

2.4.2. Electrical model of the cell membrane

This section is based on [90, Ch. 3]. The cell membrane exhibits two electrical properties that can be characterized and represented in an electric circuit. First, the lipid bilayer of the membrane acts as an insulator among the extra- and intracellular space, thereby acting a capacitor. Second, the membrane pores harbor a resistance to the permeation of specific ions, performing as resistors (Figure 2.10.a). Given these properties, the cell membrane of a neuron can be represented by the equivalent circuit shown in Figure 2.10b.

The membrane current (I_m) can be determined applying Kirchhoff's law as follows:

$$I_m = I_c + I_i = C_m \frac{dE_m}{dt} + \frac{E_m - E_r}{R_m}$$

$$I_m = C_m \frac{dE_m}{dt} + G_m \cdot (E_m - E_r) \tag{2.3}$$

Eq. 2.3 uses the specific conductance of the membrane G_m [S/cm^2], which is the reciprocal of the resistance ($G_m = 1/R_m$). Thus, I_c stands for the capacitive current, I_i for the ionic current, C_m [F/cm^2] for the specific capacitance of the membrane (~ 1 µF/cm^2), E_m for the membrane potential, and E_r for the resting potential of the cell. Considering that the ionic current is carried by different ion species (I_K, I_{Na}, I_{Cl}) and assuming a linear relationship between I_m and E_m, I_m is given by the summation of the capacitive current and individual ionic currents (Eq.2.4).

$$I_m = I_c + I_K + I_{Na} + I_{Cl}$$

$$I_m = C_m \frac{dE_m}{dt} + G_K \cdot (E_m - E_K) + G_{Na} \cdot (E_m - E_{Na}) + G_{Cl} \cdot (E_m - E_{Cl}) \tag{2.4}$$

Eq. 2.4 is known as the Hodgkin-Huxley parallel conductance model (Figure 2.10.c), where G_K, G_{Na},and G_{Cl} represent the conductance of each ion. Additionally, the model accounts for the variations depending on time and on E_m for the G_K and G_{Na} (variable conductance depicted by the diagonal arrows). Moreover, the model can be also used to determine the resting potential. Considering the equilibrium conditions where the net current across the membrane is zero ($I_m = 0$) and no membrane potential changes are produced $\left(\frac{dE_m}{dt}\right) = 0$, the resting membrane potential is given by Eq. 2.5:

$$E_r = \frac{G_K E_K + G_{Na} E_{Na} + G_{Cl} E_{Cl}}{G_K + G_{Na} + G_{Cl}} \tag{2.5}$$

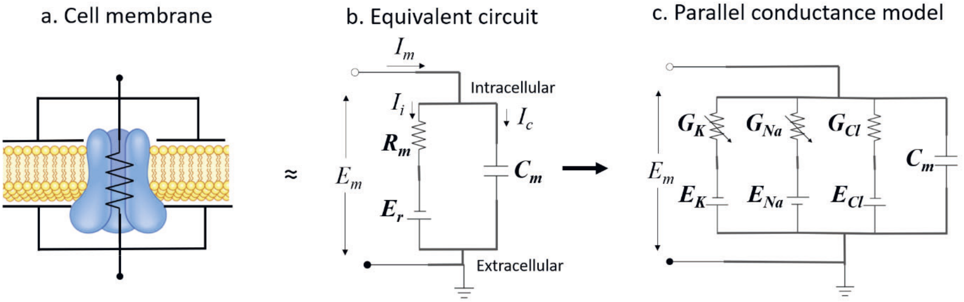

Figure 2.10. Electrical model of the cell membrane. a) The lipid bilayer of the cell membrane exhibits dielectric properties as a capacitor, while the cell membrane pores present a resistance to the permeation to specific ions. b) The electrical properties of the cell membrane are represented in the equivalent circuit, where R_m is the specific resistance [Ωcm^2] of the membrane to the ionic current (I_i), E_r is the resting potential, C_m is the specific capacitance of the membrane, I_m is the current flow across the membrane, which is the summation of I_i and I_c, the capacitive current, and E_m is the membrane potential. c) Considering the different ionic currents present in the cell membrane, a parallel conductance model is given. Here, the conductance is the reciprocal of the resistance (G=1/R), and G_i and E_i are the respective conductances and equilibrium potentials por K$^+$, Na$^+$, and Cl$^-$. Images adapted from [90], [92].

2.4.3. The electrode-electrolyte interface

When electrical stimulations and recordings are performed, the surface of the electrodes are in direct contact with the extracellular fluid (ECF) surrounding the target neurons, forming in turn an interfacial region referred as the electrical double layer. Thus, two phases can be distinguished: i) the surface of the electrode, which is an electronic conductor whose charges are carried by electrons, and ii) the ECF, which is an ionic conductor (electrolyte) whose charges are given by the ionic currents (K^+, Na^+, Cl^-) outside the cell membrane [95], [96].

This double layer was first described by Helmholtz as a parallel-plate capacitor, which assumed the formation of a compact ionic layer of opposite charge (e.g. positive ions) at the surface of the negatively charged electrode. This model was further developed by Gouy and Chapman, who considered not only the electrical but the thermal fields governing the charge distribution at the interface. Consequently, they introduced a diffuse layer model, in which the ionic density diminishes as a function of the ionic distance to the surface of the electrode. With a hybrid model, Stern introduced the compact-diffuse layer model, which accounts the Helmholtz and the Gouy and Chapman models as two capacitors connected in series [97].

Furthermore, considering that the latter model does not contemplate the role of the electrolyte's solvent with respect to the hydration and adsorption of ions, a triple-layer model was introduced by Esin and Markov, Grahame, and Devanathan [97]. As illustrated in Figure 2.11a, three regions are formed at the electrode-electrolyte interface: the inner Helmholtz plane (IHP), the outer Helmholtz plane (OHP), and a diffuse layer. The IHP spans from the electrode to the compact layer formed by water dipoles and dehydrated adsorbed ions at the surface of the electrode, the OHP extends from the center of the adsorbed ions to the center of the hydrated ions at their closest distance to the surface of the electrode, and the third region is the Gouy and Chapman's diffuse layer [96]–[99].

The triple layer can be described as three capacitors connected in series with a variable capacitance at the diffuse layer, due to the change rate of adsorbed ions at the surface of the electrode. Thus, the equivalent capacitance of the system is known as the capacitance of the double layer (C_{dl}) [96], [97]. According to the charge transfer mechanisms occurring at the electronic boundaries, the electrode-electrolyte interface can be modeled by a charge transfer resistor (R_{ct}) in parallel to C_{dl} (Figure 2.11b) [95]. The charge transfer mechanisms will be reviewed in the next section (2.4.4).

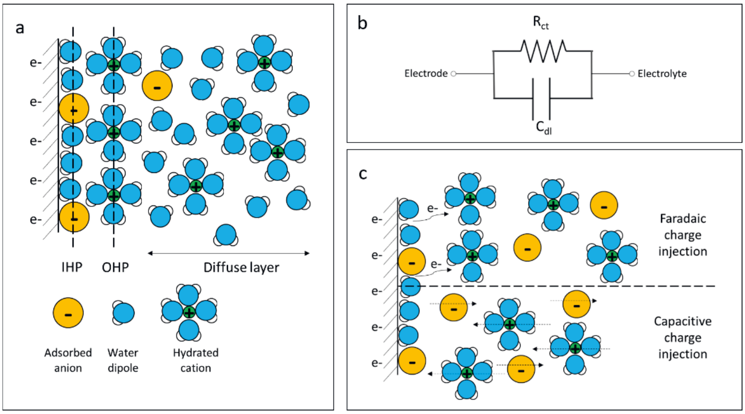

Figure 2.11. Electrode-electrolyte interface and charge transfer mechanisms. a) Illustration of the triple-layer model comprising the inner Helmholtz plane (IHP), the outer Helmholtz plane (OHP), and the diffuse layer. b) Equivalent circuit that models the electrode-electrolyte interface. R_{ct} is the charge transfer resistor and C_{dl} is the capacitance of the double layer. c) Schematic of the charge transfer mechanisms at the electrode-electrolyte interface during electrical stimulation. Both, faradaic (top) and capacitive (bottom) charge injections are displayed. Image adapted from [95], [99].

2.4.4. Neural stimulation

The aim of electrical stimulation in neural interfaces is to induce a physiological response by the depolarization of nearby neurons. The latter is accomplished by the transduction of charges carried by electrons at the surface of the stimulating electrode to ionic charges in the electrolyte (ECF) of the electrical double layer. Under the presence of an electrical stimulus, the neural tissue is stimulated by an electric field that is mediated by the flow electronic and ionic currents from the stimulating electrode through the ECF to the target neurons [95], [100]. In this way, the charge delivered by the stimulating electrode activates voltage-gated ion channels that lead to the depolarization of the target neuron, bypassing in turn the chemical synapse that interconnects pre- and postsynaptic neurons [38]. Thus, two main charge transfer mechanisms can be distinguished during electrical stimulation: capacitive and faradaic charge injection.

Pure capacitive charge transfer comprises the charging and discharging of the double layer capacitor C_{dl} (Figure 2.11b), which generates a reversible flow of charges without transferring electrons. When an electrode is subjected to an electrical pulse (voltage or current source), a charge redistribution is given by electrostatic forces that attract opposite charges and repel equal charges. For example, a negatively charged electrode attracts positively charged ions (cations) and repels negatively charged ions (anions), as depicted in Figure 2.11c. If the polarity of the electrode is reversed, the redistribution of charges is reversed and C_{dl} is discharged [95], [100].

On the other side, faradaic charge injection involves the transfer of electrons among the two phases of the double layer through the reduction (addition of an electron) and oxidation (removal of an electron) of species at the electrode surface (e.g. oxide layers) or in the electrolyte (Figure 2.11c, top) [95], [100]. Thus, faradaic processes are modeled with a charge transfer resistance R_{ct} that represents the electron flow between the electrode and the electrolyte [95].

Contrasting capacitive currents, the formation of faradaic currents can lead to changes in the composition of the electrolyte and to irreversible reactions where products in the solution cannot be recovered if they spread out from the electrode [95], [100]. Therefore, during electrical stimulation reversible faradaic reactions are approached by driving electrical potentials to small deviations from the equilibrium potential (no current flow) of the electrode and the electrolyte. In this way, the reaction rate is under kinetics control, allowing the transfer of electrons faster than the mass transport of the electrochemical products, which stay near the surface of the electrode and are then reversed to their initial form by reversed currents [95]. Likewise, some faradaic reactions are limited to the surface of the electrode, in which the products of the reaction stay and generate an effective charge storage while still transferring electrons. These cases are referred as pseudocapacitive reactions, which is the case of noble metals like platinum (Pt) [95], [100].

When performing electrical stimulation, the current flow generated by the stimulating electrode (I_e) upon the injection of an electrical pulse becomes a point of current source. Thus, assuming that a neuron is embedded in a homogenous, isotropic, and ohmic extracellular medium, the extracellular voltage (E_e) at a distance r from the point current source I_e, is defined by Eq. 2.6:

$$E_e = \frac{I_e}{4\pi\sigma_e r} \tag{2.6}$$

where σ_e is the conductivity of the extracellular medium. Thus, E_e scales inversely proportional with the distance from the current source [101], [102].

2.4.5. Neural recording

Neural prostheses that aim to record the electrical activity of neurons (for neuronal activity see section 2.4.1) use mainly microelectrodes as passive transducers to sense extracellular potential changes caused by ionic currents outside the cell membrane of nearby neurons. Given the electrical properties of the cell membrane (section 2.4.2), the electrode-electrolyte interface (section 2.4.3), and the fact that the insulating surface of the MEA allows the distinction between the conductive electrode and the electrolyte of the interface (ECF), a point contact model as pictured in Figure 2.12 can be used to describe the electrode-neuron interface [103], [104].

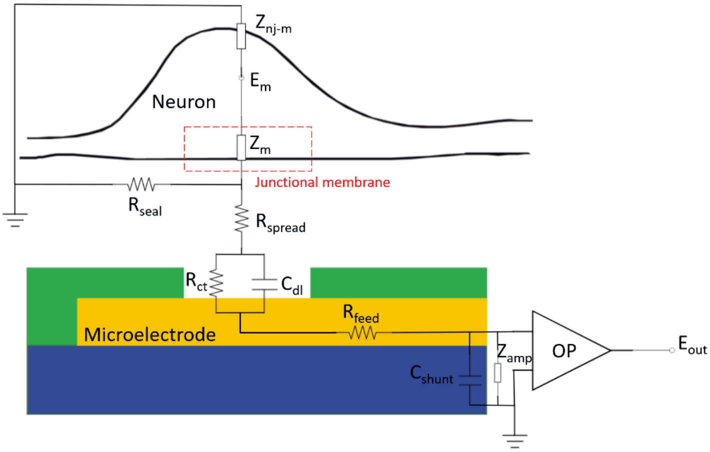

Figure 2.12. Point contact model of the electrode-neuron interface. The model includes the impedance of the junctional (Z_m) and non-junctional ($Z_{nj\text{-}m}$) sides of the cell membrane, which represent the Hodgkin-Huxley parallel conductance model, the ohmic resistance of the electrolyte (R_{spread}), the seal resistance (R_{seal}), the charge transfer resistance (R_{ct}), the double layer capacitor (C_{dl}), the resistance of the metallic feedlines (R_{feed}), the parasitic capacitance (C_{shunt}), and the input impedance of the amplifier (Z_{amp}). E_m is the intracellular voltage and E_{out} is the recorded voltage signal. Image adapted from [103]–[105].

In the model, the cell membrane is characterized by the Hodgkin-Huxley parallel conductance model (section 2.4.2). The electrode-neuron interface is represented by the junctional side of the membrane, the resistance generated by the gap between the cell and the electrode as a result of neuronal adhesion, referred as seal resistance R_{seal}, the resistance of the extracellular medium R_{spread}, the resistance (R_{ct}) and capacitance (C_{dl}) of the electrode-electrolyte interface (section 2.4.3), the resistance of the metallic feedlines R_{feed}, and the effective input impedance of the recording system. The latter includes the input impedance of the amplifier Z_{amp} and the parasitic capacitance of the whole system C_{shunt} (connectors, wires, insulation). Therefore, the electrode-neuron coupling is enhanced by a good adhesion between the neuron and the electrode (increased seal resistance), a low impedance of the electrode at 1 kHz, a low junctional membrane resistance, and low stray capacitances [96], [103], [105].

Likewise, Eq.2.6 can be applied to estimate the extracellular potential sensed by an electrode. In this case, the current point source is given by the ionic currents generated by a target neuron. Considering that the voltage captured by an electrode comes from n point current sources (I_n), representing n nearby neurons at a distance r_n from the recording electrode, Eq 2.6 can be re-written according to Eq.2.7 [103]:

$$E_e = \frac{1}{2\pi\sigma_e}\sum\frac{I_n}{r_n} \tag{2.7}$$

2.5. Requirements for the development of neural interfaces

The implantation of a synthetic device triggers the self-defense mechanism of the body, which comprises an instantaneous foreign body reaction (FBR) and an inflammatory response that progresses chronically by the activation of microglia and astrocytes along the lifetime of the device. The sustained response against the implant and the implantation site leads to the formation of scar tissue around the implant, hindering in turn the mechanical and electrical stability of the neural interface [57], [106], [107]. The latter, is influenced not only by the initial implantation trauma, but the physical and mechanical mismatch between the probe and the target tissue [57], [108]–[110]. Hence, the development of biologically safe and stable neural interfaces aims to mitigate FBRs and to enhance the mechanical compliance and electrode-tissue interface of the implant [57], [106].

2.5.1. Biocompatibility

In the presence of a foreign material, host responses inside living organisms are influenced by properties that characterize the bulk material and its surface. Examples of such properties include the chemical composition, the micro- or nano- structure, the degradation profile, the mechanical behavior, and the morphology and crystallinity of the surface [111]. Considering that neural probes are intended for acute and chronic implantation inside the body, materials composing the neural interface should be biologically, mechanically, electrically, chemically, and thermally stable. The latter means that materials that compose the implant should not be toxic or carcinogenic, should not degrade, or corrode, or leach byproducts, and should diminish the mechanical mismatch between the probe and the surrounding tissue [106], [111], [112].

2.5.2. Mechanical properties

Differences between the mechanical properties of neural interfaces and the target tissues have shown that probes based on stiff materials (e.g. Si or metal microwires) cause a stronger FBR than devices composed of soft materials, which have mechanical properties closer to neural tissues [54], [113], [114]. Likewise, adverse strains are induced to the tissues when the implant fails to conform and to deflect along with axial loads like the regular respiratory and cardiovascular micromotions, as well as with the natural movements of the body. Hence, the implant produces augmented micromotions that exacerbate the implantation injury [115]–[117].

Given the above, the mechanical mismatch is characterized by the flexibility and the compliance of the neural implant. The flexibility is an intrinsic property of the materials that compose the probe and is described by the Young's modulus (E). Compliance refers to the capability of the neural interface to conform and deflect along with the surrounding tissue and environment [57], [65], [109], [118]. The latter is described by the flexural rigidity [57] and the bending stiffness (sometimes called flexural stiffness) [118], [119, p. 215] of the devices.

Once implanted, surface conformal, circumvented, regenerative, and flexible penetrating probes can be considered as thin plates, as the thickness is small compared to the corresponding width and length [120, p. 38]. Consequently, the resistance of a thin plate to deflect upon small axial loads is defined by Eq. 2.8:

$$D = \frac{Et^3}{12(1-\nu^2)} \tag{2.8}$$

where D is the flexural rigidity, E is the Young's modulus, t is the thickness, and v is the Poisson's ratio of the material [119, Ch. 19], [120, Ch. 11]. Thus, the ability of a sheet-like implant to be compliant is mostly driven by the cube of its thickness.

In contrast, stiff penetrating implants are assumed as beams, with deflection curves that are smaller than the dimensions of the probe [121, Ch. 5]. Therefore, the small deflections of an elastic beam subjected to axial loads are described by Euler-Bernoulli's equation (Eq. 2.9):

$$EI\frac{d^2y}{d^2x} = -M_x \tag{2.9}$$

where E is the Young's modulus, I is the second moment of inertia, M_x is the bending moment at a distance x, and y is the transverse displacement or deflection of the beam. The linear relationship of EI yields to a constant defined as the flexural stiffness of the beam and the second integration gives the deflection y for any value of x [119, Ch. 13], [121, Ch. 5]. Depending on the cross-section of the beam, I can be defined according to Eq. 2.10 or Eq. 2.11 for a solid rectangular or circular cross-section, respectively:

$$I_x = \frac{wt^3}{12} \tag{2.10}$$

where w is the width and t is the thickness of the rectangular cross-section, or

$$I_x = \frac{\pi r^4}{4} \tag{2.11}$$

where r is the radius of the circular cross-section. Eq.2.9 can be resolved depending on the distribution of the external loads on the beam and the boundary conditions. Thus, considering a beam that is simply supported at both ends, e.g. one end from the holder of the implant and the other end by the surrounding tissue, and assuming a concentrated lateral force at the center of a beam with a rectangular cross-section (e.g. a Michigan Si shank), the deflection y is defined by Eq. 2.12:

$$y = \frac{FL^3}{48EI} \tag{2.12}$$

where F represents the external loads (e.g. respiratory micromotions) and L is the length of the beam [118], [119, p. 310]. Therefore, the small deflection suffered by the beam is inversely proportional to the flexural stiffness and proportional to the cube of the length of the beam.

Furthermore, it is important to assess the mechanical requirements for the insertion of penetrating probes. While it is true that the probe should allow deflections to conform with the surrounding tissue, the mechanical properties of the implant should, in turn, allow the insertion of the device itself. During implantation, penetrating shanks are subjected to an insertion force that is the summation of an axial force at the tip, frictional forces with the surrounding tissue, and a compressive force that clamps the probe among the tissue [110]. For a successful insertion, the critical buckling load (P_e) of the penetrating shanks should be higher than the insertion force [109]. Assuming penetrating probes (e.g. Michigan Si-based shanks) as fixed-pinned columns (Figure 2.13), P_e is derived after resolving Eq. 2.9 for the lateral deflections of a long beam under compressive forces. Thus, P_e is defined as:

$$P_e = \pi^2 \frac{EI}{L_e^2} \tag{2.13}$$

According to Eq. 2.13, also known as Euler's buckling load formula, P_e is directly proportional to the flexural stiffness *EI*, but inversely proportional to the square of the effective length (L_e) of the beam, which is determined by the boundary condition. For a fixed-pinned beam, $L_e = 0.7L$ (Figure 2.13) [119, Ch. 18]. In this way, when designing penetrating neural probes, a tradeoff among the material selection and the dimensions of the device is performed to ensure the mechanical stability of the implant. Additionally, when P_e is lower than the insertion force, as it is the case of most flexible penetrating probes, insertions aids comprising biodegradable coatings or stiff shuttles are used to facilitate the implantation of the device [65].

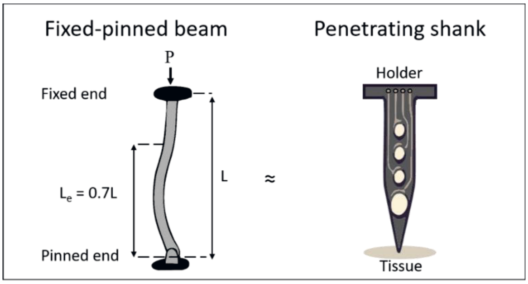

Figure 2.13. Boundary condition of a penetrating neural probe assumed as a beam. During insertion, the shanks of a penetrating neural probe are considered as fixed-pinned beams that are fixed from the holder and pinned from the tip. The effective length (L_e) of a fixed-pinned bean if given by the relation $L_e = 0.7L$, where L is the actual length of the beam.

2.5.3. Footprint

The material, design, and geometrical dimensions of a neural interface are important parameters to reduce the implantation trauma or footprint. For example, the use of tissue-like materials does not only reduce chronic FBRs, but avoids deformations of the target neural tissue, as it was demonstrated for surface conformal probes targeting the spinal cord [54]. In the case of penetrating implants, it has been shown that design optimizations comprising tapered tip designs and cross-sectional reductions can diminish both acute and chronic insertion lesions [122]–[125]. Accordingly, reduction of probe widths in the range of 4-30 µm and cross-sections below 10 μm^2 have shown cellular and subcellular surgical footprints and even glial scar-free neuro-integrations [64], [126].

2.5.4. Electrochemical properties

Most neural interfaces that record and/or stimulate the electrical activity of neural tissues fulfill these tasks through a sensing element that is typically an electrode. According to the geometric surface area (GSA), electrodes can be considered as macroelectrodes, with a GSA larger than ~100,000 µm^2, or as microelectrodes, with a GSA frequently below 10,000 µm^2. While macroelectrodes are mostly placed on a neural surface (e.g. ECoGs or some retinal implants) or embedded within the target tissue (e.g. DBS electrodes) for the interaction with populations of neurons and/or for capturing LFPs, microelectrodes are usually embedded in the neural tissue and aim to interact with single neurons [100].

Recording and stimulating electrodes are mainly characterized by the impedance at 1 kHz (Z), the charge storage capacity (CSC), and the charge injection capacity (CIC) [100], [127]. Z describes the opposition that an electrode presents to the flow of current when a voltage is applied [127], CSC refers to the total amount of cathodic or anodic charge available by the GSA of the electrode (usually given by its cathodic contribution as CSC_c), and CIC is defined by the charge density limit that an electrode can deliver avoiding the electrolysis of water [100], [127].

To perform electrical recordings and stimulation, Z is required to be as low as possible, typically in the range of 20 kΩ – 150 kΩ and preferably below 1 MΩ [100], [106]. To this end, a large GSA is important for reducing neural and thermal noise and increasing the signal-to-noise ratio (SNR) of the electrodes (a SNR ≥ 5 is preferred), as well as for decreasing stimulation voltages to inject determined currents. However, a large GSA reduces selectivity and spatial resolution (groups of neurons instead of single units), reason why efforts have been made to reduce the GSA of microelectrodes while increasing the electrochemical surface area (ESA). The latter can be achieved by enlarging the ESA of the electrodes with roughening methods to create nanoscale structures or with the use of porous materials, while still keeping a small GSA [100], [127].

Additionally, electrodes with a high CSC can deliver higher charges per stimulation phase, while a high CIC indicates that an electrode is capable of injecting higher charges within the water window. Thus, macroelectrodes allow higher charges per phase but a lower CIC, while microelectrodes permit lower charges per phase but a higher CIC [100]. The later, enables the use of microelectrodes with a small GSA (typically ≤ 2,000 µm^2) for localized stimulation, where a higher CIC is beneficial [100]; however due to the high charge densities, attention has to be given to avoid corrosion. Considering that charge density thresholds from 0.35 µC/cm^2 to 4 mC/cm^2 have been employed to stimulate the peripheral and CNS, both CSC and CIC should be high enough to cover the charge density thresholds of the target application. In the case of retinal prostheses, charge densities from 5 to 306 µC/cm^2 have been reported [100].

Furthermore, both the position and the geometric shape of the electrodes influence the current distribution during electrical stimulation and the corrosion behavior of the electrode. Regarding the position, electrodes placed at the level of the passivation layer or with no recession are prone to suffer from corrosion [128, Ch. 4] due to extremely high current densities at the edges [129]. In addition, it has been shown that unlike hemispherical geometries, disk and rectangular flat electrodes have a nonuniform current distribution, showing the rectangular geometries considerably higher current densities at the corners [128]. To achieve a more uniform current distribution during electrical stimulation, sharp corners should be avoided, disk geometries are preferred, and recessed electrodes should be used. Consequently, a recession depth between 0.1 – 0.4 times the radius of a disk is suggested [128, Ch. 4], [130].

Chapter 3

Materials and methods

3.1. Neurotechnology

3.1.1. Fabrication overview

The fabrication of neural interfaces depends on the type of probe aimed and materials used. Thus, three main processes can be distinguished: microwire, silicon-, and polymer-based (Figure 3.1). In this work the fabrication of polymer-based probes is of focus, therefore microwire and silicon-based processes will be briefly reviewed.

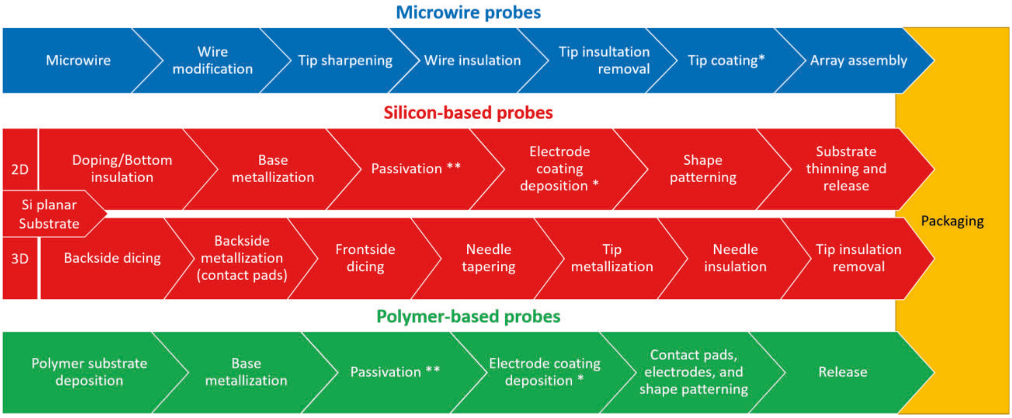

Figure 3.1. Fabrication overview of neural interfaces. Process flow depicting the main fabrication steps for microwire, silicon, and polymer-based neural probes. Steps with * indicate that are optional, and with ** denote the possibility of performing two passivation steps. Schematic adapted from [106].

Microwire arrays

The fabrication of microwire arrays starts with the modification of conductive microwires, typically from metal or more recently from carbon microfilaments, which are acquired from commercial suppliers. Modifications of the microwires include cutting, length adjustment, and straightening, followed by the sharpening of the tip. Then, the wires are passivated with a biocompatible polymer or glass, the insulation layer at the tip is removed, and finally, the wires are bundled together in an array. Depending on the process, before the assembly of the array, a conductive polymer or a metal coating can be deposited at the tip to improve the electrochemical properties of the wires [63], [106], [131].

Silicon-based probes

In the case of Si devices, two different processes are mainly performed for the fabrication of 2D (Michigan-like arrays) or 3D (Utah arrays) probes. A 2D Si micromachined process starts with a silicon-on-insulator (SOI) wafer or a boron-doped Si wafer with an insulation layer deposited on top. Then, a metallization process is performed to pattern the interconnects and the base of the electrodes. Next, an insulating layer is deposited and etched at the contact pads and electrode openings, followed by the patterning of the shape and release of the probe, which can include etching or thinning processes of the Si substrate. To enhance the electrochemical properties of the electrodes, conductive coatings at the electrode sites can be added to the process [106], [132]. In contrast, the fabrication of a 3D Si array starts by dicing the backside of the Si substrate and further metallization to generate the contact pads of the probe. Then, the frontside of the wafer is diced with vertical columns, which are tapered into needles. Afterwards, the needle-tips are coated with a conductive material and the array is covered with an insulation layer. At last, the passivation at the tip is removed for subsequent packaging [106], [112], [133].

Polymer-based probes

The base structure of polymer-based probes consists of a metal layer that is embedded between two layers, usually identified as substrate and passivation layers. The fabrication of such devices comprises the combination and permutation of processes based on microelectromechanical systems (MEMS) technology, which include additive processes (deposition), photolithography, subtractive processes (etching), and cleaning [65], [134]. The fabrication follows the surface micromachined process flow exhibited in Figure 3.1.

It starts with the deposition of a polymer-based layer (substrate of the probe) on top of a Si or a glass wafer, which serves as a carrier during the complete process. Depending on the materials selected, deposition techniques like spin-coating or chemical vapor deposition (CVD) are typically used. Then, a metal pattern is formed on top of the substrate layer after combining processes such as photolithography, sputtering or evaporation of metals using electron beams or heating coils, and subtractive processes such as lift-off or etching. Then, the deposition of an encapsulation layer is performed, followed by one or more etching steps to remove the latter layer from the electrode and contact pad sites and to pattern the shape of the probe. The etching steps comprise the combination of photolithography and dry etching techniques such as reactive ion etching (RIE). To this effect, a properly aligned photoresist mask outlines the region of interest, thereby allowing a selective etching of the substrate and passivation layers [65], [106], [110], [112].

In the fabrication development performed in this work, this base process was iterated, and extra steps were also performed to meet the design requirements, such as adding coatings to enhance the electrochemical properties of the electrodes. At the end, a release of the probes with a tweezer or wet chemical etching was performed. In a final step, the packaging comprised a manual flip chip bonding method to solder the contact pads of the probes onto an electronic board with a 16-channel connector, and the region around the contact pads was sealed using a biocompatible polymer. Specific details will be given in section 5.2.

3.1.2. Substrate and encapsulation materials

Si has been employed as a gold standard in the microfabrication of neural interfaces; however, the biocompatibility and the mechanical compliance of soft polymers like PI, PaC, and polydimethylsiloxane (PDMS) have allowed such materials to gain ground not only as encapsulation layers, but also as the main substrate of neural implants [112], [135], [136]. Table 3.1 shows the main properties for the materials mentioned above. In this work, Si was taken as reference after being the main substrate material in the fabrication of Si-BiMEAs (section 4.1.2), while the fabrication development of flexible BiMEAs was based on PI and PaC (section 5.2).

Table 3.1. Properties of substrate and encapsulation materials used in neural interfaces. The Youngs's modulus (*E*), the tensile strength, the melting temperature, the glass transition temperature, the degradation temperature, the thermal conductivity, the thermal coefficient of expansion, the electrical resistivity, the dielectric constant, the moisture absorption, and the biocompatibility are given for silicon (Si), polyimide (PI), parylene-C (PaC), and polydimethylsiloxane (PDMS). Data was mainly obtained from [65], [112], [135].[a] Values adapted from [137]. [b] Values adapted from [138]. [c] Given by the supplier. CDV stands for chemical vapor deposition. Non-available or non-applicable data are depicted with a minus (-).

Property	**Si**	**PI**	**PaC**	**PDMS**
Young's modulus [MPa]	150,000-170,000[a]	2,300-8,500	2,760	0.360-0.870
Tensile strength [MPa]	2,000[a]	392-650[b]	69	6.2
Melting temperature [°C]	1,414	-	290	-
Glass transition temperature [°C]	-	325-410	90	-
Degradation temperature [°C]	-	510-620	125	350 (oxidation) 750 (decomposition)
Thermal conductivity [W/cm K]	1.56	0.29	8.2	15-25
Thermal coefficient of expansion [ppm/K]	-	12	35	-
Electrical resistivity [Ω cm]	10^5	$>10^{16}$	$>10^{16}$	10^{15}
Dielectric constant	11.9	2.9-3.5	2.95-3.15	2.69-3.15
Moisture absorption [%]	-	0.8-1.4	0.06	<1
Biocompatibility	-	*In vivo*	USP class VI	USP class VI
Deposition method	-	Spin-coating	CVD	Spin-coating
Achievable thickness [µm]	-	1-13[c]	1-100	10-100

Polyimide

PI materials are commercially available polymers in the form of bulk films/tapes or as liquid photo- and non-photostructurable resists. However, photopatternable PIs have shown higher moisture uptakes than non-photopatternable PIs [135]. In general, PIs have a high thermal and chemical stability, low moisture absorption, high mechanical strength, an elastic modulus in the GPa range, and good insulating properties [135], [136]. Biocompatibility of some PIs, specially PI2611 has been tested by different research groups, showing low toxicity and low hemolytic capacity [135].

The liquid polymer is deposited through spin-coating and its synthesis comprises the thermal imidization of a poly (amic acid) precursor (resist), with a pre-curing step at ~120°C and a curing step at ~ 350°C under nitrogen environment. PIs can be patterned via wet chemical or dry etching techniques. Cured PI layers can be removed with wet etching using a combination of hot bases and strong acids or ozone solutions, while uncured PI layers can be removed using potassium hydroxide solutions at 5-30%. Dry etching is commonly used to remove and pattern cured PIs using O_2 plasma or its combination with fluorinated gases (CF_4, CHF_3, or SF_6). The mixture of the latter gases is generally used to etch polymers such as PaC and PDMS [136]. For the development of this work, non-photostructurable PIs were used.

Parylene-C

The most common type of poly-(para-xylylene) (PPX or parylene) polymers is poly(dicholoro-p-xylylene), known as parylene-C, which is commercially available as a granular dimer precursor [135]. PaC is popular in the fabrication of medical devices because it is FDA approved and it is rated with the highest biocompatibility rank in plastics, ISO 10993, USP class VI. In addition, PaC has an elastic modulus that is in the low GPa range, is chemically and biologically inert, allows surface modifications, has good insulating properties, and has high transmittance in the visible spectrum [112], [135], [136].

In this work, PaC coatings were achieved by a CVD process using a PDS 2010 Labcoater 2 (Specialty Coating Systems Inc., USA). The general process comprises the vaporization of the solid dimer at temperatures up to 170°C under vacuum (0.1 Torr). Then, the sublimated dimer is split into monomers in a pyrolysis process at temperatures up to 690°C, followed by the polymerization of the gaseous monomer at room temperature and under vacuum (0.05 Torr). This process allows the deposition of a conformal pinhole free coating at room temperature [139]. To enhance the adhesion of PaC, the adhesion promoter silane A-174 (Specialty Coating Systems Inc., USA) was used through a chamber swipe method, in which ~ 1 ml of silane was applied to the walls of the chamber using a cue tip. The CVD process is illustrated and described in detail in Figure 3.2. Moreover, surface modifications using O_2 plasma and dry etching processes with oxygen and fluorinated gases were used to process and structure PaC.

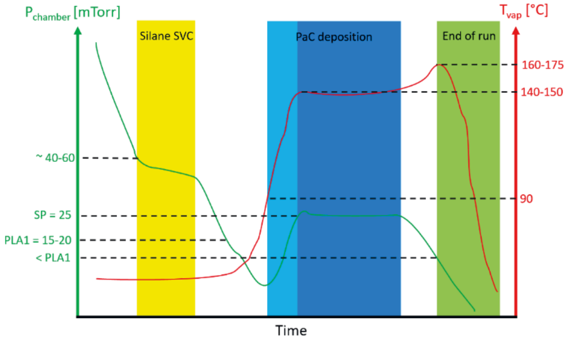

Figure 3.2. Chemical vapor deposition process of parylene-C. The schematic illustrates the phases of a typical chemical vapor deposition process (CVD) of parylene-C (PaC) using the adhesion promoter A-174 (silane) via the chamber swipe method. Once the vacuum pressure inside the deposition chamber ($P_{chamber}$) starts decreasing, the saturated vapor covering (SVC) of silane occurs around a $P_{chamber}$ of ~40-60 mTorr (yellow). When $P_{chamber}$ reaches the base pressure of the process (PLA1), the temperature of the vaporizer (T_{vap}) ramps up and $P_{chamber}$ decreases until T_{vap} reaches ~ 90 °C, starting to vaporize the dimer. In this phase (light blue) the gaseous dimer flows through the furnace and is split into monomers that area polymerized after arriving the deposition chamber at room temperature. Here, a short uncontrolled deposition occurs as $P_{chamber}$ rises. When $P_{chamber}$ reaches the deposition set point pressure (SP), T_{vap} is maintained around 140-150 °C to assure SP and a controlled deposition occurs (dark blue). After vaporizing all the dimer, $P_{chamber}$ decreases below PLA1 and T_{vap} has an overshoot around 160-175 °C to ensure the vaporization of possible dimer residues, setting then the end of the run. Schematic based on the operation manual given by the supplier [139] and the experimental usage of the PaC coater.

3.1.3. Electrode materials

Considering the direct contact and interaction that electrodes have with the target tissue during electrical recording and stimulation, materials used for this purpose should also fulfill the biocompatibility criteria and electrochemical properties described in section 2.5. Materials used as electrode coatings comprise mainly metals and metal derivatives such as Au, Pt, or $IrO_{x;}$ conducting polymers like poly(3,4-ethylenedioxythiophene) (PEDOT); carbon materials such as carbon nanotubes or graphene; and composite materials of metal-carbon or carbon-polymer materials [100], [127]. Table 3.2 shows the properties of the most used materials. In this work, IrO_x and PEDOT: PSS were pursued as electrode coatings.

Iridium oxide

In general, IrO_x has a higher electroactivity than Au and Pt. It harbors hydrated oxide layers and densely packed lumps that increase the ESA of the electrodes, thereby offering both electronic and ionic conductivity. Thus, IrO_x provides high CSCs and CICs, as well as reversible reactions during electrical stimulation. IrO_x has also proven good biocompatibility both *in vitro* and *in vivo*, showing in turn a high resistance to corrosion [100], [127], [140]. Due to these properties, IrOx has been widely implemented in retinal prostheses that perform electrical stimulation [19], [78], [140]–[142]. Given the above, IrO_x is selected as the electrode coating for the main development in this work.

Depending on the technique used to form the oxide layer and its thickness, IrO_x shows different electrochemical properties. The main methods used to form IrO_x films include activated iridium oxide film (AIROF), sputtered iridium oxide film (SIROF), and electrodeposited iridium oxide film (EIROF) [100], [127]. For the development of flexible intraretinal probes, SIROFs were provided by the Institute of Materials in Electrical Engineering 1 (*Institut für Werkstoffe der Elektrotechnik*, IWE-1, RWTH Aachen University, Germany), and were achieved using a reactive DC sputtering deposition [143], [144]. After deposition, SIROFs are usually activated and hydrated via cyclic voltammetry (CV) between potential limits that are outside or within the water window of IrO_x, respectively [128, Ch. 6.2], [140], [143], [144].

PEDOT: PSS

The use of PEDOT has been introduced in neural interfaces, not only because of the enhanced electrochemical properties that it can offer, but also because its low modulus of elasticity reduces the mechanical mismatch between the sensing electrode and the target tissue [127], [145]. Akin to IrOx, PEDOT exhibits electron and ion transport within the coating. To increase its electronic conductivity, PEDOT is usually doped with anions such as poly(4-styrenesulfonate), known as PEDOT: PSS. The electrodeposition of PEDOT: PSS on PtIr or Au electrodes has shown an increased electroactivity of PEDOT, outperforming IrOx films with CIC as high as 15 mC/cm^2 [100]. Likewise, novel techniques to facilitate the incorporation of PEDOT:PSS in the microfabrication of neural probes comprise the deposition of PEDOT:PSS via spin-coating [145]–[147].

Here, the integration of spin-coated PEDOT: PSS is tested. The PEDOT:PSS solution used in this work is based on [148]. Accordingly, the aqueous suspension of PEDOT:PSS (PH1000, Heraeus Clevios GmbH, Germany) was first filtered and mixed with 10% (v/v) of dimethyl sulfoxide (DMSO, Sigma Aldrich, Germany) and 1% (v/v) of 3-glycidoxypropyltrimethoxysilane (GOPS, Sigma Aldrich, Germany). Before use, the solution was left to rest overnight.

Table 3.2. Properties of electrode coating materials. The conductivity, the impedance (*Z*) reduction at 1 kHz in comparison with a bare or uncoated electrode, the cathodic charge storage capacity (CSC_c), the charge injection capacity (CIC), the potential limits versus a Ag/AgCl reference electrode, and the Young's modulus (*E*) are given for gold (Au), platinum (Pt), iridium oxide (IrO_x), and poly(3,4-ethylenedioxythiophene (PEDOT). Data obtained from [100], [127]. [a] Value from [149]. [b] Value from [150]. [c] Value from [151]. [d] Value from [140]. [e] Value from [152]. [f] Value from [153]. [g] Values from [154]. [c*] Indicates that the CSC was not measured in the reference.

Property	**Au**	**Pt**	**IrO_x**	**PEDOT**
Conductivity [S/m]	10^6-10^7	10^6-10^7	10^5-10^6	10^2-10^5
Impedance reduction at 1 kHz	4-50 times	2-800 times	4-150 times	2-300 times
Charge storage capacity [mC/cm^2]	0.09[a] – 2.56[b]	0.55 - [c*]	2.8 – 197[d]	8.7[f] – 123[g]
Charge injection capacity [mC/cm^2]	0.98[a]	0.05 – 3[c]	1 – 5	1.2[f] – 15
Potential limits [V] vs. Ag/Ag/Cl	-0.5 to 0.8	-0.6 to 0.8	-0.6 to 0.8	-0.9 to 0.6
Young's modulus [GPa]	70	140	262[e]	0.2 – 3
Charge transfer mechanism	Faradaic	Faradaic	Faradaic	Faradaic

3.2. Electrochemical characterization

Electrochemical characterization of the electrodes was carried out through electrochemical impedance spectroscopy (EIS), cyclic voltammetry (CV), and voltage transient measurements. EIS and CV were performed in a three-electrode cell set-up that consisted of a Ag/AgCl (3M KCl) reference electrode (DRIREF-2, World Precision Instruments, USA), a Pt wire as counter electrode, and each electrode of the probes (IrOx or PEDOT:PSS) as working electrode. Consequently, potentials are given with reference to the Ag/AgCl electrode. Most characterizations were performed in 0.1 M phosphate buffered solution (PBS) (for content and preparation of 1xPBS see Appendix 1).

3.2.1. Electrochemical impedance spectroscopy

EIS was performed in 1xPBS at room temperature applying a 10 mV sinus waveform with 51 measurement points, scanning frequencies from 1 Hz to 100 kHz. A VSP—300 potentiostat (BioLogic Science Instruments, France) of two channels was used. Thus, simultaneous measurements were performed by short-circuiting the reference and counter electrodes of each channel.

3.2.2. Cyclic voltammetry

CV was performed to activate SIROFs and to calculate the CSC_c of the electrodes. For SIROF activation, all electrodes of a single device were short-circuited and subjected to 300-600 CV cycles in 1xPBS at room temperature using a VSP—300 potentiostat (BioLogic Science Instruments, France). A sweep rate of 100 mV/s between the potential limits of -0.6 to 0.8 V (see section 5.2.1, SIROF activation) was used. Additionally, the last 5 CV cycles were performed individually for each electrode to calculate the CSC_c.

Given that the CSCc is defined as the time integral of the negative current density in a CV curve (Figure 3.3) [100], data of the last 5 CV cycles were used to calculate the CSC_c according to Eq. 3.1 [143], [144]:

$$CSC_c = \frac{1}{\upsilon} \int_{E_c}^{E_a} |i| dE_{WE} \tag{3.1}$$

where υ is the sweep rate, E_{WE} is the working electrode potential, E_a and E_c are the anodic and cathodic potential limits, and i is the negative current density.

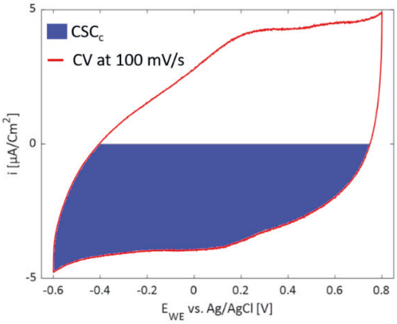

Figure 3.3. Cyclic voltammetry and charge storage capacity. Example of a CV cycle of a SIROF electrode (red) using a sweep rate of 100 mV/s between potential limits of -0.6 to 0.8 V. The colored area in blue represents the cathodic charge storage capacity (CSC_c) of the electrode. The y and x axes show the current density (i) and working electrode potential (E_{WE}), respectively.

3.2.3. Voltage transients

The CIC was determined for IrOx electrodes. Biphasic and symmetric rectangular current pulses were delivered to the stimulating electrode *in vitro* in 1xPBS and intraretinally at room temperature. Voltage transients were measured using a 2208 PicoScope oscilloscope (Pico Technology, UK) connected in parallel to the electrode and employing a Ag/AgCl pellet as counter electrode during pulsing. The pulses were generated by a custom-built current-controlled stimulator (see section 3.4), and were set as cathodic first current pulses with a phase period (T_{ph}) between 100 µs - 5 ms and an interphase of 20 µs between the cathodic and anodic phase. The cathodic (I_c) and anodic (I_a) currents were increased until the voltage drop at the interface was driven to the potential limits (-0.6 or 0.8 V for IrO_x, see Table 3.2), so that the maximum cathodic (E_{mc}) or anodic (E_{ma}) polarization voltages were determined 20 µs after the end of the cathodic or anodic phases (Figure 3.4) [100], [140], [155]. Hence, the CIC was calculated according to Eq. 3.2:

$$CIC = \frac{I_{mc} \cdot T_{ph}}{GSA} \tag{3.2}$$

where I_{mc} is the current that drives the electrode potential to E_{mc} and GSA is the geometric surface area of the electrode. CIC values for IrO_x were mainly tested for a T_{phase} of 500 µs.

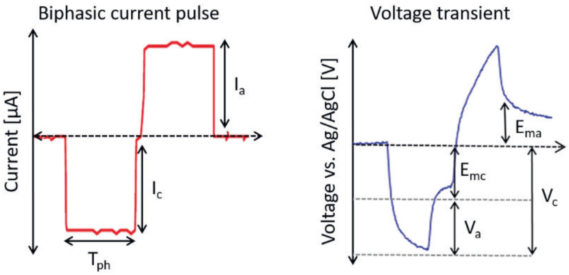

Figure 3.4. Voltage transient after current pulsing. The image illustrates the voltage response (voltage transient) at the stimulating electrode after injecting a biphasic and symmetric first cathodic current pulse with a phase period (T_{ph}) and cathodic and anodic currents I_c and I_a, respectively. In the voltage transient, Vc is the maximum cathodic voltage drop, V_a is the voltage drop across the electrolyte or tissue, E_{mc} is the maximum negative and E_{ma} is positive polarization voltages across the interface at the water window potentials. Images adapted from [100], [155].

3.3. Experimental setup

The experimental setup was based on [13], [25]. It consisted of a measurement chamber that integrated a micromanipulator system, the headstage of a bidirectional communication system, a light-emitting diode (LED) circuit, a perfusion system, and a digital light microscope (Figure 3.5a). The measurement chamber itself was a Faraday cage that held inside the components of the setup. The micromanipulator system comprised three motors with one degree of freedom each (x, y, and z axes), and a LabVIEW (National Instruments, USA) interface provided by the supplier to steer the system using a SM-6 controller (Luigs & Neumann, Germany). The headstage was coupled to the micromanipulator system, allowing not only to perform electrical recordings and stimulations (see section 3.4), but to support the movement of the penetrating probes during insertion. The LED circuit was used under the perfusion chamber to perform light stimulation.

The perfusion system included a REGLO Digital peristaltic pump (ISMATEC, Germany), a plastic bottle filled with the physiological solution, which was constantly oxygenated (section 3.5.2), and a perfusion chamber. The bottle was connected to a precision drop regulator (Exadrop, B.Braun, Germany) to allow a gravity mediated infusion. The perfusion chamber had a transparent floor with a PDMS pillow on top to support the biological sample (Figure 3.5b-c). A reservoir filled with the physiological solution was made with a glass ring (5 mm high, 19 mm in diameter) that was bonded to the base. Using needles as inlet and outlet of the system, the tissue was perfused at an approximate flow rate between 3-4 ml/min. Additionally, to allow the optical visualization of the experiments a quartz squared reservoir (8 mm high, 18 mm wide) was implemented (Figure 3.5c), and a VHX digital microscope (Keyence Deutschland GmbH, Germany) that was supported by a flexible arm from outside the cage was used.

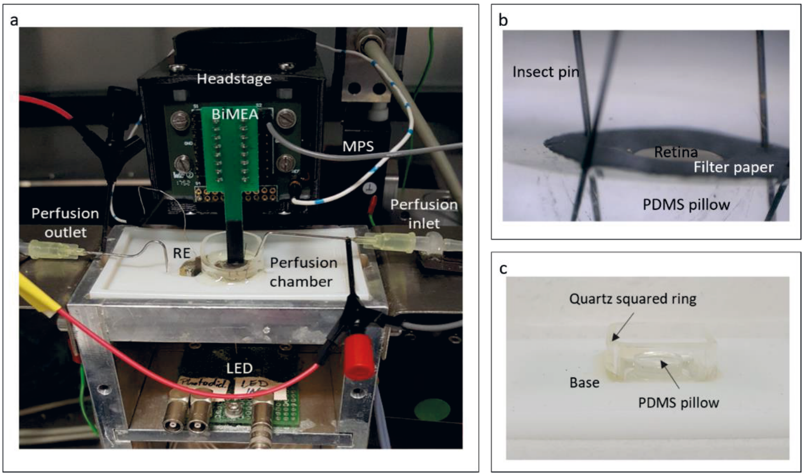

Figure 3.5. Experimental setup. a) Setup overview integrating the outlet and inlet of the perfusion system, the headstage coupled to the micromanipulator system (MPS), a BiMEA probe connected to the front-end of the headstage and inserted into the retina, the reference electrode (RE) inside the reservoir outflow, and a light-emitting diode (LED) circuit under the perfusion chamber to perform light stimulation. Imaged adapted from [13]. b) PDMS pillow supporting a retinal sample that is attached by a filter paper, which is in turn fixed by insect pins. c) Modified perfusion chamber with a quartz squared chamber to allow optical visualization of the experimental sample.

3.4. Recording/stimulation system

A bidirectional communication system based on the in-house data acquisition system, the BioMAS (Bioelectronic Multifunctional Amplifier System) [156], was implemented to record and to stimulate electrically at the same time (Figure 3.6). The BioMAS comprises a headstage, a main unit, an analog-to-digital converter (ADC), and a user interface. The headstage performs the first amplification stage of the recording system with a gain of 10x. The main unit holds the main amplifier of the system that offers a variable gain (1x, 10x, or 100x), a voltage-controlled stimulation unit, and a microcontroller. The ADC digitizes the analog signals that are then visualized through a LabVIEW (National Instruments, USA) interface from a computer.

To perform electrical stimulation while recording, the headstage of the system was upgraded to hold not only the first amplification phase of the system, but an in-built stimulator that can provide voltage- or current-controlled stimulation signals. The hybrid headstage includes a pre-amplification stage (pre-amp) for 16-channels, a switch-relay system to disconnect the stimulating electrode from the pre-amp and select the channel(s) for stimulation, a current measurement board (CMB) that measures the current delivered by the stimulating electrode(s) after a voltage-controlled stimulation (VCS) signal, and a current-controlled stimulator (CCS) based on a bipolarity current source sink [157, p. 230] (Figure 3.7 and Appendix 2). The headstage is supported by the main unit of the BioMAS, which delivers the voltage stimulation signal processed by the CMB or the CCS of the headstage and a trigger signal used to control the CCS and the switch-relay system. Additionally, the LabVIEW interface allows to select the channel(s) to be stimulated.

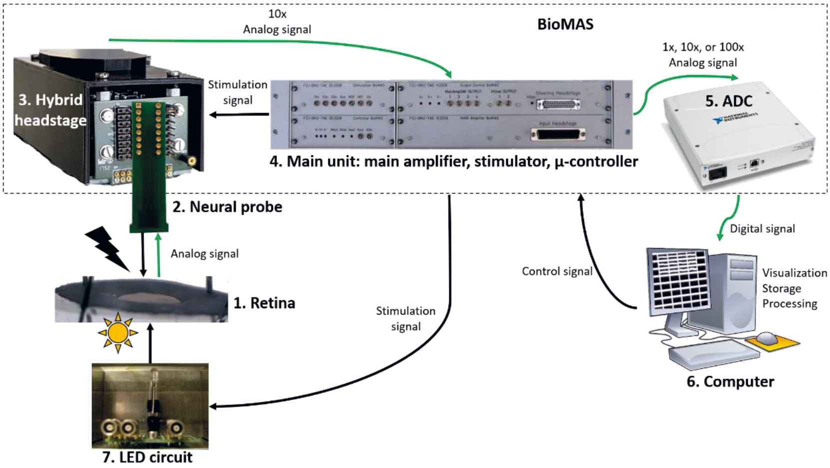

Figure 3.6. Overview of the bidirectional communication system. The system comprehends the electrical recording and stimulation of the retina. Recording: Depicted by the pathway of green arrows. The electrical activity of the retina (1) is captured by the electrodes of a neural probe (2) that is connected to a hybrid headstage (3), which comprises the first amplification stage (10x gain) of the BioMAS system. In the main unit (4), the analog signal is further amplified for total maximum gain of 1000x. The signal is then digitized by an analog digital converter or ADC (NI USB-6255, National Instruments, USA) (5) that transmits the signal to a LabVIEW interface in the computer (6) for data visualization, storage, and postprocessing. Stimulation: Depicted by the pathway of black arrows. A control signal is sent by the user from the computer (6) to the BioMAS system, where the microcontroller connected the stimulator (4) triggers a stimulation signal for optical and electrical stimulation of the tissue. In the former case, this signal reaches the LED circuit (7) setting on the LED light to stimulate the tissue (sun cartoon). In the latter case, the signal is processed by the hybrid headstage (3). Depending on the stimulation mode selected, the built-in stimulation system of the headstage will deliver a voltage- or current-controlled signal to the electrodes of the neural probe, thereby stimulating the tissue electrically (thunder cartoon).

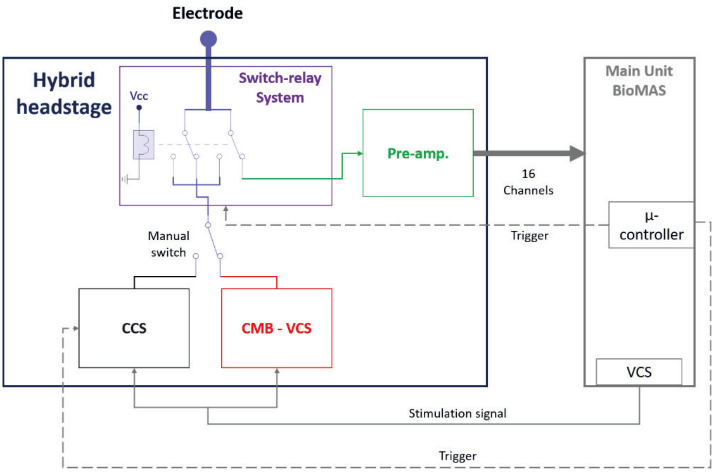

Figure 3.7. Block diagram of hybrid headstage. The headstage includes a pre-amplification stage (Pre-amp.) for 16-channels, a switch-rely system, a current-controlled stimulator (CCS), and a current measurement board (CMB) for voltage-controlled stimulation (VCS). The microcontroller (µ-controller) and the VCS of the main BioMAS unit provide a trigger and a voltage stimulation signal**.**

3.5. Retinal samples

3.5.1. Animals

Ex-planted retinas from the following mouse strains were facilitated by the Institute of Biological Information Processing-1, Molecular and Cellular Physiology (IBI-1) at *Forschungszentrum* Jülich (Germany). Intraretinal insertions and MEA recordings were mainly conducted with retinas from wildtype (WT) C57Bl/6N mice obtained from Charles River (USA) and C57Bl/6J-Pde6b^{rd10}/J mutants, hereafter *rd10*, which were bred locally from breeding pairs obtained from Jackson (strain name: B6CXB1-Pde6brd10/J, USA). In the latter, the *rd10* mutation was backcrossed onto the C57Bl/6J background for 5 generations before intercrossing to homozygosity. *Rd10* retinas were used as a model for retinal degeneration. Likewise, intraretinal recordings and dead stainings were performed in retinas from transgenic mice that express the genetically encoded Ca^{2+}- sensor TN-L15 (gift from Dr. O. Griesbeck, MPI for Neurobiology, Martinsried, Germany).

Mice were taken from the own live-stock breeding at the animal facility in *Forschungszentrum* Jülich. All animals were kept in a 12-hour dark/light cycle with water and food *ad libitum*, and all experiments were performed in accordance to the German law for the Protection of Animals and after approval was obtained by the regulatory authorities, the *Forschungszentrum* Jülich (FZJ number: ICS-4 OE2) and the *Landesamt für Natur*, *Umwelt und Verbraucherschutz* of North-Rhine Westfalia.

3.5.2. Retina preparation

Light adapted retinas were isolated under a reflected-light stereomicroscope (Stemi SV-6, Carl Zeiss GmbH, Germany) with ambient light and at room temperature as described in [13]. First, the animals were deeply anesthetized with isoflurane (Actavis Dtl. GmbH &Co. KG, Germany) and killed by decapitation. Right away, the eyeballs were enucleated and immersed in a petri dish filled with fresh Ames' medium (Sigma Aldrich, Germany), which was constantly oxygenated with carbogen gas containing 95% O_2 and 5% CO_2 (The Linde Group, Germany) at a pH of 7.4. Then, one eyeball was slit along the *ora serrata* to cut off the cornea, followed by the careful removal of the lens and the vitreous body. This procedure was performed consecutively for both eyes to provide a better oxygenation of the retina and keep its vitality. Afterwards, the retina was cut in halves. One piece was stored in the oxygenated medium until its use and the other piece was isolated from the eyeball.

The preparation continued by the fixation of the retinal sample, with the GCL facing downwards, onto a millipore filter paper (Merck KGaA, Germany) with a pre-cut central hole with a diameter of 1.5 mm. Subsequently, the retina/filter sandwich was transferred onto the PDMS pillow of the perfusion chamber with the GCL facing upwards, and finally the filter was fixed with insect pins (Figure 3.5b). The retina was then hydrated with a drop of medium and transferred to the experimental setup, where a constant perfusion was given to the tissue to keep its vitality. Details regarding the content and preparation of the Ames' medium can be found in Appendix 3.

3.6. *In vitro* electrophysiology

Intraretinal MEA recordings were performed with Si- and flexible-BiMEAs using the experimental setup and the recording/stimulation system described in sections 3.3 and 3.4. A sampling rate of 10 and 20 kHz and a Ag/AgCl pellet was used as reference electrode. Spontaneous activity (SA) and responses to physiological modulations of the electrical activity of the retina were recorded.

3.6.1. Treatment with high potassium concentration

As reported in [13], the spiking activity of WT retinas was modulated by adjusting the extracellular ionic concentration of the tissue. To this effect, a high extracellular concentration of K^+ was achieved by adding ~ 1.28 – 1.7 g of potassium bicarbonate ($KHCO_3$) to the regular Ames' medium, so that a K^+ concentration of at least 20 mM was obtained. The tissue was first perfused with normal Ames' medium, then the solution with high K^+ was given through the perfusion system for 2 min. After the induced effects were observed, the perfusion of the regular Ames' medium was re-established.

3.6.2. Light stimulation

As described in [13], light stimulation was performed using a LED circuit that consisted of a 5 mm round white LED connected in series to a 61.9 Ω resistor. The light source was placed underneath the perfusion chamber (Figure 3.5a) and was activated by squared pulses of 5 V provided the VCS unit of the BioMAS. The latter provided high photopic stimuli (7.96 $\mu W/mm^2$) akin to broad daylight for the activation of cone photoreceptors. In this way, single light stimuli with an ON duration of 500 ms were applied every 15 s during light stimulation of WT and TN-L15 retinas.

3.7. Biological characterization

Given the strong visible fluorescence exhibited by RGCs in TN-L15 mice, retinas from this mouse strain were used to conduct dead cell stainings for assessing the biological impact of acute intraretinal insertions. Once the shanks were retracted from the tissue, the biological samples were first stored in fresh oxygenated Ames' medium, followed by the staining of dead cells, the imaging of whole-mounted samples, and further post-processing of the images [158].

3.7.1. Dead stainings

Dead cells were stained using ethidium homodimer-1 (EthD-1, ThermoFisher Scientific Inc., USA), a cell-impermeable DNA binding dye. The protocol followed was adjusted from reports given to perform *ex vivo* stainings of live tissue slices [159]. The staining solution was prepared mixing 5 µl of 2 mM EthD-1 for every 1 ml of fresh oxygenated Ames' medium. Using a 24-well plate, each retinal sample was covered with 700 µl of the staining solution. To guarantee the vitality of the tissue, the well plate was placed inside a closed wet chamber that was constantly oxygenated during the staining period. The wet chamber consisted of a plastic box and lid covered with wet tissues. The staining was then performed inside the wet chamber using an orbital shaker at 60 rpm during 20 min. Afterwards, the dye was washed out with fresh Ames' medium during 10 min with constant shaking and oxygenation. At last, the samples were stored in fresh medium until imaging.

3.7.2. Confocal microscopy

Stained retinal samples were transferred into a chambered coverglass slide that was filled with fresh oxygenated Ames' medium. The whole-mounts were imaged at the Institute of Biological Information Processing-1, Molecular and Cellular Physiology (IBI-1) at *Forschungszentrum* Jülich (Germany). A confocal laser scanning microscope (TCS SP5 II, Leica Microsystems, Germany) was used to obtain Z-stacks at different focal planes with steps sizes between 5 – 9 µm and a total thickness between 60 – 150 µm. An argon laser generating wavelengths of 488 nm (typical for cy2 and A488) and a helium laser generating wavelengths of 543 nm (typical for cy3) were used to stimulate the fluorescent samples. Scanning was performed sequentially using wavelengths between 500-530 nm and 554-595 nm to detect the green and red fluorescence emitted by live RGCs and dead cells stained with EthD-1, respectively.

3.7.3. Image processing

The postprocessing of Z-stacks was performed using ImageJ [160]. First, the affected areas by the intraretinal insertion of each shank were manually segmented and selected as regions of interest (ROIs) in the maximum intensity projections of individual and merged channels (red for dead cells and green for live RGCs). These ROIs were outlined around areas comprising dead cells and visible neuronal loss at the insertion sites. Then, a manual threshold was performed to the maximum intensity projections of the red channel, obtaining in turn binary images that were further processed by the binary operation "open" and a watershed segmentation. The latter allowed the removal of isolated pixels and the separation of merged cells. At the end, the ROI manager was used to calculate the area corresponding to each ROI (hereafter referred as insertion trauma area or ITA) and the function "Analyze Particles" was employed to perform an automatic count of dead cells. Furthermore, the ratio between ITA and the cross-section of the intraretinal shank was defined as the insertion trauma area ratio or ITR.

3.8. Electrical stimulation

Electrical stimulation (ES) in voltage- and current-controlled modes were conducted in WT and *rd10* retinas using the hybrid headstage described in section 3.4. A monopolar configuration was used, so that the same Ag/AgCl reference electrode used for electrical recordings, which was placed far away from the tissue, served as counter/return electrode during ES. Thus, an IrO_x electrode in close proximity to the inner retina was selected as the stimulating electrode.

Considering that the response of indirect stimulation of RGCs is not consistent when performing repeated stimulation at frequencies higher than 1 Hz [38], six electrical pulses with a frequency of 0.05 Hz were applied during ES to avoid desensitization and to test the reproducibility of RGCs response. Moreover, the electrical stimulation efficiency (ESE) was defined as proposed by [12]:

the ratio between the firing rate (FR) during the first 400 ms after the ES artifact and the average FR of the last 8 s before the ES pulse. Hence, ESEs higher than one indicate an excitatory response, while negative ratios imply an inhibitory response in the electrical activity of the retina. An ES trial was then classified as successful if the average FR before and after ES was statistically different (see section 3.9 for statistical testing).

3.8.1. Voltage-controlled stimulation

Voltage-controlled stimulation (VCS) was performed using the protocol reported in [13]. Symmetric and biphasic voltage squared pulses with a first cathodic and a second anodic phase were employed using amplitudes of ±600 and ±800 mV and phase durations (T_{ph}) between 0.5 and 0.8 ms. Table 3.3 summarizes the parameters tested.

Table 3.3. Parameters for voltage-controlled stimulation. V_{stim} stands for the voltage amplitude and T_{ph} for one phase duration of the biphasic stimulation pulse.

Electrical stimulation code	V_{stim} [mV]	T_{ph} [ms]
ES-1	0.8	0.5
ES-2	0.8	0.6
ES-3	0.6	0.5
ES-4	0.6	0.6
ES-5	0.6	0.7
ES-6	0.6	0.8

Additionally, the current delivered by the electrodes during each ES phase ($I_{del,ph}$) was measured by the CMB of the hybrid headstage (section 3.4). Thus, the injected charge ($Q_{inj,ph}$) was calculated according to Eq. 3.3. Considering the GSA of the stimulating electrode, the charge density ($Q_{d,ph}$) was determined according to and Eq. 3.4:

$$Q_{inj,ph} = \int_0^{T_{ph}} I_{del,ph} dt \tag{3.3}$$

$$Q_{d,ph} = \frac{Q_{inj,ph}}{GSA} \tag{3.4}$$

3.8.2. Current-controlled stimulation

Current-controlled stimulation (CCS) was carried out using symmetric and biphasic current pulses with a first cathodic phase, thereby allowing charge-balanced stimulation pulses. Stimulation currents ($I_{stim,ph}$) between ± 0.5 and ± 10 µA and phase durations (T_{ph}) between 0.1 ms and 5 ms were employed. Table 3.4 summarizes the stimulation parameters tested with the corresponding $Q_{inj,ph}$ during CCS, which was calculated according to Eq. 3.5:

$$Q_{inj,ph} = I_{stim,ph} \cdot T_{ph} \tag{3.5}$$

Each $Q_{inj,ph}$ marked in green was tested for each retinal sample, referring to each tested parameter as a stimulation trial.

Table 3.4. Parameters for current-controlled stimulation. For each stimulation phase, $Q_{inj,\ ph}$ is the charge injected during current-controlled stimulation (CCS), $I_{stim,\ ph}$ is the amplitude of the stimulating current pulse, and T_{ph} is the duration of the phase. Cells shaded in green depict the parameters tested during CCS.

$Q_{inj,\ ph}$ **[nC]**	T_{ph} **[ms]**													
$I_{stim,\ ph}$ **[µA]**	***0.1***	***0.2***	***0.3***	***0.4***	***0.5***	***0.6***	***0.7***	***0.8***	***0.9***	***1***	***2***	***3***	***4***	***5***
0.5	0.05	0.1	0.15	🟩 0.2	🟩 0.25	🟩 0.3	🟩 0.35	🟩 0.4	🟩 0.45	🟩 0.5	🟩 1	🟩 1.5	🟩 2	🟩 2.5
1	0.1	0.2	0.3	🟩 0.4	🟩 0.5	🟩 0.6	🟩 0.7	🟩 0.8	🟩 0.9	🟩 1	🟩 2	3	4	5
2	0.2	0.4	0.6	🟩 0.8	🟩 1	🟩 1.2	🟩 1.4	🟩 1.6	🟩 1.8	🟩 2	4	6	8	10
3	0.3	0.6	0.9	🟩 1.2	🟩 1.5	🟩 1.8	2.1	2.4	2.7	3	6	9	12	15
4	🟩 0.4	🟩 0.8	🟩 1.2	🟩 1.6	🟩 2	2.4	2.8	3.2	3.6	4	8	12	16	20
5	🟩 0.5	🟩 1	🟩 1.5	🟩 2	2.5	3	3.5	4	4.5	5	10	15	20	25
6	🟩 0.6	🟩 1.2	🟩 1.8	2.4	3	3.6	4.2	4.8	5.4	6	12	18	24	30
7	🟩 0.7	🟩 1.4	🟩 2.1	2.8	3.5	4.2	4.9	5.6	6.3	7	14	21	28	35
8	🟩 0.8	🟩 1.6	2.4	3.2	4	4.8	5.6	6.4	7.2	8	16	24	32	40
9	🟩 0.9	🟩 1.8	2.7	3.6	4.5	5.4	6.3	7.2	8.1	9	18	27	36	45
10	🟩 1	2	3	4	5	6	7	8	9	10	20	30	40	50

3.9. Statistical testing

Statistical testing was carried out in OrginPro 2019 (OriginLab Corporation, USA) for section 4.3 and with self-written scripts in Matlab 2018b (The MathWorks Inc., USA) using the "Statistics and Machine Learning" toolbox for the other sections. Normality of data was tested applying the Kolmogorov-Smirnov test and the Lilliefors test. In addition, non-parametric bootstrap tests were carried out using a pooled resampling method [161] with ten thousand bootstrap replicates when the normality of data was rejected. For post-hoc pairwise testing, Bonferroni correction was applied. Statistical tests applied along the manuscript are summarized in Table 3.5:

Table 3.5. Summary of statistical testing. The following parameters were subjected to statistical testing: firing rate (FR) during electrical stimulation (ES), electrical stimulation efficiency (ESE), current delivery per phase ($I_{del,ph}$), charge density per phase ($Q_{d,ph}$), insertion trauma area (ITA), insertion trauma area ratio (ITR), count of dead cells (# dead cells), signal-to-noise ratio (SNR), mean spike amplitude (SPK), maximum spike amplitude (MSPK), and the success rate of insertion.

Parameter tested	**Section**	**Test**
FR differences during ES	4.3 and 6.3	Paired-t test
ESE, $I_{del,\ ph}$, $Q_{d,\ ph}$	4.3 and 6.3.2	Non-parametric Mann-Whitney-U test
ITA, ITR, # dead cells	7.1	Post-hoc pairwise testing using non-parametric bootstrap t-tests and Bonferroni correction
SNR, SPK, MSPK	7.3	Post-hoc pairwise testing using non-parametric bootstrap t-tests and Bonferroni correction
Success rate of insertion	7.4	Post-hoc pairwise testing using Fisher's Exact test with Bonferroni correction

Chapter 4

Silicon-based BiMEAs: A proof of concept

A bidirectional communication strategy between a prosthetic device and retinal cells has been proposed by the BiMEA consortium. The aim is to establish a closed-loop feedback system that tracks and modulates the electrical activity of the retina, allowing in turn the improvement and adaptation of stimulation parameters to boost the efficiency of ES based therapies. Considering that upon photoreceptor degeneration the inner retinal network that interconnects with RGCs is still viable, bidirectional multi-shank penetrating MEAs containing multiple electrode sites (BiMEA) have been proposed to interact with the tissue. Thus, stimulating electrodes can be placed in closer proximity with neurons of the inner retina, while recording electrodes capture the electrical activity of the tissue from the intraretinal space [10], [13], [24], [25], [162]. Given the above, this chapter presents a proof of concept that unveils the feasibility of using penetrating MEAs as intraretinal probes of dual purpose. To this end, Si-based BiMEAs were used to demonstrate the potential to record intraretinally the electrical activity of healthy WT and degenerated *rd10* retinas, as well as the possibility to perform simultaneously ES from the inner retina.

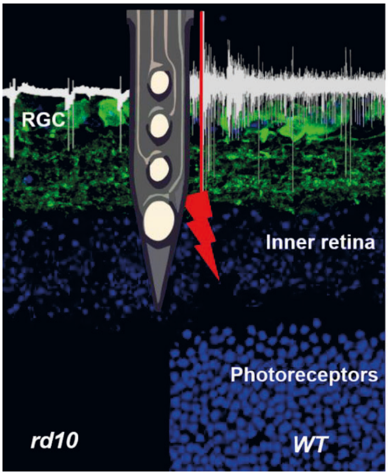

This chapter is reproduced from the following work:

Rincón Montes, V., Gehlen, J., Lück, S., Mokwa, W., Müller, F., Walter, P., and Offenhäusser, A., "Toward a bidirectional communication between retinal cells and a prosthetic device - A proof of concept," *Front. Neurosci.* 13, 1–19 (2019).

4.1. Si-BiMEAs

Based on the design evaluated by Brusius [25] and fabricated by Neuonexus Technologies (USA), Si-BiMEAs were designed and fabricated by the Institute of Materials in Electrical Engineering 1 (*Institut für Werkstoffe der Elektrotechnik*, IWE-1), RWTH Aachen University (Germany) as part of the BiMEA consortium.

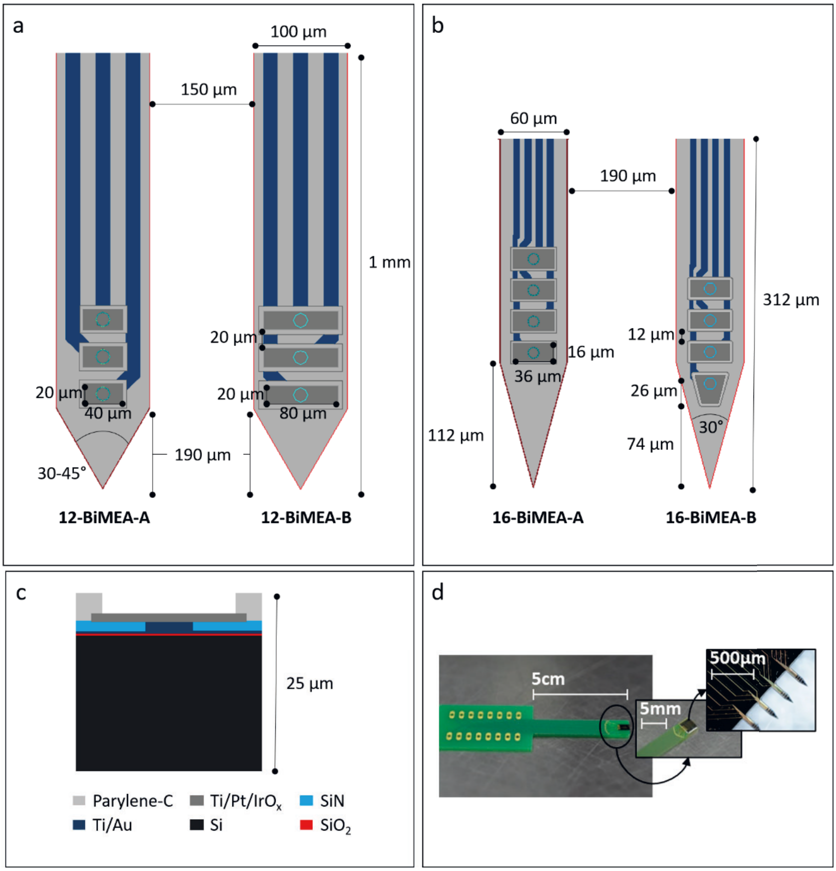

Figure 4.1. Si-BiMEAs. Design and dimensions of a) 12-BiMEAs containing three electrodes and b) 16-BiMEAs with four electrodes along each shank. c) Cross-section depicting the different materials composing individual Si-based shanks. d) The complete device comprises a Si probe containing four shanks, which is soldered onto a PCB with a 16-channels connector. Adapted from [13].

4.1.1. Design

The design of Si-BiMEAs resembles a Michigan array with four penetrating shanks. According to the dimensions and to the number of electrodes in each shank, the probes were distinguished as 12-BiMEAs and 16-BiMEAs. 12-BiMEAs (Figure 4.1a) have shanks 100 µm wide and 1 mm long, carrying each three rectangular electrodes with a total GSA of 800 µm^2

(12-BiMEA-A) or 1600 µm^2 (12-BiMEA-B). The distance from the tip to the first electrode (DTE) is ~190 µm, the inter-shank distance is 150 µm, and the inter-electrode distance is 20 µm. In contrast, the shanks of 16-BiMEAs (Figure 4.1b) are 60 µm wide, 312 µm long, and each one holds either four rectangular electrodes with a GSA of 576 µm^2 and a DTE of 112 µm (16-BiMEA-A) or three rectangular electrodes and one trapezoid electrode with a DTE of 74 µm (16-BiMEA-B). Both shank designs have a narrow tip angle of ~30-45°.

To keep track of every electrode within the penetrating MEAs, the shanks were numbered from one (left) to four (right), and the electrodes were numbered from one (bottom) to four (top). Thus, $E_{1.1}$ corresponds to the bottom electrode of the shank at most left and $E_{4.4}$ corresponds to the top electrode of the shank at the most right.

4.1.2. Fabrication

On top of a Si wafer with 300 nm of oxidized silicon (SiO_2), metal feedlines and the metal base of the electrodes were first patterned after sputtering a 30/300 nm thick titanium/gold (Ti/Au) stack. Next, a 1 µm thick silicon nitride (SiN) layer was deposited as first encapsulation layer, which was then removed at the sites of the electrodes and covered with Au. Afterwards, a second metal stack consisting of 30 nm of Ti, 250 nm of Pt, and 500 nm of IrO_x was sputtered, followed by the deposition of a 3 µm thick coating of PaC. After etching the insulation layer at the electrode sites and contact pads, the outline of the shanks was dry etched into the Si wafer, followed by the release of the Si-probes after thinning by lapping and etching the Si wafer.

With a total thickness of ~ 25 µm (Figure 4.1c), the probes were then soldered onto a printed circuit board (PCB) with a16-channel connector via ball wedge bonding (Figure 4.1d). To finalize the fabrication, the IrO_x electrodes were activated with 500 CV cycles in 0.9% PBS using a EG&G 283 Potentiostat/Galvanostat (AMETEK Scientific Instruments). A sweep rate of 100 mV/s was employed, and potential limits between -0.85 to 0.85 V and -0.8 to 0.9 V versus a Ag/AgCl reference electrode were used for 16- and 12- BiMEAs, respectively.

4.1.3. Electrochemical properties

Before starting the proof of concept, the recording and stimulating capabilities of the IrO_x electrodes of the different Si-BiMEA probes were evaluated. Hence, the impedance of individual electrodes was verified by extracting the magnitude of the impedance at 1 kHz (Z) from EIS measurements, and the average CSC_c of IrO_x electrodes was calculated at the last activation cycle. According to bode plots displayed in Figure 4.2a, by CV curves in Figure 4.2b, and the properties summarized in Table 4.1, the electrochemical properties of IrO_x electrodes for the different Si-BiMEAs showed a Z between 12.26 and 33.89 kΩ and a CSC_c between 19.94 and 34.53 mC/cm^2.

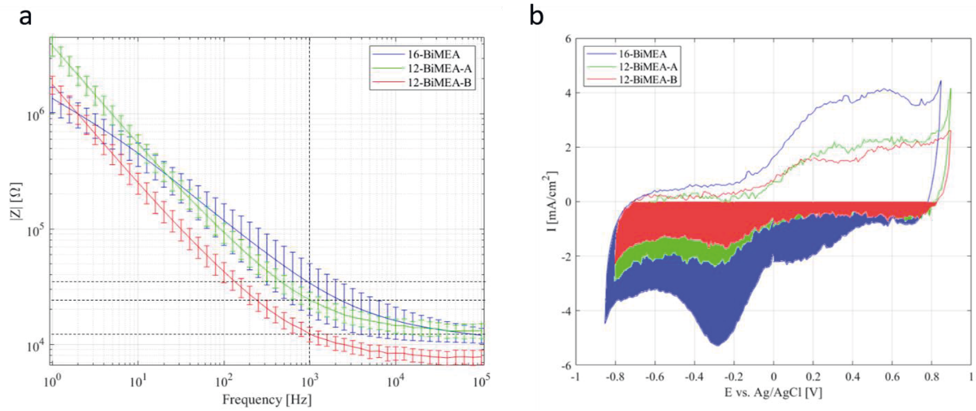

Figure 4.2. Electrochemical properties of IrO$_x$ electrodes in Si-BiMEA probes. a) The magnitude of the impedance (|Z|) is shown in the bode plot. b) The current density (I) at different electrode potentials (E) versus a Ag/AgCl reference electrode, as well as the cathodic charge storage capacity (CSC$_c$, colored areas) is exhibited in the CV curve at the last rehydration cycle for IrOx electrodes of the corresponding Si-BiMEAs

Table 4.1. Summary of electrochemical properties of IrO$_x$ electrodes in Si-BiMEA probes. GSA refers to the geometric surface area of individual IrO$_x$ electrodes, Z depicts the average magnitude of the impedance at 1 kHz, and CSC$_c$ stands for the average cathodic charge storage capacity of individual electrodes of a same probe.

BiMEA	GSA [µm^2]	Z [kΩ]	CSC$_c$ [mC/cm^2]
16-BiMEA	576	33.89 ± 16.09	34.53 ± 0.58
12-BiMEA-A	800	24.24 ± 4.03	20.33 ± 3.34
12-BiMEA-B	1600	12.26 ± 1.78	19.94 ± 2.62

As reviewed in section 2.5.4, recording electrodes should have a Z between 20 - 150 kΩ [100], [106] to obtain recordings with high SNRs, and stimulating electrodes that aim the retina should be able to provide charge densities from 5 to 306 µC/cm^2 [100]. Given the above, Si-BiMEAs had IrO$_x$ electrodes that showed suitable electrochemical properties to perform electrical recordings and stimulations. Accordingly, the different types of Si-BiMEAs were used indistinctly for the experiments performed in this chapter, albeit 16-BiMEAs were used to conduct direct comparisons among retinal samples (e.g.: WT vs. *rd10*).

4.2. Recording with Si-BiMEAs

Considering the dual purpose aimed for penetrating MEAs in retinal applications, the proof of concept started by evaluating the feasibility of recording the electrical activity of the retina using the proposed Si-BiMEAs. Consequently, the positioning of the BiMEA probes along different retinal layers was first tested in WT retinas. Then, pharmacological and light stimulations of the retina were performed to confirm the physiological origin and behavior of the electrical activity captured by the probes. Furthermore, to confirm the possibility of using such probes in degenerated retinas, intraretinal recordings were conducted in *rd10* retinas.

4.2.1. Recording at different intraretinal depths in wildtype retinas

To achieve a bidirectional communication that aims to stimulate the inner retina and to record the electrical activity of RGCs, the insertion of the penetrating probes was conducted so that the position of the intraretinal shanks could be tuned along the retinal layers located at different intraretinal depths (Z_x). Hence, stepwise insertions with step distances (ΔZ) of 20 µm and an insertion speed (V_{in}) of 62.5 µm/s were accomplished. Given that APs in the retina are only generated at the NFL and GCL by somas and axons of RGCs, the insertion method was carried out as follows:

1. The tip of a Si-BiMEA was first placed at the epiretinal surface of the tissue. Considering that no optical assistance was available, the latter was accomplished by observing with naked eyes the tip of the shanks through the glass ring of the reservoir in the perfusion chamber.
2. The insertion was guided by the spiking activity of the retina. The shanks were driven into the tissue using 20 µm steps until the first voltage peaks were observed in the lower electrodes of the shanks ($E_{x.1}$). This position, was set as Z_0, indicating that the surface of the NFL and the GCL was reached by $E_{x.1}$.
3. Further insertion steps were performed stepwise until the top electrodes ($E_{x.4}$) had recorded spikes, indicating in turn that these were at the GCL.

An example of an intraretinal insertion as described above is displayed in Figure 4.3. Here, fast voltage deflections were first captured by the lower electrodes. While the shank was inserted deeper inside the tissue, these voltage peaks were progressively shifted along the upper electrodes. A displacement of ~100 µm inside the retina was followed by the recording electrodes, capturing in turn spikes that most likely corresponded to the SA of the retina. Likewise, when contrasting the insertion depth with the amplitude of the detected spikes by each electrode, an approximate position of the electrodes within the retina and with respect to the reference position Z_0 could be established.

In the example, fast and small voltage fluctuations ($\leq$ 18 µV) were first recorded by $E_{4.1}$ at Z_0. Although these were not classified as APs, the peaks were an indication that the lower electrode was nearby the NFL. At Z_1, spikes were visible in all four electrodes (Figure 4.3 and Table 4.2), albeit the APs had higher amplitudes in $E_{4.1}$ and $E_{4.2}$.The latter implied that these electrodes were within the GCL and NFL. Consecutively, at further penetration depths, spikes with the highest amplitudes were observed at the next higher electrodes.

Thus, keeping in mind that the NFL, the GCL, and the IPL have a summed thickness of ~70 µm [163] and that the length from the bottom to the top recording electrode is between 100-110 µm (section 4.1.1), it was expected that $E_{4.1}$ was reaching the INL. Accordingly, $E_{4.2}$ was at the IPL and $E_{4.3}$ and $E_{4.4}$ were between the GCL and the NFL at Z_3. Additionally, when further steps were performed, spikes were still present at $E_{4.4}$. However, the latter were diminished in amplitude as the top electrode passed through the GCL and reached the border of the IPL at Z_4 and Z_5, respectively, confirming in turn the possibility to tune the intraretinal depth of individual electrodes along the same shank.

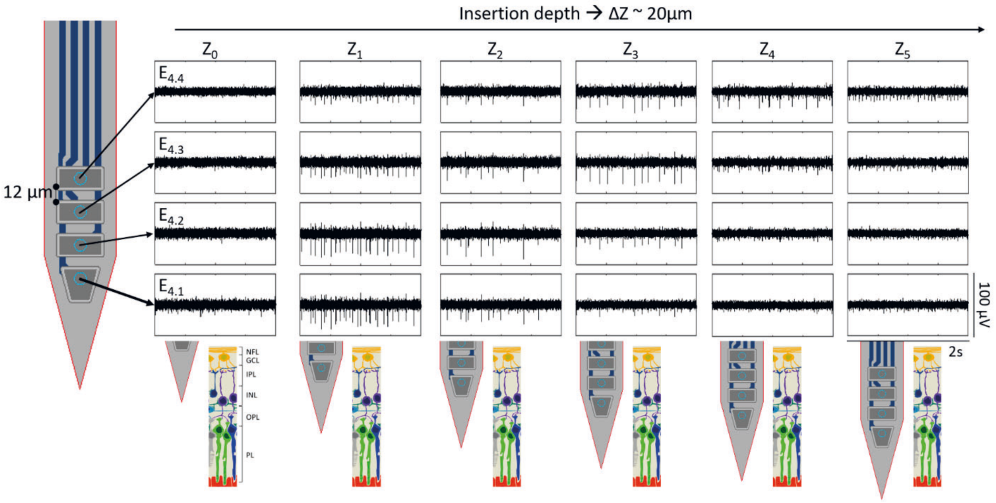

Figure 4.3. Recording at different intraretinal depths in wildtype retina with Si-BiMEAs. The figure displays a matrix of recording boxes showing snapshots of 2 s for every electrode along a recording shank (rows) at different intraretinal depths Z_x (columns) with insertion depth differences (ΔZ) of ~20 µm. Z_{1-5} correspond to 21.6 µm (Z_1), 39.7 µm (Z_2), 61 µm (Z_3), 80.8 µm (Z_4), and 100.7 µm (Z_5) with respect to Z_0, the surface of the NFL/GCL layer. Additionally, the expected intraretinal position of the recording shank is illustrated at the bottom. At the bottom, a sketch of the position of the shank within the multilayered retina is shown. Intraretinal layers are coded as: NFL = nerve fiber layer, GCL = ganglion cell layer, IPL= inner plexiform layer, INL=inner nuclear layer, OPL= outer plexiform layer, and PL = photoreceptor layer.

Table 4.2. Spike amplitude at different intraretinal depths in wildtype retina. The mean spike amplitude and the standard deviation of the spikes detected by each electrode ($E_{4.1-4.4}$) at different intraretinal depths (Z_{0-5}) is exhibited for the example shown in Figure 4.2. A minus (-) indicates that no voltage peaks were classified as action potentials.

Electrode	**Spike amplitude at different intraretinal depths [µV]**					
	Z_0	Z_1	Z_2	Z_3	Z_4	Z_5
$E_{4.4}$	-	19.72 ± 1.02	21.47 ± 1.41	26.76 ± 3.61	26.43 ± 0.30	15.86 ± 0.54
$E_{4.3}$	-	23.05 ± 1.73	27.61 ± 2.49	31.91 ± 4.66	16.44 ± 0.22	15.79
$E_{4.2}$	-	31.83 ± 3.19	29.90 ± 8.21	21.22 ± 2.79	-	-
$E_{4.1}$	-	28.52 ± 5.08	24.87 ± 2.88	17.66 ± 0.93	-	-

To confirm optically that the shanks were indeed penetrating the tissue, it was possible to capture the insertion of a Si-BiMEA in a dummy experiment. Here, the retina was kept semi hydrated and was illuminated from beneath to generate the necessary contrast to distinguish the tissue from the surrounding filter paper (Figure 4.4). In addition, the optical images in Figure 4.4 revealed that the retinal sample was not completely flat and that some shanks were penetrating the tissue at different depths.

The latter can be attributed to the fact that the tissue was not fully stretched when it was fixed onto the filter paper and that the periphery of the retina is pressed by the filter paper, generating in turn wrinkles at that the exposed part of the sample. This was confirmed when recordings of different shanks were analyzed as exhibited in Figure 4.5. While the SA of the retina was being recorded by the first two electrodes in shank 3 ($E_{3.1}$ and $E_{3.2}$), APs with higher amplitudes were captured by the middle electrodes in shank 4 ($E_{4.2}$ and $E_{4.3}$). Hence, it is important to account that Z_0 is set according to the first shank to record APs. In the example, Z_0 was defined with respect to shank 4.

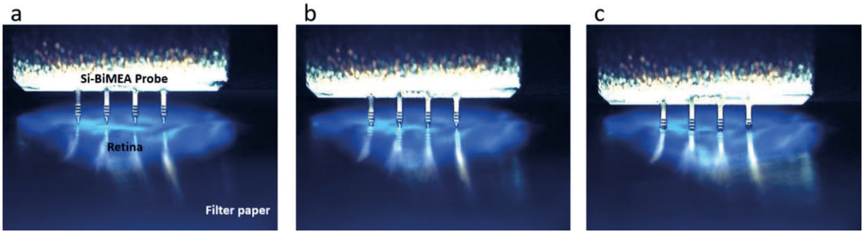

Figure 4.4. Intraretinal insertion of a Si-BiMEA into a wildtype retina. Optical images showing the insertion step of a Si-based probe into a semi hydrated retina. The shanks were first placed at the epiretinal surface of the retina (a), then tip was inserted (b), followed by the stepwise insertion of the shank (c).

Furthermore, recordings from Figure 4.3 and Figure 4.5 demonstrate that is was possible to follow the electrical activity of a same neuronal column. While it is true that electrodes belonging to the same shank recorded the same APs, these had different amplitudes. The latter indicates that the electrodes were at different intraretinal depths and distances with respect to the spiking neurons of the retina. Additionally, APs were detected with time lags between 1-3 µs, what excludes the presence of crosstalk.

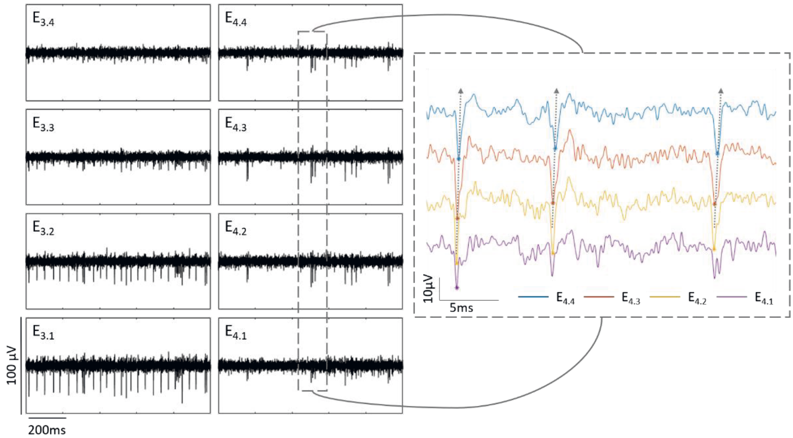

Figure 4.5. Recording shanks at different intraretinal depths in wildtype retina. The columns at the left exhibit the electrical activity of a wildtype retina captured by electrodes (rows) of two shanks of a same BiMEA probe at an insertion depth Z_2 (42.8 µm). The inset zooms the activity of the neuronal column captured by shank 4. Voltage peaks classified as action potentials are pointed out with asterisks and the direction of the signal transmission is depicted by the dashed arrows, indicating in turn a time lag in the detection of spikes.

4.2.2. Recording responses to high extracellular potassium concentration

To confirm that the spiking activity captured by intraretinal recordings came indeed from electrical impulses conveyed by RGCs, a WT retina was treated with high extracellular K^+ concentration, so that the extracellular ionic behavior could be reflected on the spiking behavior recorded by the

BiMEA probes. Figure 4.6 exhibits the electrical activity and the firing rate captured by one electrode during the execution of the complete experiment, exposing in turn four phases that confirm the physiological behavior of RGCs. At the beginning, a spontaneous spiking activity with a firing rate of ~ 16.77 ± 0.93 Hz was present (Figure 4.6a). After the application of 20 mM K^+, a lag phase of ~ 60 s was observed until the effect of the treatment was evident. The firing rate was temporarily increased reaching a maximum FR of 43 Hz (Figure 4.6b), followed by a silent phase where no APs were fired (Figure 4.6c). Finally, after restoring the perfusion of the tissue with the regular physiological solution, the SA was recovered (Figure 4.6d).

The electrical behavior captured agrees with the influence that ionic fluctuations have on cell membrane potentials that lead to the formation of APs (see section 2.4.1). When the extracellular K^+ concentration was increased, the Nernst potential corresponding to K^+ became more positive, thereby shifting the membrane potential of RGCs to more positive values. The latter induced the depolarization of the membrane, reflected with an increased firing of APs (Figure 4.6b). Given the continuous depolarization of RGCs, voltage-gated Na^+ channels did not recover from inactivation, leading in turn to a depolarization blockade in which no APs could be fired (Figure 4.6c). After reducing the extracellular K^+ concentration to a regular ionic gradient, the SA was recovered. Thus, the physiological response induced by the pharmacological treatment confirms the origin of the spiking activity to be of RGCs, the only neurons of the retina capable of firing APs.

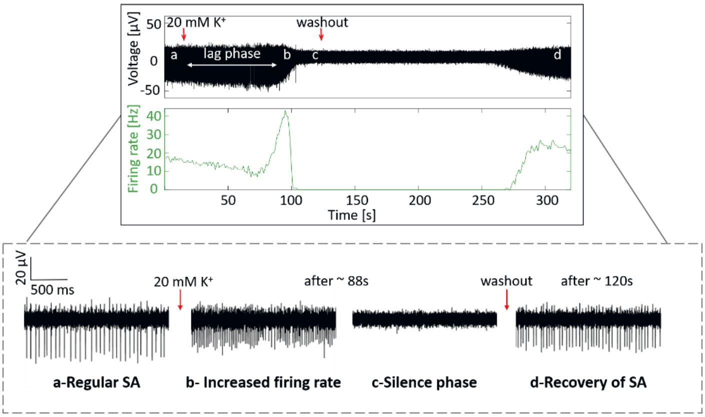

Figure 4.6. Response to treatment with high extracellular potassium concentration in wildtype retina. At the top, the electrical activity (black traces) and the firing rate with bin counts per second (green) captured by one recording site along the complete experiment. Red arrows point out the moment when 20 mM K^+ was applied to the perfusion of the tissue and the restoration of the regular physiological solution (washout). The four phases distinguished along the experiment are displayed with more detail in the inset enclosed by a dashed box. a) Regular spontaneous activity (SA) was first captured. b) Followed by the application of 20 mM K^+, an increased firing rate is triggered, c) causing in turn a silent phase. d) Finally, the SA is recovered upon washout.

4.2.3. Recording responses to light stimulation

During the penetration of the tissue, the integrity of the retinal network was verified by performing light stimulation at different intraretinal depths. Figure 4.7 shows the follow-up of an intraretinal insertion that confirmed the presence of a RGC exposing an ON behavior in response to light stimuli at different insertion depths. Despite the light-induced artifacts, which were concomitant to the onset and offset of light stimuli in all recordings (red arrows in Figure 4.7), a clear spiking response to light was observed. For example, at a depth of ~ 63 µm (Z_3), the ON response is clearly visible in all recording sites. While the lower electrode was in the inner retina showing small or no APs, the middle electrodes ($E_{2.2}$ and $E_{2.3}$) clearly captured the SA activity of RGCs. Thus, during the light stimulus, a burst of voltage peaks with higher amplitudes at the middle electrodes was visible, confirming that during the insertion the integrity of the intraretinal network responsible in this case of ON responses was preserved. Consequently, light stimulation was established to check the vitality of the tissue during intraretinal recordings in healthy retinas.

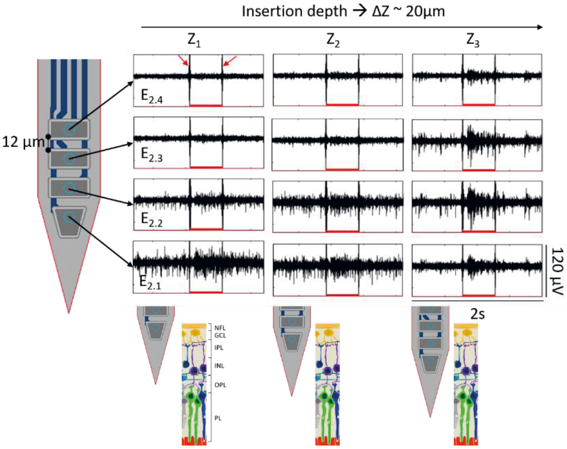

Figure 4.7. Recording responses to light stimulation at different intraretinal depths in wildtype retina. The figure displays a matrix of recording boxes showing snapshots of 2 s for every electrode along a recording shank (rows) at different intraretinal depths Z_x (columns) with insertion depth differences (ΔZ) of ~20 µm. Z_{1-3} correspond to 20.9 µm (Z_1), 42.5 µm (Z_2), and 63 µm (Z_3) with respect to Z_0. Light stimuli with an ON period of 500 ms are represented by red filled-bumps and light-induced artifacts present in all recordings are pointed out with red arrows. Additionally, a sketch of the position of the shank within the multilayered retina is shown. Intraretinal layers are coded as: NFL = nerve fiber layer, GCL = ganglion cell layer, IPL= inner plexiform layer, INL=inner nuclear layer, OPL= outer plexiform layer, and PL = photoreceptor layer.

As reviewed in section 2.1.2, RGCs can exhibit ON, OFF, or ON-OFF and transient or sustained responses during a light stimulus. Although the preparation of the tissue was not optimized to capture all responses since it was performed under ambient light, the high photopic stimuli allowed to distinguish different responses to light. For example, the recording in Figure 4.8a shows initially a SA below 1 Hz, which was increased up to 20 Hz by a burst of sustained voltage peaks with low amplitude (~15 µV) and transient spikes of higher amplitude (~38 µV) present during the ON period of the light stimulus. Likewise, the activity captured in Figure 4.8b contained discontinuous spike bursts with two different amplitudes (~ 47 µV and 22 µV) in reaction to light, thereby indicating the presence of two cells. While the higher amplitude spikes show an ON transient response, the lower amplitudes spikes resemble an ON-OFF response with the presence of APs at the offset of the stimulus.

Moreover, sustained ON responses to light were also observed in Figure 4.8c, where continuous spikes increased its firing rate from 8.5 Hz to 35 Hz during light stimulation. Additionally, two different types of responses were distinguished in Figure 4.8d. A first cell exhibited an ON response with a burst of APs during the stimuli, while a second cell showed an OFF behavior with a short bursting activity at the offset of the stimuli with a latency between 100-170 ms. As it is exhibited by the peaks in the firing rate traces, ON cells were clearly identified due to an increased firing activity.

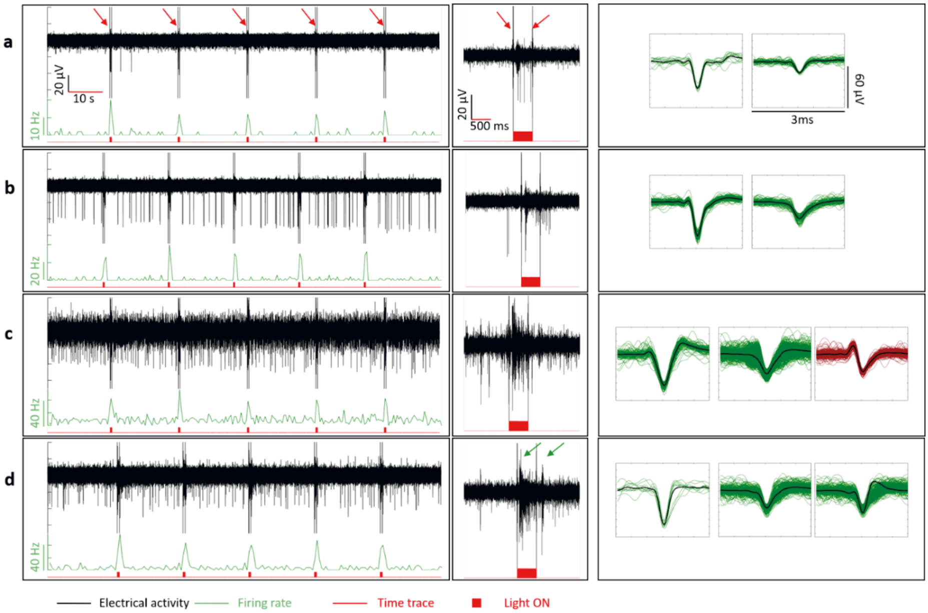

Figure 4.8. Responses to light stimulation in wildtype retina. Light stimuli with an ON period of 500 ms every 15 s were applied to stimulate the retina optically. In the first column, responses to multiple light stimuli are shown. In (a) the response of ON transient and sustained cells, in (b) an ON transient response, in (c) an ON sustained response, and in (d) the response of ON and OFF cells. In the second column, plots correspond to 3 s snapshots of the complete recording shown at the left. Traces in black represent the electrical recordings (µV), in light green the firing rate with normalized bin counts every 500 ms shown as spikes/second (Hz), and in red the corresponding time trace. The red filled-bumps represent the light stimuli during the ON period. The green arrows in (d) indicate the presence of an ON and an OFF cell. The red arrows in (a) point out high electrical artifacts induced by light seen in all the recordings. In the third column, the waveforms of the different spikes encountered for each case after a semi-automatic spike sorting using the Wave_clus toolbox [164]. Negative biphasic peaks are shown in dark green, triphasic waveforms in dark red, and the mean trace of the spike shape for each group is depicted in black.

Furthermore, somatic and axonal waveforms were encountered (third column in Figure 4.8) when analyzing the spike waveforms of the SA and optical responses of RGCs. On one side, negative peaks comparable to the biphasic shape of somatic spikes (dark green waveforms) were detected. On the other side, waveforms with an initial positive crest followed by a negative spike, resembling the triphasic nature of axonal APs [165] were also captured (dark red waveforms). Likewise, features including spike amplitude differences and somatic waveforms with a positive crest at the end of the AP could be noted among the different spike clusters, confirming in this way the presence of more than one cell at the recording sites.

4.2.4. Recording from degenerated retinas

Given the possibility of performing intraretinal recordings in WT retinas while conserving the vitality of the tissue, the penetrating Si-BiMEAs were tested in *rd10* retinas, which suffer from photoreceptor degeneration and are considered a suitable model for the retinal degenerative disease RP [166]. Recordings performed in *rd10* retinas exposed a rhythmic activity that was not observed in WT retina recordings (Figure 4.9). When analyzing the raw, the band-pass filtered (100 Hz – 3 kHz), and the low-pass filtered (cutting frequency at 50 Hz) signals, high and low frequency components including a burst of APs phase-locked to low frequency oscillations (LFPs) were evidenced in *rd10* retinas. After Fourier analysis, it was noted that in the case of the *rd10* example shown in Figure 4.9, LFPs oscillated around a peak frequency of ~2.66 Hz. This behavior matches the typical pathologic activity described for *rd10* retinas [12], [166]–[169], and contrasts the stochastic spiking activity of WT retinas.

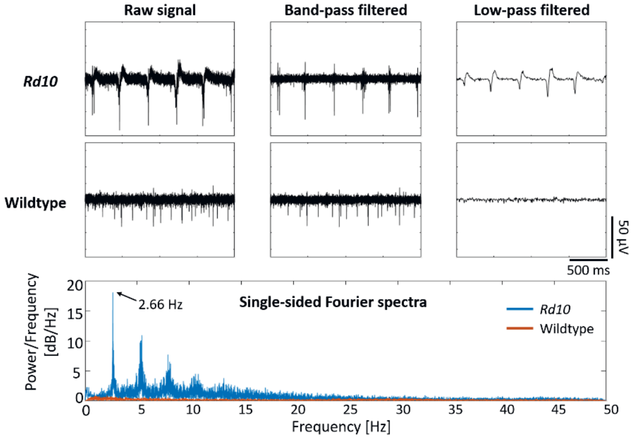

Figure 4.9. Comparison of spontaneous activity in *rd10* and wildtype retinas. The raw, the band-pass filtered (100 Hz – 3kHz), and the low-pass filtered (cutting frequency of 50 Hz) signals are shown for recordings in *rd10* (top row) and wildtype (second row) retinas. The Fourier spectra is exhibited for the low-pass filtered signals of both retinas, showing a peak frequency of ~2.66 Hz (pointed out with the black arrow) for the *rd10* retina.

Moreover, different oscillatory frequencies ranging between 2.6 to 4.3 Hz were encountered at different *x-y* locations within the same retinal sample (Figure 4.10a-c), matching the range of frequencies between 3-7 Hz reported by [166]. While this rhythmic activity was not evident in all recorded retinas, oscillatory components in LFPs were revealed after Fourier analysis. An example is shown in Figure 4.10d, where a peak frequency around 4.3 Hz was present in the single-sided Fourier spectrum while no clear oscillations were visible in the low-pass filtered signal.

Additionally, recordings at different intraretinal depths show that the pathologic rhythmic activity of *rd10* retinas can be tracked at different insertion depths. Two different cases can be observed in Figure 4.11 and Figure 4.12 . While in Figure 4.11, the oscillations were not evident, the Fourier spectra showed an increasing power between 2.5 and 7 Hz as deeper regions inside the retina were reached by the lower electrode, with a peak frequency of 4.3 Hz at the last insertion depth (Z_8).

On the other hand, LFPs with oscillatory frequencies that increased its power and shifted its peak frequency from 3.586 Hz at Z_0 to 4.88 at Z_3 were visible in Figure 4.12.

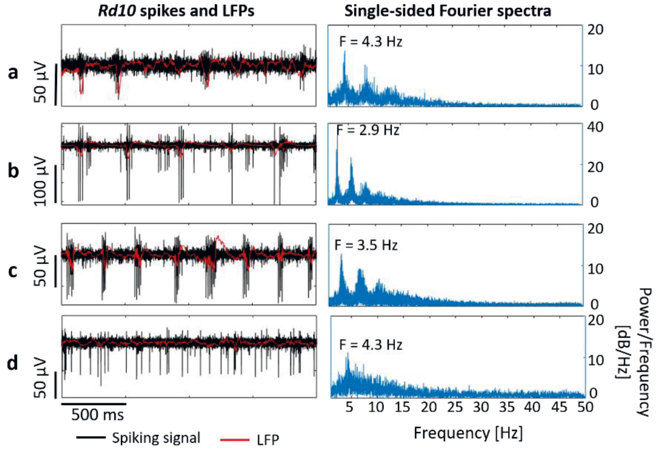

Figure 4.10. Recording different local field potentials in *rd10* retinas. The spiking activity (black) and local field potentials (LFPs in red) are displayed for *rd10* recordings (left column). The corresponding single-sided Fourier spectra is shown for each example (right column). Recordings of a same retinal sample at different x-y locations are exhibited in (a-c), and (d) shows a case where LFPs are not evident but an oscillatory component is exposed in the Fourier spectrum.

Furthermore, when contrasting *rd10* with WT intraretinal recordings, three main differences were encountered. First, intraretinal recordings at different insertion depths within *rd10* retinas revealed that initially more insertion steps where needed to position the lower electrodes in the inner retina and the top electrodes at the GCL/NFL. While a typical insertion of a Si-BiMEA into a WT retina consisted of approximately five steps of 20 µm for a total travelled distance of ~ 100 µm (Figure 4.3), up to eight steps of ~ 20 µm and a total displacement of ~ 160 µm were needed in *rd10* retinas to place the electrodes at the desired intraretinal depth (Figure 4.11). Additionally, it was noticed that in the *rd10* insertion, the spikes recorded from Z_0 to Z_3 did not shift to the upper electrodes but stayed at the lower electrode $E_{1.1}$, and that it was only from Z_4 that the spiking signal started to move to the upper the electrodes, as it was previously observed in WT retinas.

The latter indicates the presence of dimpling, as initial compressions of the tissue were necessary (Z_0-Z_3) to rupture the NFL/GCL and enable the advancement of the electrodes inside the retina (Z_4-Z_8). To achieve faster insertions, dimpling was then compensated by increasing the step size ΔZ from 20 to 40 µm. In this way, the upper electrodes reached the GCL/NFL after a total insertion of ~122 µm, which was carried out in three insertion steps (Figure 4.12).

This difference between *rd10* and WT insertions might have been caused by the altered viscoelastic properties of the diseased retina. While retinas undergoing photoreceptor degeneration are in general softer than WT retinas [170], neurodegenerative diseases such as RP or AMD induce the activation and therefore an increased stiffness of glial cells in the retina [171]–[173], which are located along the retina (Müller cells) and at the NFL (astrocytes). Therefore, reactive glial cells might have interfered during the insertion, leading in turn to more dimpling in the degenerated tissue.

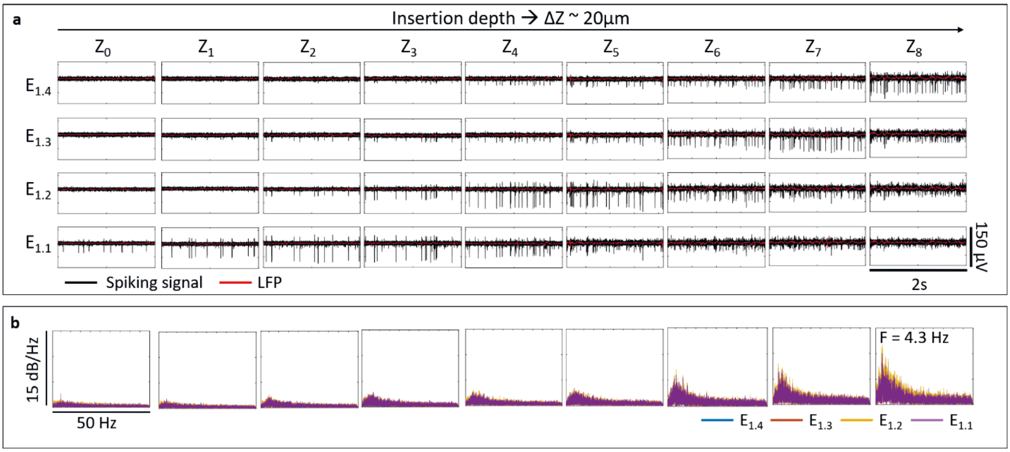

Figure 4.11. Recording intraretinal depths in rd10 retina with 20 µm steps. a) Matrix of recording boxes showing snapshots of 2 s for every electrode along a recording shank (rows) at different intraretinal depths Z_x (columns) with insertion depth differences (ΔZ) of ~20 µm. Z_{1-8} correspond to 21 µm (Z_1), 42.6 µm (Z_2), 63.8 µm (Z_3), 82.3 µm (Z_4), 101.7 µm (Z_5), 121.7 (Z_6), 141 µm (Z_7), and 162.1 µm (Z_8) with respect to Z_0. Black and red traces show the spiking activity and local field potentials (LFPs), respectively. b) Single-sided Fourier spectra at each intraretinal depth (matching columns with a) for all the electrodes of the shank.

The second difference can be observed when the top electrode ($E_{x.4}$) is at the GCL/NFL. Conversely to WT recordings, RGCs spikes were still detected by the lower electrodes at the last insertion step in *rd10* retinas. As it is exhibited at Z_8 in Figure 4.10 and Z_3 in Figure 4.11, higher amplitude spikes were captured by $E_{1.4}$ (~ 54.20 µV) and $E_{2.4}$ (~70 µV), while APs with smaller amplitudes between 30.48 – 44. 43 µV were still recorded by the lower electrodes $E_{1.1}$ and $E_{2.1}$. This behavior can be a consequence of the reduced resistivity of *rd10* retinas [174], thereby enabling the recording of potentials at further distances from RGCs.

The decreased resistivity in *rd10* retinas, which is ~ 2.5 times lower than WT retinas [174], explains in turn the third difference exhibited by recordings in both retina types, characterized by the higher spike amplitudes detected in *rd10* recordings. While the latter presented an average spike amplitude of 48.27 ± 14 µV with maximum peaks of ~ 100 µV, APs detected in WT recordings had an average peak amplitude of 25.96 ± 4.43 µV with maximum heights of ~ 39 µV.

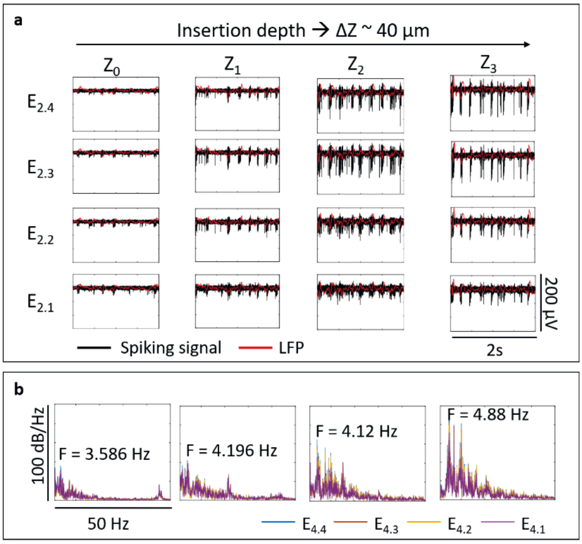

Figure 4.12. Recording at different intraretinal depths in rd10 retina with 40 µm steps. a) Matrix of recording boxes showing snapshots of 2 s for every electrode along a recording shank (rows) at different intraretinal depths Z_x (columns) with insertion depth differences (ΔZ) of ~40 µm. Z_{1-3} correspond to 41.5 µm (Z_1), 80 µm (Z_2), and 122.9 µm (Z_3) with respect to Z_0. Black and red traces show the spiking activity and local field potentials (LFPs), respectively. b) Single-sided Fourier spectra at each intraretinal depth (matching columns with a) for all the electrodes of the shank.

4.3. Electrical stimulation and recording of the retina

Proven the feasibility of performing intraretinal recordings while accessing different intraretinal layers, in both WT and *rd10* retinas, Si-BiMEAs were used to stimulate electrically the retina while recording simultaneously its electrical activity. Thus, the probes were inserted following the protocol described previously, so that the lower electrode ($E_{x.1}$) of at least one shank was placed in the inner retina (IPL/INL) and the upper electrodes ($E_{x.3}$ and $E_{x.4}$) were interfacing the outer retina (GCL/NFL). In this way, the lower most electrode, capturing low amplitudes spikes or none, was selected as the stimulating electrode, and the upper electrodes, exhibiting the spiking activity of RGCs, were used as recording electrodes. As shown in previous sections, once the penetrating shanks were in position, the vitality of the tissue was confirmed by recording the SA and responses to light stimulation, in the case of WT retinas. Six different stimulation parameters (ES-1 – ES-6) were used (section 3.8.1) in a VCS mode, so that biphasic voltage pulses with amplitudes between 0.6 - 0.8 mV and phase periods between 0.5 – 0.8 ms were applied. ES-1 to ES-6 were tested in WT retinas, and ES-1, ES-2, and ES-6 were employed in *rd10* retinas.

ESs performed in WT retinas revealed the presence of a burst of APs when the cells close to the stimulating electrode were successfully excited. Figure 4.13a displays an example of a retinal sample that showed successful stimulations in all recording electrodes of the stimulating shank after applying the stimulation parameters from ES-3 (0.6 mV, 0.5 ms). In this case, all six stimuli produced a bursting activity within the first 80 ms after the ES artifact. While successful stimulations were observed for all tested parameters (Figure 4.13b), ES-3 generated the strongest response with an ESE between 8.04 - 10.27.

Likewise, it was noted that the firing activity in the next neighboring shank (Shank$_2$) was in average increased by 1.26 – 2.5 times the FR of the SA after the electrical stimuli were applied. However, this behavior was not constant along the stimulation trial, yielding in turn unsuccessful stimulations of neighboring shanks. While in most of the cases no stimulation was induced to the non-stimulating shanks, significant inhibitory effects, characterized by ESEs below one, were occasionally encountered in the electrical activity captured by some of the recording electrodes belonging to the immediate neighboring shank during ES-1 and ES-4 (see Appendix 4).

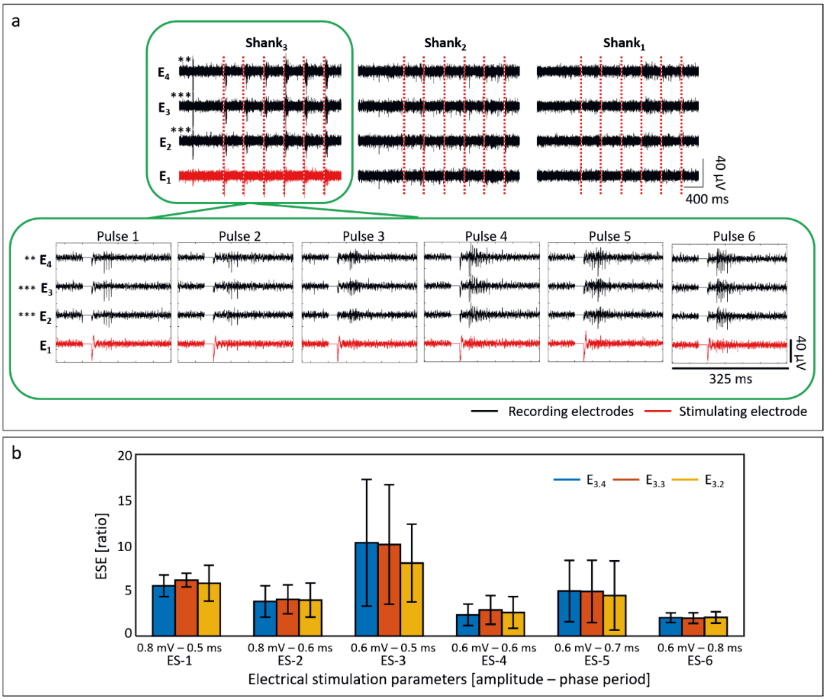

Figure 4.13. Voltage-controlled stimulation and recording in wildtype retina. a) Example of a wildtype retina stimulated with six consecutive first cathodic biphasic voltage pulses with an amplitude of 0.6 mV and a phase period of 0.5 ms (ES-3) every 20 s using E$_1$ from Shank$_3$ as the stimulating electrode (red). At the top, recordings show 1 s before and 400 ms after the stimulation pulse (dashed red lines) for three shanks of a Si-BiMEA. Shank$_4$ is not shown due to non-working electrodes. The inset enclosed in a green rectangle depicts a zoom with 325 ms snapshots, showing 75 ms before and 225 ms after the stimulation artifact (line of 0 V). Significant stimulations are depicted by stars (* for p <= 0.05, ** for p <= 0.01 *** for p <= 0.001) after performing paired t-tests to the firing rate before and after the stimulation. b) Average electrical stimulation efficiency ratios (ESE) for six different stimulation parameters tested in the same retinal sample exhibited in a). Error bars denote the standard deviation.

In contrast to WT, electrical responses evoked in *rd10* retinas comprised a combination of bursting activity with transient spikes that presented an increased FR within the first 180 ms after the electrical stimulus, as it can be observed in the example shown in Figure 4.14a. Here, electrical responses were achieved using ES-2, ES-3, and ES-6, however, it was ES-2 (0.8 mV, 0.6 ms) that induced the strongest excitatory responses with ESEs between 2.19 - 2.74 (Figure 4.14b). In addition, both excitatory or inhibitory responses that consisted in a significant FR increase or decrease were encountered in neighboring shanks when testing all three sets of parameters (see Appendix 5). This behavior was observed consistently with the nearest non-stimulated shank ($Shank_2$), which was located 190 µm away and whose electrical activity captured by electrodes at the NFL/GCL (E_1 and E_2) was increased at the same rate of the stimulated shank ($Shank_1$).

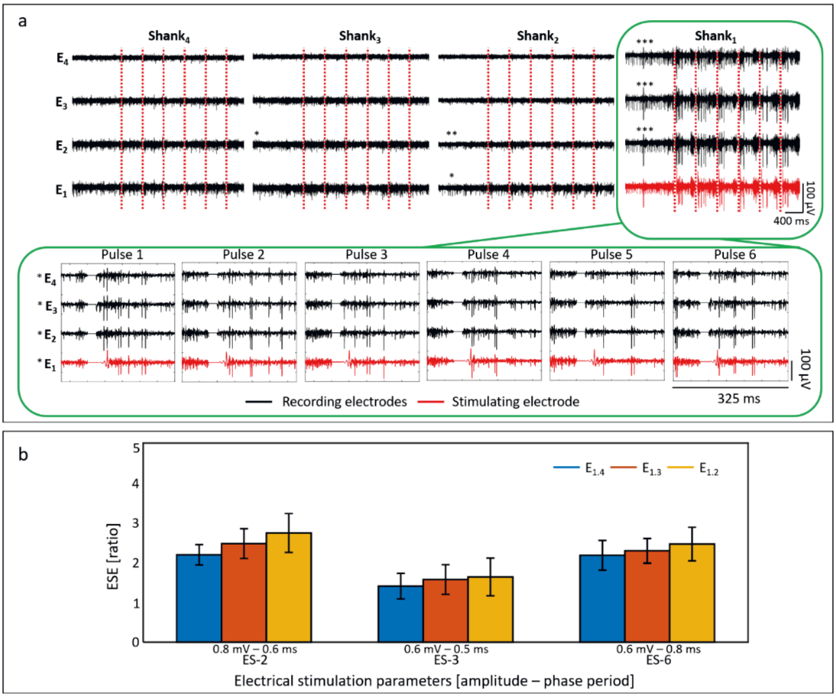

Figure 4.14. Voltage-controlled stimulation and recording in *rd10* retina. a) Example of an *rd10* retina stimulated with six consecutive first cathodic biphasic voltage pulses with an amplitude of 0.8 mV and a phase period of 0.6 ms (ES-2) every 20 s using E_1 from $Shank_1$ as the stimulating electrode (red). At the top, recordings show 1 s before and 400 ms after the stimulation pulse (dashed red lines) for three shanks of a Si-BiMEA. The inset enclosed in a green rectangle depicts a zoom with 325 ms snapshots, showing 75 ms before and 225 ms after the stimulation artifact (line of 0 V). Significant stimulations are depicted by stars (* for $p <= 0.05$, ** for $p <= 0.01$ *** for $p <= 0.001$) after performing paired t-tests to the firing rate before and after the stimulation. b) Electrical stimulation efficiency ratio (ESE) for three different stimulation parameters tested in the same retinal sample exhibited in a). Error bars denote the standard deviation.

When performing direct comparisons between the ES performance in WT and *rd10* retinas, significantly weaker responses were revealed for stimulations carried out in *rd10* samples. While ES-6 produced in average an ESE of ~ 2.3 in both retinas, ES-1, ES-2, and ES-3 resulted in ESEs that were between 1.75 and 6.14 times lower in *rd10* stimulations (Figure 4.15a), agreeing in turn with the reduced stimulation efficiencies reported by [12] for *rd10* retinas. Additionally, measurements of the injected currents during ES showed that for the stimulation parameters ES-3 and ES-6 more energy was required to evoke successful stimulations in *rd10* samples, as cathodic currents ~ 1.44 – 1.55 times higher than in WT were discharged in the degenerated tissues (Figure

4.15b-c and Table 4.3). This stimulation behavior matches with *in vivo* reports that expose higher charge density thresholds for diseased retinas [14].

Accordingly, VCS parameters that elicited successful responses yielded cathodic charge densities that were substantially higher in *rd10* stimulations, ranging between 334.76 ± 94.65 μC/cm^2 and 686.10 ± 304.16 μC/cm^2 versus 248.28 ± 58.96 μC/cm^2 and 508.55 ± 329.14 μC/cm^2 in WT samples (Table 4.3). In both cases, values were within the recommended safe limit for IrO_x electrodes (1 mC/cm^2) [14]. Moreover, considering the small surface area of the stimulating electrodes (GSA = 576 μm^2), as well as their position in the inner retina, charge densities during intraretinal VCS were comparable to subretinal thresholds (100-900 μC/cm^2) reported by [175] after using electrodes with a GSA of ~ 706 μm^2. However, the charge densities used for this proof of concept exceeded the threshold of ~ 50 μC/cm^2 reported by [21] after using Si-nanoneedles with a GSA of ~ 1000 μm^2 in embryonic chick retinas.

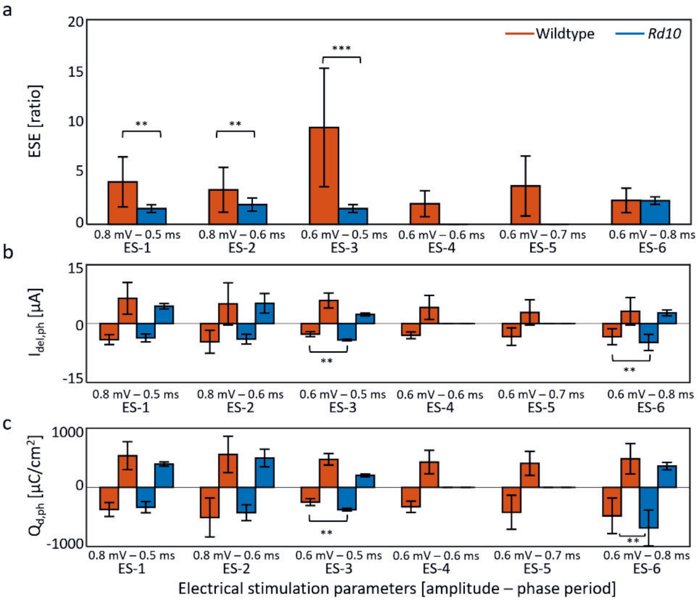

Figure 4.15. Voltage-controlled stimulation comparison between wildtype and rd10 retinas. Data shown for six different sets of stimulation parameters (ES-1 to ES-6) tested in three wildtype (WT) and two *rd10* retinas. The data correspond to trials that led to successful excitatory responses in the stimulated shank. a) Average electrical stimulation efficiency ratio (ESE) of the recording electrodes of the stimulated shank. b) Average cathodic and anodic delivered currents ($I_{del,\,ph}$) by the stimulating electrode. c) Average cathodic and anodic charge densities ($Q_{d,\,ph}$) given by the stimulating electrode with a geometric surface area of 576 μm^2. Significant differences between WT and *rd10* retinas are depicted by stars (* for $p <= 0.05$, ** for $p <= 0.01$ *** for $p <= 0.001$) after performing non-parametric Mann-Whitney U-tests. Error bars denote the standard deviation.

Given the above, it is important to highlight that the stimulation parameters used during VCS in this chapter were not optimized to uncover intraretinal current and charge density thresholds but intended to demonstrate electrically evoked potentials in RGCs with simultaneous intraretinal recordings to track such ES behavior. Considering that CICs were not determined for the stimulating electrodes in this chapter, voltage biphasic pulses, which have proven to activate RGCs successfully, especially in diseased retinas [25], [176], were used to avoid the incursion of high electrode potentials (> 1V) that might generate irreversible reactions, such as water electrolysis, or tissue damage during ES [25], [100], [140], [177]. Nonetheless, further experiments to determine optimal currents and charge densities during intraretinal stimulations will be addressed in section 6.3.

Table 4.3. Intraretinal current and charge density thresholds for voltage-controlled stimulation. Lower and upper cathodic current ($I_{del,\ ph}$) and charge density ($Q_{d,ph}$) thresholds in intraretinal voltage-controlled stimulations (VCS) using first cathodic biphasic and symmetric voltage pulses that led to significant evoked responses in wildtype and *rd10* retinas. A geometric surface area of 576 µm^2 was considered.

Retina Type	**Threshold**	$I_{del,\ ph}$ **[µA]**	$Q_{d,\ ph}$ **[µC/cm^2]**
Wildtype	Lower	2.69 ± 0.62	248.28 ± 58.96
	Upper	4.62 ± 2.92	508.55 ± 329.14
Rd10	Lower	3.64 ± 1	334.76 ± 94.65
	Upper	4.79 ± 2.06	686.10 ± 304.16

4.4. Intraretinal insertion footprints

To investigate the damages induced to the tissue after using penetrating MEAs to interact with the retina, intraretinal insertions in TN-L15 retinas, which harbor RGCs with a strong visible fluorescence, and dead cells stainings were performed in search of acute intraretinal insertion footprints. In this way, green cells correspond to live RGCs and red cells to dead neurons in the retina. Images in Figure 4.16 clearly reveal the penetration holes left by Si-BiMEAs, showing in turn neuronal loss, tissue displacement, and a concentration of dead cells at the penetration sites.

Likewise, differences among Si-BiMEAs are visible. Bigger holes and a higher quantity of dead cells are evident after the insertion of 12-Si-BiMEAs (Figure 4.16a-b), while smaller marks and fewer dead cells are encountered for 16-Si-BiMEAs (Figure 4.16c). Considering that 12-Si-BiMEAs have wider shanks (100 µm) than 16-Si-BiMEAs (60 µm), these observations agree with findings reported by [178], in which acute insertion footprints are proportional to the cross-section of Si micromachined shanks.

Moreover, the shank width optimization in 16-Si-BiMEAs shows an apparent reduced trauma, albeit it is important to notice that attempts to insert fully the penetrating shanks can amplify the damage induced to the tissue, as exposed in Figure 4.16d. Here, a higher quantity of dead cells, axons disruption, and RGC-somas diminishment is observed in addition to the neuronal loss at the penetration site. This amplified trauma can be explained, as the Si-probes were directly soldered onto the PCB that supports the penetrating shanks (Figure 4.1d). Hence, if the stiff connector-probe interface touches the tissue, additional compressive forces are generated on the tissue, magnifying in turn the trauma produced by Si shanks. While these results give an overview of the damages that can be induced to the tissue after intraretinal insertions, an assessment of the acute biological impact of intraretinal probes will be addressed in section 7.1.

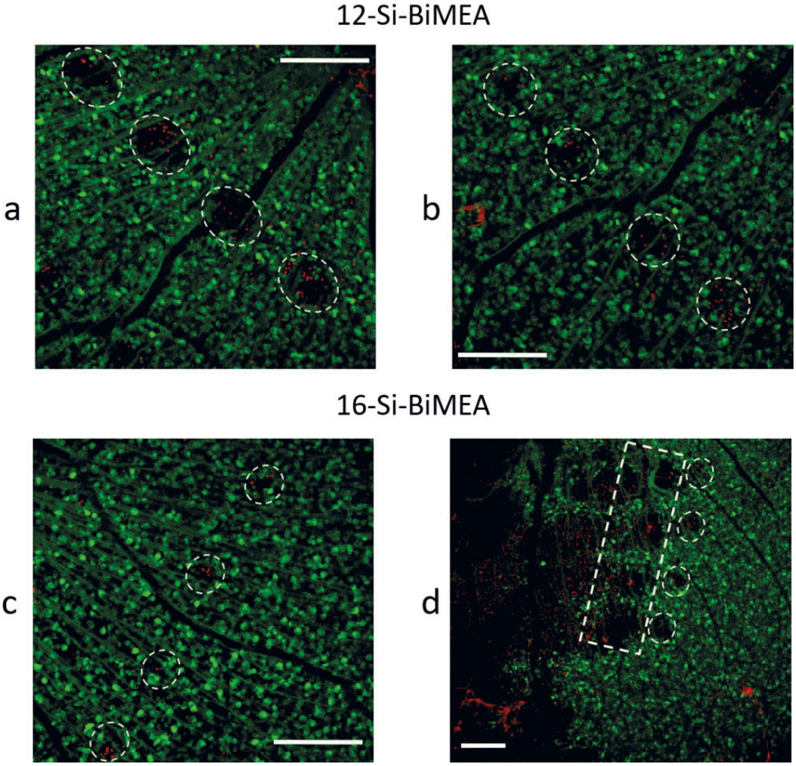

Figure 4.16. Dead cell stainings after intraretinal insertions of Si-BiMEAs in TN-L15 retinas. Top view of maximum intensity projections of intraretinal insertions using 12-Si-BiMEAs (a-b) and 16-Si-BiMEAs (c-d). In green, live retinal ganglion cells (RGCs) expressing the Ca^{2+} sensor TN-L15. In red, dead cells stained with ethidium homodimer (EthD-1). Penetration holes are pointed out with dashed circles, and in d), the square marks the footprint of a second insertion in the retinal sample. Scale bars: 200 µm.

4.5. Outlook

In this chapter, a proof of concept that reveals the feasibility of an intraretinal bidirectional communication was conducted. To this end, penetrating MEAs based on Si were tested as bidirectional devices (Si-BiMEAs) to interact with the retina. First, the access to different intraretinal layers while recording the spiking activity of RGCs was evaluated. The fact that the Michigan-like design of the BiMEA probes comprises multiple penetrating shanks with multiple electrode sites along each shank made viable the possibility to reach simultaneously different intraretinal regions. Thus, the positioning of Si-BiMEAs along different intraretinal depths was demonstrated in WT and *rd10* retinas, so that the lower electrodes of the penetrating shanks were driven into the inner retina (INL/IPL) while the upper electrodes lay close to RGCs in the outer retina (GCL/NFL). The correct positioning of the probes was then confirmed by the spikeless or low amplitude peaks captured by recordings of the lower electrodes, while APs were detected by the upper electrodes.

Despite the intraretinal penetration, preservation of the retinal network was shown by meaningful physiological responses to changes in the extracellular ionic gradients and to light stimulation of WT retinas. In the first case, the progressive depolarization of RGCs, followed by a depolarization blockade, and further recovery of the SA in response to a transitory high extracellular potassium treatment proved that the spiking activity captured by intraretinal recordings came indeed from RGC. Likewise, it confirmed that this activity follows the physiological behavior that gives rise to the generation of APs. In the second case, the identification of transient and sustained ON, OFF, and ON-OFF reactions to light stimuli proved that different signaling pathways were viable during the penetration of the tissue. Hence, the vitality of the tissue was demonstrated.

Moreover, stochastic SA in WT and typical pathologic rhythmic activity in *rd10* retinas was captured by intraretinal recordings. The latter showed the capability of Si-BiMEAs to detect not only the spiking activity of RGCs, but LPFs originated by the activity of different retinal neurons. While low frequency signals were detected in the degenerated retina, electrical artifacts induced by light during optical stimulation hindered the possibility to record LFPs like the ERG, present in healthy retinas upon light stimuli.

Proven the viability of performing intraretinal recordings, simultaneous recording and stimulation of the retina was carried out intraretinally. While it is true that surface planar probes are less invasive and can also record/stimulate the electrical activity of the retina, the intraretinal access of the tissue allows to track neurons belonging to a same neuronal column and at different (*x*, *y*, and *z*) locations. Thus, access to the intraretinal space enabled by penetrating MEAs improve not only the electrical coupling with the tissue but widens the spatial resolution and the scope of retinal prosthetic devices.

A bidirectional interaction with the retina was conducted successfully during ES, as electrically evoked potentials in both WT and *rd10* retinas were detected after voltage pulses were applied to the inner retina. Although an ES artifact with a mean duration of ~ 14 ms after the stimulus was present in the recording electrodes, the latter did not impede the detection of RGCs activation, which were mostly detected within a latency of ~ 80 – 180 ms after the stimulation artifact. The latter implies that the recorded responses correspond to medium- and long-latency potentials (~ 5 – 160 ms after the electrical stimulus) mediated by an indirect stimulation of the retina [38], [179]. However, since the first 14 ms after the electrical stimulus were not properly recorded, a direct stimulation of the retina, whose latency is within the first 5 ms after the stimulation pulse [179], cannot be ruled out completely.

Furthermore, the follow-up of the electrical behavior in healthy and diseased retinas confirmed the necessity of a bidirectional approach in visual prosthesis. In accordance with findings in [12] and [14], degenerated retinas showed weaker responses to ES and higher charge density thresholds were used to activate RGCs. This behavior has shown to reduce the efficiency of the stimulation in terms of electrically evoked potentials and energy required to elicit a response [12], [14]. Therefore, providing a way to monitor the electrical activity of the retina during ES opens the door to provide quantitative feedback on the success of the ES treatment and to tune accordingly the parameters needed to induce a successful stimulation.

Additionally, footprints comprising neuronal loss, dead cells, and tissue displacement were encountered at the insertion sites after acute intraretinal insertions. Lesion areas left by Si-BiMEAs were proportional to the shank width of the devices, and the narrow shanks of 16-Si-BiMEAs seem to diminish the acute insertion trauma. Nonetheless, under the presence of external forces, Si-shanks showed the potential to amplify the insertion trauma, even in controlled *in vitro* environments. While these findings give an overview of the potential damages that intraretinal probes can generate to the retina, they also raise the question whether Si should be used as a main substrate material. Although most initiatives that develop penetrating or protruding pillars for retinal applications, including the one presented in this chapter, use Si as the main substrate material [21], [23], current retinal implants are based on flexible substrate materials like PI, PaC, or silicone rubber [180]. Accordingly, further developments of an intraretinal implant should consider the use of those materials that have proven to be viable for retinal prostheses.

Chapter 5

Development of flexible BiMEAs

The feasibility of an intraretinal bidirectional communication between a prosthetic device and the retina was demonstrated in the previous chapter, however, potential damages induced by intraretinal insertions and stiff connector/probe interfaces questioned the use of Si as the main substrate material for an intraretinal implant. Even more, considering that Si is a stiff and non-compliant material that has shown strong FBRs in long-term applications and enhanced trauma due to micromotions (see section 2.5.2), the necessity of implementing flexible and compliant materials in further developments of an intraretinal implant becomes evident.

With the aim to minimize the insertion footprint and the biological impact of an intraretinal device, this chapter exposes the development of flexible bidirectional intraretinal probes, hereafter referred as flexible BiMEAs. Here, the design and the fabrication principles to fulfill the mechanical and electrochemical requirements of flexible BiMEAs are revealed. Additionally, the new probes are characterized to demonstrate not only the of recording and stimulating capabilities of the electrodes, but to assure a successful insertion into the target tissue, the retina.

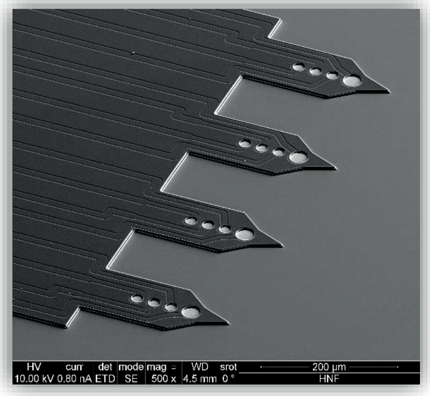

This chapter is in part reproduced from the following work:

Rincón Montes, V., Gehlen, J., Ingebrandt, S., Mokwa, W., Walter, P., Müller, F., and Offenhäusser, A., “Development and *in vitro* validation of flexible intraretinal probes” *Sci Rep* 10, 19836 (2020)

5.1. Design and fabrication considerations

To reduce the insertion footprint and biological impact of intraretinal devices, an approach in which intraretinal probes harmonize with the microstructure and the mechanical properties of the retina was pursued. Considering in turn the development requirements of neural interfaces reviewed in section 2.5, the following design considerations were contemplated:

- To reduce the mechanical mismatch between intraretinal probes and the retina, as well as chronic FBRs for future long-term applications, biocompatible, flexible, and compliant materials should be employed.
- To avoid unnecessary penetrations and collateral damage to neighboring structures (e.g.: the choroid), the length of the shanks should match the thickness of the retina.
- To minimize the implantation trauma (footprint), as well as FBRs for future long-term applications, the cross-section of the penetrating shanks should be as small as possible.
- To facilitate the insertion of the penetrating probes and to reduce insertion lesions, shanks with sharp tips and angles below 40° should be aimed [25], [122].
- Considering the bidirectional purpose of intraretinal probes and to improve neuronal selectivity during electrical recording and stimulation, electrodes should be small enough to interact with one or with a small group of neurons while guaranteeing the electrochemical properties to conduct safely electrical stimulation. Therefore, an appropriate electrode coating should be part of the design and fabrication.

Given the above, flexible polymer materials with an elastic modulus in the low GPa range, such as PI and PaC, were selected as two options for main substrate materials. Additionally, IrO_x and PEDOT: PSS were selected as possible electrode coatings. Preserving the Michigan-like design but optimizing the dimensions of the original Si-BiMEAs, flexible BiMEAs were designed as follows (Figure 5.1 and Figure 5.2).

Flexible probes comprise three main parts: a contact pad area, a tether holder, and four penetrating shanks. The contact pad area contains either 12 or 16 contact pads (300 µm x 200µm) with a pitch of 300 µm. Likewise, the distance between the border and the first contact pads (both left and right) is of 3.65 mm, thereby allowing enough space to handle the probe for a further packaging process. A tether holder 800 µm wide and 200 µm long was implemented to provide a flexible interface between the top end of the shanks and the contact pad area, which will be the border of the external connector/carrier interface after packaging. Each probe contains four penetrating shanks with three or four electrodes each and an inter-shank distance of 100 µm (Figure 5.1).

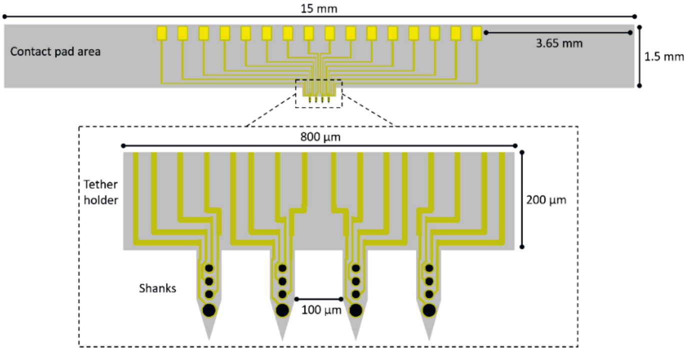

Figure 5.1. Flexible BiMEA design. The BiMEA probes contain a contact pad area, a tether holder, and four penetrating shanks.

Moreover, since healthy mouse retinas are ~ 200 – 225 µm [163] and degenerated mouse retinas are ~ 100 – 120 µm thick [181], [182], shank lengths between 140 – 225 µm were proposed. The cross-section was reduced taking into account a feature resolution limit in photolithography processes of ~ 2 µm [134, Ch. 3] and the achievable thicknesses for PI and PaC. To give clearance to the structures patterned and aligned at different steps of the fabrication process (e.g.: metal electrodes aligned with electrode openings), shank widths of 50 µm and 100 µm were selected. Thus, each shank contains two (for a length of 140-145 µm) or three (for a length of 180-225 µm) recording electrodes and one stimulating electrode with a metal base and passivation opening diameters of 21/15 µm and 31/25 µm, respectively. To enhance the impedance, a bigger diameter was procured for the stimulating electrode. Accordingly, the shanks have a minimum feedline width of 3 µm and a minimum inter-feedline distance of 3.5 µm. Additionally, a two-layer (substrate and passivation) and a three-layer (substrate, interlayer, and passivation) design with a total thickness between 3 – 7 µm were proposed. The shank design described above is displayed in Figure 5.2.

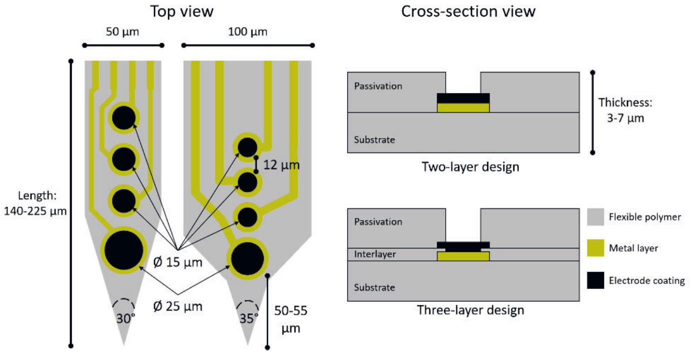

Figure 5.2. Design of flexible intraretinal shanks. The top view. Dimensions of flexible penetrating shanks with varying lengths between 140/145, 180/185, and 220/225 µm. Cross-section view: A total thickness between 3- 7µm is proposed, as well as the implementation of a two-layer (substrate and passivation) and a three-layer design (substrate, interlayer, and passivation) based on flexible polymers. Additionally, an electrode coating is contemplated in the design.

5.2. Fabrication of flexible BiMEAs

The fabrication of flexible BiMEAs was based on the process described in section 3.1.1. For the implementation of IrO_x (flexible IrO_x-BiMEAs) and PEDOT: PSS (flexible PP-BiMEAs), the base process was adapted to each electrode coating. All processes were performed on four inch Si wafers that served as a host substrate during fabrication, allowing in turn a fabrication yield of 128 flexible probes per wafer.

5.2.1. Flexible BiMEAs with IrO_x electrodes

Two fabrication processes were tested for the development of flexible IrO_x BiMEAs: process A for a two-layer design and process B for a three-layer design. For both processes, PI and PaC were used each as the main flexible materials. Additionally, for the fabrication of PI probes a sacrificial layer comprising a metal stack of Cr/Au/Cr with thicknesses of 10/100/50 nm was deposited on top of a blank Si wafer prior to the beginning of the fabrication to enable the release of the probes at the end of the process, as proposed by [183]. Afterwards, a packaging process and further activation of SIROFs were performed.

Process A: two-layer design

For a two-layer design, the fabrication flow comprised the interleaved deposition of two flexible and two metal layers. The latter was completed with two dry etching steps to expose the passivation openings and to outline the shape of the probe. Thus, seven steps were performed as follows (Figure 5.3):

1. Flexible substrate layer:

A first flexible layer was deposited by spin-coating and curing PI-2611 (HD MicroSystems, Germany) or via CVD for PaC with a thickness that corresponds approximately to half of the total thickness of the probe. The adhesion promoter VM-652 (HD MicroSystems, Germany) was used before the deposition of the PI layer to ensure the stability of the layer along the whole fabrication process.

2. First metallization:

A metal stack of 10/100 nm of Ti/Au or Ti/Pt was patterned onto the flexible substrate after a photolithographic and a lift-off process to form the metal base of the electrodes, the contact pads, and the corresponding feedlines (Figure 5.4a). Here, Ti was used as an adhesion layer between the polymer and the conductive layer, Au or Pt.

3. Flexible passivation layer:

A second flexible layer with the same thickness as the first substrate layer was deposited as in step 1. To enhance the adhesion between the flexible and the sandwiched metal layer, VM-652 (HD MicroSystems, Germany) and Silane A-174 (Specialty Coating Systems Inc., USA) were used as adhesion promoters for PI and PaC, respectively.

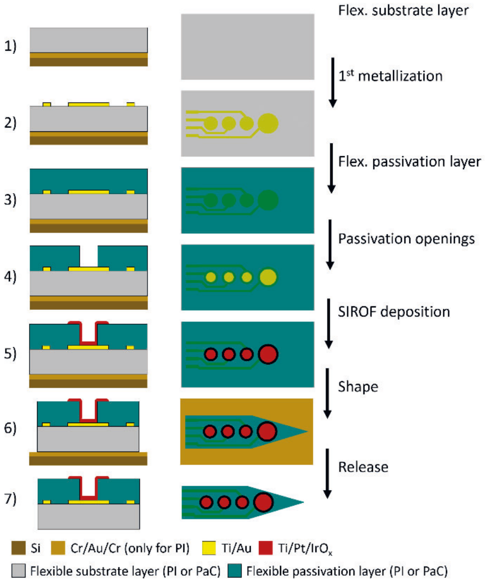

Figure 5.3. Fabrication flow of flexible IrO$_x$ BiMEAs - Process A. Details are given in the text. Fabrication recipes can be found in Appendix 7, Flexible IrOx BiMEAs – Process A.

4. Passivation openings:

Given that the etching selectivity of PI was lower (1:1.2) and of PaC was similar (~1:0.95) to the etch mask resist, AZ 9260 (MicroChemicals GmbH, Germany) was used to patterned an etch mask of at least 1.5 times the thickness of the layer to be etched, thereby allowing to selectively remove the polymer at the electrode and contact pad sites via reactive-ion etching (RIE) (Figure 5.4b). The latter rule was applied for the etch masks of all RIE steps. Likewise, an etch rate of ~ 600 and 800 nm/min was obtained for PI and PaC, respectively.

5. SIROF deposition:

An IrO$_x$ coating was patterned onto the passivation at the electrode sites after sputtering a metal stack of 10/100/250 nm or 10/100/500 nm of Ti/Pt/IrO$_x$. The SIROF had the same diameter as the metal base (21 µm for recording and 31µm for stimulating electrodes), making sure that the smaller passivation opening (15 µm for recording and 25 µm for stimulating electrodes) was completely covered (Figure 5.4c). Considering that the SIROF was going to be in direct contact with the polymer, Ti was used as an adhesion layer and Pt was added as a second conductive layer for IrO$_x$.

6. Shape:

The same rule from step 4 was applied for the thickness of the etch mask, however, this time it was thicker, as the total thickness of the probe had to be considered. Thus, the outline of the probe was etched after a second RIE step (Figure 5.4d).

7. Release:

To release PI probes from the host Si wafer, wet chemical etching was performed using a Cr-etchant solution (Sigma Aldrich, Germany) for ~ 40 min. Afterwards, the probes were rinsed three times in Milli-Q water to remove any Cr-etchant residues. In the case of PaC probes, a drop of water was used to facilitate the release of the probes, and tweezers were used to peel them off completely from the Si wafer.

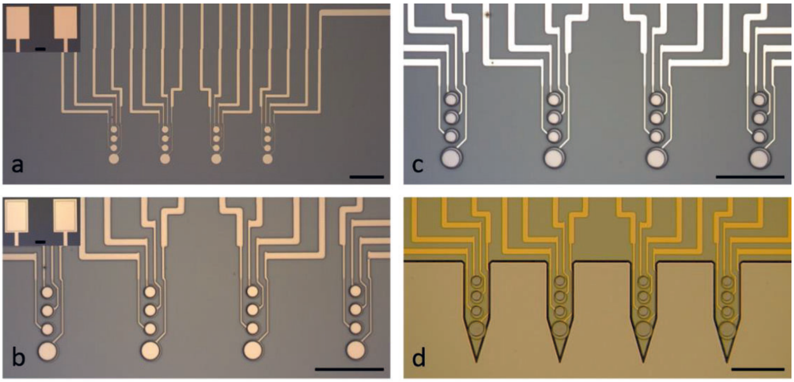

Figure 5.4. Fabrication follow-up of flexible IrO_x BiMEAs - Process A. Optical images following the execution of process A for a flexible IrOx BiMEA with a two-layer design. a) 1st metallization process: patterning of base electrode, feedlines, and contact pads. b) Passivation openings: Removal of the passivation layer at the electrode sites and contact pads. c) Deposition of IrO_x at the electrode sites. d) Shape etching. The scale bars are 100 µm.

Process B: three-layer design

A three-layer design was implemented to achieve recessive electrodes with a SIROF coating. To this end, the deposition of IrO_x was performed before the passivation layer. To ensure the insulation of the metal feedlines after the SIROF deposition, an interlayer between the first metal layer and the SIROF was added to the fabrication flow. The latter implied an extra RIE step to etch the interlayer at the electrode openings, therefore, the passivation openings and the outline of the shape were etched in one RIE step to minimize processing steps. Hence, eight steps were carried out as illustrated in Figure 5.5.

The deposition of the flexible substrate layer, the first metallization process, and the release of the probes were conducted as in Process A, however, since the idea to reduce the thickness of the probe as much as possible prevailed, PI-2610 (HD MicroSystems, Germany) was used instead of PI-2611 to achieve thinner layers. Consequently, steps 3-7 were performed as follows:

3. Flexible interlayer:

A minimum interlayer thickness of ~ 1.3 – 1.5 µm was deposited after spin-coating PI-2610 at 5000 rpm and curing the polymer, and a thickness of ~ 600 nm was achieved via CVD after using 1 g of the PaC dimer. Likewise, VM-652 (HD MicroSystems, Germany) and silane A-174 (Specialty Coating Systems Inc., USA) were used as adhesion promoters for PI and PaC, respectively.

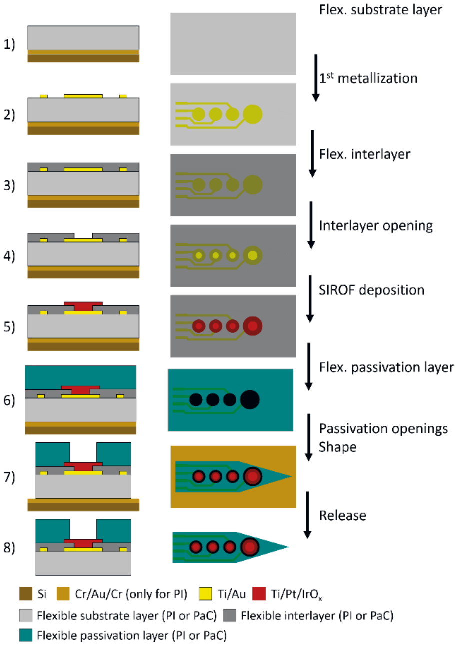

Figure 5.5. Fabrication flow of flexible IrO$_x$ BiMEAs - Process B. Details are given in the text. Fabrication recipes can be found in Appendix 7, Flexible IrOx BiMEAs – Process B.

4. Interlayer opening:

An etch mask using AZ 9260 (MicroChemicals GmbH, Germany) was patterned with photolithography. A first RIE step was performed to remove the interlayer at the electrode sites with a diameter that could be equal or smaller than the base metal electrodes, 31/15 µm and 21/10 µm for the big and the small electrodes, respectively (Figure 5.6a).

5. SIROF deposition:

Considering that etching shape and passivation at the same time implies a longer etching time, a Ti etch stop layer was included in the SIROF stack and tested to avoid a possible physical removal of the IrO$_x$ layer during RIE. Therefore, a 10/100/250/10 nm stack of Ti/Pt/IrO$_x$/Ti was sputtered. After lift-off, an electrode coating with the same size as the base metal electrode was patterned. As follow-up, a concentric circle underneath the SIROF and corresponding to the interlayer opening was visible when the interlayer opening was smaller than the base electrode (Figure 5.6b).

6. Flexible passivation layer:

See step 3 in Process A for flexible IrO$_x$ BiMEAs.

7. Shape and passivation etching:

An etch mask comprising the shape and the passivation openings was patterned as described before (Step 4, Process A for flexible IrOx BiMEAs). Then, a RIE process was performed to etch the passivation openings and outline the shape of the probe at the same time; therefore, the etching time was calculated according to the total thickness of the probe. When applicable, a second process was carried out to etch the 10 nm Ti layer protecting the SIROF. At the end, two concentric circles were visible at the electrode openings, a small inner circle corresponding to the interlayer opening, which was covered with IrOx, and a second outer circle corresponding to the passivation opening (Figure 5.6c). When the interlayer opening was the same size of the base electrode and the passivation opening was smaller than the SIROF coating, only the circle corresponding to the electrode opening was visible (Figure 5.6d). In this way, an effective electrode diameter of 25 µm and 15 µm for the big and small electrodes was achieved.

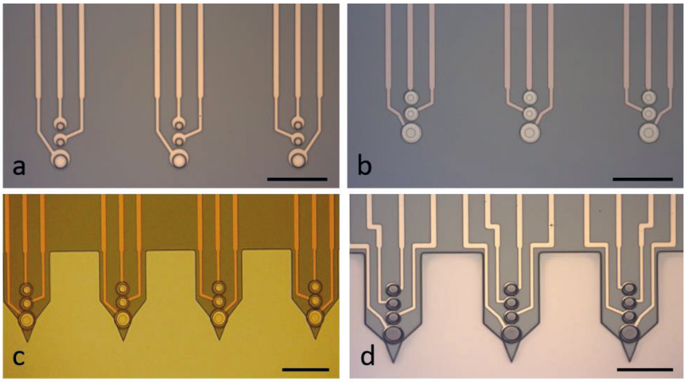

Figure 5.6. Fabrication follow-up of flexible IrOx BiMEAs - Process B. Optical images following the execution of process B for a flexible IrOx BiMEA with a three-layer design. a) Interlayer opening with a diameter small than the base metal electrode. b) SIROF at the electrode sites with a diameter equal to the base electrode. (c-d) Final probes after etching shape and passivation in a same RIE step. c) Interlayer opening smaller than SIROF coating, passivation opening smaller than SIROF coating but bigger than the interlayer opening. d) Interlayer opening was the same size of the base electrode and the passivation opening was smaller than the SIROF coating. The scale bars are 100 µm.

Packaging

A manual flip chip bonding was carried out to solder the flexible probes onto a PCB with a connector for 16 channels. The process was performed on a hot plate at 180°C. The board was first preheated for ~ 60 s, then the low temperature solder alloy Sn42/Bi58 (AMTECH, USA) was applied onto the metal contacts of the board using a syringe, forming in turn liquid bumps on each contact pad. Under a microscope and using tweezers, the flexible probes were manually aligned and placed on top of the liquid solder paste bumps, which solidified after quickly removing the new chip from the hot plate and cooling it down at room temperature.

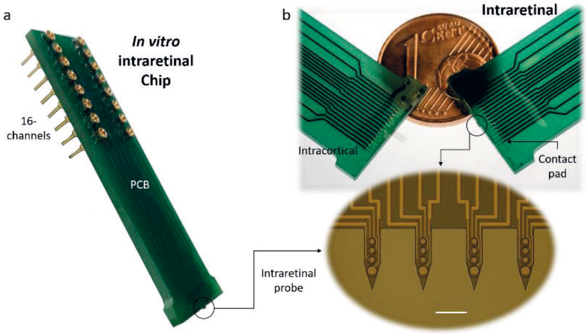

Figure 5.7. *In vitro* intraretinal chip. The images show an *in vitro* intraretinal device after microfabrication and packaging. a) Chip composed of a 16-channels PCB and an intraretinal probe. b) Size comparison of an intraretinal chip with short shanks, which are barely visible with naked eyes, versus an intracortical chip with long shanks, and one euro cent. The inset shows the intraretinal probe soldered on the lower border of the electronic board. Scale bar is 100 µm.

Keeping in mind that the glass transition temperature and degradation temperature of PaC is 90°C and 125°C (Table 3.1), respectively, degradation of the probes was avoided by reducing the liquidus temperature of the solder paste to ~ 160°C and procuring a short exposure (< 60 s) of PaC probes to this temperature. Additionally, the interface between the probe and the electronic board was sealed with a PDMS (mix ratio 1:10) coating cured at 120°C for 30 min. Figure 5.7 displays an example of a chip after microfabrication and packaging.

SIROF activation

After microfabrication and packaging, SIROF activation was performed. As a first step, the potential limits for SIROF stability during activation were investigated. To this end, the protocol reported by [140] was followed. Thus, CV cycles in which the cathodic potential E_c was decreased from -0.6 to -0.9 V and anodic potential E_a was increased from 0.8 to 1.1 V in decrements/increments of 50 mV were performed. Figure 5.8 displays an overview of the SIROF stability experiment. As it can be observed, a sharp increase in the cathodic and anodic currents was visible in the voltammograms during SIROF activation at -0.85 V and 1 V (dark and light blue arrows in Figure 5.8), respectively, thereby indicating the onset of water reduction and oxidation [140].

Moreover, anodic and cathodic peaks at 0.3 V, 0.6 V, and -0.2 V became more visible when the potential limits were broader and when more CV cycles were performed (black arrows in Figure 5.8),. Hence, these peaks indicate redox reactions that lead to changes of the oxidation state of Ir and a charge transfer across the electrolyte-electrode interface [184], [185]. Depending on the CV potential limits, sweep rate, and phosphate buffer concentration, these peaks have been reported at different potentials [185]–[187]. Additionally, anodic peaks have been mostly associated to the oxidation of Ir^{3+} to Ir^{4+} (peaks I and II in Figure 5.8a-g) and the cathodic peak (III in Figure 5.8b-f) to the reduction of Ir^{4+} to Ir^{3+} [140], [187], [188]. The additional anodic peak at -0.43 V (IV in Figure 5.8g) has been attributed to hydrogen desorption/adsorption at the interface of the electrode or to the redox reaction of Ir^{3+} to Ir^{+} [185], [186]. Furthermore, a color change from brown to dark blue/black was visible with increasing anodic potentials. These color changes were more prominent when more activation cycles were performed and at anodic potentials equal or higher than 1 V (dashed squared box in Figure 5.8). Consequently, the coloration indicates the formation of oxide layers associated to the oxidation of Ir^{3+} to Ir^{4+}, as it has been reported for the activation of AIROFs using anodic potentials outside the water window limit [186], [188]–[190].

SEM and FIB cut images in Figure 5.8 show that SIROF activations at lower potential limits presented a homogenous porous topography, while activations at the water window potentials generated a non-homogenous, rough, and porous surface with a higher growth of oxide layers. This behavior matches reports given by [185], [191] after potential cycling at ± 1V. Thus, SIROFs were stable until anodic potentials higher or equal than 1 V were approached. At these potentials, cracks and delamination of the SIROFs were noticed at the interface of the SIROF and the interlayer (red arrows Figure 5.8). Considering that the films did not delaminate from the Ti/Au base layer (inner circles, Figure 5.8), the former can be mostly attributed to the mechanical stresses given the growth of oxide layers during activation [185].

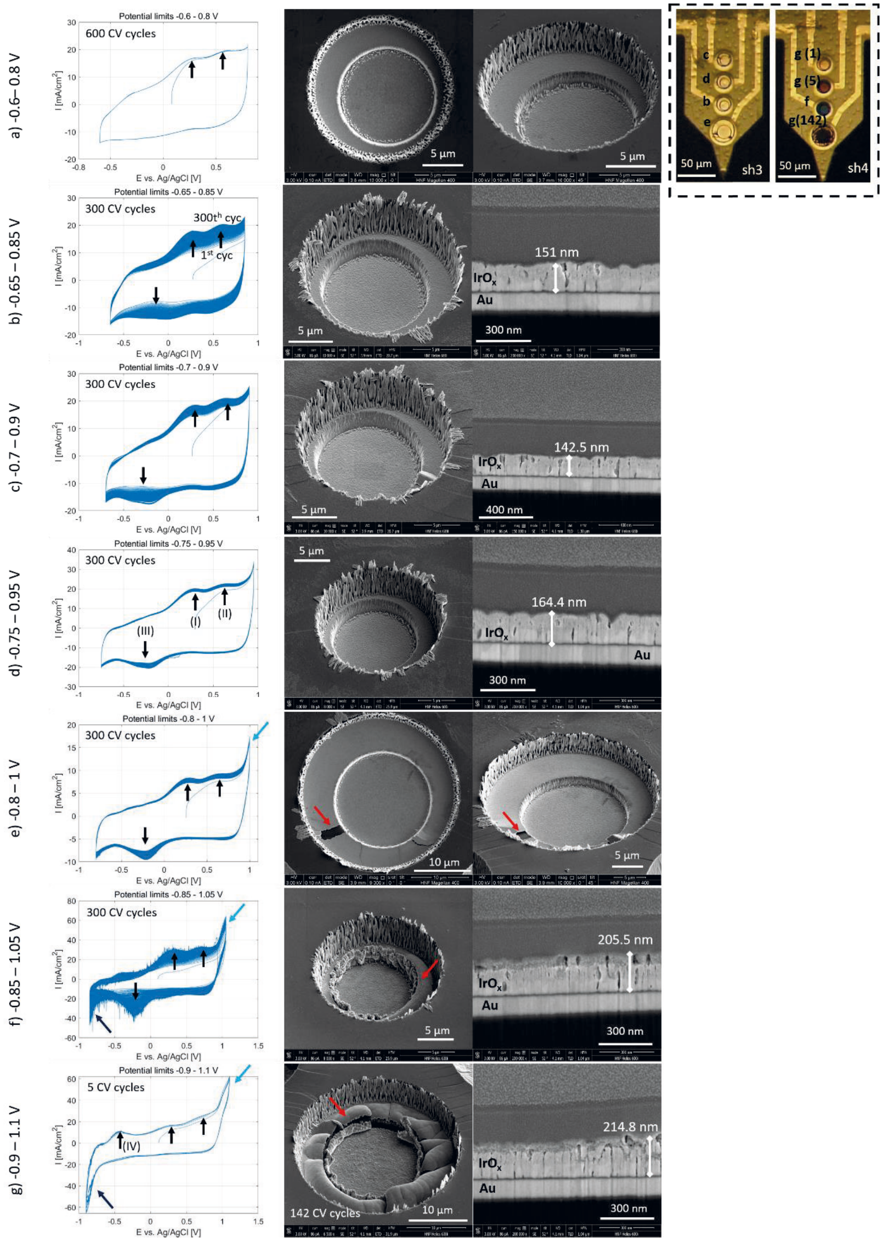

Figure 5.8. Potential limits for SIROF stability. Cyclic voltammograms (first column) and SEM/FIB cuts images (second – third columns) of SIROFs subjected to CV cycling with a sweep rate of 100 mV/s between cathodic potentials of -0.6 and -0.9 V and anodic potentials between 0.8 to 1.1 V (a-g). Light and dark blue arrows indicate the onset of water oxidation and reduction, black arrows point out anodic and cathodic peaks (I-IV), and red arrows show delamination. At the upper right (squared dashed box), optical images of the corresponding PI-based shanks containing the activated electrodes of the experiment.

Given that delamination of SIROFs were encountered beyond the water windows potentials (-0.85 V and 1 V), and that in seldom cases cracks occurred when cycling between -0.7 and 0.9 V, potential limits between -0.6 V and 0.8 V were used for the activation of SIROFs (Methods in section 3.2.2). At these potential limits, the activation is dominated by the hydration of the film (adsorption/desorption of hydrogen), increasing in turn the thickness of the film and its charge storage capacity. Consequently, the voltammograms expand with more activation cycles until the film is fully hydrated, thereby stabilizing the CV response [140], [190], [191]. Hence, to determine the optimal number of cycles for SIROF rehydration, five steps of 100 CV cycles were carried out for probes with a two-layer and a three-layer design.

The effect described above was partially observed for SIROFs on 2-layer probes. Figure 5.9a exhibits a typical voltammogram measured during the activation of a 2-layer probe. Here, the current density and the CSC_c (Figure 5.9a) of the SIROF had a sharp increase during the first 200 cycles, followed by a smooth growth as 300 cycles were completed, and achieving a peak CSC_c of ~19.5 mC/cm^2. Potential cycling was continued until 500 cycles were completed, wherein the CSC_c was reduced by 10% (Figure 5.9c, black trace).

This behavior matches the optical follow-up performed during SIROF activation (Figure 5.10, top row). After 300 activation cycles SIROF degradation was visible at the border of the passivation of all stimulating electrodes (big lower electrodes). After 500 cycles, it was evident that SIROFs that were adhered to the passivation with a Ti/Pt layer without the presence of the base metal layer (1st metallization), were prone to delamination (SEM picture aa-500cyc in Figure 5.10, top row).

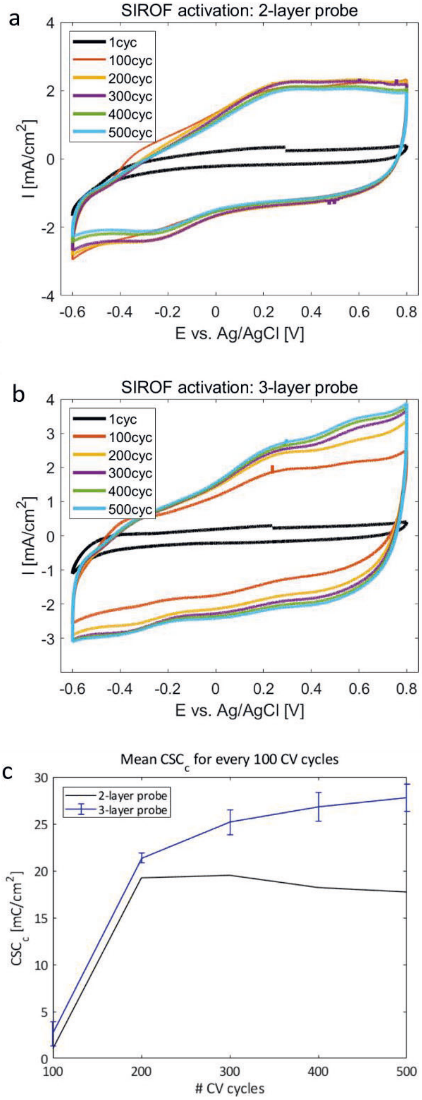

Figure 5.9. SIROF activation. Cyclic voltammograms corresponding to the cyclic activation of SIROFs in devices with a 2-layer (a) and a 3-layer (b) design. The current density (*I*) at different electrode potentials (*E*) versus a Ag/AgCl reference electrode is shown. *I* considers the geometric surface area of the 16 electrodes that were short-circuited during activation. c) Comparison of the cathodic charge storage capacity (CSC_c) for both probe designs.

On the other hand, SIROFs on 3-layer probes showed the expected behavior during activation (Figure 5.9b). As more activation cycles were performed, a continuous increase of the CSC_c was observed until the CV response started to stabilize, reducing in turn its increase rate as 500 activation cycles were approached, where a peak value of ~ 27.8 mC/cm^2 was reached (Figure 5.9c, blue trace). As comparison, the follow-up of a successful SIROF activation for a 3-layer probe is displayed in Figure 5.10 (bottom row), showing the integrity of the layer after 500 activation cycles. Although SIROFs showed stability even after 600 CV cycles (Figure 5.8a), only a 4% increase was observed in the CSC_c from 400 to 500 cycles, therefore, 500 CV cycles showed to be optimal for the activation of IrO_x electrodes.

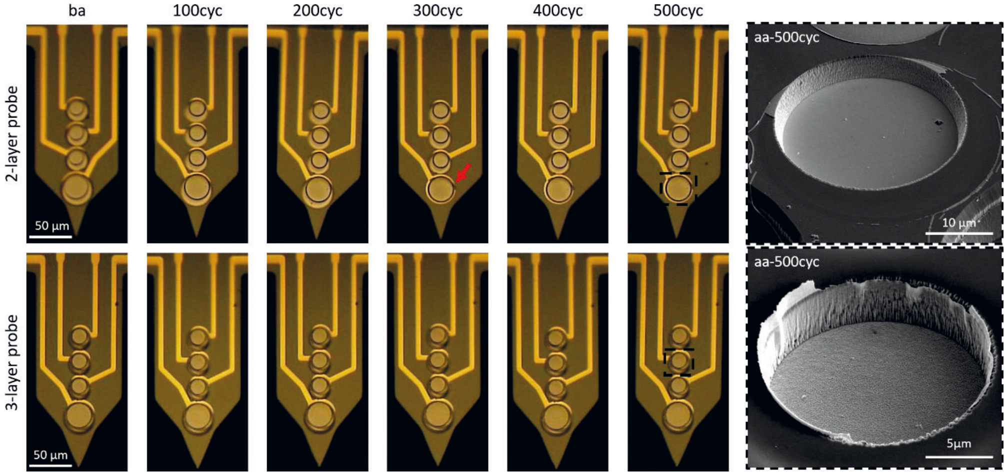

Figure 5.10. Follow-up of SIROF activation. Optical images tracking SIROFs before activation (ba) and every 100 cycles during activation after 500 cycles were completed (aa-500cyc). SEM images (right most column) inspecting one electrode aa-500cyc (enclosed with black dashed lines). The SIROF activation is shown for a 2-layer (top row) and a 3-layer (bottom row) probe. The red arrow indicates a visible degradation of the SIROF after 300 activation cycles for a 2-layer probe.

5.2.2. Flexible BiMEAs with spin-coated PEDOT: PSS electrodes

Probes with a two-layer design and a PEDOT: PSS electrode coating that matched exactly the electrode opening of the passivation were fabricated. To achieve such coating, a sacrificial PaC layer was used to structure PEDOT: PSS at the desired electrode sites. Figure 5.11 illustrates the fabrication flow followed, which was adapted from [146], [147] to achieve electrode coatings for both PI- and PaC-based probes. Steps 1-3 are the same as in Process A for flexible IrO_x probes (see section 5.2.1). Hereunder, steps 4-9 will be described:

4. Etching shape:

Once the metal layer (Ti/Au or Ti/Pt) was sandwiched between two flexible layers (steps 1-3), the first RIE step was carried out. Here, the shape of the probes was first etched, reducing in this way the contact area between the sacrificial layer that will be used in further steps and the passivation layer (second flexible layer). Likewise, the openings corresponding to the contact pads can be also etched along with the shape. Hereafter, the process followed when etching initially the shape will be referred as process A, and the process followed when etching initially shape and contact pad openings process B.

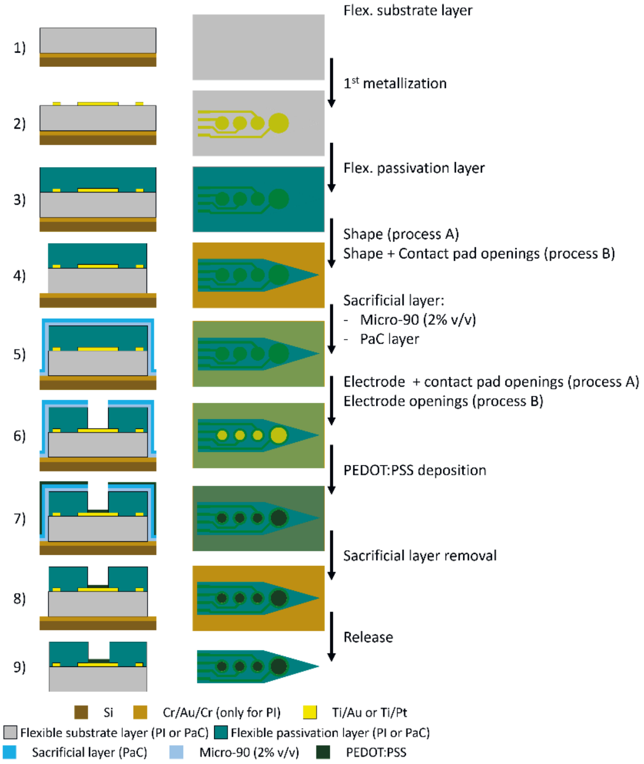

Figure 5.11. Fabrication flow of flexible BiMEAs with spin-coated PEDOT: PSS. Details are given in text. Fabrication recipes can be found in Appendix 7, Flexible PEDOT: PSS BiMEAs .

5. Sacrificial layer:

A sacrificial layer that consisted of a PaC coating of ~ 2.5 µm thick was deposited onto the wafer. To facilitate the removal of the sacrificial layer in further steps, the cleaning solution Micro-90 (International Products Corporation, UK) was spin-coated at a concentration of 2% in deionized water (v/v) prior to the deposition of PaC.

6. Etching electrode openings:

In this step, an etch mask exposing both the electrode and contact pad sites was patterned via photolithography (process A). In the case of process B, an etch mask comprising only the electrode openings was employed. Then, a RIE process was performed to etch together the sacrificial layer and the passivation layer.

7. PEDOT: PSS deposition:

To enhance the adhesion of PEDOT:PSS on the electrode sites and to facilitate the deposition via spin-coating, the surface of the wafer, which comprised the sacrificial PaC layer and the electrode sites (Au or Pt), was first activated with O_2 plasma. Then, two layers of PEDOT: PSS were spin-coated one after the other (see fabrication details in Appendix 6, A.6.8. PEDOT: PSS coating).

8. Sacrificial layer removal:

After spin-coating PEDOT: PSS, the sacrificial layer was first lifted from one edge of the wafer using a tweezer, and droplets of water were dropped in the underlying area between the sacrificial layer and the substrate. As the water spread underneath the sacrificial layer, the latter was peeled-off slowly (Figure 5.12a). The sacrificial layer was removed easily from the Si surface and from PaC-based probes, however in the case of PI, the removal was not straight forward (see section 5.3. Microfabrication challenges). Therefore, the sacrificial layer had to be removed probe by probe in the case of PI. In cases where the contact pads were also coated (process A), PEDOT: PSS was removed physically with a wet cue tip (Figure 5.12b). However, given the reduced space between probes, using this method led to the undesired removal of PEDOT: PSS on the recently coated electrodes, as well as to the forced delamination of the passivation layer at the contact pad area (Figure 5.12c). Given the latter, it was preferred to etch the contact pads along with the shape in step 4 (process B), so that the sacrificial PaC layer would also cover them, avoiding to coat the contact pads during step 7 (Figure 5.12d).

9. Release:

PaC probes were released as described before in the last step for the fabrication of flexible IrOx probes (see section 5.2.1). In the case of PI probes, prior to the wet chemical etching of the sacrificial layer based on Cr, an etching mask covering the probes shape was used to protect the electrode coating (see details in Appendix 6, A.6.9. Wet chemical etch mask).

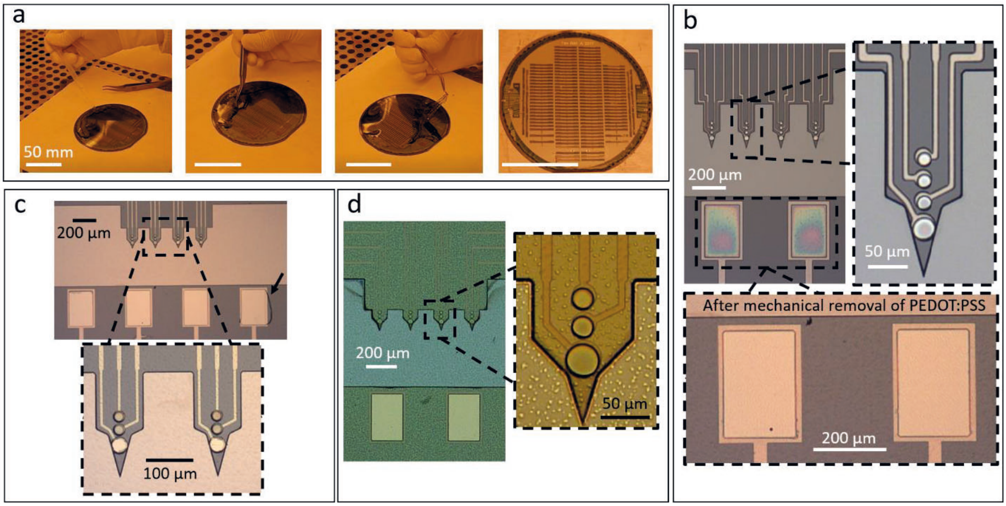

Figure 5.12. Fabrication follow-up of flexible PEDOT: PSS BiMEAs. a) Removal of sacrificial PaC layer. Details are given in text, step 8. b) Flexible PEDOT: PSS BiMEAs following process A. c) Undesired removal of electrode coating and damage to the passivation layer (black arrow) after physical removal of PEDOT: PSS from the contact pads. d) Flexible PEDOT: PSS BiMEAs following process B. Images from (b-d) were performed after removal of the sacrificial layer. PEDOT: PSS can be distinguished as a bluish coating at the electrode and contact pad sites.

5.3. Microfabrication challenges

During the microfabrication of flexible BiMEAs, challenges were encountered along the different processing steps. The most representative problems with their respective solutions, if available, are summarized here below.

5.3.1. Processing polymer-based materials

Metallization

During the process of metallization, PaC wrinkles around the metal structures were observed when evaporating 200 nm of Pt and the formation of micro cracks were visible after evaporating 200 nm or 100 nm of Pt on PaC (Figure 5.13a). It was also observed that cracks after 100 nm Pt were smaller and milder with lengths between 0.5 – 2 µm, while the evaporation of 200 nm Pt yielded bigger cracks with lengths between 6 – 15 µm, thereby implying a thickness or evaporation time dependency on the formation of cracks. Despite the cracks, the metal layers were still conductive and working devices were still fabricated with Pt as the conductive layer.

Temperature measurements during Pt evaporation with a deposition rate of 0.5 nm/s revealed a final substrate temperature of ~ 58°C for one deposition step of 100 nm Pt and a temperature increase of ~ 35°C/100 nm Pt if two deposition steps of 100 nm Pt with a cooling step of 10 mins in between are performed. This suggests that it is indeed possible to reach temperatures above 90°C during the evaporation of 200 nm Pt in one single step, temperatures that can already induce the degradation of PaC and the formation of metal cracks given the mismatch of the thermal coefficients of expansion between PaC and the metal layers. The latter implies that thermal radiation might be one of the causes for the formation of cracks, yet crack formation was still visible in stepwise depositions of Pt, indicating that cracks could be a result of a combined effect of local heating on the PaC coating and the thermal radiation from the target.

Similar issues concerning the evaporation of Pt on PaC have been described before by [192], reporting that the use of metals with a high melting point, such as Pt, and processes with high heat transfer like e-beam assisted evaporation generated a mismatch of the thermal coefficients of expansion between the polymer and the metal, inducing in turn thermal stresses that formed cracks on Pt and deformations of PaC.

Moreover, cracks and PaC deformation was not observed when evaporating Au (Figure 5.13a). Differences between the evaporation of Pt and Au comprise not only higher evaporation temperatures for Pt, but the generation of more secondary electrons during evaporation, suggesting in turn that both thermal and electron radiation could influence the evaporation of Pt on PaC, however further tests should be performed to confirm the hypotheses. Thus, regarding metallization processes on PaC coatings, the use of Ti/Au layers is recommended, and in the case of Pt, stepwise depositions with cooling steps in between could ease the formation of cracks.

Dry etching

For etching PI and PaC via RIE, photoresist etch masks with a thickness between 5-20 µm were patterned. In steps where only the contact pad and electrode openings were to be etched, the photoresist covered the complete wafer, except at the contact pad and electrode sites. Hence, problems were encountered as the wafer was stuck to the clamp of the RIE machine due to melted photoresist after running a RIE process to etch PI or PaC, impeding this way the transfer of the etched wafer to the load-lock. In this case, either the wafer had to be cooled down for ~ 30 min to attempt a manual transfer of the wafer, or the machine had to be opened to extract the wafer. In either case, there is a risk to break down the wafer. An initial solution to the given problem consisted in the implementation of a resist-free ring at the edges of the wafer, which was accomplished by patterning the ring along with the passivation during photolithography. After RIE, the ring was visible as the polymer at the resist-free edges of the wafer had been etched (Figure 5.13b).

While resist-free edges produced successful processes most of the times, occasionally the wafers kept sticking to the clamp, even when no resist was present at the edges. To avoid the latter, etching processes consisting of several etching steps alternated with cooling steps of ~3 min each and cooling down the substrate temperature from 10°C to 5°C were tested together with resist-free edges, however cases of sticking wafers were still present. The latter suggests that not only the resist at the edges of the wafer, but etching residues could influence the sticking behavior of polymer coated wafers after RIE. Therefore, a more permanent solution should include resist-free edges and avoid the direct contact of the clamp with the polymer coated edges of the wafer. To this end, a metal ring (e.g.: 100 nm of Ti) at the edges of the wafer is suggested. The disadvantage of this solution would be that structures at the edges of the wafer (e.g.: alignment markers) would be lost, therefore shadow masks should avoid structures at the edges of the wafer in its design.

Removal of photoresist etch mask

The removal of the photoresist etch masks are usually performed in a bath of acetone followed by a rinse of isopropanol [192], though, the latter was unsuccessful when trying to remove the photoresist etch mask after performing RIE processes on polymers with metal layers embedded. Figure 5.13c exposes residues, visible as black sheaths, after stripping the photoresist etch mask in acetone. During dry etching processes, re-deposited materials on the etch mask can hinder the removal of the etch mask [193], therefore AZ-100 remover (MicroChemicals GmbH, Germany), a high performance stripper, was used in an ultrasound bath for at least 10 min to remove completely the photoresist etch mask (Figure 5.13c).

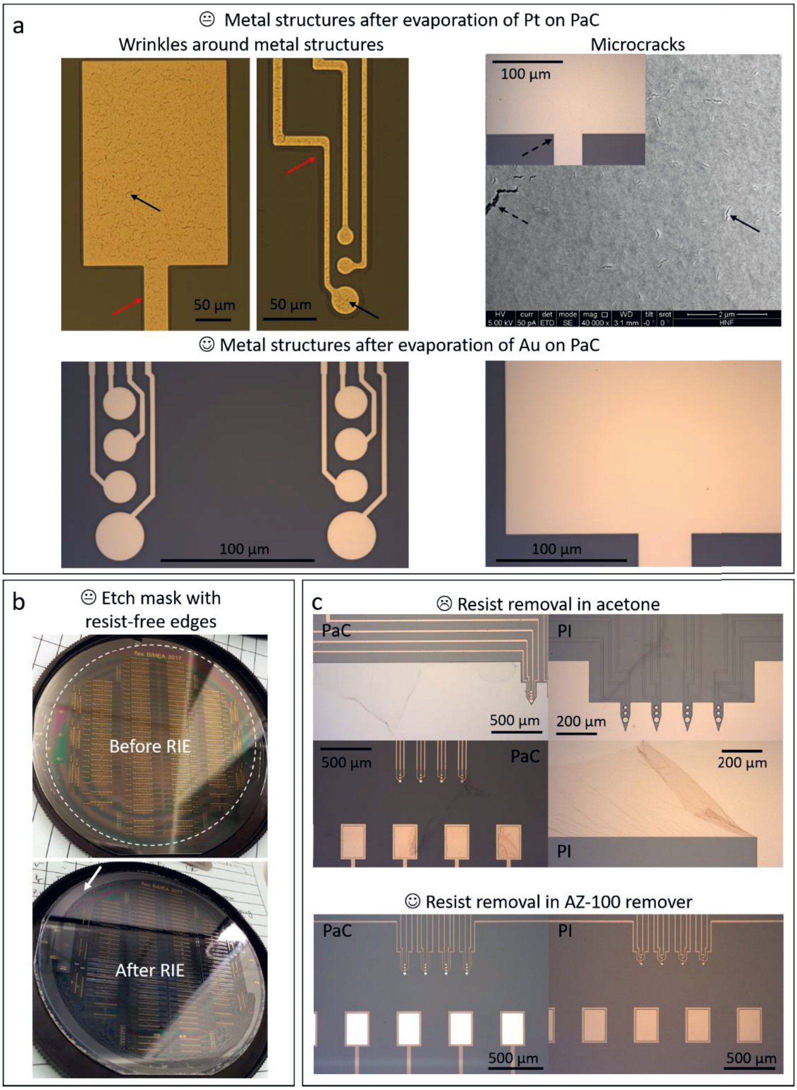

Figure 5.13. Fabrication challenges processing polymer-based materials. a) Metallization. PaC wrinkles around 200 nm Pt structures (red arrows) and the formation of cracks (black arrows) on the metal structures are visible after the evaporation of 200 nm and 100 nm of Pt on PaC. The latter was not visible when evaporating Au. More details are given in the text. b) 4-inch wafers coated with a thick photoresist tend to stick to the clamp of a RIE machine, therefore, an etch mask on a wafer with resist-free edges is advisable. E.g.: The white dashed circle outlines the border of the passivation etch mask, where the contact pad and electrode openings, as well as the edges of the wafer are exposed (resist-free). After performing the RIE process, the resist-free edges of the wafer avoided the wafer to stick to the clamp of the machine, etching in turn the polymer at the edges (white arrow). More details are given in the text. c) Photoresist stripping. After RIE, resist and etching residues (black sheaths) were visible when stripping the etch mask in acetone for both polymer materials (PaC and PI). The use of the stripper AZ-100 remover (MicroChemicals GmbH, Germany) in an ultrasound bath was used to remove completely the etch mask and etching residues after RIE. More details are given in the text. The happy, serious, and sad emoticons indicate if the process works, partially works, or fails with the given method.

5.3.2. SIROF coatings

SIROF delamination

SIROF delamination from the interlayer (2nd flexible layer in IrO_x BiMEAs - Process B) or the passivation layer (2nd flexible layer in IrO_x BiMEAs - Process A) was mostly observed when using high potential limits during activation (Figure 5.8) or during the activation with safe potential limits in probes with a two-layer design (Figure 5.10). While probes with a three-layer design showed SIROF stability in most of the cases, SIROF delamination was observed occasionally in probes whose SIROF coatings were bigger than the interlayer opening (red arrow in Figure 5.14a). Thus, the interlayer (~ 600 nm for PaC and ~ 1.5 µm for PI) generated a step thicker than the thickness of the coating (~ 150-200 nm after fabrication).

During activation, the coating at the edge of the interlayer step did not withstand the stresses generated, rupturing the layer and causing a mild delamination. The latter was solved using a three-layer design with SIROF coatings that matched the size of the interlayer opening and with a passivation opening that was smaller than the SIROF coating, thereby offering mechanical stability to the coating and avoiding geometrical stresses to the coating (Figure 5.14b). The latter is important, considering that the activation of SIROFs comprises an increment in thickness and consequently in volume, as it was shown in section 5.2.1, SIROF activation.

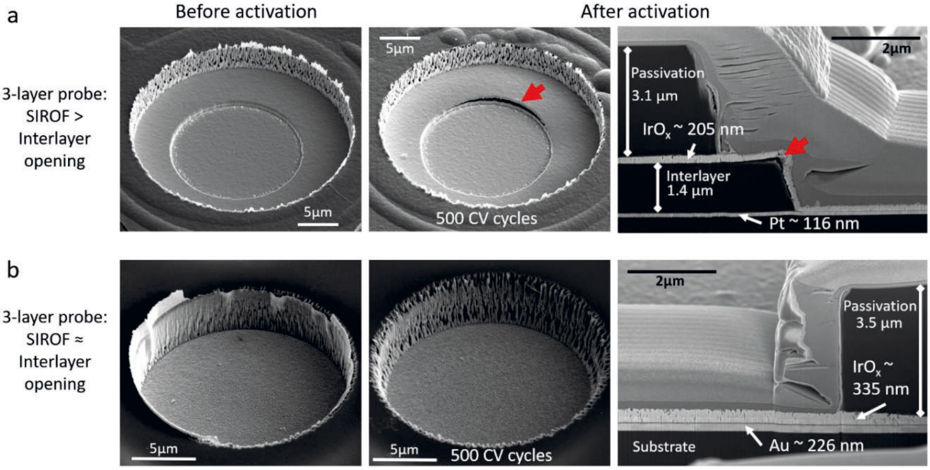

Figure 5.14. Challenges processing SIROFs. SEM images before activation (left column) and after activation (middle column) are shown and FIB cut showing the electrode cross-section is displayed in the right column. a) SIROF delamination of a probe with a three-layer design whose SIROF coating was bigger than the interlayer opening (concentric circle). Delamination occurred during SIROF activation at the edge of the step generated by the interlayer thickness (red arrows). b) SIROF coating before and after activation in a three-layer probe with a coating similar in size to the interlayer opening and a passivation opening smaller than the coating. The electrode cross-section (right column) does not show the interlayer.

SIROF thickness and morphology

Before SIROF deposition, a Ti/Au (10/100 or 10/200 nm) stack was mainly used in the first metallization process to pattern the metal feedlines and the metal base layer of the electrodes. For the second metal deposition, comprising the deposition of SIROFs, three main processes were tested: i) a Ti etch stop layer on top of 250 nm of IrO_x to prevent etching the SIROF while etching the passivation and the shape of the probes in the same RIE step, ii) the deposition of 250 nm of IrO_x, in order to perform two RIE steps to etch individually the passivation and the shape of the probes, and iii) the deposition of 500 nm of IrO_x to etch in one RIE step the passivation and the shape of the probes.

In the first case, after etching the passivation and shape of the probe, an extra RIE step was carried out to remove the Ti layer on top of the SIROF. Nonetheless, despite the initially deposited 250 nm of IrO_x, a final thickness of ~ 96.79 ± 14.06 nm was achieved after microfabrication (Figure 5.15a). In the second case, although a SIROF thickness of ~ 250 nm was expected, SIROFs had in average a thickness of 202.3 ± 14.4 nm (Figure 5.15b). In the last case, SIROFs with an average thickness of 411.23 ± 11.67 nm were obtained (Figure 5.15c).

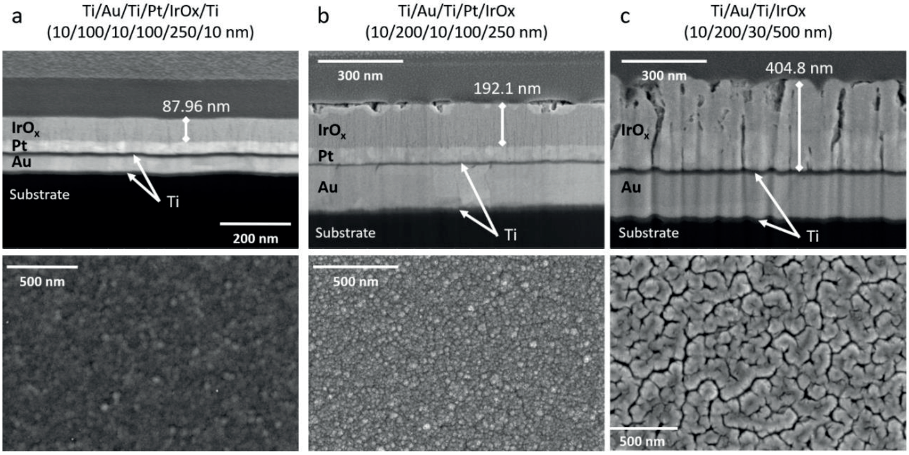

Figure 5.15. SIROF thickness and morphology. FIB cut (top row) and SEM images (bottom row) after the microfabrication of flexible probes with SIROFs with a) a 250 nm thickness deposition and a Ti etch stop layer, b) a 250 nm thickness deposition, and c) 500 nm thickness deposition. More details in text.

Considering that SIROFs with a minimum thickness of 200 nm are recommended for optimal electrochemical properties in stimulating electrodes [140], the best results were obtained for ii) (Figure 5.15b) and iii) (Figure 5.15c). In the case of ii), the SIROF was not subjected to the ionized gases during RIE, indicating that the SIROF deposition *per se* produced an IrO_x layer ~ 50 nm below the expected thickness. Hence, a SIROF reduction of ~ 50% was obtained in the case of i), while in iii) the SIROF was reduced by ~ 8.6% after RIE. On one side, the latter suggests that the Ti etching recipe etched also the SIROF, indicating that a Ti etch stop layer is not beneficial to the process. On the other side, the recipe used to etch PI and PaC generated a SIROF thickness reduction below 10% (case iii), implying that either one or two RIE steps can be performed without dramatically affecting the SIROF.

Furthermore, as it can be observed in Figure 5.15, the surface morphology of SIROFs showed a dense granular structure and porous structure for thickness of ~ 200 nm (Figure 5.15b). When the thickness was reduced, as it was the case of i) (Figure 5.15a), the granular structure was not clear, thereby diminishing the porosity of the layer and reducing the effective surface area of the electrode. Conversely, when the thickness was increased (Figure 5.15c), despite the thickness reduction in iii), the porosity of the layer was plentiful and more fractal, increasing in turn the effective surface area of the electrode. Hence, 500 nm SIROFs are preferred to ensure an adequate thickness and surface morphology of the electrodes after microfabrication.

5.3.3. Spin-coated PEDOT: PSS

Bubbles during photolithography on the sacrificial PaC layer

During the photolithographic process to pattern an etch mask on the sacrificial PaC layer (step 6, Figure 5.11), bubbles underneath the sacrificial layer were formed in big surface areas that were exposed to UV light (Figure 5.16a). In this case, the shadow mask exposed the electrode openings (bubbles not observed in small areas), the edges of the wafer (for a resist-free edge), and at the alignment markers area (close to the edge of the wafer, enclosed with a dashed rectangle). This phenomenon has been reported in the literature when using thick photoresist layers (≥ 20 µm) and high exposure doses of UV light ($> 12 J/cm^2$), and has been attributed to the gas permeability of PaC and photoresist off-gassing during UV exposure [192].

In the case presented here, UV doses of maximum 2100 mJ/cm^2 for a 20 µm thick etch mask were used. Likewise, bubbles were observed when the release agent Micro-90 (International Products Corporation, UK) was employed. Consequently, to reduce the solvent concentration of Micro-90, soft-bake times between 1 – 4 min were applied after spin-coating the soap and before the deposition of PaC, yet bubbles were still formed. Therefore, before continuing with the next processing step, which comprises a RIE process, bubbles were moved to the edges of the wafer with a cue tip and in some cases pierced. During RIE, the high vacuum slowly diffused the bubbles away, allowing the process to continue. In this way, it was possible to finish the spin-coated PEDOT: PSS process after the formation of bubbles.

Removal of sacrificial PaC layer

During the removal of the sacrificial PaC layer, PaC residues that were difficult to remove, even under rinsing with water, were observed on PaC probes (top photo in Figure 5.16b). On the other hand, regardless of Micro-90 (International Products Corporation, UK), the sacrificial layer had a better adhesion on PI probes than on PaC probes or the Si wafer, what hindered the removal of the sacrificial layer from the top layer of PI probes (lower photo in Figure 5.16b). Hence, a manual removal of the sacrificial layer was performed on PI probes. Additionally, it was observed that the longer the time window between spin-coating Micro90 and the final removal of the sacrificial layer, the more difficult it was to release the latter. Therefore, it is suggested to perform such process within the same week. Moreover, the use of a water dissolvable resist instead of Micro-90 should be considered in future fabrications before the deposition of the sacrificial PaC layer, what could in principle facilitate the removal of the sacrificial layer.

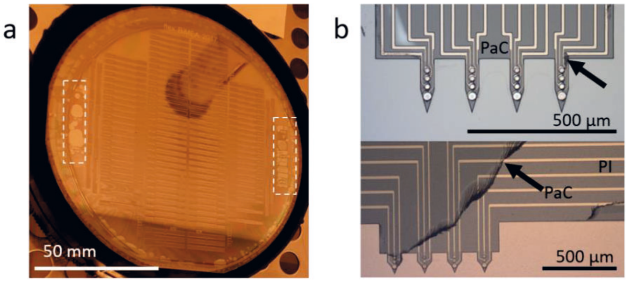

Figure 5.16. Challenges of spin-coated PEDOT: PSS. a) Bubbles formation under the sacrificial PaC layer during photolithography at the big UV exposed areas of the wafer: the edges and the areas enclosed with the white dashed rectangles, corresponding to the alignment markers area. b) PaC residues after the removal of the sacrificial PaC layer from a PaC (top) and a PI (bottom) probe.

5.4. Electrochemical characterization of recording/stimulating electrodes

5.4.1. SIROFs

The recording and stimulation capabilities of the SIROF-based electrodes were evaluated after 500 activation cycles. In general, the electrodes exhibited good electrochemical properties with an average Z between 55 – 80 kΩ, a CSC$_c$ between 31 – 77 mC/cm^2, and a CIC between 0.68 – 1.65 mC/cm^2 (see summary in Table 5.1).

Table 5.1. Summary of electrochemical properties of SIROF electrodes. The average and the standard deviation of the following parameters are shown. GSA stands for the geometric surface area, Z for the impedance magnitude at 1 kHz, CSC$_c$ for the cathodic charge storage capacity, $I_{inj,\,ph}$ and $Q_{inj,\,ph}$ for the maximum current and charge injection thresholds, and CIC for the charge injection capacity. $I_{inj,\,ph}$, $Q_{inj,\,ph}$, and CIC were calculated for a 500 µs current pulse with a maximum cathodic polarization voltage (E_{mc}) of -0.6 V. ^{a} $N_{25\mu m} = 37$, $N_{15\mu m} = 110$. ^{b} $N_{25\mu m} = 24$, $N_{15\mu m} = 68$.

Parameter	**Electrode diameter**	
	25 µm	***15 µm***
GSA [µm^2]	490	176.7
Z before activation [kΩ] ^{a}	382.72 ± 212.64	461.63 ± 306.66
Z after activation [kΩ] ^{a}	55.66 ± 28.68	80.25 ± 43.43
CSC$_c$ [mC/cm^2] ^{a}	31.3 ± 14.43	77.48 ± 50.24
$I_{inj,\,ph}$ [µA] ^{b}	6.70 ± 2.71	6.04 ± 2.97
$Q_{inj,\,ph}$ [nC] ^{b}	3.35 ± 1.35	3.02 ± 1.48
CIC [mC/cm2] ^{b}	0.68 ± 0.28	1.65 ± 0.92

As shown by Figure 5.17 and Table 5.1, the Z was reduced ~ 82 – 85% after SIROF activation for a frequency range between 1Hz and 10 kHz. Likewise, in this frequency range the electrodes presented a pseudocapacitive behavior with a phase angle of ~ 58°, while a more resistive behavior was observed at frequencies higher than 10 kHz, matching in turn the electrochemical behavior of SIROFs reported by others [194]–[198]. As expected, the dependency of the impedance on the

GSA of the electrodes was observed, as the impedance for the bigger electrode diameter (25 µm) was higher than for the smaller diameter (15 µm).

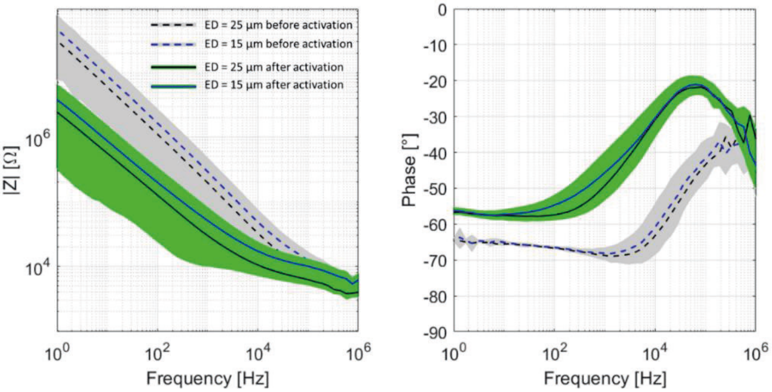

Figure 5.17. SIROF impedance. Typical bode plot showing the impedance of SIROF electrodes in one intraretinal probe. The average impedance magnitude |Z| (left) and the corresponding phase angles (right) are shown for the electrode diameters (ED) 25 µm (N = 4, solid lines) and 15 µm (N = 12, dashed lines) before (gray) and after (green) SIROF activation. The colored shaded areas show the standard deviation.

Inversely, current densities measured for the smallest GSA were higher than for the bigger electrodes (Figure 5.18). Consequently, the CSCc of the smallest GSA (176 μm^2) doubled the values of the biggest GSA (490 μm^2) (Table 5.1). These results agree with those reported by [199], that shows an inversely proportional relationship between CSCc and the GSA, especially with GSAs below 200 μm^2. Additionally, the CSC_c and current densities measured during CV show high variability, even among electrodes of a same GSA (Figure A.8. 1, in Appendix 8), what can be attributed to the fact that electrodes of a same device were activated in parallel, leading in turn to an inhomogeneous activation with variable current densities from electrode to electrode [197].

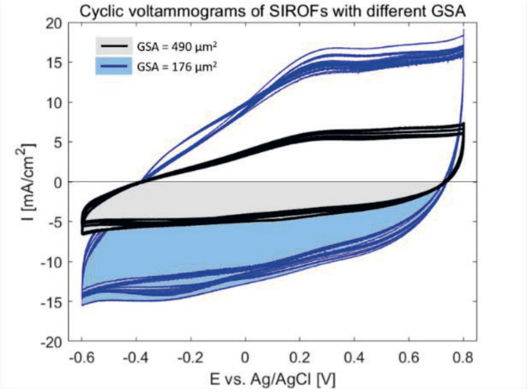

Figure 5.18. Cyclic voltammograms of SIROFs with different GSA. Cyclic voltammograms measured of the electrodes of two devices are displayed for SIROFs with a geometric surface area (GSA) of 490 μm^2 (N = 8, black-gray) and 176 μm^2 (N = 24, blue). The shaded areas represent the cathodic charge storage capacity (CSC_c) of the electrodes. The *y* and *x* axes show the current density (*I*) and working electrode potential (*E*) versus a Ag/AgCl reference electrode, respectively.

Furthermore, the maximum CIC of the electrodes was investigated by determining current and charge injection thresholds to avoid the polarization of the electrodes beyond the water window limits. Although cathodic and anodic limits of -0.85 V and 1 V were observed for the SIROFs obtained after fabrication, voltage transients were characterized considering a maximum cathodic polarization voltage of -0.6 V, as it is commonly reported in the literature [100]. Given that the maximum cathodic polarization voltage E_{mc} (-0.6 V) was reached first than the maximum anodic polarization voltage E_{ma} (0.8 V), current and charge thresholds were estimated for the cathodic phase of the current pulse. As exposed in Figure 5.19, an electrode will present a higher polarization voltage if the phase period of the current pulse is longer, therefore the CIC should be characterized for the expected pulse width range or phase periods (T_{ph}) of the current stimuli for all electrodes within a device that intends to perform electrical stimulation.

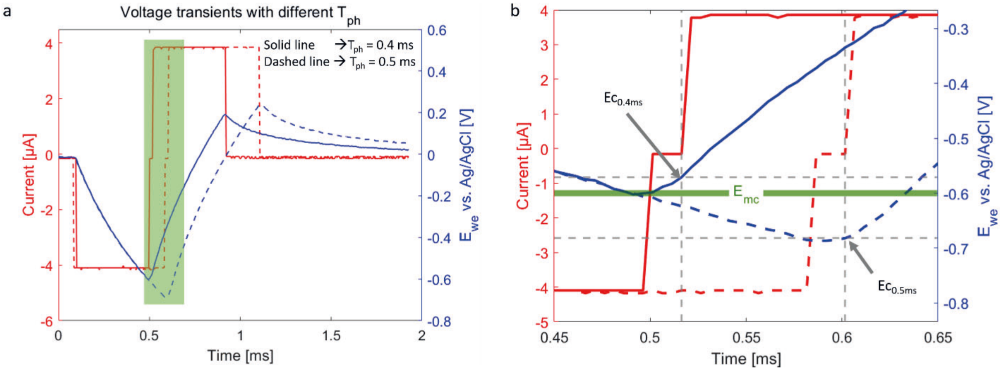

Figure 5.19. Voltage transients of SIROFs. a) Comparison of voltage transients for biphasic first cathodic current pulses of 4µA with a phase period (T_{ph}) of 0.4 and 0.5 ms. E_{we} refers to the working electrode potential, which reaches different polarization voltages according to the T_{ph} of the current pulse. b) Zoom of the green shaded area in (a) showing in detail the cathodic polarization potentials (E_c) of the electrode. If E_c reaches the maximum cathodic polarization voltage (E_{mc}, green line) of -0.6 V, the applied current is set as the maximum injection threshold for electrical stimulation. If E_c is beyond E_{mc}, the current pulse is unsafe for the electrical stimulation of neural tissues using SIROF electrodes.

Current-charge injection thresholds were obtained during the measurement of voltage transients. An example of a current-charge threshold curve of a SIROF electrode is displayed in Figure 5.20 for a range of T_{ph} between 0.1 ms and 5 ms. The thresholds show an inversely proportional relationship between the cathodic injected current ($I_{inj,\,ph}$) and T_{ph}, as higher currents can be injected with short pulses and lower currents for longer pulses. Consequently, when applying longer current pulses higher charges were achieved. Depending on the purpose of the stimulation protocol, either short or long current pulses might be applied to achieve an specific neural response [38], [100].

Moreover, SIROFs with an electrode diameter of 25 µm (GSA = 490 µm^2) showed a CIC ~ 2.5 times lower than electrodes with a diameter of 15 µm (GSA = 176 µm^2) for a current pulse of 500 µs (0.68 ± 0.28 vs. 1.65 ± 0.92 mC/cm^2, see Table 5.1), trend that has been reported before by [100], [199]. While bigger electrodes exhibit a lower CIC, bigger currents can be applied in comparison with smaller electrodes (see Table 5.1). In this case, a maximum average current ($I_{inj,ph}$) of 6.70 ± 2.71 µA and charge ($Q_{inj,ph}$) of 3.35 ± 1.35 nC can be applied for a current pulse of 500 µs with the bigger SIROF electrodes, which are intended for electrical stimulation.

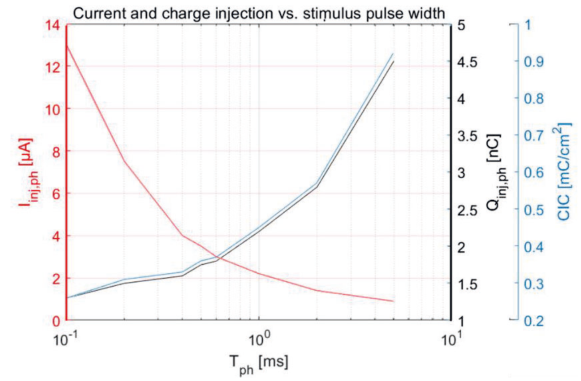

Figure 5.20. Current-charge injection thresholds of SIROFs. Example of the current-charge threshold curves of a SIROF with a GSA of 490 µm^2 for different stimulus phase periods. $I_{inj,\,ph}$ and $Q_{inj,\,ph}$ refer to the current and charge injection threshold of the cathodic phase and CIC stands for the cathodic charge injection capacity. The thresholds were determined for a maximum cathodic polarization voltage (E_{mc}) of -0.6 V.

The CIC obtained for SIROFs was lower than those reported by [199] for an electrode diameter of 25 µm and a SIROF thickness of 300 nm (1.9 ± 0.03 mC/cm^2) in response to a 200 µs current pulse. A reduced CIC can be a result of thinner SIROF layers (~100 nm), which have a higher *Z* and a lower CSC$_c$ [140]. Likewise, the inhomogeneous activation of the electrodes could have contributed to a low CIC, given the high variability of the CSC$_c$ of the electrodes (Figure A.8. 1 in Appendix 8). Nonetheless, considering that charge density thresholds between 5 to 306 µC/cm^2 have been used to evoke visual responses using retinal implants [100], [175], and that current density thresholds are expected to be in the lower range when the electrode come in closer contact to the target neurons, as it is expected with an intraretinal approach, the SIROF-based electrodes fabricated for this work show a CSC$_c$ and a CIC high enough to carry out electrical stimulation.

5.4.2. Spin-coated PEDOT: PSS

After the fabrication and packaging of spin-coated PEDOT: PSS probes, EIS and CV measurements were performed to assess the electrochemical properties of the electrodes. These showed an average *Z* and a CSC$_c$ of ~ 30 kΩ and 0.27 mC/cm^2 for 25 µm electrodes and ~ 71 kΩ and 0.76 mC/cm^2 for 15 µm electrodes (Table 5.2). Regarding the impedance, the bode plot in Figure 5.21a shows the typical capacitive and resistive behavior of PEDOT: PSS at low and high frequencies [200], [201], respectively. Additionally, when compared to SIROFs, spin-coated PEDOT:PSS electrodes exhibited an impedance that was slightly better and with less variability, proving in turn stable impedance profiles from probe to probe (Figure 5.21a, Figure 5.17, Table 5.2, and Table 5.1).

Moreover, spin-coated PEDOT: PSS electrodes showed poor charge storage capacities that were ~ 100 times lower than those obtained for SIROFs and ~ 4 – 11 times lower than those reported by [145], [200] for electrodes with similar dimensions. These results reflect the low CSC observed in the voltammograms measured, which exhibited a narrow sigmoidal shape and a steady current sate prominent during cathodic potentials (Figure 5.21b).

Table 5.2. Summary of electrochemical properties of spin-coated PEDOT: PSS electrodes. The average and the standard deviation of the following parameters are shown. GSA stands for the geometric surface area, *Z* for the impedance magnitude at 1 kHz, and CSCc for the cathodic charge storage capacity. [a] N = 20. [b] N = 60.

Parameter	**Electrode diameter**	
	25 µm[a]	***15 µm***[b]
GSA [µm²]	490	176.7
Z [kΩ]	36.13 ± 8.41	71.74 ± 14.95
CSCc [mC/cm²]	0.27 ± 0.17	0.76 ± 1.03

Sigmoidal voltammograms have been reported in general for electrodes with diameters below 25 µm, also referred as ultramicroelectrodes. Sigmoid voltammograms indicate that the diffusion layer of the interface is larger than the dimensions of the electrode (radial diffusion), inducing in turn diffusion rates higher than the reaction rate at the electrode-electrolyte interface. The latter gives rise to redox currents at the electrode interface under kinetics control, which are visualized as a steady state current in the voltammograms [199], [202]–[204]. Such behavior was not observed and has not been reported in SIROF-based ultramicroelectrodes [199], however, PEDOT: PSS microelectrodes with a diameter of 40 µm have shown wide sigmoid-like shapes [145].

While current densities of spin-coated PEDOT: PSS microelectrodes with diameters of 15 and 25 µm reported in this work were in the range of those reported in the literature for electrodes with similar diameters [145], the narrow sigmoidal shape of the CV responses yielded low charge storage capacities. Thus, the narrow nature of the voltammograms can be attributed to the fact that thinner PEDOT: PSS films yield lower charge storage capacities [200] and that the use of different additives can increase with a different range the conductivity of the PEDOT : PSS layers [205].

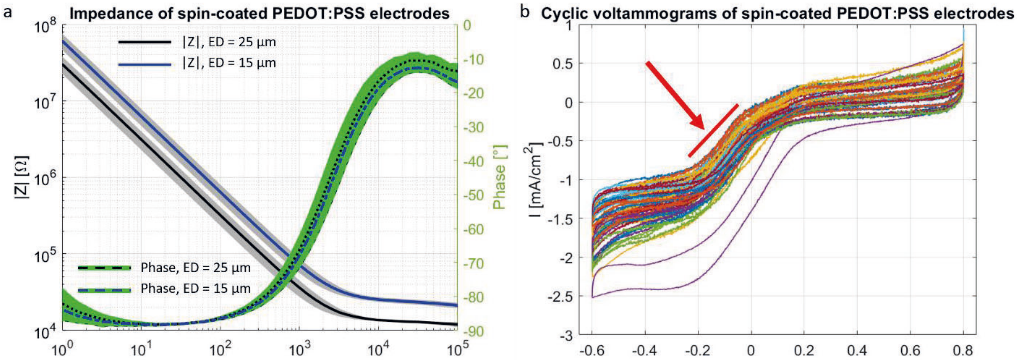

Figure 5.21. Electrochemical properties of spin-coated PEDOT: PSS. a) Bode plot showing the impedance magnitude |Z| (solid lines) and the corresponding phase angles (dashed lines) for electrodes with diameters (ED) of 25 µm (N = 8, black) and 15 µm (N = 24, blue). The gray and green shadow corresponds to the standard deviations of the |Z| and the phase, respectively. b) Cyclic voltammograms for electrodes of two probes (N = 32). Each color corresponds to a different electrode. The *y* and *x* axes show the current density (*I*) and working electrode potential *(E)* versus a Ag/AgCl reference electrode, respectively. The red arrow points out the steady state current behavior of the CV curve, tendency that is shown by the red line.

In the first case, the films produced for this work were spin-coated at 1000 and 3000 rpm, in contrast to [145], who reported spin-coated PEDOT: PSS microelectrodes using a spin speed of 650 rpm. While [145] did not report the thickness of the spin-coated layers, PEDOT: PSS thicknesses of 325 and 60 nm have been reported for spin speeds of 500 and 5000 rpm, yielding in turn a higher and a lower CSC, respectively [200]. The latter confirms CSC discrepancies due to film thickness differences using lower or higher spin speeds during the deposition of the conductive polymer.

In the second case, in order to increase the conductivity of the conductive polymer, PEDOT: PSS solutions include usually a mixture of pristine PEDOT: PSS with the surfactant dodecylbenzene sulfonic acid (DBSA) to facilitate film processing; a conductivity enhancer such as glycerol, ethylene glycol, or DMSO; and the cross-linking agent GOPS [205]. Unlike to [145], [146], [205], the PEDOT: PSS solution used in this work did not contain DBSA, component that has shown to influence significantly the conductivity of PEDOT: PSS [205]. Thus, differences in the composition of the spin-coated solution could have produced films with different conductivities, what can lead to different current measurements during CV, yielding in turn to wider or narrower voltammograms.

Additionally, cracks were found in the underlying Pt layer of PEDOT: PSS electrodes (see Appendix 9). The latter could have been caused by the deformation of the PaC substrate layer during Pt evaporation (see section 5.3.1), leading in turn to possible current leaks during CV. Given the poor charge storage capacities exhibited by the spin-coated PEDOT: PSS electrodes, voltage transients were not measured, as the process of fabricating stable PEDOT: PSS coatings still has to be optimized for it use in applications comprising electrical stimulation.

5.5. Characterization of intraretinal insertion

The feasibility of inserting flexible penetrating probes into the retinal tissue was investigated as follows. First, an intraretinal insertion model was established based on the theoretical computation of the buckling force of the penetrating shanks. Then, the model was experimentally tested by performing insertion tests into a phantom retina.

5.5.1. Intraretinal insertion model

Taking as reference the insertion models reported for intracortical probes [109], [206], flexible penetrating shanks were assumed as fixed-pinned columns (see also section 2.5.2). Depending on the length, a column can fail due to compressive stresses given by material failure or crushing, as it is the case of short columns; due to buckling in the case of long columns; or because of combined compressive and buckling stresses in the case of medium columns [121, Ch. 8], [207, Ch. 9]. Moreover, depending on the slenderness ratio of a column (λ), which refers to the ratio of the length of a column and the least radius of gyration of its cross-section (r_x), a column can be classified as long ($\lambda > 120$), medium ($32 \leq \lambda \leq 120$), or short ($\lambda < 32$) [119, Ch. 18], [207, Ch. 9].

Therefore, λ was calculated following Eq. 5.1 and Eq. 5.2:

$$\lambda = \frac{L_e}{r_x} \tag{5.1}$$

$$r_x = \left(\frac{I_m}{A}\right)^{\frac{1}{2}} \tag{5.2}$$

where L_e is the effective length of the column, r_x is the radius of gyration, I_m is the second moment of inertia, and A is the cross-section of the column. Assuming a fixed-pinned column with a solid rectangular cross-section, $L_e = 0.7L$, where L is the total length of the column (see section 2.5.2), I_m was calculated according to Eq. 2.10, and $A = wt$, where w is the width and t is the thickness of the column.

Considering the dimensions proposed in section 5.1. Design and fabrication considerations, flexible intraretinal shanks were classified as medium columns, if shanks with a thickness of 5 – 7 µm or 3 µm with a length of 140 – 145 µm are selected, or as long columns if the length of the shanks is between 180 – 225 µm with a thickness of 3 µm. In contrast, the shanks of Si-BiMEAs fall in the category of short and medium columns. Thus, from Eq 5.1 and Figure 5.22 it can be deduced that narrowing the width and thickness increases the capability of a column to bend, while shortening the effective length reduces λ, thereby decreasing the potential of a column to fail due to bending.

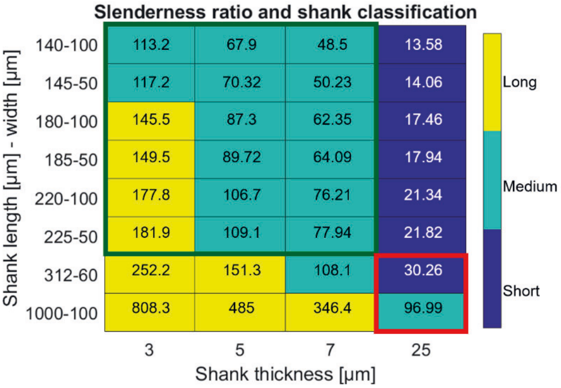

Figure 5.22. Slenderness ratio and classification of intraretinal shanks. The slenderness ratio (λ) is shown for the dimensions of interest (green square) and as reference for the dimensions of the silicon shanks (red square). According to λ, shanks are classified as long (λ > 120, yellow), medium (32 ≤λ ≤ 120, aquamarine), and short (λ < 32, dark blue).

According to the shank classification exposed in Figure 5.22, the optimized dimensions of intraretinal shanks generate middle and long columns, failing the assumption of long and slim columns for the calculation of the buckling force according to Euler's formula (Eq. 2.13). Therefore, in this case, Rankine-Gordon's formula (Eq. 5.3 and Eq. 5.4), a semi-empirical approach that takes into account the Young's modulus (E), the crushing strength (σ_c) of the material of a column, and the slenderness ratio (λ), should be used to calculate the theoretical buckling force (P_R).

$$P_R = \frac{\sigma_c A}{1 + \alpha(\lambda)^2} \tag{5.3}$$

$$\alpha = \frac{\sigma_c}{\pi^2 E} \tag{5.4}$$

P_R was then calculated according to the mechanical properties displayed in Table 5.3 for the flexible materials PaC and PI and for Si as reference. In the context of this work, the crushing strength is taken as the tensile strength, being the latter the maximum stress that a material can bear before failure.

Table 5.3. Mechanical properties of substrate materials for intraretinal shanks. The Young's modulus (*E*) and the tensile strength (σ_c) are given for PaC, PI, and Si. PaC data were obtained by the supplier (Specialty Coating systems, USA), PI data were extracted from the characterization results reported for thin neural probes based on the polyimide type PI-2611 [138], and Si data were taken from reported parameters for thin Si films[137].

Material	*E* [GPa]	σ_c [MPa]
PaC	2.76	68.95
PI	8.45	650
Si	170	2000

Furthermore, as reviewed in section 2.5.2, a penetrating shank will be inserted without bending if the insertion force (F_{in}) is below the buckling force of an specific shank. Insertion forces to penetrate the retina were not found in the literature, therefore, considering that the retina has been reported to be as soft and marginally stiffer than the brain (*E* ~ 7 kPa for mouse cerebral cortex [65] and *E* ranges from 2.5 kPa to 41.9 kPa for degenerated and healthy mouse retinas, respectively [170]), intracortical insertion forces, which span between 0.5 to 2 mN [109], were taken as reference. Hence, the upper limit of 2 mN was assumed as the insertion force threshold to evaluate the theoretical insertion feasibility of flexible intraretinal shanks into the retina (black dashed line in Figure 5.23).

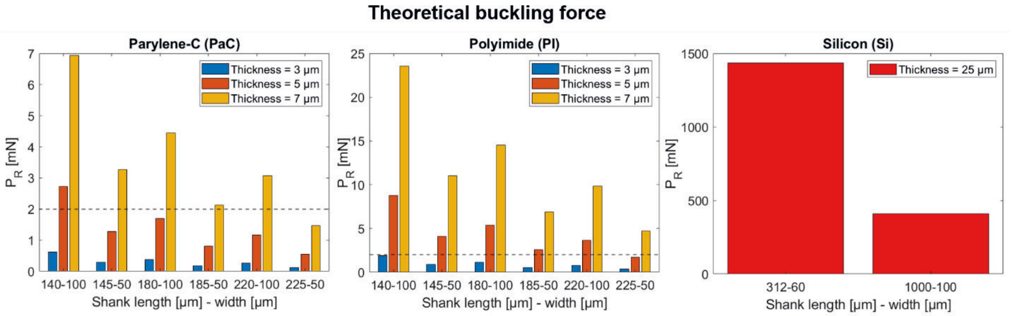

Figure 5.23. Theoretical buckling force of intraretinal shanks. The theoretical buckling force (P_R) is shown for the optimized dimensions of intraretinal shanks considering parylene-C (left) and polyimide (middle) as flexible materials. As reference, P_R is shown for silicon-based shanks considering the dimensions of Si-BiMEAs (right). Additionally, the black dashed line illustrates an insertion force threshold of 2 mN.

The theoretical buckling force for PaC- and PI-based shanks with optimized dimensions for intraretinal applications is shown in Figure 5.23, which displays also the buckling force of the Si-BiMEA shanks used in the previous chapter as comparison. For simplicity, shanks will be referred hereafter by the following code: material-length-width-thickness. Compared to Si, flexible shanks yielded a buckling force that is 2 – 3 orders of magnitude lower. Nonetheless, almost all shank dimensions with a thickness of 5 and 7 µm for PI (except PI-225-50-5) and a thickness of 7 µm for PaC (except PaC-225-50-7) exhibited a buckling force high enough to withstand an insertion force of 2 mN. These results imply that the latter shanks can be inserted into the retina without bending. In the case of 5 µm thick PaC, only PaC-140-100-5 showed a buckling force higher than 2 mN. Conversely, all flexible shanks with a thickness of 3 µm showed a buckling force below 2 mN, thereby implying that for the thinnest dimension, the shanks will fail if the insertion force surpasses their buckling force threshold.

5.5.2. Insertion into a phantom retina

To prove experimentally the results of the intraretinal insertion model exposed in the previous section, insertion tests into a phantom retina were performed. First, a phantom tissue was developed to mimic the mechanical properties of the retina. Given that PDMS offers the possibility to tune its mechanical properties according to the mixing ratio of the curing agent and the pre-polymer [208], PDMS was selected for the preparation of the phantom. According to [170], WT mouse retinas are stiffer than retinas with photoreceptors degeneration, and the compressive Young's modulus of the retina varies with the age of the animal, ranging from 2.5 – 8.8 kPa (11 – 3 weeks) and 12.5 – 41.9 – 19.8 kPa (5 – 13 – 36 weeks) in degenerated and WT retinas, respectively. Hence, a modulus of elasticity between 20 – 30 kPa was pursued.

According to preliminary tests (Figure A.10. 1 in Appendix 10), a PDMS mixing ratio of 1:45 (0.022) was selected to mimic the softness of the retina, as it could achieve a Young's modulus of ~ 23 kPa. Thus, a phantom retina was prepared using PDMS (Sylgard 184, Dow Corning, USA) with a mix ratio of ~ 1:45 (w/w). PDMS was degassed under vacuum for ~ 30 min, drop casted into a circular metal mold with a diameter of 30 mm and a height of 7 mm, and cured for 4 h at 120°C. The sample was subjected to a micro-indentation test, which confirmed a compressive Young's modulus of ~29 kPa (Figure A.10. 2 in Appendix 10). Additionally, PI and PaC dummy probes consisting of one flexible and one metal layer (steps 1- 2 from the fabrication flows presented in section 5.2) were fabricated with thicknesses of 3, 5, and 7 µm. Consequently, insertion tests using a PDMS phantom retina were carried out for the shank dimensions that showed the lowest buckling forces, that is for shanks with a length of 220/225µm and a width of 100/50 µm (Figure 5.24)

As exposed by Figure 5.24, all the probes tested were successfully inserted into the phantom tissue using a stepwise insertion with step distances of 20 µm and a V_{in} of 62.5 µm/s, insertion parameters that were based on the insertion of Si-BiMEAs (see section 4.2.1). As expected, 7 µm thick probes were successfully inserted. Even more, exceeding the expectations from the theoretical assessment, 5 µm thick PaC and 3 µm thick PI were also inserted into the phantom tissue. These positive results suggest that the insertion forces achieved during the test did not exceed the buckling force threshold of the samples. Moreover, dimpling was observed during the insertions, implying that tissue compressions should be expected in further *in vitro* experiments. Hence, these positive results gave an initial proof that the optimized dimensions of flexible intraretinal probes could insert the retina without the need of an external insertion aid.

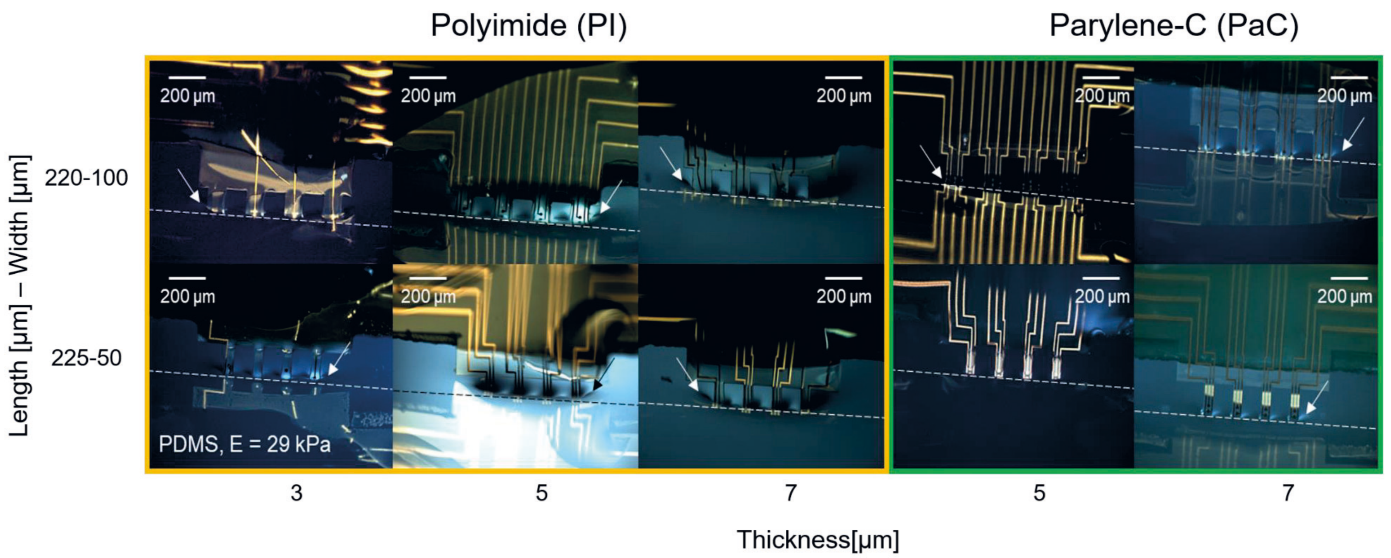

Figure 5.24. Insertion test into a PDMS phantom retina. Optical pictures exposing the insertion test of flexible dummy probes into a PDMS phantom retina with a Young's modulus of ~ 29 kPa. The surface of the phantom is depicted by the white dashed lines, and the white arrows point out when dimpling (compression of the phantom tissue) was observed. PI and PaC shanks with a length-width of 220-100 µm and 225-50 µm and thicknesses of 3, 5, and 7 µm were tested. PaC probes with a thickness of 3 µm were not tested due failure during the final assembly of the probes, as the contact pad area rolled up after its release from the Si wafer.

5.6. Outlook

Penetrating neural probes have been widely used in neuroscience for intracortical applications that study the brain and to establish chronic brain machine interfaces. In the last decades, such development has focused on diminishing the insertion trauma and FBRs that hinder the performance of the implants. To this end, efforts have been made to enhance the long-term stability of the implants by reducing the mechanical mismatch between the penetrating probes and the brain. Thus, strategies comprising the use of flexible polymer-based materials, design optimizations like cross-section reduction, and the consideration of the mechanical properties of the target tissue have been established for the development of penetrating devices aiming the brain [65], [109], [110].

Given the above, flexible intraretinal probes were designed and fabricated not only to match the anatomical structure of the retina but to reduce the trauma caused by an intraretinal insertion. Therefore, the length of the penetrating shanks was reduced to tally the thickness of both healthy and degenerated retinas. Likewise, the dimensions of the shanks were optimized to fulfill the insertion requirements while reducing the cross-sectional footprint of flexible penetrating shanks. Hence, compared to the shank dimensions of Si-BiMEAs (width – thickness of 60 – 25 µm and 100 – 25 µm), flexible BiMEAs (widths of 50 or 100 µm and thicknesses between 3 – 7 µm) achieved a cross-sectional reduction of ~ 53 – 94 % from the original BiMEA design.

Moreover, the fabrication of flexible BiMEAs comprised the use of polymer-based materials, such as PI and PaC, using standard MEMS technology. While PI is a polymer that can withstand processes with high temperatures, PaC can be easily degraded. Therefore, special attention must be taken when performing processes that can induce thermal stresses on PaC layers (e.g.: metal evaporation and flip chip bonding). Additionally, microfabrication challenges arose mainly while establishing a process flow to add an electrode coating to enhance the electrochemical properties of metal electrodes (e.g.: Au or Pt). On one side SIROFs were implemented in the fabrication. Here, it was shown that the growth of oxide layers during activation can lead to delamination if the IrO_x film is subjected to geometrical stresses, like for example the formation of non-passivated metal steps. The latter was overcome with a three layer design comprising passivation openings smaller than both, the interlayer opening and the SIROF coating. On the other hand, the implementation of spin-coated PEDOT: PSS films showed that further efforts must be performed to optimize and facilitate PaC as deposition mask to pattern the conductive polymer. In this case, the use water-soluble or orthogonal resists could be explored in further developments [209].

Furthermore, the electrochemical properties of SIROFs and spin-coated PEDOT: PSS coatings were characterized. While the former showed a suitable impedance, high charge storage capacities, and charge injection limits high enough to conduct electrical stimulation of neural tissues, the latter exhibited a good impedance but poor charge storage capacities. In both cases, there is a directly proportional relationship between the thickness and the charge storage capabilities of the coating, therefore, improvements should be focused on the implementation of thicker layers.

In the case of SIROFs, the sputtered layer could be increased to 500 – 800 nm, however, it should be considered that thicker SIROFs will increase the stiffness of the probe. Additionally, high variability was observed in SIROF-based electrodes, presumably because a parallel activation was carried out. While this could be improved if the electrodes are activated individually, such approach would be even more time-consuming than the process already is. Hence, a wafer scale activation of SIROFs could be pursued in the future. In the case of PEDOT: PSS, stacked layers of the spin-coated polymer can be performed to increase its thickness up to ~ 900 nm, as reported by [200].

Finally, the intraretinal insertion of flexible BiMEAs was characterized. To this end, an intraretinal insertion model based on the computation of the theoretical buckling force was implemented, and the experimental insertion of flexible shanks into a PDMS phantom mimicking the mechanical properties of the retina was tested. In this way, it was demonstrated that the optimized dimensions of intraretinal shanks provide the capabilities to penetrate a soft tissue without the necessity of an additional shuttle to aid the insertion, as it is commonly performed in intracortical applications using flexible shanks [65], [109]. Even more, reducing the effective length of the flexible penetrating shanks permitted not only to better match the microstructure of the target tissue, but enhanced the insertion potential of the shanks, as it was demonstrated by the calculation of the slenderness ratio. Consequently, approaches like the effective length reduction of penetrating shanks can be used to customize the insertion strategies of penetrating probes for applications targeting other electrogenic tissues, such as intracortical and peripheral nerve tissues. Hence, the implementation of shuttles or coatings that can increase the cross-sectional footprint of the shank itself can be avoided [109].

Chapter 6

Applications of flexible BiMEAs

In the previous chapter, flexible BiMEAs were tailored to match exclusively the anatomy of our target tissue, the retina. Additionally, the probes were characterized, showing the viability of inserting such probes into a tissue phantom that mimicked the mechanical properties of the retina. Moreover, the electrochemical properties of flexible IrO_x BiMEAs (hereafter referred as flexible BiMEAs) showed to be suitable for performing both, electrical recording and electrical stimulation.

Consequently, this chapter will cover the *in vitro* application of flexible BiMEAs for retinal applications. Here, the parameters for a successful insertion will be revealed, the capabilities to record the spiking activity of RGCs and LFPs at different intraretinal depths in both healthy WT and degenerated *rd10* retinas will be exposed. Furthermore, electrical stimulation of the intraretinal space was conducted with the aim to achieve a low charge injection. Thus, current stimulation thresholds to evoke electrical responses in RGCs will be exposed.

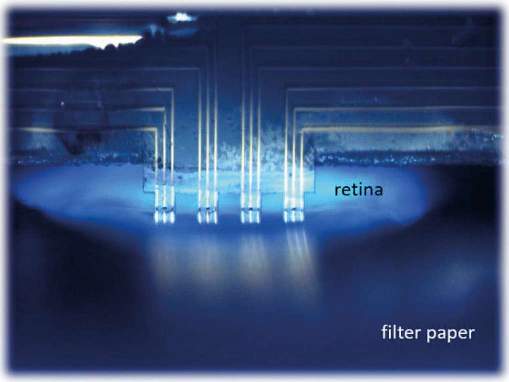

This chapter is in part reproduced from the following work:

Rincón Montes, V., Gehlen, J., Ingebrandt, S., Mokwa, W., Walter, P., Müller, F., and Offenhäusser, A., “Development and *in vitro* validation of flexible intraretinal probes” *Sci Rep* 10, 19836 (2020)

6.1. Adjusting insertion parameters of flexible BiMEAs

Since the insertion forces into the retina were not measured, Flexible BiMEAs with a thickness of 7 µm were used to provide a high buckling force threshold during *in vitro* experiments (section 5.5.1). Initial attempts to insert flexible BiMEAs were performed using PI-based probes 100 µm wide and 180 µm long in WT mouse retinas. As a starting point, the insertion method reported previously for Si-BiMEAs [13] was employed for the flexible probes.

First, the tips of the shanks were placed at the surface of the retinal tissue (Figure 6.1a), followed by an initial step (Z_{in}) and subsequent insertion steps (Z_x) of 20 µm with a V_{in} of 62.5 µm/s. As shown in Figure 6.1b-c, once the lower electrodes (E-1) started capturing small and fast voltage peaks, this depth was taken as the reference position Z_0. Here, E-1 is assumed to be at the surface of the NFL. Step by step, the amplitude of the APs captured by E-1 was increasing, just like some spikes were starting to appear in E-2. However, after E-1 had theoretically traveled ~ 100 µm inside the retina (summed distance from Z_0 - Z_5), the activity was still being captured by the lower electrode. In some cases, after further steps were carried out ($Z_x > Z_5$), an abrupt attenuation of spikes was observed (Figure 6.1b), as for other attempts the spiking activity remained only in E-1 (Figure 6.1c). Despite the optical indication that the shanks were completely inside the tissue (Figure 6.1a), the electrical activity of the retina was not within reach of the upper electrodes, thereby suggesting that the flexible BiMEAs were only pushing and did not penetrate the GCL of the retina.

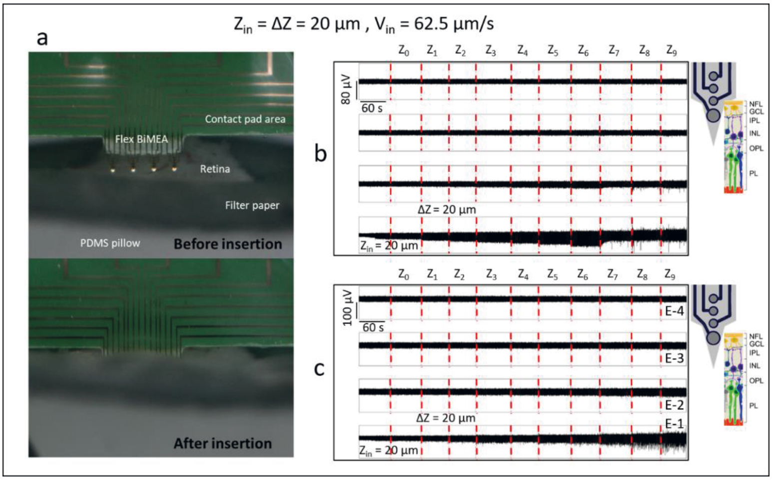

Figure 6.1. Stepwise insertion of flexible BiMEAs into wildtype mouse retinas. Intraretinal insertions after using an initial insertion step (Z_{in}) and further insertion steps (ΔZ) of 20 µm with an insertion speed (V_{in}) of 62.5 µm/s. a) Optical images exhibiting the placement of the tips of PI shanks (100 µm wide, 180 µm long, 7 µm thick) at the surface of the nerve fiber layer (NFL) of the retina (before insertion) and the complete insertion of the shanks (after insertion). b-c) Merged recordings of the electrical activity captured throughout different insertion steps (Z_{0-x}). Each row corresponds to each one of the four electrodes along each shank, being E-1 and E-4 the lower and upper electrodes, respectively. Red dashed lines separate different insertion depths. At the bottom, a sketch of the position of the shank within the multilayered retina is shown. Intraretinal layers are coded as: NFL = nerve fiber layer, GCL = ganglion cell layer, IPL= inner plexiform layer, INL=inner nuclear layer, OPL= outer plexiform layer, and PL = photoreceptor layer.

To enable the insertion and correct positioning of flexible intraretinal probes, parameters like Z_{in}, further step distances (ΔZ), and V_{in} were tuned. Thus, to induce a higher compression force to penetrate beyond the GCL, different Z_{in} distances were tested (Figure 6.2). Successful insertions were obtained when Z_{in} was initially increased to 50 and 100 µm (ΔZ = 20 µm, V_{in} = 62.5 µm/s). In these cases, the spiking activity of the retina was first captured by the lower electrodes and moved to the upper electrodes (E-3 and E-4) while the shanks were inserted deeper into the retina (Figure 6.2b-c). Despite the positive results, it was noticed that the distance traveled by each electrode did not match the expected depth inside the retina. In other words, if an electrode was displaced 120 µm inside the tissue, its real position within the retina was not 120 µm below the surface of the NFL. The latter was noticed since the activity of RGCs was still captured after an insertion depth of ~ 120 µm (from Z_0-Z_6), depth that corresponds theoretically to the outer margin of the INL [163], which is beyond the outreach of RGCs.

Considering the mechanical properties reported for porcine retinas, this behavior can be explained by the mechanical anisotropy and inhomogeneity of the tissue caused by blood vessels [210] and the increase of the elastic modulus of the tissue along deeper retinal layers. In the latter case, it has to be considered that the NFL/GCL (~ 5.8 kPa) is softer than the IPL (6.7 kPa), the INL/OPL (10 kPa), and the photoreceptor layer (~25.9 kPa) [211]–[213]. Consequently, the inversely proportional relationship between the retinal depth and softness could have hindered the displacements of the shanks within the retina.

Additionally, increasing V_{in} to 162.5 µm/s and Z_{in} to 40, 80, and 100 µm resulted as well in successful insertions (Figure 6.2d-f), even when Z_{in} was further increased to 150 and 180 µm. The effect of setting Z_{in} higher than 20 µm was observed again. For example, in Figure 6.2e (Z_{in} = 40 µm, ΔZ = 20 µm , and V_{in} = 162.5 µm/s) E-4 reached its best position within the GCL (higher amplitude spikes) at Z_9, condition that was not achieved in Figure 6.2a (Z_{in}=20 µm, ΔZ = 20 µm, and V_{in} = 62.5 µm/s), even after traveling the same step distances from Z_0-Z_9. Likewise, a higher V_{in} might have accelerated the path of E-4 to reach the GCL, as the first APs were detected in Z_5, while in Figure 6.2b (Z_{in} = 50 µm, ΔZ = 20 µm , and V_{in} = 62.5 µm/s) the first spikes were captured at Z_7.

Moreover, the GCL was crossed in fewer steps when a longer Z_{in} and ΔZ were set, as shown in Figure 6.2e-f. For example, in Figure 6.2e a rapid transition between layers was evident after a third step of 80 µm was performed (from Z_1-Z_2), albeit the high amplitude spikes that were observed at the beginning were not seen in the upper electrodes. Since APs were captured already by E-2, E-3, and E-4 (smaller in amplitude) at Z_2, further ΔZs of 20 µm were carried out to avoid an insertion beyond the desired depth. The effect of increasing ΔZ and V_{in} while having a long Z_{in} was revealed in Figure 6.2f. Here, a Z_{in} of 100 µm was inserted two times with a time difference of ~ 10 s (red arrows). Considering that the first attempt yielded no other effect but a slight increase in the background noise captured by E-1, a second Z_{in} was performed. This time, a burst of spikes and the smooth onset of APs that also reached E-2 was observed. Setting ΔZ to 40 µm allowed the upper electrodes to reach the GCL in only one or two extra steps.

Hence, the results of this section demonstrate the feasibility of successful intraretinal insertions using flexible BiMEAs in WT retinas, and unveiled as well, the control parameters of an intraretinal insertion. Thus, a Z_{in} of at least 40 µm should be used to guarantee the insertion, ΔZ can be set between 20 – 40 µm to fine tune the desired intraretinal depth, and V_{in} showed to enhance the insertion in order to achieve faster insertions.

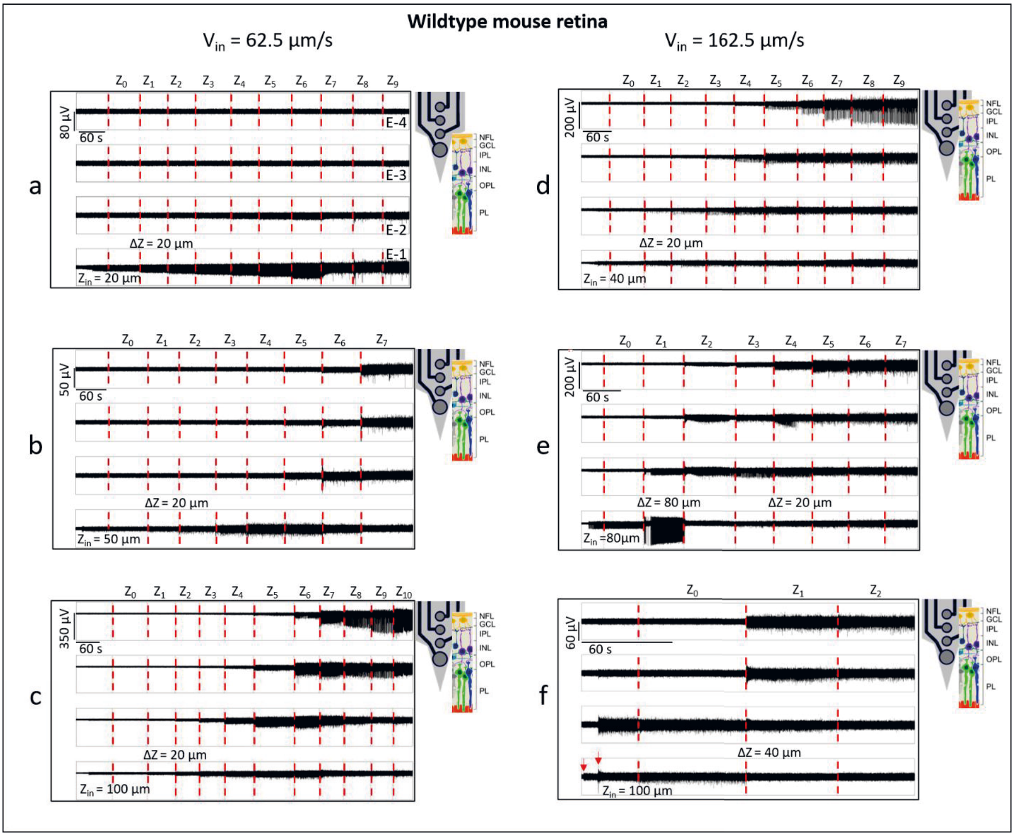

Figure 6.2. Adjusting intraretinal insertion parameters in wildtype retina retinas. Merged recordings of the electrical activity captured by PI shanks (100 µm wide, 180 µm long) inserted at different intraretinal depths ($Z_{0\text{-}x}$) inside wildtype mouse retinas. From (a-c), an insertion speed (V_{in}) of 62.5 µm/s and an initial insertion step (Z_{in}) of 20 (a), 50 (b), and 100 µm (c) were used. From (d-f), a V_{in} of 162.5 µm/s with Z_{in} of 40 (d), 80 (e), and 100 µm (f) were employed. Insertion step distances posterior to Z_{in} (ΔZ) were mostly set to 20 µm along the different insertion steps (Z_x). Additionally, ΔZ of 80µm (e) and 40 µm (f) were tested. Red dashed lines separate different insertion depths, and the red arrows point out when Z_{in} was performed. At the bottom, a sketch of the position of the shank within the multilayered retina is shown. Intraretinal layers are coded as: NFL = nerve fiber layer, GCL = ganglion cell layer, IPL= inner plexiform layer, INL=inner nuclear layer, OPL= outer plexiform layer, and PL = photoreceptor layer.

6.2. *In vitro* recordings with flexible BiMEAs

6.2.1. Recording at different intraretinal depths in wildtype retinas

As it was shown in the previous section, $Z_{in,}$ ΔZ, and V_{in} can be tuned to achieve a specific intraretinal depth. To show the capability of flexible BiMEAs to record at different intraretinal depths, as it was previously demonstrated with Si-BiMEAs (section 4.2.1), a Z_{in} of 180 µm, a

ΔZ of 20 µm, and a V_{in} of 162.5 µm/s were employed. Likewise, to verify the vitality of the tissue during insertion, light stimuli 500 ms long were applied.

Figure 6.3 exhibits the intraretinal insertion of a 50 µm wide and 180 µm long PI shank. Given the spiking activity observed in the lower electrode (E-1), the intraretinal depth achieved after Z_{in} was set as Z_0. After a travel distance of ~ 60µm (Z_3), a clear shift in the intraretinal position of E-1 was noticed, as the spikes were displaced to the next upper electrode (E-2). This behavior matches with the microstructure of the retina, as the summed thickness of the NFL – IPL is ~70 µm [163]. Therefore, it was expected that E-1 was already at the border of the IPL, what explains the spikeless recording at Z_3. The spiking signal, which was now captured by E-2, was shifted to the next upper electrodes in the next insertions until the top electrode reached its closest position to the GCL at Z_6. As expected, further insertions of the shank led to low amplitude spikes in E-4 and spikeless recordings in E-1 – E-3 at Z_7. Matching the findings reported previously for Si-BiMEAs [13], flexible BiMEAs showed to access successfully the different layers within the retina.

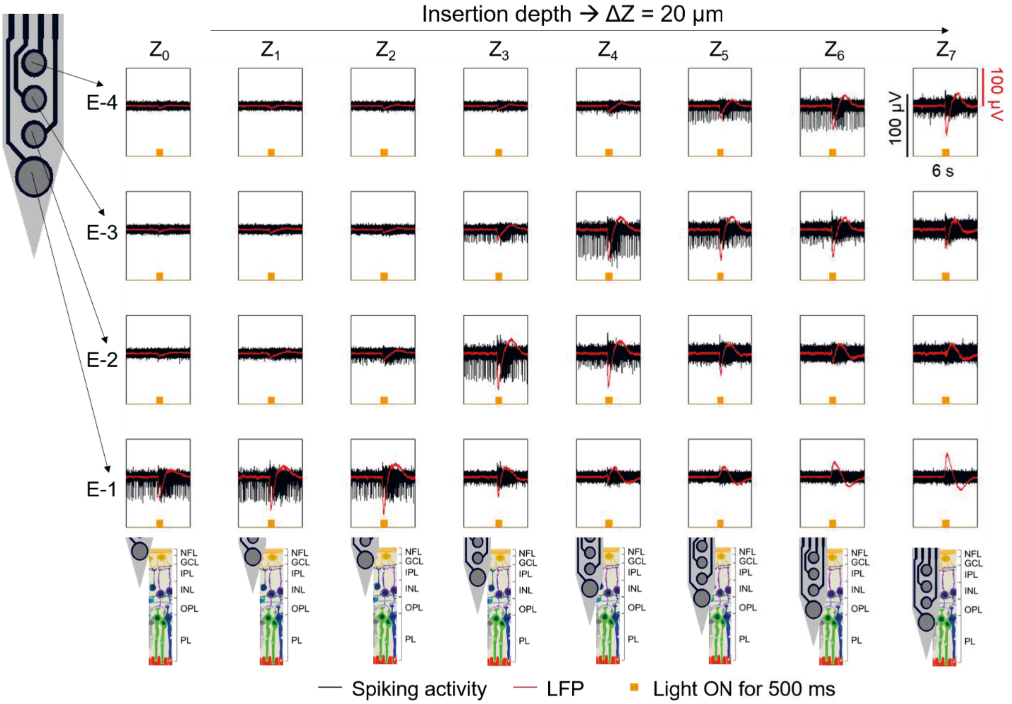

Figure 6.3. Recording at different intraretinal depths in wildtype retinas with flexible BiMEAs. The figure displays a matrix of recording boxes showing snapshots of 6 s for every electrode along a recording shank (rows) at different intraretinal depths Z_x (columns) with insertion depth differences (ΔZ) of ~20 µm. Recordings were performed using a 50 µm wide and 185 µm long PI shank. An initial insertion step (Z_{in}) of 180 µm and an insertion speed (V_{in}) of 162.5 µm/s were used. The spiking activity and local field potentials are displayed with black and red traces, respectively. Additionally, light stimulation was performed using a light stimulus 500 ms long (yellow bumps). At the bottom, a sketch of the position of the shank within the multilayered retina is shown. Intraretinal layers are coded as: NFL = nerve fiber layer, GCL = ganglion cell layer, IPL= inner plexiform layer, INL=inner nuclear layer, OPL= outer plexiform layer, and PL = photoreceptor layer.

Moreover, light stimulation performed at each intraretinal depth showed the capability of flexible BiMEAs to capture both, the spiking response of RGCs and LFPs that resemble the b-wave of an intraretinal electroretinogram (ERG) [214], [215]. This ERG-like waveform increased in amplitude while the electrodes reached the GCL, diminished as the electrodes travelled deeper in the inner retina, and showed a reverse polarity as the electrodes reached the outer margin of the INL and entered the OPL (Z_4 – Z_5 in Figure 6.3). This behavior matches findings reported previously by [215]. Consequently, responses to light stimuli indicate that the phototransduction pathway from photoreceptors to RGCs is well preserved during an intraretinal insertion. In addition, LFPs in WT retinas were not captured before by Si-BiMEAs, as the recordings showed light induced artifacts (see section 4.2.3) due to the photoelectric effect [216]. Hence, flexible BiMEAs show superiority in this sense, allowing noise-free recordings during optical stimulation. Considering that the ERG represents the summed activity of the retina (see section 2.1.2), its recording is beneficial for the assessment of retinal electrophysiology.

6.2.2. Recording from degenerated retinas

Flexible BiMEAs were tested successfully in degenerated *rd10* mouse retinas fixing Z_{in} to 100 µm, using ΔZ between 20 – 40 µm, and setting V_{in} to 187.5 µm/s. Figure 6.4a exhibits an example of a PaC probe 50 µm wide and 185 µm long that was fully inserted into the degenerated tissue. Akin to findings showed with Si-BiMEAs in section 4.2.4, burst of spikes concomitant with low frequency oscillations in a frequency range between 3.3 Hz and 7 Hz were captured by the flexible probe (single-sided Fourier spectra in Figure 6.4a), showing in turn the insertion feasibility of PaC-based probes.

Moreover, PaC shanks with a length of 145 µm and containing only three electrodes per shank were successfully inserted into the thin degenerated retina (Figure 6.4b). Here, different insertion possibilities were unveiled. On one side, performing only one Z_{in} step allowed to control better the positioning of the electrodes within the tissue, capturing in turn the intraretinal insertion of the electrodes at different depths(Figure 6.4b, left). In contrast, performing two consecutive steps ($Z_{in} = 2\text{x}100$ µm) with a time difference of 10 s showed the possibility of performing fast insertions in only one or two steps. In any case, both options yielded successful insertions in which the upper electrode recorded the spiking activity of RCGs, and the lower electrode presented a reduced activity with low amplitude spikes or not spikes at all. Thus, the use of intraretinal shanks as short as 145 µm proved to successfully penetrate a neural tissue as thin as ~ 100 µm, as it is the degenerated *rd10* retina.

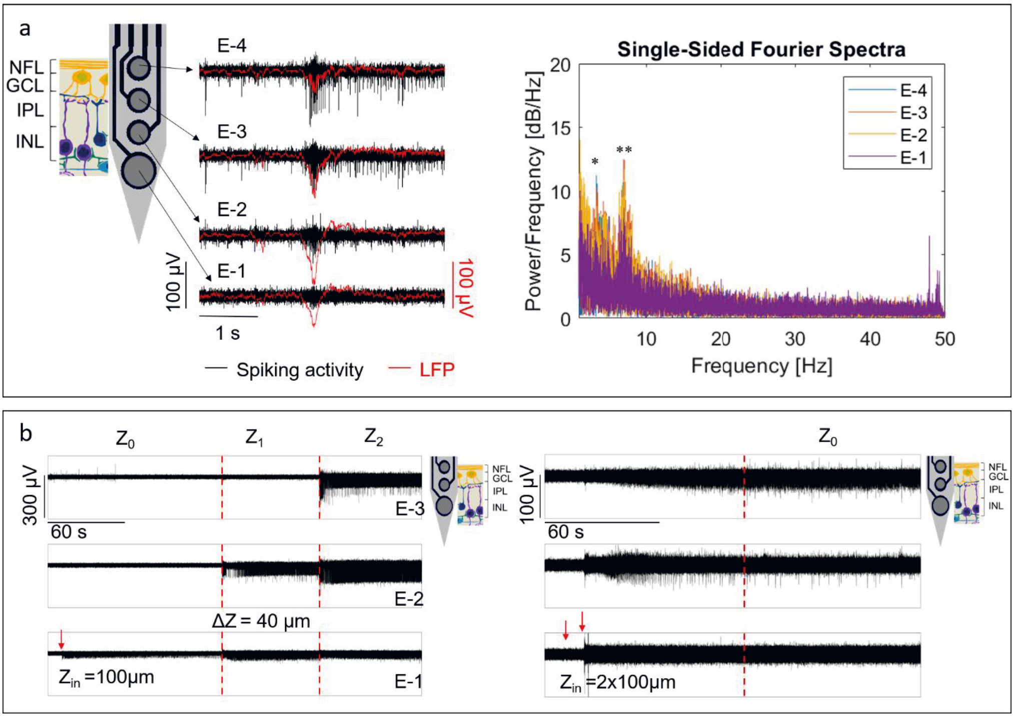

Figure 6.4. Recording from degenerated retinas with flexible BiMEAs. a) At the left, the spiking activity (black) and local field potentials (red) captured by a fully inserted flexible shank (PaC probe with width of 50 µm and a length of 185 µm) in an *rd10* retina. At the right, the single-sided Fourier spectra of the LFP signal. Asterisks point out the oscillatory frequencies exhibited by the LFPs at 3.3 Hz (*) and 7 Hz (**). b) Merged recordings of the electrical activity captured by PaC shanks 50 µm wide and 145 µm long inserted at different intraretinal depths (Z_{0-x}) inside *rd10* retinas using a V_{in} of 187.5 µm/s. Red dashed lines separate different insertion depths, and the red arrows point out when Z_{in} was performed. At the left, an intraretinal insertion with a Z_{in} of 100 µm, a ΔZ of 40 µm. At the right, an intraretinal insertion with a Z_{in} of 2x100 µm with a lag of 10 s between each initial step. At the bottom, a sketch of the position of the shank within the multilayered retina is shown. Intraretinal layers are coded as: NFL = nerve fiber layer, GCL = ganglion cell layer, IPL= inner plexiform layer, INL=inner nuclear layer.

6.3. Intraretinal current-controlled stimulation with flexible BiMEAs

Given the feasibility of stimulating the inner retina electrically while recording the electrical activity of RGCs simultaneously (see section 4.3), this section explores further this application. Here, intraretinal charge injection thresholds of electrically evoked potentials in RGCs, in both WT and degenerated *rd10* retinas, are investigated. To this effect, CCS was carried out, permitting in turn to tune the injected currents and charges during ES. To ensure a safe stimulation that avoids the excursion of electrode potentials beyond the water window of the electrodes, voltage transients were recorded simultaneously during ES.

6.3.1. Charge injection capacity

While the CIC of the electrodes was characterized in 1xPBS prior to their usage for ES (section 5.4.1), voltage transients recorded in ex-planted retinas revealed that the CIC of the electrodes was reduced ~ 20% when applying current pulses within the neural tissue. For example, the CIC of a stimulating electrode for a 10 µA current pulse with a T_{ph} of 0.1 ms was reduced from 0.26 in 1xPBS to 0.2 mC/cm^2 intraretinally. The latter is a consequence of the cathodic voltage drop within the retinal tissue, which was ~ 1.39 ± 0.06 times higher than potentials measured in 1xPBS (see Figure 6.5).

This behavior has been reported previously by [100], [155], [217], [218], and it can be explained given the fact that the tissue *per se* exhibits a higher resistance than the electrolyte model (e.g.: PBS). Due to the presence of organic and ionic species in the tissue, which are most of the times not fully determined, higher potentials to achieve the same charge are required. Thus, 49 different stimulation parameters mapping a charge injection range between 0.2 nC and 2.5 nC (see stimulation parameters in section 3.8.2) were used during ES. Given the above, attention was given to avoid cathodic potentials at the stimulating electrode more negative than -0.85 V, the cathodic water window limit established for the SIROFs used in this work (see SIROF activation in section 5.2.1).

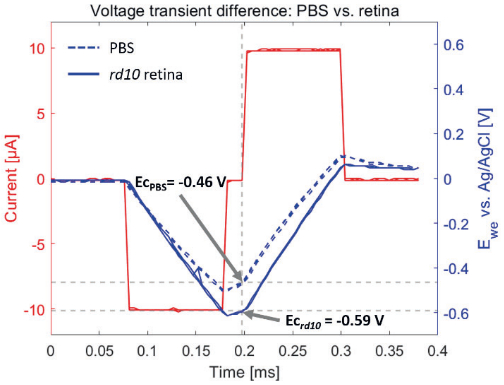

Figure 6.5. Voltage transient difference in PBS and in retinal tissue. Voltage transients measured *in vitro* in 1xPBS (dashed blue lines) and inside an *rd10* retina (solid blue lines) after applying a 10 µA current pulse with a phase period T_{ph} of 0.1 ms (red traces). The cathodic potentials of the electrodes Ec_{PBS} and Ec_{rd10} measured versus a Ag/AgCl reference electrode are pointed out by the gray arrows.

6.3.2. Intraretinal charge injection thresholds

With the aim to map intraretinal charge stimulation thresholds of electrically evoked responses of RGCs, first cathodic biphasic pulses with a current amplitude per phase ($I_{inj,\,ph}$) from 0.5 – 10 µA and T_{ph} from 0.1 ms – 5 s were tested in WT and *rd10* retinas. As exposed by the heatmap in Figure 6.6, regions with a high electrical stimulation efficiency (ESE) were obtained when applying a $I_{inj,ph}$ between 2 – 5µA with T_{ph} between 0.3 – 0.6 ms in WT retinas. Here, a highest average ESE of 7.9 was obtained after applying 3 µA pulses 0.5 ms long, which correspond to a $Q_{inj,\,ph}$ of 1.5 nC.

Conversely, stimulation efficiencies in *rd10* were lower than in WT retinas, with a maximum ESE between 1.34 and 1.38 after applying current pulses with a $I_{inj,\,ph}$ and a T_{ph} of 8µA - 0.2 ms and

3μA - 0.4 ms. For both retinal tissues, an ESE below one was also detected, thereby implying that some stimulation parameters induced an inhibitory effect by reducing the firing rate of RGCs. The latter was observed as isolated events for current amplitudes between 0.5 – 1 μA with T_{ph} between 0.4 ms –1 s in WT, and in broader stimulation regions with current amplitudes between 1 – 2 μA or 4 – 7 μA with a T_{ph} between 0.5 – 0.6 ms or 0.1 ms, respectively, in *rd10* retinas.

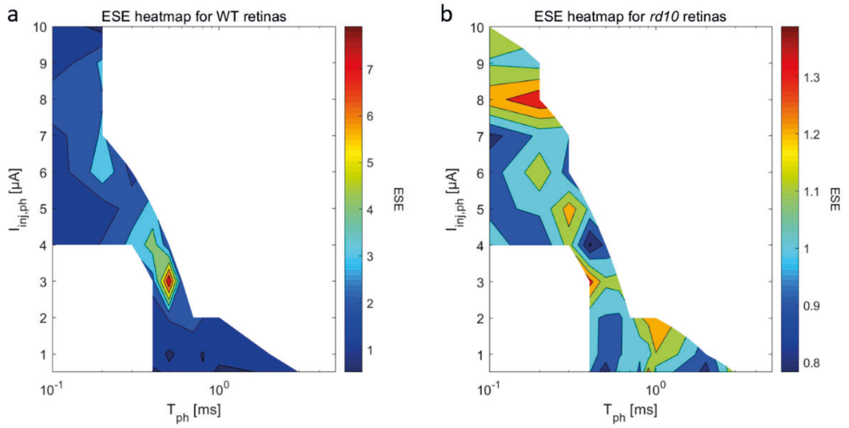

Figure 6.6. Electrical stimulation efficiency heatmap of intraretinal current-controlled stimulation. Average electrical stimulation efficiency (ESE) heatmap for a) four wildtype (WT) and b) five degenerated *rd10* retinal samples after applying first cathodic biphasic stimulation pulses with a current injection per phase ($I_{inj,ph}$) between 0.5 – 10 μA and a phase period (T_{ph}) between 0.1 ms – 5 s. The contours in the plots correspond to the isolines of the ESE, which are in turn color coded according to the color bar at the right.

Moreover, Figure 6.7 maps the average ESE for the different charges injected per stimulation phase ($Q_{inj,\,ph}$) during CCS for both retinal tissues. In the case of WT retinas, Figure 6.7a shows that in average higher efficiencies denoting excitatory responses (ESE > 1) were achieved for a $Q_{inj,ph}$ between 1.2 – 2.1 nC. On the contrary, ESEs in *rd10* samples were significantly lower than in WT ($p = 0.037$, non-parametric Mann-Whitney U-test with 5% significance level), with an average ESE slightly higher than one. In general, *rd10* responses comprised excitatory responses of low strength with a $Q_{inj,\,ph}$ between 0.9 – 2 nC, with a maximum excitatory peak with an average ESE of 1.261 after a $Q_{inj,\,ph}$ of 0.45 nC.

Stimulation trials that yielded significant changes in the spontaneous firing rate of RGCs were classified as significant stimulations after performing paired t-tests between the average FR 8 s before and 400 ms after the ES artifact for six stimulation pulses (see Methods, section 3.8). Additionally, the minimum and maximum cathodic charge densities that produced significant stimulations were considered as charge density ($Q_{d,\,ph}$) thresholds. Thus, a minimum $Q_{d,\,ph}$ threshold of 81.5 μC/cm^2 ($Q_{inj,\,ph} = 0.4$ nC) yielded significant excitatory responses in both retina types, with ESEs of 1.2 and 1.5 for *rd10* and WT, respectively. With even lower charges, a minimum $Q_{d,\,ph}$ threshold between 40 – 50 μC/cm^2 ($Q_{inj,\,ph}$ = 0.2 – 0.25 nC) yielded significant inhibitory responses with ESEs between 0 – 0.22 for both retinas.

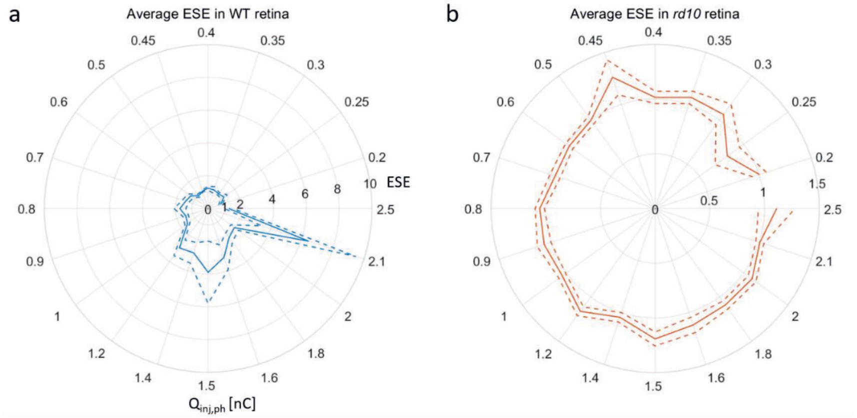

Figure 6.7. Electrical stimulation efficiency and charge injection relation. Radar plots showing the average electrical stimulation efficiency (ESE) relation with the charges injected during the cathodic phase in a) four WT and b) five *rd10* retinal samples. The angular axis represents the charge injection per phase ($Q_{inj,\ ph}$) and the radial axis depicts the ESE. Solid and dashed traces show the average and the standard error of the mean, respectively.

Table 6.1 exposes the average $Q_{d,\ ph}$ thresholds for both excitatory and inhibitory responses in WT and *rd10* samples and compares the results obtained during CCS with those reported in section 4.3 after VCS. During CCS, *rd10* retinas exhibited a lower stimulation threshold than WT samples, however, as it was shown in Figure 6.6 and Figure 6.7, ESEs in *rd10* were significantly lower than in WT by ~ 6-fold. Additionally, while similar lower thresholds were measured in both CCS and VCS for WT retinas, a narrower $Q_{d,\ ph}$ range was captured during CCS (~ 255 – 382 μC/cm^2 vs. 248 – 509 μC/cm^2). On the other hand, CCS thresholds for *rd10* samples were lower than in VCS (~ 200 – 318 μC/cm^2 vs. 335 – 686 μC/cm^2). The use of higher charge densities during VCS can explain the fact that a maximum ESE of 2.74 was obtained in *rd10* samples, compared to a maximum ESE of 1.8 obtained during CCS. The latter implies that while it is true that the low charges used during CCS produced already significant changes in the firing rate of degenerated retinas, higher charges should be tested during CCS to achieve higher ESEs.

Table 6.1. Intraretinal charge density thresholds. Average and standard deviation of cathodic charge density thresholds ($Q_{d,\ ph}$) for wild type (WT) and *rd10* retinas that yielded significant excitatory and inhibitory electrically evoked responses during current-controlled (CCS) and voltage-controlled (VCS) stimulation. [a] Stimulation electrode with a geometric surface area (GSA) of 490.87 μm^2. [b] Stimulation electrode with a geometric surface area (GSA) of 576 μm^2. NM = not measured. Data from VCS are taken from section 4.3 [13].

Retina type	**Threshold**	**$Q_{d,\ ph}$ [μC/cm^2]**			
		Excitatory		**Inhibitory**	
		CCS [a]	***VCS*** [b]	***CCS*** [a]	***VCS***
WT	Lower	254.65 ± 157.36	248.28 ± 58.96	89.13 ± 43.51	NM
	Upper	381.97 ± 45.17	508.55 ± 329.14	272.47 ± 219	NM
rd10	Lower	199.64 ± 115.60	334.76 ± 94.65	79.45 ± 37.01	NM
	Upper	317.80 ± 136.35	686.10 ± 304.16	342.25 ± 84.49	NM

Akin to the thresholds obtained during VCS, $Q_{d,\ ph}$ during intraretinal CCS were comparable to subretinal thresholds (100-900 μC/cm^2) reported by [175] for electrodes with a GSA of 706 μm^2.

Likewise, the lower $Q_{d,\,ph}$ threshold obtained during CCS was higher than the 50 µC/cm^2 threshold reported by [21] using Si-nanoneedles with a GSA of ~ 1000 µm^2 in embryonic chick retinas. Differences arise from the GSA of the electrodes, as $Q_{d,\,ph}$ thresholds are dependent on the size of the electrodes, presenting a higher threshold those electrodes with a smaller GSA [175]. Nonetheless, $Q_{inj,\,ph}$ were comparable with those reported using Si-nanoneedles (below 0.5 nC), as the lowest $Q_{inj,ph}$ that produced excitatory and inhibitory responses for both retinas was 0.4 nC and 0.2 – 0.25 nC, respectively (see Table 6.2).

Furthermore, Table 6.1 and Table 6.2 show that the range of charges that induced both excitatory and inhibitory responses for both types of retina overlapped in most of the cases. The latter was true even for a same $Q_{inj,\,ph}$ within a same sample, thereby indicating that two different sets of stimulation parameters ($I_{inj,\,ph}$ and T_{ph}) that yield the same $Q_{inj,\,ph}$ can produce opposite responses for a same neuronal column. For example, a $Q_{inj,ph}$ of 1.6 nC, which can be achieved by applying a 4 µA – 0.4 ms or a 8 µA – 0.2 ms current pulse, induced significant ESEs of 0.49 and 1.56, respectively, in a same group of neurons (*rd10* sample S3 in Table 6.2). This overlap indicates that stimulation pulses with different currents strengths and durations can induce different effects on a same group of neurons.

Table 6.2. Summary of significant responses during current-controlled stimulation. Significant excitatory (E, green) and inhibitory (I, red) responses obtained per cathodic charge ($Q_{inj,\,ph}$) stimulus for four wildtype (WT) and five *rd10* samples. Stars indicate the statistical significance of the stimulation (* for p <= 0.05, ** for p <= 0.01 *** for p <= 0.001) after performing paired t-tests to the firing rate 8 s before and 400 ms after six stimulation pulses.

Retina type	**WT**								***rd10***									
Sample	**S1**		**S2**		**S3**		**S4**		**S1**		**S2**		**S3**		**S4**		**S5**	
$Q_{inj,ph}$ [nC]	***E***	***I***	***E***	***I***	***E***	***I***	***E***	***I***	***E***	***I***	***E***	***I***	***E***	***I***	***E***	***I***	***E***	***I***
0.2						*												
0.25														***				
0.3										*						**		
0.35				*														
0.4			*							***	*							*
0.45																		
0.5		***				***								*			*	
0.6																		
0.7			*					***		*		**						
0.8		*	**		*													*
0.9			*					*				*					*	
1			**					*		*			*					*
1.2			**		*							*			*	**		
1.4			***										*	*			**	
1.5			**															
1.6			**		*					**			**	*	*			
1.8	**		**						***			***			**	*		
2		*	***				*	*	*					**		***	***	
2.1			***															
2.5		*																

6.3.3. Electrically evoked responses in WT and rd10 retinas

Excitatory and inhibitory responses upon CCS were observed in both healthy and degenerated retinas. Figure 6.8 and Figure 6.9 show each one an example of the responses obtained after employing intraretinally 49 stimuli with different current strengths and time durations. Each stimulus was then applied to neuronal columns that were tracked by the recording electrodes of the shank harboring the stimulating electrode, which was in turn located at the inner retina.

Trial #	CCS parameters
1	10 µA - 0.1 ms
2	9 µA - 0.2 ms
3	9 µA - 0.1 ms
4	8 µA - 0.2 ms
5	8 µA - 0.1 ms
6	7 µA - 0.3 ms
7	7 µA - 0.2 ms
8	7 µA - 0.1 ms
9	6 µA - 0.3 ms
10	6 µA - 0.2 ms
11	6 µA - 0.1 ms
12	5 µA - 0.4 ms
13	5 µA - 0.3 ms
14	5 µA - 0.2 ms
15	5 µA - 0.1 ms
16	4 µA - 0.5 ms
17	4 µA - 0.4 ms
18	4 µA - 0.3 ms
19	4 µA - 0.2 ms
20	4 µA - 0.1 ms
21	3 µA - 0.6 ms
22	3 µA - 0.5 ms
23	3 µA - 0.4 ms
24	2 µA - 1 ms
25	2 µA - 0.9 ms
26	2 µA - 0.8 ms
27	2 µA - 0.7 ms
28	2 µA - 0.6 ms
29	2 µA - 0.5 ms
30	2 µA - 0.4 ms
31	1 µA - 2 ms
32	1 µA - 1 ms
33	1 µA - 0.9 ms
34	1 µA - 0.8 ms
35	1 µA - 0.7 ms
36	1 µA - 0.6 ms
37	1 µA - 0.5 ms
38	1 µA - 0.4 ms
39	0.5 µA - 5 ms
40	0.5 µA - 4 ms
41	0.5 µA - 3 ms
42	0.5 µA - 2 ms
43	0.5 µA - 1 ms
44	0.5 µA - 0.9 ms
45	0.5 µA - 0.8 ms
46	0.5 µA - 0.7 ms
47	0.5 µA - 0.6 ms
48	0.5 µA - 0.5 ms
49	0.5 µA - 0.4 ms

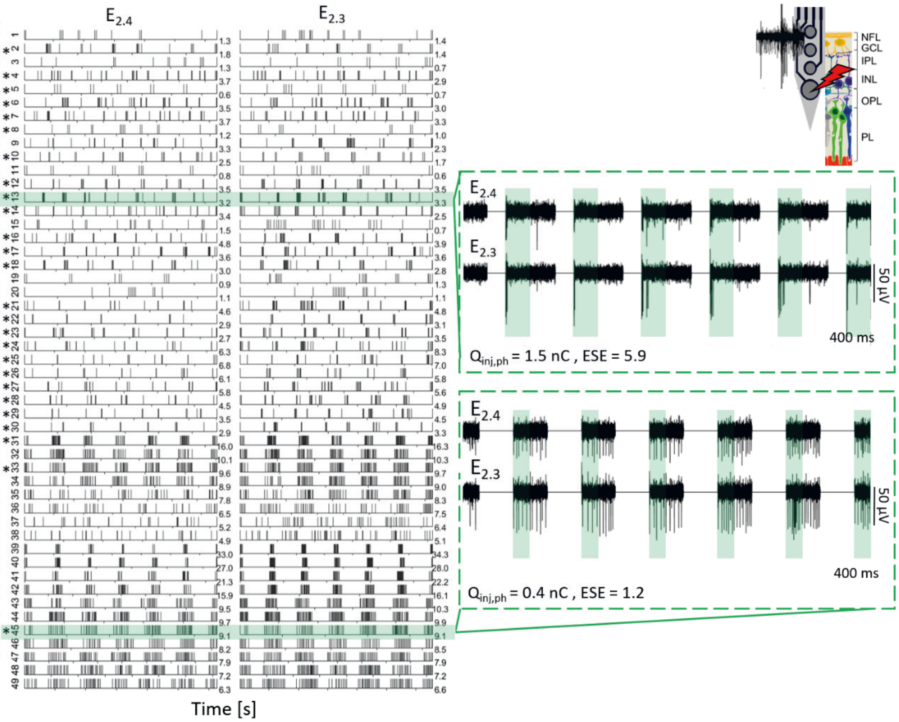

Figure 6.8. Electrical evoked responses in wildtype retina. Responses to electrical stimulation after 49 different trials are shown in the raster plots for the recording channels (upper electrodes) of a stimulating shank located intraretinally in a wildtype (WT) retina (see schematic at the upper right). The raster plots show the spiking activity 400 ms before and 400 ms after each stimulation pulse (white spaces). If no spike was detected within this time window, a blank space is also shown. The table at the left maps the current-controlled stimulation (CCS) parameters applied during each trial. The numbers at the most left *y* axis map the stimulation trial, the numbers at the right *y* axis of each raster plot corresponds to the time duration of the plot, and the stars (*) denote a significant stimulation ($p < 0.05$, paired t-test) after six stimulation pulses with a frequency of 0.05 Hz. The insets at the right display electrical recordings corresponding to stimulation trials that yielded a high electrical stimulation efficiency (upper inset) and a significant stimulation with low charge stimuli (lower inset), showing in turn 400 ms before and 400 ms after each stimulation pulse (line of 0 V). The shaded areas show time windows of 400 ms wherein a response was expected, and unshaded areas show the spontaneous activity. Intraretinal layers are coded as: NFL = nerve fiber layer, GCL = ganglion cell layer, IPL= inner plexiform layer, INL=inner nuclear layer, OPL= outer plexiform layer, and PL = photoreceptor layer.

As an example of intraretinal stimulation in healthy retinas, Figure 6.8 exhibits the responses of a neuronal column that presented low spontaneous activity at the beginning of the experiment and ended up with a FR increase of ~ 10-fold at the end of the experiment (see raster plots). To determine the stimulation parameters that induced electrical responses with the lowest $Q_{inj,\ ph}$, electrical stimuli were applied with descendent current amplitudes and with decreasing T_{ph} within each current level (see parameters table at the left). In the example, the neuronal column showed high excitability along the experiment, producing 26 significant responses out of 49 trials. Likewise, neuronal excitability was higher for current pulses between 2 – 10 µA and decreased for currents between 0.5 – 1 µA. The latter coincided with the low and high spontaneous activity shown by RGCs during the time windows of the stimuli, as it can be observed at the upper and lower insets in Figure 6.8. Although high neuronal activity hindered the identification of electrical responses upon low current stimuli, a significant excitatory stimulation with a $Q_{inj,\,ph}$ as low as 0.4 nC was identified (lower inset in Figure 6.8).

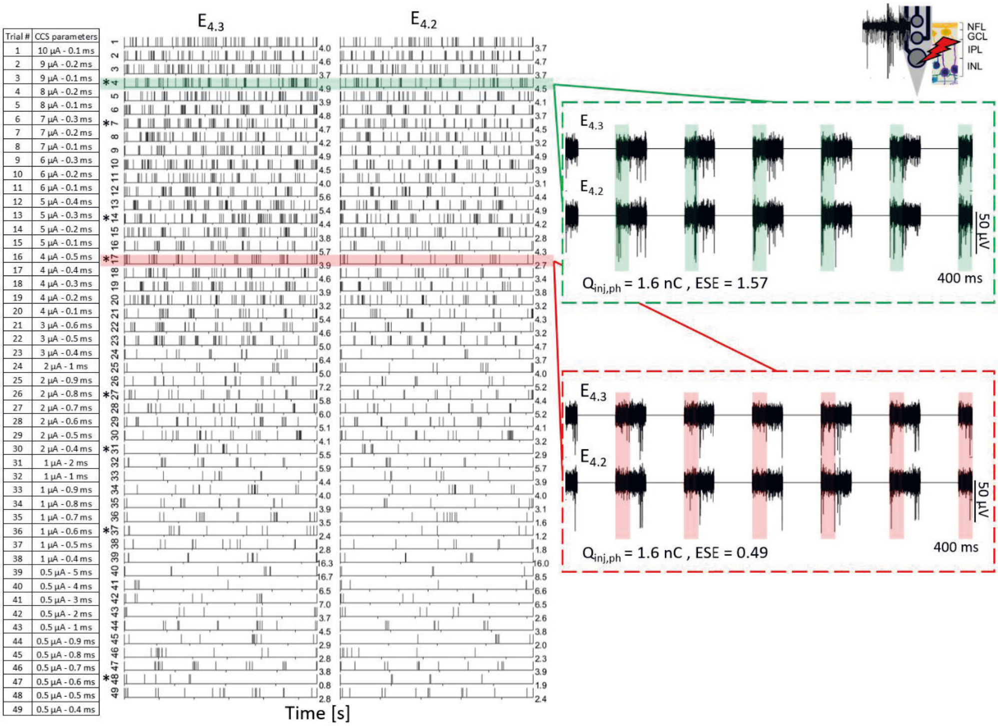

Trial #	CCS parameters
1	10 µA - 0.1 ms
2	9 µA - 0.2 ms
3	9 µA - 0.1 ms
4	8 µA - 0.2 ms
5	8 µA - 0.1 ms
6	7 µA - 0.3 ms
7	7 µA - 0.2 ms
8	7 µA - 0.1 ms
9	6 µA - 0.3 ms
10	6 µA - 0.2 ms
11	6 µA - 0.1 ms
12	5 µA - 0.4 ms
13	5 µA - 0.3 ms
14	5 µA - 0.2 ms
15	5 µA - 0.1 ms
16	4 µA - 0.5 ms
17	4 µA - 0.4 ms
18	4 µA - 0.3 ms
19	4 µA - 0.2 ms
20	4 µA - 0.1 ms
21	3 µA - 0.6 ms
22	3 µA - 0.5 ms
23	3 µA - 0.4 ms
24	2 µA - 1 ms
25	2 µA - 0.9 ms
26	2 µA - 0.8 ms
27	2 µA - 0.7 ms
28	2 µA - 0.6 ms
29	2 µA - 0.5 ms
30	2 µA - 0.4 ms
31	1 µA - 2 ms
32	1 µA - 1 ms
33	1 µA - 0.9 ms
34	1 µA - 0.8 ms
35	1 µA - 0.7 ms
36	1 µA - 0.6 ms
37	1 µA - 0.5 ms
38	1 µA - 0.4 ms
39	0.5 µA - 5 ms
40	0.5 µA - 4 ms
41	0.5 µA - 3 ms
42	0.5 µA - 2 ms
43	0.5 µA - 1 ms
44	0.5 µA - 0.9 ms
45	0.5 µA - 0.8 ms
46	0.5 µA - 0.7 ms
47	0.5 µA - 0.6 ms
48	0.5 µA - 0.5 ms
49	0.5 µA - 0.4 ms

Figure 6.9. Electrical evoked responses in *rd10* retina. Responses to electrical stimulation after 49 different trials are shown in the raster plots for the recording channels (upper electrodes) of a stimulating shank located intraretinally in an *rd10* retina (see schematic at the upper right). The raster plots show the spiking activity 400 ms before and 400 ms after each stimulation pulse (white spaces). If no spike was detected within this time window, a blank space is also shown. The table at the left maps the current-controlled stimulation (CCS) parameters applied during each trial. The numbers at the most left *y* axis map the stimulation trial, the numbers at the right *y* axis of each raster plot corresponds to the time duration of the plot, and the stars (*) denote a significant stimulation ($p < 0.05$, paired t-test) after six stimulation pulses with a frequency of 0.05 Hz. The insets at the right display electrical recordings corresponding to stimulation trials that yielded an excitatory (green, upper inset) and a inhibitory (red, lower inset) response, showing in turn 400 ms before and 400 ms after each stimulation pulse (line of 0 V). The shaded areas show time windows of 400 ms wherein a response was expected, and unshaded areas show the spontaneous activity. Intraretinal layers are coded as: NFL = nerve fiber layer, GCL = ganglion cell layer, IPL= inner plexiform layer, and INL=inner nuclear layer.

In the case of *rd10* retinas, low excitability was observed, and significant responses with a reduced FR, accounted as inhibitory responses, were captured. Contrary to the example shown for WT retinas (Figure 6.8), Figure 6.9 exposes an example of a degenerated retina that had high spontaneous activity at the beginning of the experiment, presenting in turn a FR reduction of ~ 3.8-fold at the end of the experiment. As mentioned before, cases in which different current pulses with a same $Q_{inj,\,ph}$ generated opposite responses were observed, as it is the case of the excitatory and inhibitory responses exhibited in the upper and lower insets of Figure 6.9, respectively. In the example, the activity was increased by 50% when a strong current pulse with short duration was used (8 µA – 0.2 ms, $Q_{inj,\,ph}$ = 1.6 nC) and reduced by 50% when a current pulse with low strength and long duration was applied (4 µA – 0.4 ms, $Q_{inj,\,ph}$ = 1.6 nC). Similar cases were captured by different retinal samples (see Table 6.2), thereby implying that modulation of excitatory and inhibitory responses is possible.

Inhibitory effects have been reported upon ES of neural tissues by different groups [219]–[223]. Two main explanations have been given in the literature to explain such effects: i) strong electrical stimuli can induce sodium reversal currents setting up an upper threshold from which no AP can be fired [221] and ii) cathodal block can occur after stimulating the dendritic tree of a neuron, thereby inducing a strong hyperpolarization that stops the propagation of an AP from the beginning of the axon [219], [220]. Considering the low range of currents and charges applied in this section, the cathodal block hypothesis supports the inhibitory effects observed, pondering also that the position of the stimulating electrodes during an intraretinal stimulation are closer to the axons of bipolar cells and to the dendrites of RGCs rather than the axons of RGCs. Consequently, the latter could be an indication that both excitatory and inhibitory effects are possible during intraretinal stimulations. Nonetheless, further experiments comprising higher charges, cathodal and anodal first biphasic pulses, and stimulations at different intraretinal depths should be performed to confirm such hypothesis.

Furthermore, according to the FR response upon ES, neuronal responses can be identified as saturated, if the spiking response increases with stronger stimuli and reaches a maximum response forming a plateau; as non-monotonic, if the spiking response increases with stronger stimuli but decreases until a certain point is reached; or as monotonic, if the spiking response increases continually with stronger stimuli [175], [222], [224]. Although the stimulation parameters used during CCS were not optimized to identify specific stimulus response relationships, non-monotonic, monotonic, and inverse-saturated responses were observed. Figure 6.10 displays the ESE for both WT and *rd10* retinas along the different stimuli applied (trials), thereby allowing to identify specific responses to stimuli with increased charge injection.

For example, the response of S2 in WT retinas exhibited mostly a non-monotonic response. In this case, the ESE reached a maximum excitability at 1.2 nC and decreased when higher charges were applied with a $I_{inj,\,ph}$ of 2 µA. Likewise, when $I_{inj,ph}$ was 4 µA, an excitability peak at 1.6 nC was captured (Figure 6.10, left inset). Thus, the latter shows that a response of a same group neurons follow a same pattern, however, peak responses can be achieved at different $Q_{inj,\,ph}$ if different current strengths are used.

Despite the low excitability in *rd10* retinas, a monotonic response was identified for S1, which exhibited an increased ESE when using current stimuli of 2 µA with increasing phase periods (increasing also $Q_{inj,\,ph}$). This behavior produced a response that was fitted to a linear relationship between ESE and $Q_{inj,\,ph}$ (Figure 6.10, middle inset). Contrary to WT samples, not all current stimuli produced the same response for a same group of neurons. For example, the same sample could also fit a non-monotonic response for current stimuli of 4 µA (S1, *rd10* in Figure 6.10), however, given the low excitability of the tissue, it is possible that a wider charge spectrum was needed to identify the complete response. Moreover, while saturated responses *per se* were not identified, an inverse saturated response was observed for S2 in *rd10* samples, which exhibited an

ESE below one (Figure 6.10, right inset). In the latter case, a minimum ESE of 0.8 was reached (plateau) when current stimuli of 4 µA with charges higher than 1.2 nC were applied.

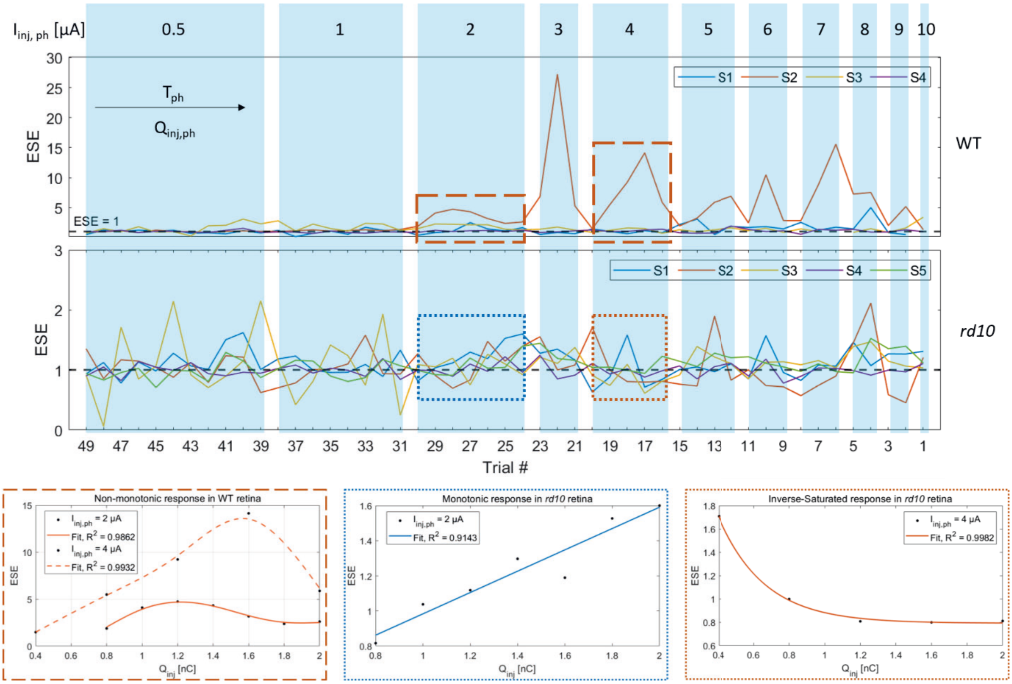

Figure 6.10. Stimulus response relationship. Electrical stimulation efficiency (ESE) per stimulation trial (see parameters in Figure 6.8 and Figure 6.9) for four (S1-S4) WT and five (S1-S5) *rd10* samples. Individual shaded areas indicate the cathodic current injection ($I_{inj,\ ph}$) applied during the trial, and phase period (T_{ph}), as well as cathodic charge injection per phase ($Q_{inj,\ ph}$) increases from left to right for each current level. The insets at the bottom show an example of a non-monotonic (bottom left, smoothing spline fit), a monotonic (bottom center, 1st degree polynomial fit), and an inverse-saturated (bottom right, negative exponential fit) stimulus response relationship.

6.4. Outlook

In this chapter, the insertion feasibility, as well as the recording and ES capabilities of flexible BiMEAs were demonstrated *in vitro* in healthy and degenerated retinas. Optimal insertion parameters that allowed the use of flexible BiMEAs were first established. Then, intraretinal recordings at different retinal depths were performed, followed by an exploration of the $Q_{d,\ ph}$ thresholds needed to evoke electrical responses in the retina upon ES from the intraretinal space.

To enable the successful insertion of flexible BiMEAs, adjustments to the insertion protocol reported previously for Si-BiMEAs were made (see section 4.2.1). As it was shown, stepwise insertions of 20 µm did not allow the proper penetration of flexible probes through the GCL. Therefore, longer insertions steps were implemented, exposing in turn that Z_{in} should be long enough to poke the first intraretinal layer and to enable further penetration of the tissue. In the literature, this initial displacement inducing the compression of the tissue until rupture is known as dimpling [225], [226]. The dimpling distance to penetrate the NFL and GCL was estimated to be between 40-50 µm, corresponding not only to the minimum Z_{in} distances that allowed successful insertions but to the approximate thickness of the NFL-GCL layers [163]. Given the above, a combined insertion protocol with a Z_{in} of 100 µm and ΔZ of 20 – 40 µm was established to facilitate the shank insertion and to tune the position of the shanks within the intraretinal layers. Thus, the successful insertion of flexible BiMEAs in both WT and degenerated mouse retinas was achieved. Nonetheless, to optimize further the insertion of intraretinal devices, tests measuring insertion forces into the retina and dimpling should be performed in the future.

Furthermore, akin to Si-BiMEAs, flexible BIMEAs showed the capability of performing intraretinal recordings at different retinal depths for both healthy and degenerated retinas. Here, intraretinal shanks as short as 145 µm long were used to access the thin retina, capturing in turn the spontaneous spiking activity of RGCs in both retina types and LFPs in *rd10* retinas. Even more, during light stimulation flexible BiMEAs did not show the light-induced artifacts present in the recordings of Si-BiMEAs at the onset and offset of light stimuli (see section 4.2.3). Thus, flexible BiMEAs showed the possibility of recording LFPs such as intraretinal ERG-like waveforms in WT retinas during light stimulation, being the latter an important feature for future medical use to assess the overall function of the retina [39].

Regarding ES, CCS was used to explore the $Q_{d,\, ph}$ limits evoking electrical responses in the retina. Low current stimuli that produced a $Q_{inj,\, ph}$ range between 0.2 – 2.5 nC were tested, showing in turn the feasibility of evoking excitatory and inhibitory responses in the spiking activity of the retina when injecting charges as low as 0.4 nC or 0.2 – 0.25 nC, respectively. Thus, to have a better understanding of the modulation of excitatory and inhibitory responses, further tests including both cathodic and anodic first biphasic current pulses, as well as the stimulation of different intraretinal depths should be performed.

Moreover, while significant responses were captured after applying stimuli with low $Q_{inj,\, ph}$, the excitability of *rd10* retinas was low, indicating that a wider range of charges should be tested. To this end, the CIC of the stimulating electrodes must be considered. Contrasting the results obtained in 1xPBS, voltage transients recorded intraretinally revealed a reduction of the CIC of the electrodes. Hence, to test stimuli with higher charges, the electrochemical properties of the electrodes must be improved. To this effect, strategies like increasing the thickness of SIROFs to enhance both Z and CSC, or the implementation of a positive potential bias with asymmetric current pulses to raise the CIC of SIROFs [140] should be tested in future experiments.

Chapter 7

Si vs. Flexible BiMEAs

Proven the viability of Si and flexible BiMEAs for intraretinal applications *in vitro*, the performance of both devices was evaluated according to the following aspects:

i) The acute insertion footprint
ii) The electrophysiological effects induced during intraretinal insertions
iii) The quality of electrical recordings
iv) The success rate of insertion

To this end, intraretinal probes with Si, PI, or PaC as the main substrate material and shank cross-sections of 1500 or 2500 μm^2 for Si and 350 or 700 μm^2 for PI and PaC were used. Considering that Si and flexible devices had a thickness of 25 and 7 µm, respectively, each intraretinal probe will be referred hereafter according to the substrate material and the shank width as follows: Si-100, Si-60, PI-100, PI-50, PaC-100, and PaC-50. Additionally, insertion speeds of 62.5, 112,5, 162.5, and 187.5 µm/s were tested for each device. Thus, four insertions separated each one by 300 µm with a same V_{in} were carried out per retinal sample for each device, for a total of 24 retinal samples and 96 insertions. Moreover, to ensure comparability among samples, intraretinal insertions followed the insertion protocol established in Chapter 1. Therefore, differences among intraretinal devices were established according to the main substrate material, the shank cross-section, and V_{in}.

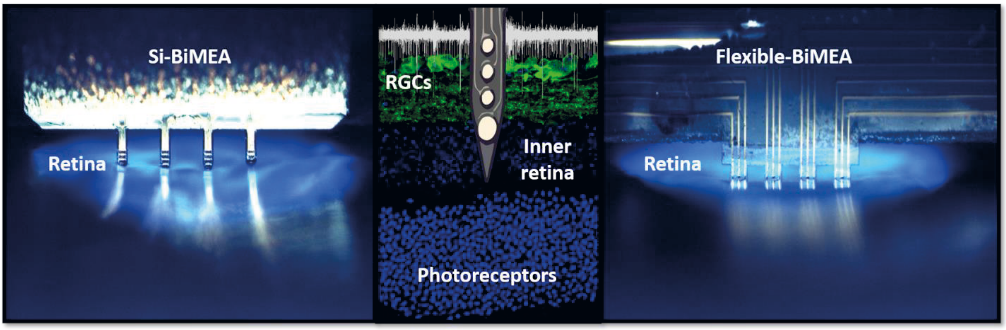

This chapter is in part reproduced from the following work:

Rincón Montes, V., Gehlen, J., Ingebrandt, S., Mokwa, W., Walter, P., Müller, F., and Offenhäusser, A., "Development and *in vitro* validation of flexible intraretinal probes" *Sci Rep* 10, 19836 (2020)

7.1. Acute insertion footprint

The biological impact of intraretinal insertions on the retina was assessed according to the acute insertion footprint of the devices, which was quantified after dead cells stainings in TN-L15 retinas according to three parameters: i) the insertion trauma area (ITA), defined as the insertion hole area comprising the dead cells within and around the borders of the insertion site; ii) the insertion trauma area ratio (ITR), which refers to the ratio of ITA to the shank-cross section; and iii) the count of dead cells within ITA (see methods in section 3.7). Figure 7.1 displays an overall picture of the acute insertion footprint caused by intraretinal devices using different V_{in}.

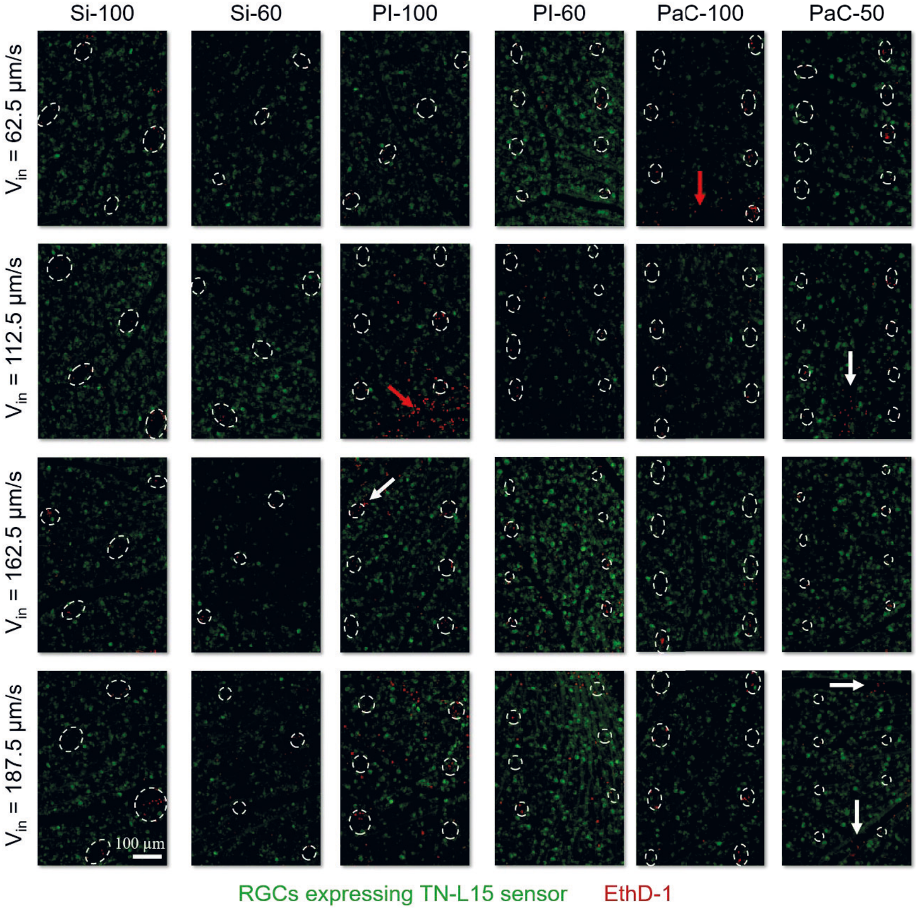

Figure 7.1. Dead cell stainings after intraretinal insertions in TN-L15 retinas. Top view of the maximum intensity projections of dead cells stainings using ethidium homodimer (EThD-1) as a dye for dead cells (red) after intraretinal insertions in TN-L15 retinas with RGCs (green) expressing the Ca^{2+} sensor TN-L15. The images show the insertion footprint of six intraretinal probes (columns) for each insertion speed (V_{in}) tested (rows). The ITA of shank insertions is enclosed by white dashed lines. The red

arrows indicate an artifact from the preparation that corresponds to dead cells at the border of the filter paper that supported the retinal sample, and white arrows point out dead cells encountered within blood vessels.

Similar to the stainings reported previously in section 4.4, Si-100 showed the biggest visible trauma, while probes with narrower shank widths using the highest V_{in} generated insertion footprints that were barely visible (Figure 7.1). For a direct comparison, Figure 7.2 zooms in the dead stainings of a Si-100 insertion using a V_{in} of 112.5 µm/s and a PaC-50 insertion using a V_{in} of 187.5 µm/s. The latter exposes an example of the biggest and smallest ITA with the highest and lowest count of dead cells, respectively. Additionally, in some cases dead cells were found inside blood vessels, increasing in turn the dead cell count of some insertions that went through blood vessels (see white arrows in Figure 7.1). Considering that the biological samples were ex-planted retinas and that blood vessels do not have a nucleus, some of these cells could correspond to endothelial cells that died during the preparation of the tissue. Nonetheless, only dead cells matching the holes of intraretinal insertions were considered in the study.

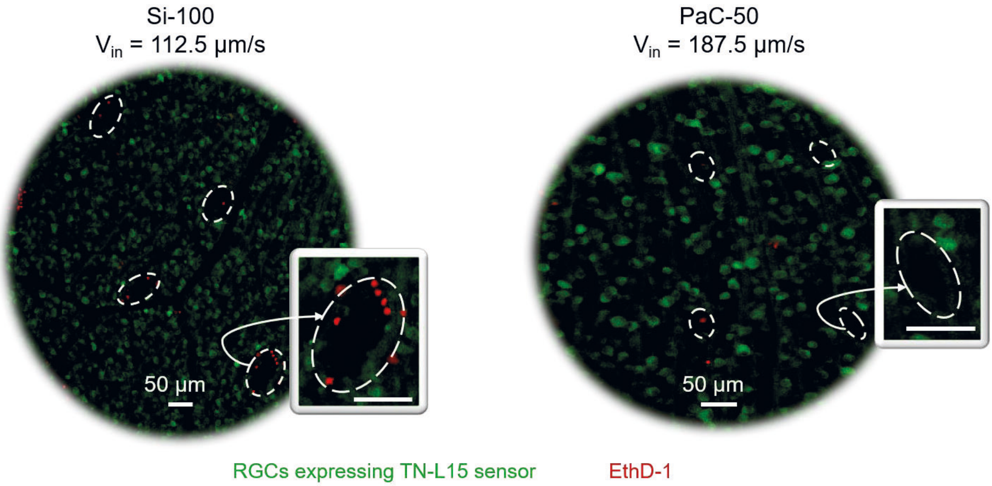

Figure 7.2. Zooming in dead cell stainings after intraretinal insertions in TN-L15 retinas. Top view of the maximum intensity projections of dead cells stainings using ethidium homodimer (EThD-1) as a dye for dead cells (red) after intraretinal insertions in TN-L15 retinas with RGCs (green) expressing the Ca^{2+} sensor TN-L15. The images show an example of the biggest and smallest insertion trauma area (ITA) induced by a Si-100 (left) and a PaC-50 (right) device, respectively. The ITA of different shank insertions is enclosed by white dashed lines.

The effects of the main substrate material of the probes, the shank cross-section, and V_{in} on ITA are exhibited in Figure 7.3. Results reveal that the conjugation of flexible materials with a narrow shank width of 50 µm and a V_{in} as high as 187.5 µm/s produced the smallest ITA, with an average trauma area of 782.17 ± 309.48 µm^2 for PI and 861.7 ± 396.72 µm^2 for PaC. These results were ~ 2 times smaller than the smallest ITA of Si devices (Si-60 = 1757.63 ± 517.28 µm^2) and showed to be significantly smaller than 70% of all the conditions tested. The latter was evidenced, as PI-50 and PaC-50 using the highest V_{in} produced an ITA that was lower than all insertions carried out with Si-100 and PI-100, than three out of four insertions performed with Si-60 and PaC-100, and lower than the ITA produced by the lowest insertion speed tested for both PI-50 and PaC-50 (Figure 7.3a and Figure A.11. 1a in Appendix 11).

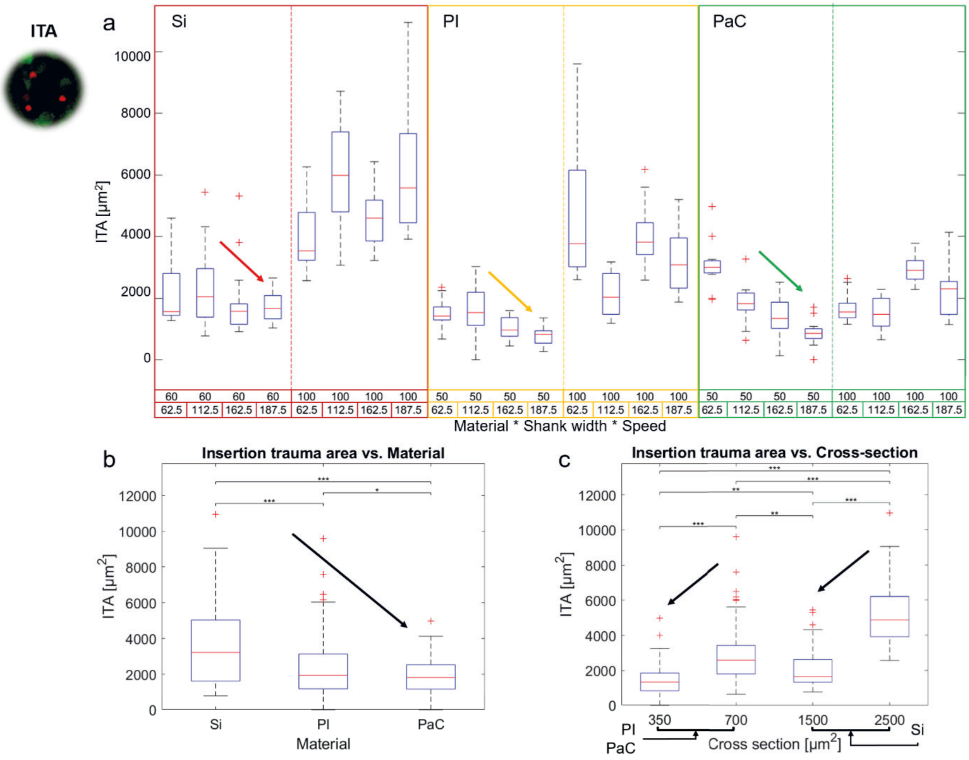

Figure 7.3. Insertion trauma area. The boxplots show the influence of the probe material, the shank cross-section, and the insertion speed on the insertion trauma area (ITA) after acute intraretinal insertions. a) General comparison among the tested probes grouped by material (Si, PI, or PaC), shank width (100 or 50/60 µm), and insertion speed (62.5, 112.5, 162.5, or 187.5 µm/s). b) Comparison among main substrate materials. c) Comparison among shank cross-sections, matching 350 and 1500 μm^2 to shank widths of 50 and 60 µm, and 700 and 2500 μm^2 to shank widths of 100 µm. The main trends are illustrated by arrows and significance differences in (b) and (c) are shown by stars (* for p <= 0.05, ** for p <= 0.01 *** for p <= 0.001) after performing post-hoc pairwise testing using non-parametric bootstrap t-tests and Bonferroni correction.

Moreover, despite the thickness bias favoring flexible probes (Si and flexible probes were 25 and 7 µm thick, respectively), a significant ITA reduction induced by the material *per se* was observed in the case of PaC probes, which showed an ITA that was ~ 1.2-1.9-fold lower than both, Si and PI, even when the latter had the same thickness of PaC probes (Figure 7.3b). Additionally, when pondering the effect of the shank cross-section on ITA, a strong influence of the shank width was exposed. These findings are evidenced as the shank cross-sections of 350 and 700 μm^2, corresponding each to shank widths of 50 and 60 µm, produced ITAs that were significantly and proportionally (~ 2 – 2.5-fold) lower than the ITA of the shank cross-sections of 700 and 2500 μm^2, which match in turn to shank widths of 100 µm (Figure 7.3c). Furthermore, while no clear influence of the combined interaction between the main substrate material and V_{in} was found (see Appendix 11, Figure A.11. 1b), increasing V_{in} yielded significantly smaller ITAs in shanks widths of 50 – 60 µm (Figure 7.3a and Figure A.11. 1b-c in Appendix 11).

Conversely, when normalizing ITA to the shank cross-section, a strong influence of the probe material on ITR was observed, where clear differences between Si and flexible materials arose (Figure 7.4b-c and Figure A.11. 2a-b in Appendix 11). Si showed significantly the lowest ITR, inducing in average an ITA that was 1.73 ± 0.8 times the cross-section of the intraretinal shanks, compared with PI and PaC, whose ITRs were 4.12 ± 2.07 and 3.88 ± 2.34 (Figure 7.4b), respectively. This trend was also observed when analyzing the effect of the shank cross-sections on ITR, as the cross-sections corresponding to Si yielded the lowest ITR (Figure 7.4c).

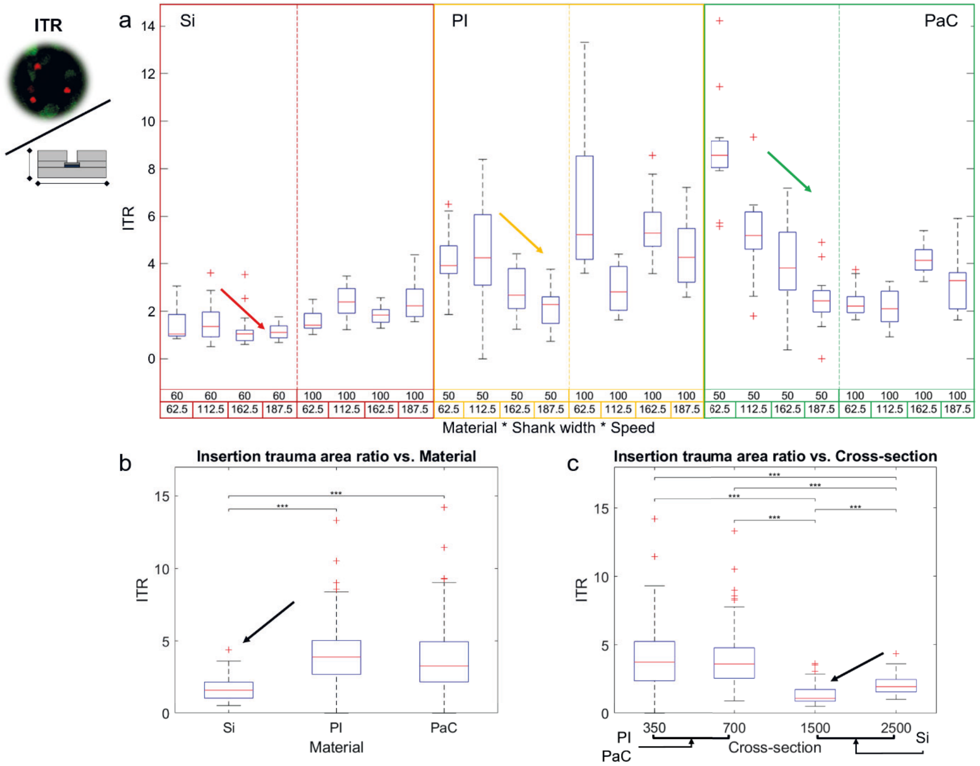

Figure 7.4. Insertion trauma area ratio. The boxplots show the influence of the probe material, the shank cross-section, and the insertion speed on the insertion trauma area ratio (ITR) after acute intraretinal insertions. a) General comparison among the tested probes grouped by material (Si, PI, or PaC), shank width (100 or 50/60 µm), and insertion speed (62.5, 112.5, 162.5, or 187.5 µm/s). b) Comparison among main substrate materials. c) Comparison among shank cross-sections, matching 350 and 1500 µm^2 to shank widths of 50 and 60 µm, and 700 and 2500 µm^2 to shank widths of 100 µm. The main trends are illustrated by arrows and significance differences in (b) and (c) are shown by stars (* for p <= 0.05, ** for p <= 0.01 *** for p <= 0.001) after performing post-hoc pairwise testing using non-parametric bootstrap t-tests and Bonferroni correction.

Likewise, a significant difference was observed between different shank cross-sections within Si devices, thereby revealing a directly proportional relationship between ITR and shank cross-section. This trend matches the cross-sectional proportionality of the acute insertion footprint of

Si devices reported by [178], however, the latter does not apply to flexible probes (Figure 7.4c). ITR differences among the different substrate materials tested could arise due to surface properties differences. The latter have shown to modify the insertion mechanics of penetrating probes in intracortical applications, producing clean and hydrophilic surfaces reduced insertion forces and dimpling [225]. Considering that neural probes used in this study were not subjected to a cleaning or surface modification treatment prior to use, intrinsic properties of the materials, such as the hydrophobicity of PaC, could have influenced ITR results.

Moreover, after screening the insertion footprints produced by penetrating probes in the literature, a trend where Si yields a lower ITR than flexible probes was observed (Table 7.1). Nonetheless, this behavior has not influenced the fact that in comparison with stiff materials like Si, flexible neural probes have reduced FBRs in chronic applications [114], [227]. Likewise, ITRs of flexible probes in the literature tend to be higher than those reported here, generating discrepancies that could be caused by insertion shuttles in the case of flexible intracortical neural probes. Furthermore, an ITR reduction was achieved in the case of Si and flexible probes for shank widths of 50 – 60 µm when higher insertion speeds were used (Figure 7.4a, and Figure A.11. 2c in Appendix 11). Thus, when using a V_{in} of 187.5 µm/s, the tested samples achieved a minimum ITR of 1.17 ± 0.34 for Si-60, of 2.17 ± 0.86 for PI-50, and of 2.46 ± 1.13 for PaC-50.

Table 7.1. Literature review of cross-sectional footprints of penetrating neural probes. Comparison of the bare insertion footprint (insertion trauma area) and the insertion trauma area ratio (ITR) of acute and chronic implantations of penetrating neural probes. The bare footprint (corresponding only to the insertion hole) and ITR were estimated from the given references for probes whose main substrate materials was silicon (Si), polyimide (PI), or parylene-C (PaC).

Probe material	Dimensions [µm] (thickness x width) or (diameter)	Cross-section [µm^2]	Footprint type	Bare footprint [µm^2]	ITR	Reference
Si	15x120	1800	Acute	2538.81	1.41	Szarowski et al., 2003[178]
Si	200	31416	Chronic (6-12 weeks)	-	1.33-2.1	Thelin et al., 2011[124]
Si	50	1963	Chronic (6-12 weeks)	-	1-1.89	Thelin et al., 2011[124]
Si	15x250	3750	Chronic (4-8 weeks)	3708.82	0.99	Lee et al., 2017[227]
Si	**25x100**	**2500**	**Acute**	**4064.93**	**1.63**	**This work**
Si	**25x60**	**1500**	**Acute**	**1757.63**	**1.17**	**This work**
PI	21.3x250	5325	Chronic (4-8 weeks)	7808.64	1.47	Lee et al., 2017[227]
PI	**7x100**	**700**	**Acute**	**2095.49**	**2.91**	**This work**
PI	**7x50**	**350**	**Acute**	**782.17**	**2.17**	**This work**
PaC	11x300	3300	Chronic (28 days)	44070.91	13.35	Kim et al., 2013[228]
PaC	20x35	700	Chronic (6 months)	38888.12	55.55	Sohal et al., 2014[229]
PaC	8x36	288	Chronic (6 weeks)	3973.83-9488.54	13.8-32.9	Wu et al., 2015[230]
PaC	**7x100**	**700**	**Acute**	**1496.61**	**2.14**	**This work**
PaC	**7x50**	**350**	**Acute**	**861.71**	**2.46**	**This work**

Akin to the results exposed previously for ITA, PI-50 (1.42 ± 1.02) and PaC-50 (0.63 ± 0.72) induced the lowest number of dead cells after acute intraretinal insertions using a V_{in} of 187.5 μm/s (Figure 7.5a). Nevertheless, only PaC-50 with the highest speed showed significantly lower counts than 58% of all tested conditions. The latter yielded lower values than all Si-100 insertions, than three out of four insertion conditions of PI- and PaC-100, and lower than the counts produced by the lowest insertion speeds used for PI- and PaC-50 (Figure A.11. 3a in Appendix 11). Moreover, although all PaC insertions had an average count of dead cells lower than PI (3.42 ± 2.87 vs. 4.15 ± 4.04), and that the latter were in turn lower than for Si (4.41 ±4.03), no significant differences were found among the main substrate materials (Figure 7.5 b). Additionally, shank cross-sections corresponding to narrow shank widths produced counts of dead cells that were significantly lower than wider shank widths (Figure 7.5c), inducing the former fewer dead cells with a higher V_{in} (Figure 7.5a and Figure A.11. 3c in Appendix 11).

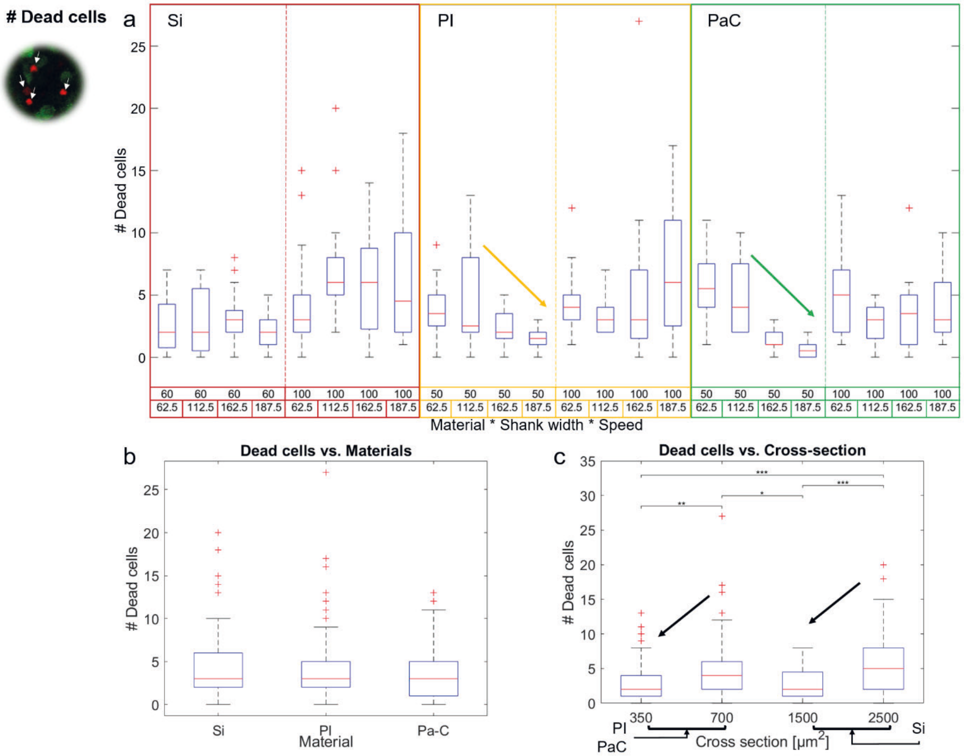

Figure 7.5. Count of dead cells. The boxplots show the influence of the probe material, the shank cross-section, and the insertion speed on the count of dead cells after acute intraretinal insertions. a) General comparison among the tested probes grouped by material (Si, PI, or PaC), shank width (100 or 50/60 μm), and insertion speed (62.5, 112.5, 162.5, or 187.5 μm/s). b) Comparison among main substrate materials. c) Comparison among shank cross-sections, matching 350 and 1500 μm^2 to shank widths of 50 and 60 μm, and 700 and 2500 μm^2 to shank widths of 100 μm. The main trends are illustrated by arrows and significance differences in (b) and (c) are shown by stars (* for $p <= 0.05$, ** for $p <= 0.01$ *** for $p <= 0.001$) after performing post-hoc pairwise testing using non-parametric bootstrap t-tests and Bonferroni correction.

7.2. Electrophysiological effects during intraretinal insertions

The electrical activity of RGCs was followed during every intraretinal insertion by the recording electrodes of individual shanks. Thus, five insertion effects were distinguished according to the FR behavior and peak amplitude of the APs captured. These were classified as instant recovery (IR), peak instant recovery (PIR), peak smooth recovery (PSR), smooth recovery (SR), and peak valley recovery (PVR) as displayed in Figure 7.6.

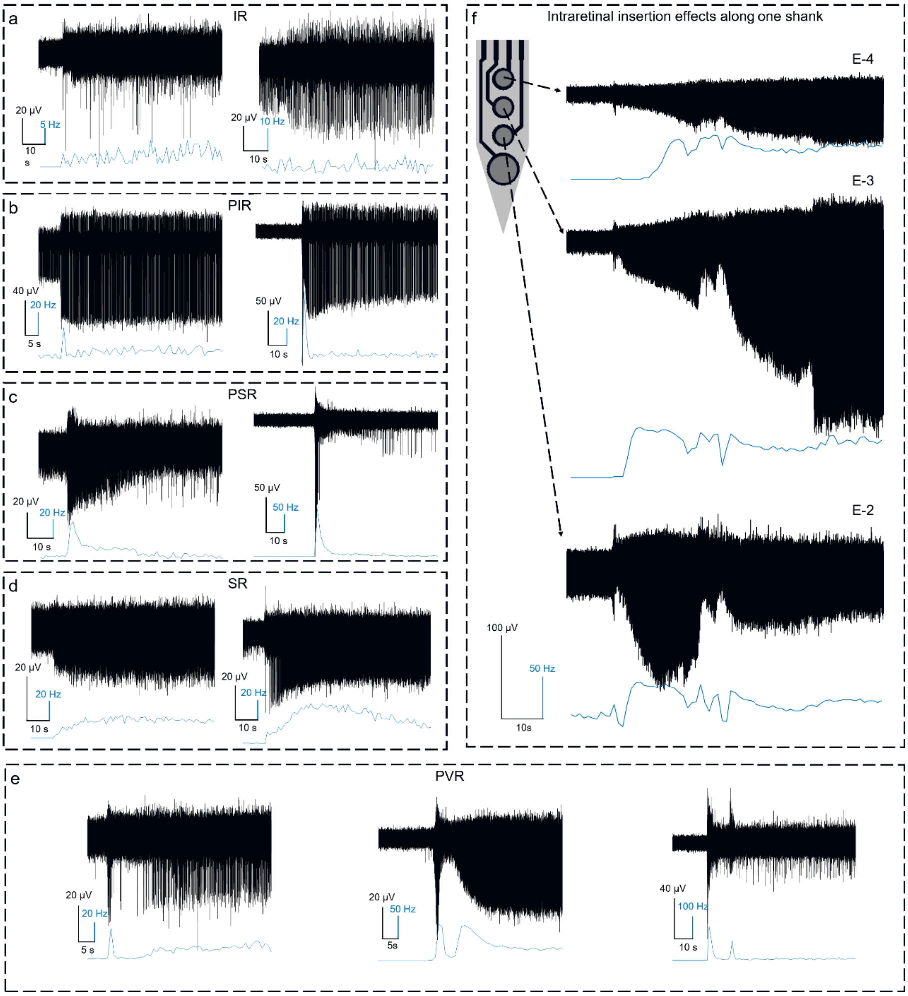

Figure 7.6. Electrophysiological effects during intraretinal insertions. Effects on the activity of RGCs captured during intraretinal insertions. Black and blue traces show the electrical activity of RGCs and the firing rate of the action potentials detected, respectively. The following effects were identified: a) IR, instant relaxation, b) PIR, peak instant relaxation, c) PSR, peak smooth relaxation, d) SR, smooth relaxation, and e) PVR, peak valley relaxation. The electrophysiological effects captured by the insertion of one shank is displayed as an example in f).

An IR effect was observed when an immediate and sustained FR change was observed from 0 Hz (no APs detected) to the spontaneous FR of the units recorded. If APs were already visible, the next insertion produced no visible variation in the FR but an immediate and sustained increase in the peak amplitude of the spikes (Figure 7.6a). PIR describes those insertions that showed a burst of APs (FR peak) during the insertion, followed by a fast and sustained recovery of the spontaneous activity with a maximum duration of 5 seconds (Figure 7.6b). A PSR effect comprises those insertions with a slow (> 5 seconds) FR decay after the FR peak of the insertion, which goes along with spike amplitude changes (Figure 7.6c). In contrast, a SR characterizes those insertions where a slow FR increment, together with spike amplitude changes occur (Figure 7.6d). Additionally, PVR outlines those insertions with mixed effects. First, a burst of spikes that is observed as a FR peak, then a silent phase with low activity or no APs, forming a valley in the FR trace, and a third phase that replicates either a SR, a PSR, or a PIR (left, middle, and right plots in Figure 7.6e).

While these insertion effects were captured by individual electrodes, it was possible to notice the relaxation of the tissue along the shanks after an insertion step has been made to penetrate further the GCL. As exhibited in the example in Figure 7.6f, the second lower electrode (E-2) was already recording APs when the next insertion step was carried out. While a PVR was first seen in E-2, a SR was present in the upper electrodes (E-3 and E-4). Thus, as E-2 got closer to RGCs (high amplitude spikes and FR increment), the tissue relaxed and went up along the shank. This effect can be observed, as the amplitude of APs was reduced in E-2 but slowly increased in the upper electrodes, which reached smoothly a position within the retina closer to RGCs.

After analyzing the activity recorded by electrodes successfully inserted in 96 insertions, the pie chart in Figure 7.7a reveals that PVR, PSR, and PIR was captured in almost equal proportions. These findings indicate that 63% of the times a spike burst phase-locked with the moment of the insertion was observed. Likewise, the bar plot in Figure 7.7b shows that the most dominant effect observed when using Si-BiMEAs was SR (36.4%), while PVR was mostly observed in both PI- and PaC-BiMEAs (34.8% and 37% each). Nonetheless, no significant insertion effects were established among the probes. Additionally, it was found out that IR and PIR effects were in average observed within the first two seconds from the moment of the insertion, whereas PSR, PVR, and SR had in average an observable duration of 35 ± 29 seconds. Likewise, it was observed that in some cases these effects endured at least 5 minutes (boxplot in Figure 7.7c).

Thus, electrical recordings revealed that for all BiMEAs, the recovery after an intraretinal insertion comprises changes in the spontaneous FR of RGCs. Such recovery was observed mostly within the first 35 seconds after the moment of the insertion. These effects were captured easily by the recording electrodes, as the FR variations were coupled in most of the cases with the amplitude of the APs and generated as well burst of spikes that had the highest peak amplitudes of the detected APs. Considering the mechanical forces involved during the insertion of intraretinal probes, recovery effects, such as PIR, PSR, PVR, and SR, might indicate that the tissue was mechanically stimulated during the insertion.

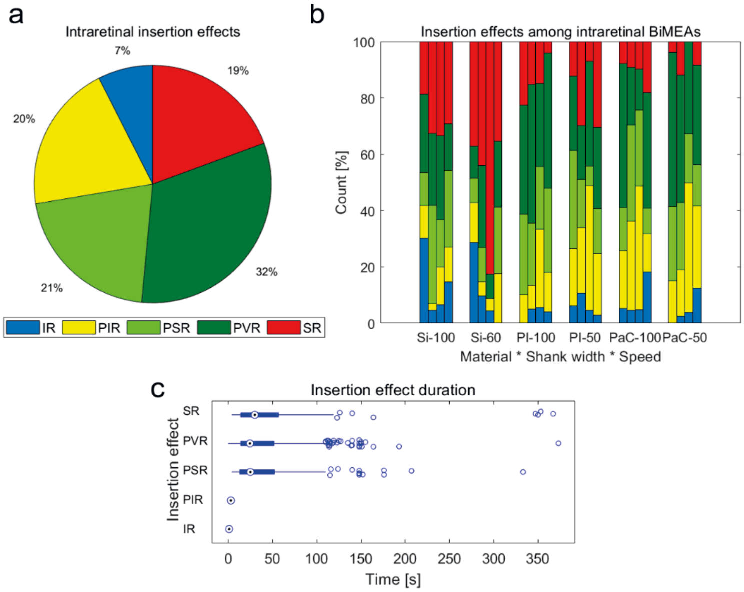

Figure 7.7. Overview of intraretinal insertion effects in retinal activity. a) Pie chart illustrating the incidence of intraretinal insertion effects captured by 1041 electrodes. b) Grouped bar plot showing the incidence of intraretinal insertion effects (color coded as in a) observed by the different types of BiMEAs at different insertion speeds (V_{in} of 62.5, 112.5, 162.5, and 187.5 µm/s). Each one of the four bars per group represents each V_{in} in ascending order. c) Boxplot displaying the duration recorded for each insertion effect.

7.3. Quality of electrical recordings

The recording performance among the different BiMEAs was determined comparing the average SNR of the recordings and the mean and maximum spike amplitude (absolute peak amplitude of an AP), referred hereafter as SPK and MSPK, respectively. As exposed by Figure 7.8a, PaC-50 with a V_{in} of 112.5 µm/s showed the best recording performance with an average SNR of 5.28 ± 1.50, a SPK of 32.63 ± 16 µV, and a MSPK of 88.47 ± 47.8 µV. The latter results were higher than 83.3% of all tested conditions. On the other hand, the poorest performance was exhibited by Si-100 with a V_{in} of 187.5 µm/s and by Si-60 with a V_{in} of 162.5 µm/s. These probes exposed each an average SNR of 4.14 ± 0.34 and 3.87 ± 0.15, a SPK of 15.5 ± 1.9 and 17.4 ± 3.6 µV, and a MSPK of 21.51 ±4.91 and 20.52 ± 4.55 µV.

Likewise, as revealed by Figure 7.8b and regardless of V_{in}, PaC-50 captured the best recordings, being the only probe type to show an average SNR higher than 5 with significantly the highest SPKs and MSPKs among all tested probes (Figure A.11. 4 in Appendix 11). Despite the low amplitude spikes captured by PaC-100, PaC probes showed in general the best SNRs, SPKs, and MSPKs among all substrate materials, with a maximum SNR of 12.49, a maximum SPK of 130 µV, and capturing of all recordings the highest MSPK of 363 µV. Hence, these results agree with the low acute footprint generated by PaC-50 probe reported in section 7.1, considering that a smaller ITA and fewer dead cells surrounding the probe diminish the distance between the electrodes and the target neurons, thereby enhancing the quality of the recordings.

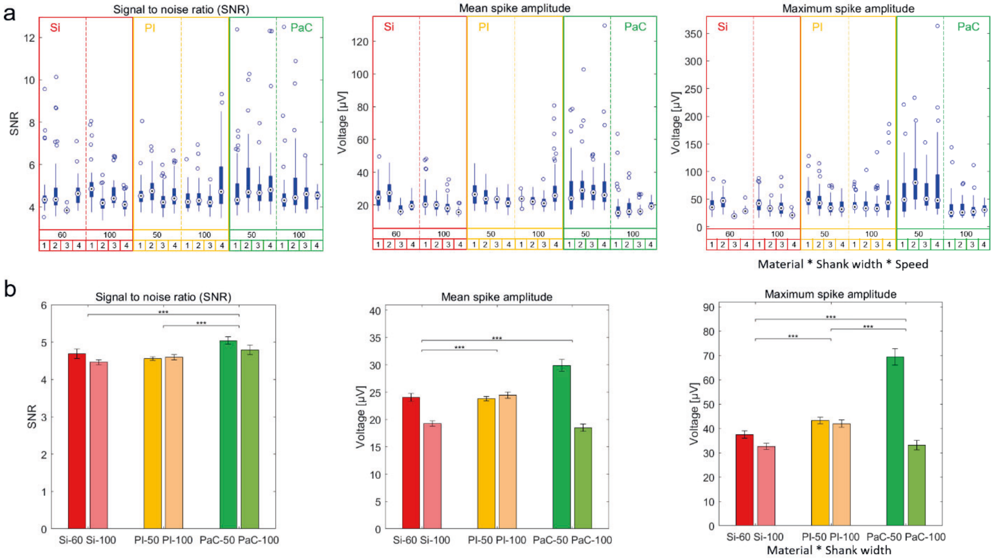

Figure 7.8. Quality of intraretinal recordings. The signal to noise to ratio (SNR) and the mean (SPK) and maximum (MSPK) spike amplitude (absolute peak amplitude of APs) captured during intraretinal recordings by electrodes (N = 966) of successfully inserted shanks are shown in a) for all tested conditions in boxplots grouped by main substrate material (Si, PI or PaC), shank width (50, 60, or 100 µm), and insertion speed (1 = 62.5 µm/s, 2 = 112.5 mm/s, 3 = 162.5 µm/s, and 4 = 187.5 µm/s). Comparisons among the six BiMEA probes are displayed in b) in bar plots grouped by main substrate material and shank width. The error bars show the standard error of the mean and significance differences among material groups (red for Si, yellow for PI, and green for PaC) are depicted by stars (* for $p \leq 0.05$, ** for $p \leq 0.01$, *** for $p \leq 0.001$) after performing post-hoc pairwise testing using non-parametric bootstrap t-tests and Bonferroni correction.

7.4. Success rate of insertion

Considering the goal of developing dual purpose devices capable of recording intraretinally the electrical activity of RGCs while stimulating the inner retina, a successful insertion was defined as an insertion in which the upper electrodes of an individual shank recorded APs after the last penetration step (E-4 and E-3 for shanks with four electrodes or E-3 and E-2 for shanks with two electrodes, see section 4.2.1 and 6.2.1). Thus, besides the optical confirmation showing the insertion of penetrating shanks into the retina (Figure 7.9), electrical recordings were used as guidance to position the electrodes at the desired intraretinal depth and determine whether an insertion was successful or not.

Ruling out Si-60 and PaC-100 probes, BiMEAs showed a combined success rate of 87.24%, exposing a 100% success when Si-100 and PaC-50 probes with a V_{in} of 187.5 and 112.5 µm/s, respectively, were used. While an unclear influence of V_{in} was observed for almost all probes, increasing V_{in} influenced positively the success rate of insertion of Si-100 and negatively the insertion of PaC-100 devices (Figure 7.10a). Additionally, when evaluating the overall insertion of individual probe types, PaC-50 devices exhibited the best performance with a general insertion yield of 93.33% (Figure 7.10b).

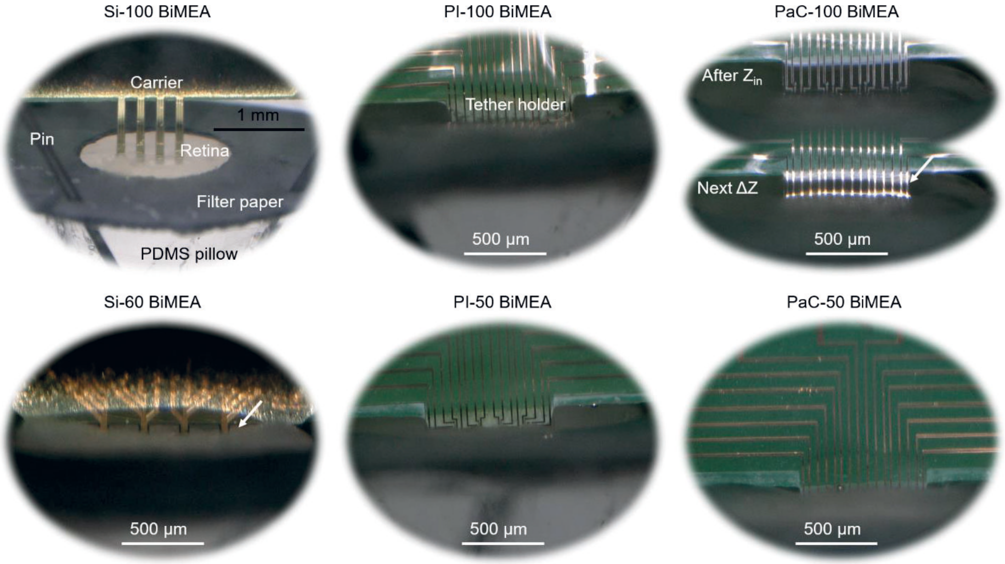

Figure 7.9. Tracking intraretinal insertions. Optical images showing characteristic insertions of Si-100, Si-60, PI-100, PI-50, PaC-100, and PaC-50 BiMEAs. As shown in the images, Si-based probes were directly supported by a stiff carrier and flexible probes (PI and PaC) had a flexible tether holder between the stiff carrier and the probe itself (see section 5.1 for design considerations). In the case of Si-60, the white arrow indicates the non-inserted region of the probe, and for PaC-100, the arrow points out the bending point of the tether holder. See text for more details.

Conversely, Si-60 and PaC-100 probes significantly showed the poorest insertion performance, with a success rate of insertion that was roughly 50%. When contrasting the statistics with the optical follow-up of intraretinal insertions, it was possible to track the failure source of such devices. In the case of Si-60 probes, a complete insertion of the shanks was avoided (see white arrow in Si-60, Figure 7.9) to prevent exogenous compressions on the retina (e.g.: the stiff carrier) that could have amplified the insertion trauma, as it was previously reported in section 4.4. On the other side, a bending failure of the flexible tether holder that supported the shanks is attributed to PaC-100 devices. As exposed by Figure 7.9, shanks seemed inserted after the first insertion step Z_{in}. Nonetheless, further efforts to place the electrodes at the desired intraretinal depth (ΔZ) led to indirect attempts to insert the tether holder, which bended due to the dimensions and shape of the structure (800 µm x 200 µm, rectangular shape, see section 5.1), generating in turn a concomitant retraction of the shanks. Furthermore, to avoid a potential bias of the insertion failure of Si-60 and PaC-100 on the assessments reported previously in this section, only retinal samples that showed clear insertion footprints and those recordings that yielded successful insertions were considered for the analysis.

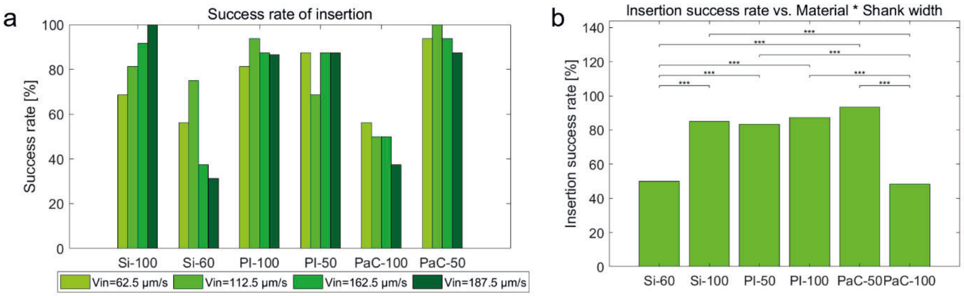

Figure 7.10. Success rate of intraretinal probes. The success rate of intraretinal insertions was evaluated for individual shanks (N = 383) after 96 intraretinal insertions. a) Success rate of insertion of all tested conditions grouped probe type (Main substrate material – shank width) and insertion speeds (V_{in}). b) Success rate comparison of the combined interaction of main substrate material and shank width. Significant differences are shown with stars (* for p <= 0.05 and *** for p <= 0.001) after performing post-hoc pairwise testing using Fisher's Exact test with Bonferroni correction.

7.5. Summary

The acute biological impact on the retina, the quality of intraretinal recordings, as well as the success rate of intraretinal insertions were analyzed to evaluate the performance of intraretinal probes.

Dead cell stainings of intraretinal insertions revealed that the conjugation of the main substrate material and the shank dimensions of a penetrating probe has a direct impact on the acute insertion footprint of intraretinal devices. Moreover, depending on the latter combination, the insertion speed can diminish the insertion trauma. In this sense, flexible, narrow, and high insertion speeds significantly yielded the smallest ITA. Additionally, ITR results revealed the proportion at which the insertion footprint was generated, exposing in turn that ITR can be reduced if narrow shanks and higher insertion speeds are employed. Likewise, ITR was influenced by the main substrate material of the probes, implying that further optimizations such as surface modifications could be employed to reduce the footprint of intraretinal devices. As for the count of dead cells, smaller shank widths yielded lower counts, and higher insertion speeds along with flexible narrow shanks resulted in less dead cells. The latter demonstrates that the strategy followed during the development of flexible intraretinal probes was successful in reducing the insertion footprint and the acute biological trauma of the initially proposed Si-based BiMEAs (Figure 7.11).

In addition, a characterization of the electrophysiological behavior of the retina upon the penetration of intraretinal devices exposed a possible mechanical stimulation of the retina, however, the spontaneous behavior of the tissue showed an average recovery time of ~ 35 s after an insertion step. In this case, probe-specific induced behaviors were not encountered. Furthermore, to complete the assessment, electrical recordings of the spiking activity of the retina exposed that PaC-50 probes produced the recordings with the highest SNR and captured APs with the highest amplitudes. Consequently, PaC-50 devices showed the best performance among all probes, with an acute insertion footprint as small as 2.46 times the shank cross-section, a dead cell count as low as 0.63, recordings with a maximum SNR of 12.49 and a maximum peak spike amplitude of 363 µV, and a success rate of insertion of 93.33%.

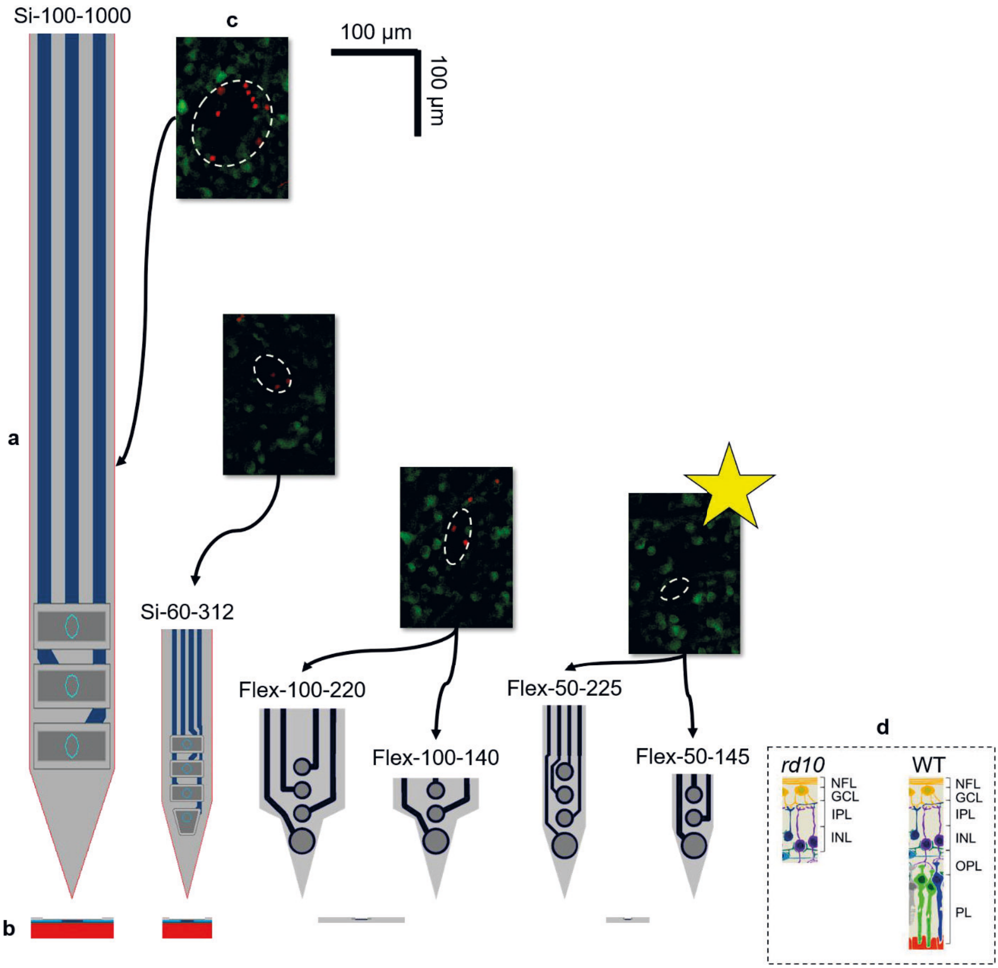

Figure 7.11. BiMEA comparison. Comparison of shank dimensions and the acute insertion footprint of BiMEA devices. a) Front view. b) Cross-section. c) Top view of the maximum intensity projection images of the corresponding dead cell stainings, showing in red dead cells stained with ethidium homodimer and in green RGCs expressing the Ca^{2+} TN-L15. Intraretinal shanks are coded as: material (Si or flexible) – shank width [µm] – shank length [µm]. As comparison among the penetrating shanks and the target tissue, d) illustrates a coronal section of a degenerated and a healthy retina. Intraretinal layers are coded as: NFL = nerve fiber layer, GCL = ganglion cell layer, IPL = inner plexiform layer, INL = inner nuclear layer, OPL = outer plexiform layer, and PL = photoreceptor layer. All images are in the same scale. The yellow star is given to the device that showed the best performance, a flexible probe based on PaC with a shank width of 50 µm (see details in text).

Chapter 8

Conclusions and outlook

Visual prostheses that perform electrical stimulation of the retina have shown meaningful progress in the restoration of useful vision in blind patients that suffer from retinal degenerative diseases [6], [7], [71]. With the aim to improve the performance of retinal implants during ES, the BiMEA consortium proposed a bidirectional communication strategy in which a closed loop feedback system between the retina and a prosthetic device is aimed, so that the electrical activity of the retina is tracked during the ES therapy. Thus, multi-shank and multi-site penetrating MEAs, named BiMEAs, were proposed to reach different retinal depths using dual purpose electrodes, capable of performing electrical stimulation while recording the electrical activity of the retina [10], [13], [24], [25]. The work presented in this thesis developed further the concept of a BiMEA probe, showing not only the potential use of such devices for retinal applications, but approaching the idea of a future intraretinal implant.

To this end, the first generation of BiMEA probes, which were based on Si, were employed to perform a proof of concept, thereby showing in chapter 4 the feasibility of using the penetrating BiMEAs to establish a bidirectional communication between a prosthetic device and the retina. Hence, access to different retinal layers, assurance of the vitality of the tissue during insertion, recording of physiological behaviors, and simultaneous recording and ES of the retina using safe stimulation parameters were demonstrated [13]. Nonetheless, preliminary assessments of the insertion trauma induced by such devices revealed that the Si shanks, in combination of exogenous compression forces (e.g.: contact with stiff carriers or micromotion) can amplify the trauma on the tissue.

In order to go a step further in the development of potential intraretinal implants, chapter 5 unveiled the design and fabrication strategies of the development of the second generation of BiMEA probes, flexible BiMEAs, which aimed a cross-sectional reduction of the device and the use of materials that diminish FBRs when used in long-term applications. Ergo, the development was focused on optimizing the dimensions of the penetrating shanks and using tissue-like materials, such as PI and PaC, to tally the anatomy of the retina and better match the mechanical properties of the target tissue. Additionally, considering the dual functionality of the probes, appropriate electrode coatings, such as IrO_x and PEDOT: PSS, were tested and characterized, showing the former appropriate electrochemical properties for neuronal recording and stimulation and the latter a door for further improvement for its implementation in future flexible BiMEAs.

Furthermore, considering the flexibility of the materials used, the insertion feasibility of flexible BiMEAs was unknown. Thus, an intraretinal insertion model was established to demonstrate theoretically that optimized dimensions. The latter comprised mainly a reduction of the width and the effective length of the penetrating shanks, allowing in turn the insertion of the penetrating shafts into the retina without the need of an insertion aid, as it is commonly used in intracortical applications [65]. Moreover, the insertion of flexible BiMEAs was tested successfully using initially a phantom tissue that mimicked the mechanical properties of the retina, and was proved *in vitro* in chapter 6 in healthy and degenerated retinas after performing an adjustment to the intraretinal insertion parameters that were previously established for the first generation of BiMEAs. Hence, the use of a long insertion step followed by micro-steps showed to be appropriate for the successful insertion and correct positioning of intraretinal devices. Even so, further characterization comprising the measurement of intraretinal insertion forces and dimpling should be performed in the future to optimize the insertion protocol of intraretinal probes.

Additionally, chapter 6 exposed the successful use of flexible BiMEAs *in vitro*. Here, artifact-free recordings upon optical stimulation were exposed, in contrast to Si-BiMEAs which showed light-induced artifacts. These findings open the door to combine in the future optical modalities to modulate the neural activity of the retina. Moreover, CCS was performed to explore the charge injection limits of intraretinal stimulations, thereby revealing significant excitatory and inhibitory responses of the retina. Nonetheless, the low excitability of degenerated retinas imply that a wider range of current strengths should be tested. Likewise, voltage transients measured within the retina revealed that the CIC of the electrodes was reduced, suggesting the necessity to enhance the electrochemical properties of the electrodes. Thus, the latter can be achieved from a fabrication point of view (e.g.: coating thickness, materials [127], [231]) or from the implementation of different stimulation strategies (e.g: anodic bias [140]).

In chapter 7, the performance of Si and flexible BiMEAs was evaluated, establishing in turn the acute biological impact of intraretinal insertions, the quality of intraretinal recordings, and the success rate of intraretinal insertions. This assessment demonstrated that narrow flexible probes reduced the acute insertion footprint when compared to the initial Si-BiMEA design, showed a good recording quality, and exhibited a high success rate of insertion. While long-term stability tests are still needed, the study presented in this last chapter validated the potential use of flexible BiMEAs for future *in vivo* applications, especially for PaC-based probes.

While there is still a long way for the full restoration of vision, it has been shown that the pursuit of bidirectional intraretinal implants comprehends the implementation of a new generation of implants. These aim for closed loop feedbacks systems capable to provide a deeper insight regarding retinal activity, the efficiency of neuromodulatory therapies like ES, and the understanding of neuromodulatory responses in the retina. Even more, this approach could enable the *in situ* characterization and the automatic adjustment of stimulation parameters.

Thus, the development performed in this work exposed the potential of penetrating neural probes for the implementation of intraretinal implants. In this way, future developments should focus on the implementation of a fully three-dimensional (3D) BiMEA (Figure 8.1a), widening in turn the scope of the implant to reach the 3D space of the retina. To this end, the number of penetrating shanks, hence the number of electrodes, should be increased. From the fabrication perspective, a stack principle (Figure 8.1b) overlaying 2D arrays with spacers in between to generate the desired inter-shank pitch [232], or kirigami and cut-out principles (Figure 8.1c) to build a 3D structure out of a 2D design [233], [234] can be considered.

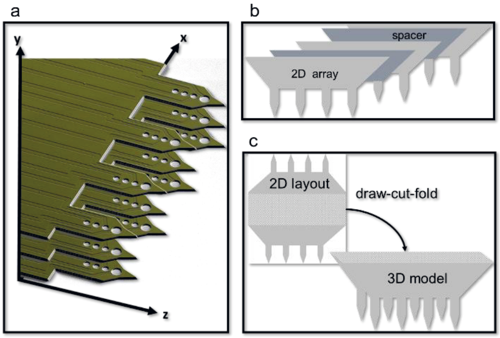

Figure 8.1. Concept of a three-dimensional (3D) intraretinal implant. a) Intraretinal implant covering three spatial axes: *x* and *y*, depending on the number of two-dimensional (2D) overlaid arrays, and *z*, depending on the length of individual shanks. b) 3D assembly out of 2D stacked arrays with spacers in between. c) 3D assembly following kirigami and cut-out principles.

Likewise, the following questions should be addressed for the future implementation of an intraretinal implant: i) What is the number of intraretinal shanks/electrodes required to achieve a functional intraretinal device? ii) How invasive is the method? How to avoid losing a high amount of neuronal tissue? iii) How is such device going to be implanted considering the reduced space that offers the eye? At the moment no answer is certain, yet the following hypotheses can be derived from the literature and the results provided by this thesis.

i) Current retinal implants granted with commercial approval employ a number of stimulating electrodes that go from 60 (Argus II, Second Sight, USA) [8] to 1600 (Alpha-AMS, Retinal Implant AG, Germany) [9], achieving in both cases the recovery of useful vision. The implementation of a bidirectional intraretinal implant comprises an increment of at least 3-fold the number of electrodes of a conventional surface retinal implant. Therefore, as a starting point and to establish a proof of concept of the benefits of such system, one could equate the number of intraretinal shanks with the least number of electrodes available in the market, that is 60 electrodes. The latter implies the implementation of a minimum of 180 electrodes distributed in 60 shanks, each one with two recording and one stimulating electrode.

ii) The use of penetrating neural implants is *per se* a highly invasive method, however, the development of penetrating probes with subcellular shank cross-sections and tissue-like materials have shown seamless integration into the neural tissue [64], [126]. Following this idea and given the reduced shank length needed for intraretinal applications, cross-sectional dimensions of individual shanks can still be optimized to achieve a width of 20 – 30 µm and a thickness of 7 µm, while still enabling a buckling force threshold to suffice the insertion of intraretinal shanks.

iii) The development of an implantation strategy requires joined forces between medical doctors and engineers. On one side, intraretinal probes should comprise a flexible access cable to connect the probe to an external amplification and stimulation system. Additionally, proper tools, such as a temporary stiff shuttle should be considered to give support and drive the implantation, as well as to stabilize the access cable. On the other side, a surgical protocol has yet to be established to enable the insertion of such devices. For example, to facilitate the access to the eye, the implementation of an open-sky surgery [235], in which the cornea and the lens are temporarily removed, could be contemplated, approaching in this way an epiretinal insertion of intraretinal probes akin to insertions performed *in vitro*.

Acknowledgements

I would like to express my gratitude to all my colleagues, friends, and family, who helped me and encouraged me along this journey called PhD. Without your support and input, this work would not have been possible. I would like to thank especially to:

Prof. Dr. Andreas Offenhäusser: Thanks for trusting me and supervising my work, and thanks especially for giving me the opportunity to be part of this great institute, first ICS-8 and now IBI-3. This experience has certainly been of great enrichment to my professional career, and overall has taught me to value interdisciplinary and intercultural work.

Prof. Dr. Sven Ingebrandt: Thanks for the scientific discussions, your input in the paper, and for offering the facilities of IWE-1 to complete part of the fabrication. Special thanks for being my second supervisor.

Prof. Dr. Frank Müller: Thanks for your engagement in supporting my work and facilitating me retinal samples, equipment, and scientific support to complete my retina experiments.

Dr. Jana Gehlen: Thanks for your engagement and your scientific input in all the retina experiments we performed together.

BiMEA group: Thank you all for the hard work and for being the best example of interdisciplinary teamwork!

Kagithiri Srikantharajah: Thanks for being my partner in fabrication. Special thanks for all the collaborative work, for all the input in conferences we went together, and for all the brainstorming and scientific discussions we had.

Dr. Vanessa Maybeck and **Dr. Dirk Mayer:** Thanks for having your door always open and for the willingness to answer questions and help, no matter how basic the question or the problem was. Off course thanks for the scientific input from the biological (Vanessa) and chemical (Dirk) side.

Dr. Bernhard Wolfrum: Thanks for the spontaneous discussions and ideas to solve problems at the time and for the good mood in all summer- and winterschools.

Norbert Wolters: Special thanks for your support and efforts in building and assembling the hybrid headstage. **Dieter Lomparski:** Thanks for adding the necessary changes to the BioMAS software. **Stefan Kirch:** Thanks for solving all software problems. **Fabian Brings and Jan Schnitker:** Thanks for introducing me to the BioMAS.

Bettina Breuer: Big thanks for your support finding lost carbogen bottles, and for your support in the lab and in the institute.

Elke Brauweiler-Reuters, **Dr. Elmar Neumann**, and **Stephany Bunte:** Thanks for your support with SEM. **Elke**, special thanks for all the hard work with SEM images and FIB cuts at the end.

Marko Banzet and Michael Prömpers: Thanks for the cleanroom support and the discussion of processes. **HNF team:** Thanks for supporting and helping out with all cleanroom problems.

Dr. Xuan Thang Vu: Thanks for facilitating the supply of SIROFs.

Dr. Dmitry Kireev: Thanks for introducing me to the cleanroom world, for the collaborative work, and for all the scientific and non-scientific discussions.

Bohdan Lenyk and Pegah Shokoohimehr: Thanks both of you for the scientific and non-scientific discussions; for the ideas that we implemented, the ones we tried, and the ones we didn't; and thanks for the good atmosphere in all our bus trips.

Timm J. J. Hondrich: Danke für unsere zwangslosen Diskussionen über Arbeit, Wissenschaft, Leben, Familie, etc…und natürlich danke, dass du mein Deutsch korrigiert hast und mich es zur Verbesserung motiviert hast.

Lena Nörbel, Erfan Hassani, Gabriela Figueroa, Yuanying Liang, Corinna Meeßen, Christopher Beale, Stefanie Hamacher: Thanks for always being willing to help.

Andreea, Stella, Nouran, Irina: Thanks for helping me when I was a newcomer and for the good memories of our lunch-break discussions.

Zidu, Duc, and Jaqueline: Thanks for your work and efforts in the development of flexible neural probes at IBI-3.

Gabriela, Yurii, Bohdan, Jamal, Lucas, Volodymir, Dmitry, Antonio M., Ihor, Michael P., and Dirk: Thanks for making possible our Bioelectronics' football team!

Former members of ICS-8 and current members of IBI-3: Thanks for creating such an intercultural, interdisciplinary, and homey working environment.

My parents Jaime Rincón Lugo and Esperanza Montes de Rincón: Thanks for the legacy of education and persistence, for the constant support, for the motivation, and the good energies, that even across continents were felt. *Gracias por el legado de la educación y la perseverancia, por el constante apoyo, por la motivación y las buenas energías, que aún desde la distancia se sentían.*

My sisters Catalina, Esperanza, Sofía, and Jimena Rincón Montes: Union means strength. Thanks for being faithful to that precept, because with mutual support we have achieved our goals. *La unión hace la fuerza. Gracias por ser fieles a ese precepto, porque con el apoyo mutuo hemos logrado nuestras metas.*

Andrea Niessen Barth and Juan Carlos Uribe Rivas: Thank you for the good energies and the interest shown in my work. *Gracias por las buenas energías y por la curiosidad mostrada por mi trabajo.*

My husband Miguel Uribe Niessen: Thanks for being always by my side, for encouraging me every day, and supporting me unconditionally. Thanks for everything! *Gracias por estar siempre a mi lado, por motivarme día a día y apoyarme incondicionalmente. ¡Gracias por todo!*

Appendices

Appendix 1: Content and preparation of 1xPBS (Phosphate buffered saline solution)

0.1 M PBS formulation according to recipe provided by Sambrook et al. [236]		
Component	**Concentration**	
NaCl	137 mM	
KCl	2.7 mM	
Na_2HPO_4	10 mM	
KH_2PO_4	2 mM	
Preparation of 1 M PBS (10xPBS) in 1l of Aqua Bidest (double distilled water)		
Component	**Concentration**	**g/l**
NaCl (Sigma Aldrich, S7653)	1370 mM	80.06
KCl (Sigma Aldrich, 60130)	270 mM	20.13
Na_2HPO_4 (Sigma Aldrich, S5011)	100 mM	14.20
KH_2PO_4 (Sigma Aldrich, 795488)	20 mM	2.72
Preparation of 0.1 M PBS (1xPBS) in 1l of Aqua Bidest (double distilled water)		
Component	**ml**	
10xPBS	100	
Aqua Bidest	1000 ml	
Mix and adjust pH to 7.4 with 2M HCl (Sigma Aldrich, 31448) and 1M NaOH (Sigma Aldrich, 320331)		

Appendix 2: Simplified schematic of hybrid headstage

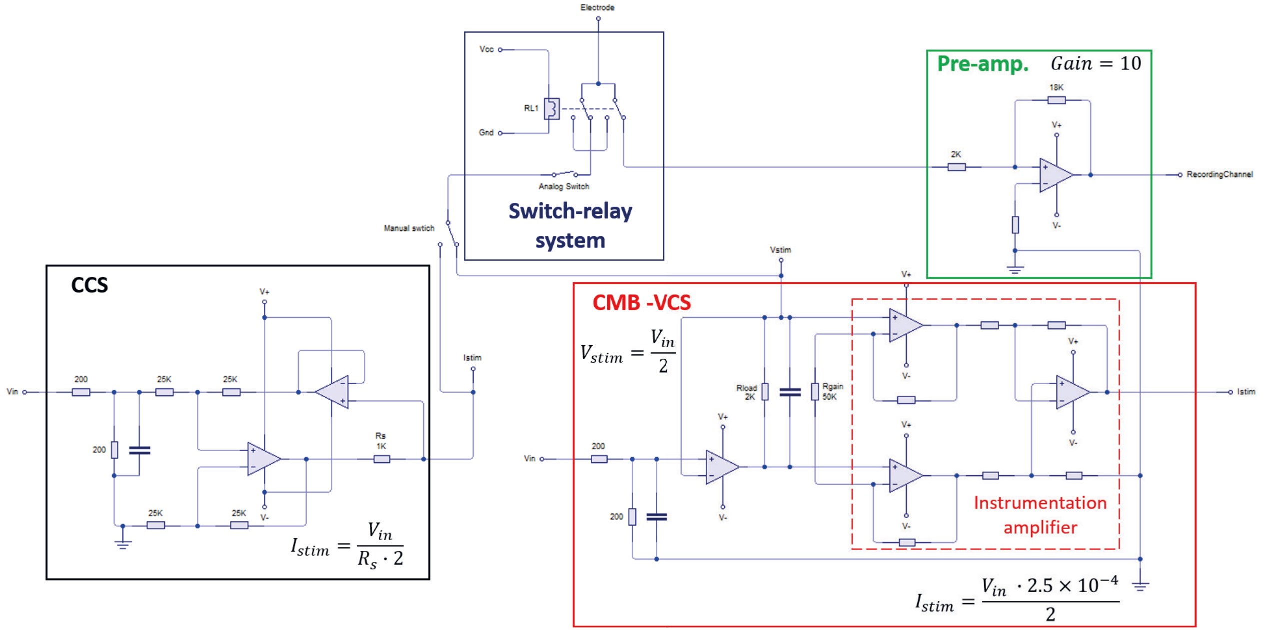

Appendix 3: Content and preparation of Ames' medium

Ames' medium formulation (Sigma Aldrich, Germany)	
Component	**g/l**
Inorganic Salts	
Calcium Chloride	0.1275
Magnesium Sulfate	0.1488
Potassium Chloride	0.231
Potassium Phosphate Monobasic (anhydrous)	0.068
Sodium Chloride	7.01
Amino Acids	
L-Alanine	0.0024
L-Arginine • HCl	0.00421
L-Asparagine (anhydrous)	0.00084
L-Aspartic Acid	0.00012
L-Cystine • 2HCl	0.000065
L-Glutamine	0.073
L-Glutamic Acid (sodium)	0.001183
Glycine	0.00045
L-Histidine • HCl • H_2O	0.002513
L-Isoleucine	0.00058
L-Leucine	0.00144
L-Lysine • HCl	0.003648
L-Methionine	0.00039
L-Phenylalanine	0.00132
L-Proline	0.00007
L-Serine	0.00252
L-Taurine	0.00075
L-Threonine	0.00333
L-Tryptophan	0.00049
L-Tyrosine • 2Na • $2H_2O$	0.00211
L-Valine	0.00176
Vitamins	
Ascorbic Acid • Na	0.01796
D-Biotin	0.0001
Choline Chloride	0.0007
Folic Acid	0.0001
myo-Inositol	0.0272
Niacinamide	0.0001
D-Pantothenic Acid (hemicalcium)	0.0001
Pyridoxal • HCl	0.0001
Riboflavin	0.00001
Thiamine • HCl	0.0001
Other	
Cytidine	0.00073
D-Glucose	1.081
Hypoxanthine	0.00082
Pyruvic Acid (sodium)	0.01333
Thymidine	0.00024
Uridine	0.00073
Preparation	
Ames' medium (A1420, Sigma Aldrich)	1 bottle (8.8 g/l)
Sodium bicarbonate ($NaHCO_3$) (S5761, Sigma Aldrich)	1.9 g/l
Distilled water	1 l
A bottle of Ames' medium and the sodium bicarbonate were dissolved in distilled water. The solution was oxygenated with carbogen gas containing 95% O_2 and 5% CO_2 (The Linde Group, Germany) for at least 30 mins. The pH was adjusted to 7.4.	

Appendix 4: Significant responses in wildtype retina during VCS

ES parameter	Electrical stimulation efficiency (ESE)											
ES-1 (0.8 mV - 0.5 ms)	**Pulse**	**Shank3**			**Shank2**				**Shank1**			
		3.4***	3.3***	3.2***	2.4*	2.3*	2.2	2.1	1.4	1.3	1.2	1.1
	p1	3.78	5.14	3.75	0.00	0.00	1.11	0.00	0.00	0.00	0.00	0.00
	p2	5.95	6.47	5.16	0.00	1.25	0.95	1.18	2.67	1.43	20.00	NA
	p3	6.67	7.41	6.36	1.05	0.69	1.21	0.95	0.00	0.00	0.00	0.00
	p4	5.71	6.06	5.00	0.00	0.00	1.74	0.00	1.00	4.44	20.00	NA
	p5	6.67	6.15	9.47	0.00	0.80	1.94	2.00	0.00	2.50	0.00	NA
	p6	4.44	5.71	5.16	0.95	0.00	0.00	0.00	6.67	1.67	0.00	NA
	mean	**5.54**	**6.16**	**5.82**	**0.33**	**0.46**	**1.16**	**0.69**	**1.72**	**1.67**	**6.67**	**0.00**
	SD	**1.18**	**0.76**	**1.97**	**0.52**	**0.53**	**0.68**	**0.83**	**2.64**	**1.67**	**10.33**	**0.00**
ES-2 (0.8 mV - 0.6 ms)	**Pulse**	**Shank3**			**Shank2**				**Shank1**			
		3.4**	3.3***	3.2**	2.4	2.3	2.2	2.1	1.4	1.3	1.2	1.1
	p1	2.22	3.38	2.67	0.00	1.74	1.54	2.35	1.05	1.67	10.00	NA
	p2	3.10	3.28	2.76	1.05	0.91	0.83	0.00	1.00	2.50	0.00	0.00
	p3	2.86	3.25	2.54	0.00	0.00	1.05	0.00	2.00	0.00	0.00	0.00
	p4	4.29	3.46	4.55	1.33	1.67	3.75	5.71	6.00	10.00	20.00	NA
	p5	7.06	7.27	7.44	1.67	0.00	0.00	2.22	0.00	0.00	0.00	NA
	p6	3.33	3.61	3.82	1.25	1.90	1.18	4.62	5.00	2.86	0.00	0.00
	mean	**3.81**	**4.04**	**3.96**	**0.88**	**1.04**	**1.39**	**2.48**	**2.51**	**2.84**	**5.00**	**0.00**
	SD	**1.73**	**1.59**	**1.88**	**0.71**	**0.87**	**1.26**	**2.34**	**2.42**	**3.71**	**8.37**	**0.00**
ES-3 (0.6 mV - 0.5 ms)	**Pulse**	**Shank3**			**Shank2**				**Shank1**			
		3.4**	3.3***	3.2***	2.4	2.3	2.2	2.1	1.4	1.3	1.2	1.1
	p1	9.09	8.33	6.67	3.53	2.11	1.54	0.00	0.00	0.00	0.00	NA
	p2	6.67	7.27	6.67	2.22	1.00	2.11	0.00	0.00	0.00	0.00	0.00
	p3	2.86	5.45	3.33	0.00	1.43	0.87	0.00	0.00	0.00	0.00	NA
	p4	23.33	23.33	16.00	1.43	1.43	1.25	2.50	0.00	0.00	0.00	NA
	p5	10.91	8.57	8.89	6.67	3.64	1.54	2.22	3.08	0.00	0.00	NA
	p6	8.75	7.50	6.67	1.18	0.00	2.50	2.86	0.00	0.00	0.00	NA
	mean	**10.27**	**10.08**	**8.04**	**2.50**	**1.60**	**1.63**	**1.26**	**0.51**	**0.00**	**0.00**	**NA**
	SD	**6.97**	**6.59**	**4.29**	**2.35**	**1.21**	**0.59**	**1.40**	**1.26**	**0.00**	**0.00**	**NA**
ES-4 (0.6 mV - 0.6 ms)	**Pulse**	**Shank3**			**Shank2**				**Shank1**			
		3.4**	3.3**	3.2*	2.4*	2.3	2.2	2.1	1.4	1.3	1.2	1.1
	p1	3.11	4.29	3.41	0.00	1.05	1.54	0.00	0.00	0.00	NA	NA
	p2	4.33	5.26	5.77	1.33	0.00	2.50	0.00	0.00	0.00	NA	NA
	p3	2.22	2.89	2.19	0.00	0.00	0.00	0.00	2.22	0.00	0.00	NA
	p4	1.60	1.46	1.41	0.00	0.00	0.00	0.00	0.00	0.00	0.00	0.00
	p5	1.56	1.75	1.44	0.00	2.86	2.22	0.00	0.00	0.00	0.00	NA
	p6	1.22	1.59	1.36	0.00	0.00	1.11	0.00	0.00	0.00	0.00	NA
	mean	**2.34**	**2.87**	**2.60**	**0.22**	**0.65**	**1.23**	**0.00**	**0.37**	**0.00**	**0.00**	**NA**
	SD	**1.18**	**1.59**	**1.74**	**0.54**	**1.16**	**1.07**	**0.00**	**0.91**	**0.00**	**0.00**	**NA**
ES-5 (0.6 mV - 0.7 ms)	**Electrical stimulation efficiency (ESE)**											
	Pulse	**Shank3**			**Shank2**				**Shank1**			
		3.4*	3.3*	3.2	2.4	2.3	2.2	2.1	1.4	1.3	1.2	1.1
	p1	0.70	0.92	0.44	0.00	3.08	0.00	4.00	0.00	0.00	0.00	0.00
	p2	5.66	5.71	4.39	5.00	2.86	2.00	3.33	0.00	0.00	0.00	NA
	p3	2.86	2.40	1.70	0.00	0.00	1.82	2.86	0.00	0.00	0.00	NA
	p4	5.79	5.95	4.71	3.33	4.29	8.00	0.00	0.00	0.00	0.00	0.00
	p5	10.67	10.71	11.43	1.43	0.00	1.54	0.00	1.18	1.43	5.00	0.00
	p6	4.06	3.78	4.13	1.18	2.86	1.00	2.86	1.54	0.00	20.00	0.00
	mean	**4.96**	**4.91**	**4.47**	**1.82**	**2.18**	**2.39**	**2.17**	**0.45**	**0.24**	**4.17**	**0.00**
	SD	**3.38**	**3.43**	**3.81**	**1.98**	**1.77**	**2.84**	**1.74**	**0.71**	**0.58**	**8.01**	**0.00**
ES-6 (0.6 mV - 0.8 ms)	**Pulse**	**Shank3**			**Shank2**				**Shank1**			
		3.4**	3.3**	3.2	2.4	2.3	2.2	2.1	1.4	1.3	1.2	1.1
	p1	1.73	1.79	1.79	2.22	1.90	1.67	0.00	3.08	0.00	0.00	0.00
	p2	2.26	2.62	2.75	0.00	0.00	0.00	0.00	2.50	3.64	10.00	NA
	p3	2.86	2.62	2.81	2.67	1.67	4.29	4.00	2.00	3.33	0.00	0.00
	p4	2.20	2.12	2.15	1.00	1.67	1.33	4.00	0.00	0.00	0.00	0.00
	p5	1.40	1.27	1.36	0.00	1.18	1.00	0.00	1.25	3.33	5.00	NA
	p6	1.70	1.43	1.47	2.22	2.50	1.25	4.00	0.00	0.00	0.00	0.00
	mean	**2.02**	**1.98**	**2.05**	**1.35**	**1.49**	**1.59**	**2.00**	**1.47**	**1.72**	**2.50**	**0.00**
	SD	**0.52**	**0.58**	**0.63**	**1.19**	**0.85**	**1.44**	**2.19**	**1.29**	**1.88**	**4.18**	**0.00**

The average and the standard deviation (SD) of the electrical stimulation efficiency (ESE) of each recording electrode after six electrical stimuli (p1-p6) is displayed for the six stimulation trials (ES-1 – ES-6) performed in the retinal sample exhibited in Figure 4.13. Significant stimulations are depicted by stars (* for p <= 0.05, ** for p <= 0.01 *** for p <= 0.001) after performing paired t-tests to the firing rate before and after the stimulation. Electrodes that presented a significant excitatory effect (ESE >1) are marked in dark green, and those with a significant inhibitory effect (ESE <1) are marked with light green. “NA” stands for not applicable, indicating the cases where no activity was detected.

Appendix 5: Significant responses in *rd10* retina during VCS

ES parameter	**Electrical stimulation efficiency (ESE)**															
ES-2 (0.8 mV - 0.6 ms)	**Pulse**	**Shank4**				**Shank3**				**Shank2**				**Shank1**		
		4.4	***4.3***	***4.2***	***4.1***	***3.4***	***3.3***	***3.2****	***3.1***	***2.4***	***2.3***	***2.2*****	***2.1****	***1.4******	***1.3******	***1.2******
	p1	4.00	1.08	1.05	1.36	5.00	2.58	2.26	1.36	0.00	1.43	1.30	1.43	2.06	2.36	2.38
	p2	3.08	1.48	1.77	1.51	0.00	3.81	2.82	1.66	6.67	6.67	3.23	2.90	2.29	2.77	2.82
	p3	1.43	1.54	0.78	0.48	0.00	1.00	0.51	0.76	0.00	0.87	1.76	1.10	2.08	1.85	2.11
	p4	5.71	1.60	0.96	0.92	13.33	5.45	2.22	1.30	0.00	2.86	1.48	1.68	2.40	2.69	2.76
	p5	2.22	0.67	1.57	2.24	6.67	0.74	2.04	1.35	20.00	1.82	2.46	2.83	1.82	2.34	2.84
	p6	1.82	1.57	0.96	0.82	20.00	1.11	2.05	1.26	20.00	3.81	2.90	3.03	2.52	2.85	3.54
	mean	**3.04**	**1.32**	**1.18**	**1.22**	**7.50**	**2.45**	**1.98**	**1.28**	**7.78**	**2.91**	**2.19**	**2.16**	**2.19**	**2.48**	**2.74**
	SD	**1.60**	**0.37**	**0.39**	**0.62**	**7.87**	**1.88**	**0.78**	**0.29**	**9.81**	**2.12**	**0.79**	**0.85**	**0.25**	**0.37**	**0.49**
ES-3 (0.6 mV - 0.5 ms)	**Pulse**	**Shank4**				**Shank3**				**Shank2**				**Shank1**		
		4.4	***4.3***	***4.2***	***4.1***	***3.4***	***3.3***	***3.2****	***3.1***	***2.4***	***2.3***	***2.2*****	***2.1****	***1.4******	***1.3******	***1.2******
	p1	0.00	1.00	0.71	0.79	0.00	0.00	1.00	0.71	0.00	1.11	0.93	1.64	1.72	1.98	2.14
	p2	2.00	0.41	0.85	0.85	0.00	0.00	0.89	0.78	0.00	0.95	2.03	1.15	0.92	1.01	1.33
	p3	0.00	1.05	2.11	1.41	0.00	1.36	0.74	1.03	0.00	0.63	1.98	1.93	1.71	1.84	2.02
	p4	0.00	1.00	1.23	1.03	0.00	2.22	1.72	0.78	10.00	2.22	2.31	2.56	1.54	1.68	1.90
	p5	1.54	0.00	0.44	0.56	0.00	0.00	0.35	0.71	0.00	0.77	1.69	1.26	1.14	1.24	0.90
	p6	0.00	0.39	0.51	0.55	20.00	0.59	0.51	0.65	0.00	2.67	1.71	1.71	1.42	1.68	1.54
	mean	**0.59**	**0.64**	**0.97**	**0.86**	**3.33**	**0.70**	**0.87**	**0.78**	**1.67**	**1.39**	**1.77**	**1.71**	**1.41**	**1.57**	**1.64**
	SD	**0.93**	**0.44**	**0.62**	**0.32**	**8.16**	**0.92**	**0.48**	**0.13**	**4.08**	**0.84**	**0.47**	**0.51**	**0.32**	**0.37**	**0.47**
ES-6 (0.6 mV - 0.8 ms)	**Pulse**	**Shank4**				**Shank3**				**Shank2**				**Shank1**		
		4.4	***4.3***	***4.2***	***4.1***	***3.4***	***3.3***	***3.2****	***3.1***	***2.4***	***2.3***	***2.2*****	***2.1****	***1.4******	***1.3******	***1.2******
	p1	0.00	0.92	0.86	1.11	0.00	2.31	2.37	1.68	5.00	6.00	2.18	2.29	1.85	2.11	2.03
	p2	4.00	1.14	1.50	1.12	0.00	2.07	1.10	1.96	10.00	0.95	2.05	1.40	1.87	1.91	2.11
	p3	1.43	2.26	1.22	0.87	0.00	0.67	1.27	3.27	0.00	2.00	1.39	1.27	2.02	2.09	2.12
	p4	2.86	1.05	1.49	1.51	NA	3.48	1.47	1.60	0.00	4.00	2.06	3.26	2.76	2.61	2.87
	p5	0.00	0.43	0.94	1.04	Inf	3.33	2.73	0.90	0.00	5.00	2.90	1.34	2.52	2.68	2.93
	p6	0.00	0.67	0.75	1.04	0.00	0.00	2.22	1.26	NA	2.50	3.16	2.53	2.08	2.38	2.73
	mean	**1.38**	**1.08**	**1.13**	**1.11**	**0.00**	**1.98**	**1.86**	**1.78**	**3.00**	**3.41**	**2.29**	**2.02**	**2.18**	**2.29**	**2.46**
	SD	**1.72**	**0.63**	**0.32**	**0.21**	**0.00**	**1.40**	**0.67**	**0.82**	**4.47**	**1.92**	**0.64**	**0.81**	**0.37**	**0.31**	**0.42**

The average and the standard deviation (SD) of the electrical stimulation efficiency (ESE) of each recording electrode after six electrical stimuli (p1-p6) is displayed for the three stimulation trials (ES-2, ES-3, and ES-6) performed in the retinal sample exhibited in Figure 4.14. Significant stimulations are depicted by stars (* for p <= 0.05, ** for p <= 0.01 *** for p <= 0.001) after performing paired t-tests to the firing rate (FR) before and after the stimulation. Electrodes that presented a significant excitatory effect (ESE >1) are marked in dark green, and those with a significant inhibitory effect (ESE <1) are marked with light green. “NA” stands for not applicable, indicating the cases where no activity was detected, and “Inf” shows the case when the FR after the electrical stimuli was increased but not activity was present before the stimulation.

Appendix 6: Microfabrication recipes

A.6.1. Sacrificial metal layer

- Machine: Balzer PLS 570 (e-beam assisted evaporation)
- Ar sputtering, recipe 1 (150 V, 5A), 1 min
- Metal layers: Cr/Au/Cr (10 nm /100 nm/50 nm)
- Deposition rate:
  - Cr = 0.3 nm/s
  - Au = 0.5 nm/s

A.6.2. Polymer deposition

Polyimide (PI)

- Deposition of sacrificial metal layer (details in A.6.1)
- Dehydration:
  - @150°C, 10 min on hot plate
  - Let the wafer to cool down to room temperature
- Spin-coating:
  - VM-652 (3ml) @5000 rpm, 60 s, closed lid
  - PI-2610 or PI-2611 @ desired (see Table A.6. 1) rpm for 30 or 60 s, closed lid

Table A.6. 1. Spin-speed - Thickness relation for PI-2611 and PI-2610. NM stands for not measured. [a] Given by the supplier.

Spin-speed [rpm]	**PI-2611**			**PI-2610**	
	Datasheet [a] ***(30 s)***	***Measured (30 s)***	***Measured (60 s)***	***Datasheet*** [a] ***(30 s)***	***Measured (30 s)***
2000	8.5-9	NM	NM	2.6	3.3
3000	6	NM	4	1.8	NM
4000	4.5-5	NM	3	1.4	NM
5000	3.5-4	3.6	2.5	1.2	1.35

- Soft-bake:
  - @120°C, 4 min, slow ramp on proximity hot plate
- Curing:
  - Use convection oven in a nitrogen environment
  - Temperature ramp:
    - 200°C @4°C/min, hold temperature for 30 min
    - 350°C @2.5°C/min, hold temperature for 30 min
    - Cool down to room temperature @2.5°C/min

Parylene-C (PaC)

- Machine: PDS 2010 LABCOATER 2
- Adhesion promoter (optional)
  - Use only to enhance the adhesion of PaC with another PaC layer or any other substrate

  - Apply silane A-174 via chamber swipe method: Add ~ 1 ml of silane into a petri dish and use a cue tip to apply the silane around the walls of the coating chamber
- PaC dimer and coating thickness relation is ~ 6 g: 3 µm. The measured thicknesses for different dimer mass are displayed in Figure A.6. 1:

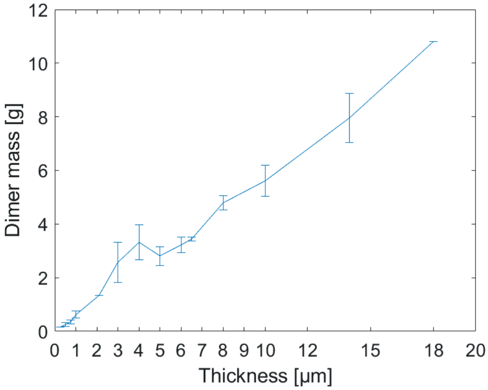

Figure A.6. 1. Parylene-C dimer mass vs. Thickness relation. Measured thicknesses after experimental use of the PaC coater.

- Deposition parameters in Table A.6. 2:

Table A.6. 2. Parameters for CVD of parylene-C.

Expected thickness [µm]	Deposition parameters			Comments
	Vacuum		Vaporizer	
	PLA1	*SP*	*PhA1*	
2 – 10	15	25	174 or 160	If pump and vacuum sensor are in optimal conditions
	20	25	160	If process does not reach PLA1=15
< = 1	7 or 8	10	174 or 160	Thin layers

A.6.3. Metallization

- Dehydration:
  - @150°C, 5 min on hot plate
  - Let the wafer to cool down to room temperature
- Surface activation (only for PaC coated wafers):
  - Machine: TePl Gigabatch 360
  - Gas/Flow: O_2 plasma, 80 sccm
  - Power/Time: 50 W, 2 min
  - Use Faraday cage
- Spin-coating:
  - LOR3B (5 ml) @3000 rpm, 30 s, closed lid, disperse around the whole wafer
- Soft-bake:
  - @150°C, 5 min on hot plate
- Spin-coating:
  - nLOF2020 (4 ml) @3000 rpm, 30 s, closed lid

- Soft-bake:
    - @110°C, 1 min on hot plate
- Exposure:
    - Machine: Süss MA8/BA8 (MA4)
    - Dose: 40 mJ/cm^2 (i-line)
- Post-exposure bake:
    - @ 110°C, 1 min on hot plate
- Development:
    - AZ 326 MIF for 33-35 s
    - Rinse in water cascade
    - Spin dry using N_2 gun
- Deposition of metal layer:
    - Machine: Balzer PLS 570 (e-beam assisted evaporation)
    - Ar sputtering, recipe 3 (100 V, 7 A), 1 min
    - Metal layers of choice
    - Deposition rate:
        - Ti = 0.1 nm/s
        - Au = 0.5 nm/s
        - Pt = 0.5 nm/s
- Lift-off:
    - Immerse wafer in acetone for 2-3 h for PaC or overnight for PI
    - Use a pipette to help remove metal residues
    - Rinse in isopropanol
    - Dry with N_2 gun
- Removal of LOR3B:
    - Immerse wafer in AZ 326 MIF for 5 min
    - Rinse in water cascade
    - Spin dry using N_2 gun

A.6.4. IrO_x coating

Performed for the deposition or SIROFs.

- Dehydration:
    - @150°C, 5 min on hot plate
    - Let the wafer to cool down to room temperature
- Surface activation (only for PaC coated wafers):
    - Machine: TePl Gigabatch 360
    - Gas/Flow: O_2 plasma, 80 sccm
    - Power/Time: 50 W, 2 min
    - Use Faraday cage
- Spin-coating:
    - LOR3B (5 ml) @2000 rpm, 30 s, closed lid, disperse around the whole wafer

- Soft-bake:
    - @150°C, 5 min on hot plate
- Spin-coating:
    - nLOF2020 (4 ml) @2000 rpm, 30 s, closed lid
- Soft-bake:
    - @110°C, 1 min on hot plate
- Exposure:
    - Machine: Süss MA8/BA8 (MA4)
    - Dose: 40 mJ/cm^2 (i-line)
- Post-exposure bake:
    - @ 110°C, 1 min on hot plate
- Development:
    - AZ 326 MIF for 33-35 s
    - Rinse in water cascade
    - Spin dry using N_2 gun
- Deposition of SIROF:
    - DC sputtering deposition performed at the cleanroom facility at IWE-1, RWTH Aachen University
    - Ar cleaning for 2 min
    - Sputtering parameters shown in Table A.6. 3

Table A.6. 3. Deposition parameters for second metallization.

Metal target	**Ar [sccm]**	**O_2 [sccm]**	**DC power [W]**
Ti	55	-	250
Pt	75	-	100
Ir	100	6	100

- Lift-off:
    - Immerse wafer in acetone for 2-3h for PaC or overnight for PI
    - Use a pipette to help remove metal residues
    - Rinse in isopropanol
    - Dry with N_2 gun
- Removal of LOR3B:
    - Immerse wafer in AZ 326 MIF for 5 min
    - Rinse in water cascade
    - Spin dry using N_2 gun

A.6.5. Structure polymer layer

Surface pre-treatment

- Dehydration:
    - Dehydrate the wafer on a hot plate @150°C for 5 min and let the wafer to cool down
- Surface activation (only for PaC coated wafers):

  - Machine: TePl Gigabatch 360
  - Gas/Flow: O_2 plasma, 80 sccm
  - Power/Time: 50 W, 2 min
  - Use Faraday cage

Etch mask

Note$_1$: Use an etch mask at least 1.5 times thicker than the thickness of the polymer to be etched

Note$_2$: The recipes are given for the photoresist AZ 9260; however, the latter is no longer available. The supplier MicroChemicals GmbH (Germany) offers in replacement the photoresist AZ 10XT, which can be used with the same processing parameters as AZ 9260.

Etch mask 5-10 µm thick:

- Spin-coating:
  - AZ 9260 (5 ml) @ desired (see Table A.6. 4) rpm for 60 s, closed lid

Table A.6. 4. Spin-speed - Thickness relation for AZ 9260. NA stands for not available. [a] Given by the supplier.

Spin-speed [rpm]	**Photoresist thickness [µm]**	
	Datasheet [a]	***Measured***
2000	11.4	9.132 ± 0.138
3000	8.8	7.287 ± 0.057
4000	NA	6.311 ± 0.077
5000	NA	5.638 ± 0.03

- Soft-bake:
  - @110°C, 3 min on hot plate
- Exposure:
  - Machine: Süss MA8/BA8 (MA4)
  - Dose: 900 mJ/cm^2 (i-line)
- Development:
  - AZ 326 MIF for 9-10 min or AZ 400K 1:4 (with deionized water) for 2-4 min
  - Rinse in water cascade
  - Spin dry using N_2 gun

Etch mask 20 µm thick:

- Spin-coating:
  - AZ 9260 (5 ml) @2400 rpm for 60 s, closed lid
- Soft-bake:
  - @110°C, 80 s on hot plate
- Spin-coating:
  - AZ 9260 (5 ml) @2100 rpm for 60 s, closed lid
- Soft-bake:
  - @110°C, 160 s on hot plate
- Exposure:
  - Machine: Süss MA8/BA8 (MA4)

  - Dose: 2100 mJ/cm^2 (i-line)
- Development:
  - AZ 326 MIF for 15-20 min or AZ 400K 1:4 (with deionized water) for 4-7 min
  - Rinse in water cascade
  - Spin dry using N_2 gun

Edge mask:

- Make sure the edges of the wafer are resist-free, use a cue tip with acetone to remove any resist residues after development
- Deposit a metal ring at the edges of the wafer to avoid transfer problems after RIE
  - Shadow mask: For a 4 inch wafer, use an Al plate with a dimeter of 90 mm to cover the center of the wafer
  - Machine: Balzer PLS 570 (e-beam assisted evaporation)
  - Metal layer: Ti (100 nm)
  - Deposition rate of Ti = 0.1 nm/s

RIE

- Parameters of RIE process to etch PI or PaC are given in Table A.6. 5:

Table A.6. 5. RIE recipe to etch PI or PaC.

Machine	Oxford PL 100 / ICP (RIE-7)
RF power [W]	50
ICP power [W]	500
O_2 [sccm]	36
CF_4 [sccm]	4
Cryo Temp [°C]	10
Strike pressure	0.03
He backing pressure [mbar]	12
He backing flow [sccm]	20
Etch rate PI [µm/min]	600
Etch rate PaC [µm/min]	800
Etch rate AZ 9260 [µm/min]	760

A.6.6. Ti etch stop layer

- Parameters of RIE process to etch Ti etch stop layer are given in Table A.6. 6:

Table A.6. 6. RIE recipe to etch Ti etch stop layer.

Machine	Oxford PL 100 / ICP (RIE-7)
RF power [W]	150
ICP power [W]	-
O_2 [sccm]	20
Ar [sccm]	20
Cryo Temp [°C]	10
Strike pressure	0.045
He backing pressure [mbar]	10
He backing flow [sccm]	20
Etch rate Ti [nm/min]	6.6-10

A.6.7. Sacrificial PaC layer

- Dehydration:
  - @150°C, 5 min on hot plate
  - Let the wafer to cool down to room temperature
- Spin-coating:
  - 2% v/v Micro-90 (5ml) @1000 rpm, 20 s, closed lid
- Soft-bake
  - @90°C, 2 min on hot plate
- PaC deposition with a thickness of ~ 2-2.5 µm, apply silane (details in A.6.2. Polymer deposition)

A.6.8. PEDOT: PSS coating

- Prepare PEDOT: PSS solution as described in section 3.1.3
- Surface activation:
  - Machine: TePl Gigabatch 360
  - Gas/Flow: O_2 plasma, 80 sccm
  - Power/Time: 50 W, 2 min
  - Use Faraday cage
- Spin-coating:
  - PEDOT: PSS (5 ml) @3000 rpm for 30 s, closed lid
- Soft-bake:
  - @110°C, 1 min on hot plate
- Spin-coating:
  - PEDOT: PSS (5 ml) @1000 rpm for 30 s, closed lid
- Soft-bake:
  - @110°C, 1 min on hot plate
- Peel-off sacrificial layer:
  - Peel edges with a tweezer
  - Put drops of water at the edge of the sacrificial layer
  - Wait until the sacrificial layer loosens
  - Gently remove sacrificial layer with tweezers
- Removal of PEDOT: PSS from contact pads (only process A)
  - Use a wet cue tip to physically remove the coating from the contact pads
- Hard-bake:
  - @140°C, 1 h on hot plate
- Immerse wafer in deionized water

A.6.9. Wet chemical etch mask

Note: Use AZ 1505 or AZ 1518 (MicroChemicals GmbH, Germany) in further developments to avoid resist residues after wet chemical etching

- Dehydration:
    - @150°C, 10 min on hot plate
    - Let the wafer to cool down to room temperature
- Spin-coating:
    - AZ 5214E (3 ml) @3000 rpm for 30 s, closed lid
- Soft-bake:
    - @110°C, 1 min on hot plate
- Exposure:
    - Machine: Süss MA8/BA8 (MA4)
    - Dose: 50 mJ/cm^2 (i-line)
- Development:
    - AZ 326 MIF for 60-70 s
    - Rinse in water cascade
    - Spin dry using N_2 gun

Table A.6. 7. Chemical reagents.

Chemical reagent	Supplier	Country
PI-2611	HD MicroSystems	Germany
PI-2610	HD MicroSystems	Germany
VM-652	HD MicroSystems	Germany
PaC dimer (DPX-C)	Specialty Coating Systems	USA
Silane A-174	Specialty Coating Systems	USA
AZ 9260	MicroChemicals GmbH	Germany
AZ 326 MIF	MicroChemicals GmbH	Germany
AZ 400 K	MicroChemicals GmbH	Germany
LOR3B	MicroChem Corp	USA
nLOF 2020	MicroChemicals GmbH	Germany
AZ 5214E	MicroChemicals GmbH	Germany
PH1000 (PEDOT: PSS)	Heraeus Clevios GmbH	Germany
DMSO	Sigma-Aldrich	Germany
GOPS	Sigma-Aldrich	Germany
Cr etchant	Sigma-Aldrich	Germany

Appendix 7: Fabrication protocol of flexible BiMEAs

Flexible IrO_x BiMEAs – Process A

- **Host substrate:** 4-inch Si wafer
- **Flexible substrate layer:** First flexible layer with a thickness of 3 µm (details in A.6.2. Polymer deposition)
- **First metallization:** 10/100 nm of Ti/Au or Ti/Pt (details in A.6.3. Metallization)
- **Flexible passivation layer:** Second flexible layer with a thickness of 3 µm, apply adhesion promoter (details in A.6.2. Polymer deposition)
- **Passivation openings:** Etch electrode and contact pad openings, use an etch mask 7 µm thick (details in A.6.5. Structure polymer layer)
- **SIROF deposition:** Sputter 10/100/250 nm or 10/100/500 nm of Ti/Pt/Ir (details in A.6.4. IrO_x coating)
- **Shape:** Etch shape of probe, use an etch mask 10 µm thick (details in A.6.5. Structure polymer layer)
- **Release:**
    - PI:
        - Dice the wafer into sections to facilitate the release of small groups of probes
        - Use Cr etchant solution for ~ 40 min and rinse released probes in three phases of MilliQ water
    - PaC: Use droplets of water to facilitate the release using tweezers

Flexible IrO_x BiMEAs – Process B

- **Host substrate:** 4-inch Si wafer
- **Flexible substrate layer:** First flexible layer with a thickness of 3 µm (details in A.6.2. Polymer deposition)
- **First metallization:** 10/100 nm of Ti/Au or Ti/Pt (details in A.6.3. Metallization)
- **Flexible interlayer:** Second flexible layer with a thickness of 1-1.5 µm, apply adhesion promoter (details in A.6.2. Polymer deposition)
- **Interlayer opening:** Etch electrode and contact pad openings, use an etch mask 7 µm thick (details in A.6.5. Structure polymer layer)
- **SIROF deposition:** Sputter 10/100/250/10 nm of Ti/Pt/Ir/Ti (details in A.6.4. IrO_x coating)
- **Flexible passivation layer:** Third flexible layer with a thickness of 1-1.5 µm, apply adhesion promoter (details in A.6.2. Polymer deposition)
- **Passivation openings and shape:** Etch shape, electrode, and contact pad openings, use an etch mask 20 µm thick (details in A.6.5. Structure polymer layer). Etch Ti etch stop layer (details in A.6.6. Ti etch stop layer)
- **Release:**
    - PI:
        - Dice the wafer into sections to facilitate the release of small groups of probes

        - Use Cr etchant solution for ~ 40 min and rinse released probes in three phases of MilliQ water
    - PaC: Use droplets of water to facilitate the release using tweezers

Flexible PEDOT: PSS BiMEAs

- **Host substrate:** 4-inch Si wafer
- **Flexible substrate layer:** First flexible layer with a thickness of 3 µm (details in A.6.2. Polymer deposition)
- **First metallization:** 10/100 nm of Ti/Au or Ti/Pt (details in A.6.3. Metallization)
- **Flexible passivation layer:** Second flexible layer with a thickness of 3 µm, apply adhesion promoter (details in A.6.2. Polymer deposition)
- **Shape and contact pad openings (A.6.5. Structure polymer layer):**
    - Process A: Etch shape of probe, use an etch mask 10 µm thick
    - Process B: Etch shape and contact pad openings, use an etch mask 10 µm thick
- **Sacrificial layer:** Deposit a sacrificial PaC layer (details in A.6.7. Sacrificial PaC layer)
- **Electrode openings (A.6.5. Structure polymer layer):**
    - Process A: Etch electrode and contact pad openings, use an etch mask 10 µm thick
    - Process B: Etch electrode openings, use an etch mask 7 µm thick
- **PEDOT: PSS coating:** Spin-coat two layers of PEDOT: PSS and remove sacrificial PaC layer (details in A.6.8. PEDOT: PSS coating)
- **Release:**
    - PI:
        - Pattern wet chemical etch mask covering the shape of the probes (details in A.6.9. Wet chemical etch mask)
        - Dice the wafer into sections to facilitate the release of small groups of probes
        - Use Cr etchant solution for ~ 40 min and rinse released probes in three phases of MilliQ water
        - Remove photoresist in acetone and rinse in isopropanol
        - Dry gently with a N_2 gun
    - PaC: Use droplets of water to facilitate the release using tweezers

Appendix 8: Cyclic voltammograms variability of SIROFs

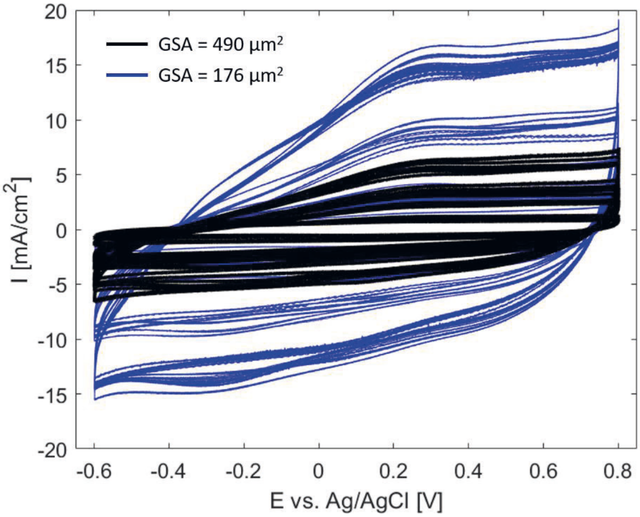

Figure A.8. 1. Cyclic voltammograms variability of SIROFs. Cyclic voltammograms measured of the electrodes of eight devices are displayed for SIROFs with a geometric surface area (GSA) of 490 µm² (N=32, black-gray) and 176 µm² (N=92, blue). The *y* and *x* axes show the current density (*I*) and working electrode potential *(E)* versus a Ag/AgCl reference electrode, respectively.

Appendix 9: Spin-coated PEDOT: PSS microelectrodes

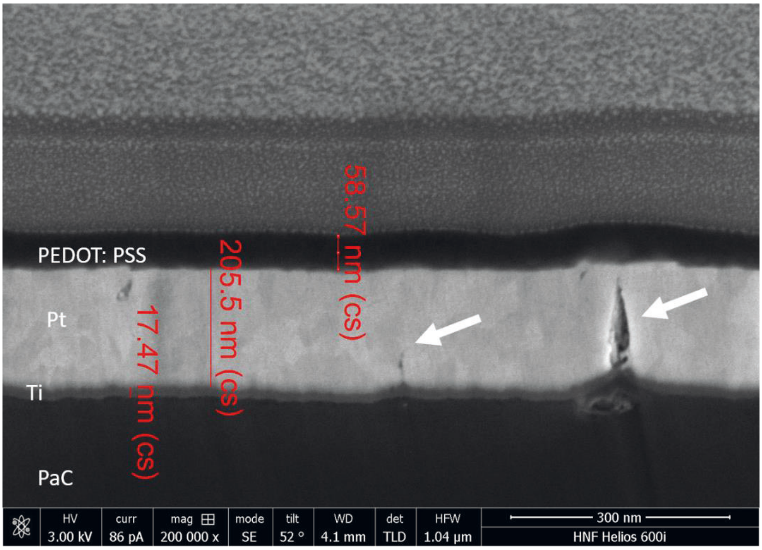

Figure A.9. 1. Cross-section of a spin-coated PEDOT: PSS electrode. FIB cut that shows the cross-section a PEDOT: PSS electrode with a Ti/Pt (10/200 nm) base layer on a flexible PaC-based substrate. The white arrows point out cracks on the Pt layer.

Appendix 10: Compressive Young’s modulus of PDMS phantoms.

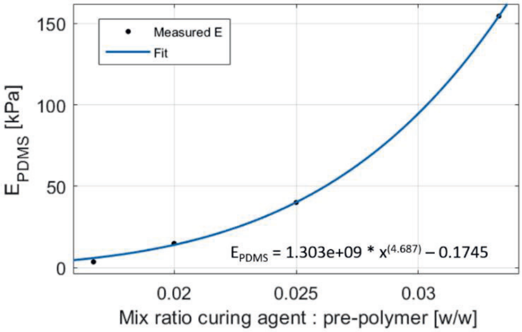

Figure A.10. 1. PDMS mixing ratio and Young's modulus relation. The Young’s modulus (*E*) of PDMS (Sylgard 184, Dow Corning) samples with curing agent: pre-polymer mixing ratios of 1:30, 1:40, 1:50, and 1:60 was measured with the micro-indentation setup of the Institute of Biological Information Processing-2 (IBI-2) at Forschungszentrum Jülich. PDMS samples were cured at 120°C for 4h.

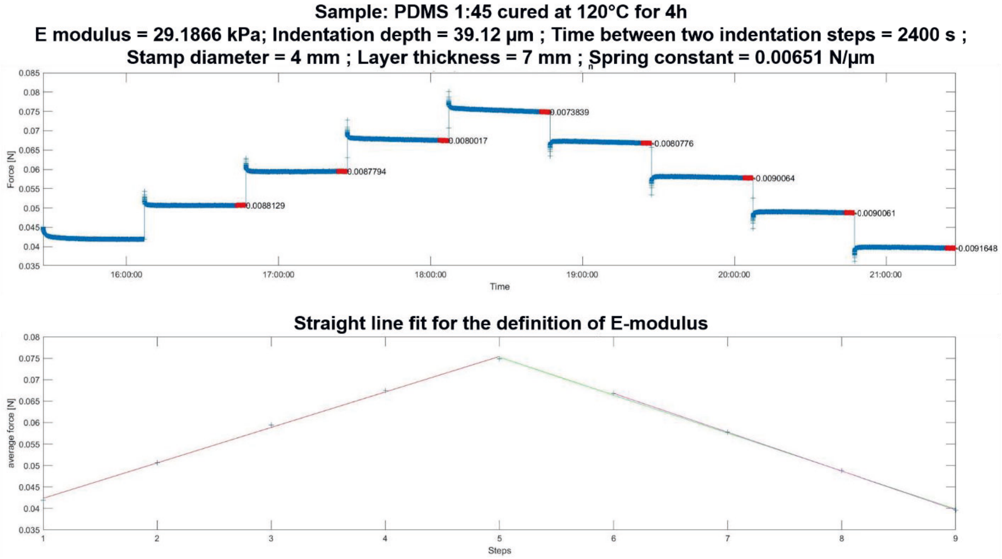

Figure A.10. 2. Results of micro-indentation test of phantom retina. A micro-indentation test was performed to determine the compressive Youngs’ modulus of a phantom retina made of PDMS with a mix ratio of 1:45 (curing agent: pre-polymer) cured for 4 h at 120°C. The test was performed with experimental setup of the Institute of Biological Information Processing-2 (IBI-2) at Forschungszentrum Jülich, which is based on the indentation setup reported by [237].

Appendix 11: Performance of intraretinal insertions

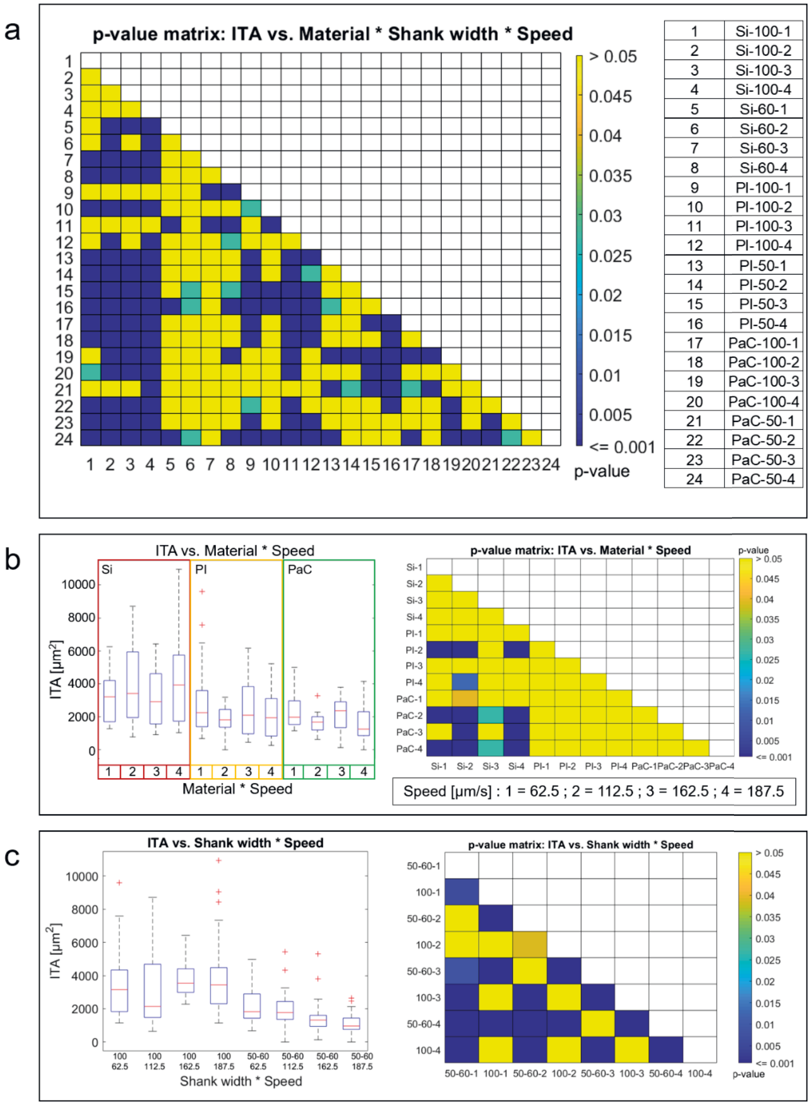

Figure A.11. 1. Effects of acute intraretinal insertions on the insertion trauma area (ITA). a) P-value matrix showing the combined effect of the main substrate material, shank width, and insertion speed. The insertion conditions are coded with numbers according to Material – Shank width – Insertion speed as mapped by the table at the right. Likewise, each insertion speed is numbered as follows: 1 = 62.5 µm/s, 2 = 112.5 µm/s, 3 = 162.5 µm/s, and 4 = 187.5 µm/s. b-c) Boxplot comparisons with the corresponding p-value matrix for the combined effect of (b) main substrate material and insertion speed and (c) shank width and insertion speed. P-value matrices were obtained after performing post-hoc pairwise comparisons using non-parametric bootstrap t-tests and Bonferroni correction. P-values showing no statistical significance are colored light yellow ($p > 0.05$), and significant differences ($p \leq 0.05$) are colored following the color code at the right.

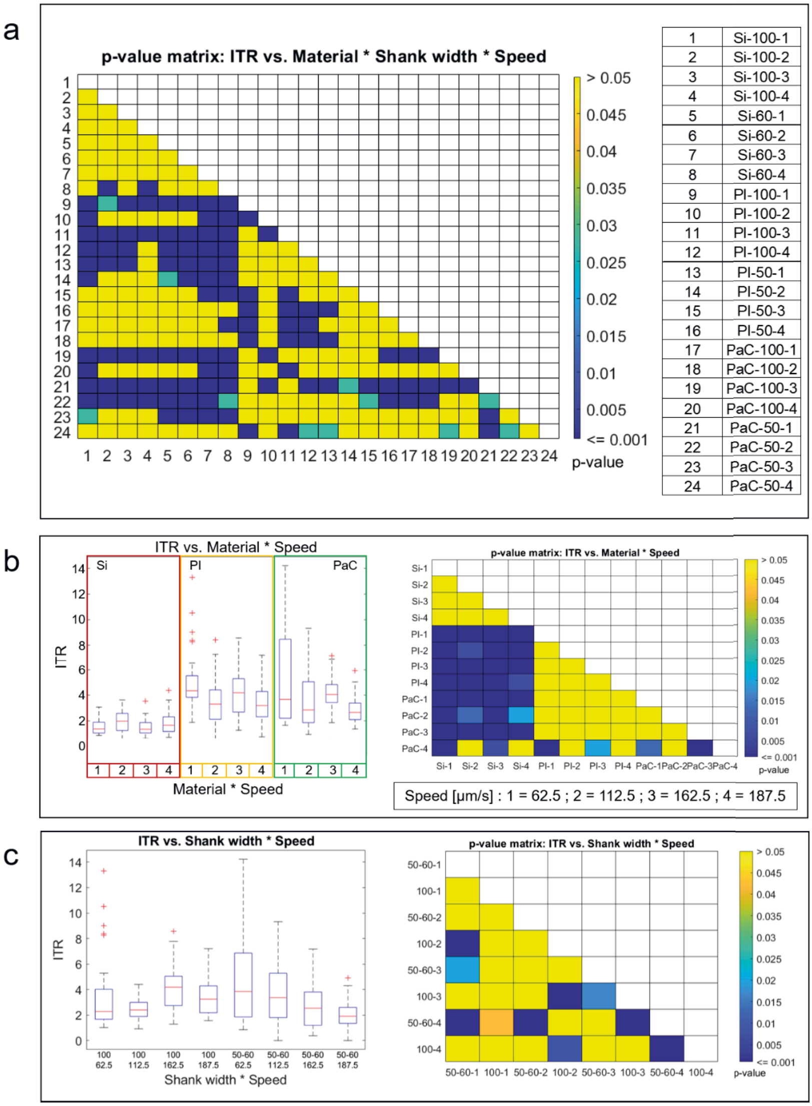

1	Si-100-1
2	Si-100-2
3	Si-100-3
4	Si-100-4
5	Si-60-1
6	Si-60-2
7	Si-60-3
8	Si-60-4
9	Pl-100-1
10	Pl-100-2
11	Pl-100-3
12	Pl-100-4
13	Pl-50-1
14	Pl-50-2
15	Pl-50-3
16	Pl-50-4
17	PaC-100-1
18	PaC-100-2
19	PaC-100-3
20	PaC-100-4
21	PaC-50-1
22	PaC-50-2
23	PaC-50-3
24	PaC-50-4

Speed [µm/s] : 1 = 62.5 ; 2 = 112.5 ; 3 = 162.5 ; 4 = 187.5

Figure A.11. 2. Effects of acute intraretinal insertions on the insertion trauma area ratio (ITR). a) P-value matrix showing the combined effect of the main substrate material, shank width, and insertion speed. The insertion conditions are coded with numbers according to Material – Shank width – Insertion speed as mapped by the table at the right. Likewise, each insertion speed is numbered as follows: 1 = 62.5 µm/s, 2 = 112.5 µm/s, 3 = 162.5 µm/s, and 4 = 187.5 µm/s. b-c) Boxplot comparisons with the corresponding p-value matrix for the combined effect of (b) main substrate material and insertion speed and (c) shank width and insertion speed. P-value matrices were obtained after performing post-hoc pairwise comparisons using non-parametric bootstrap t-tests and Bonferroni correction. P-values showing no statistical significance are colored light yellow ($p > 0.05$), and significant differences ($p \leq 0.05$) are colored following the color code at the right.

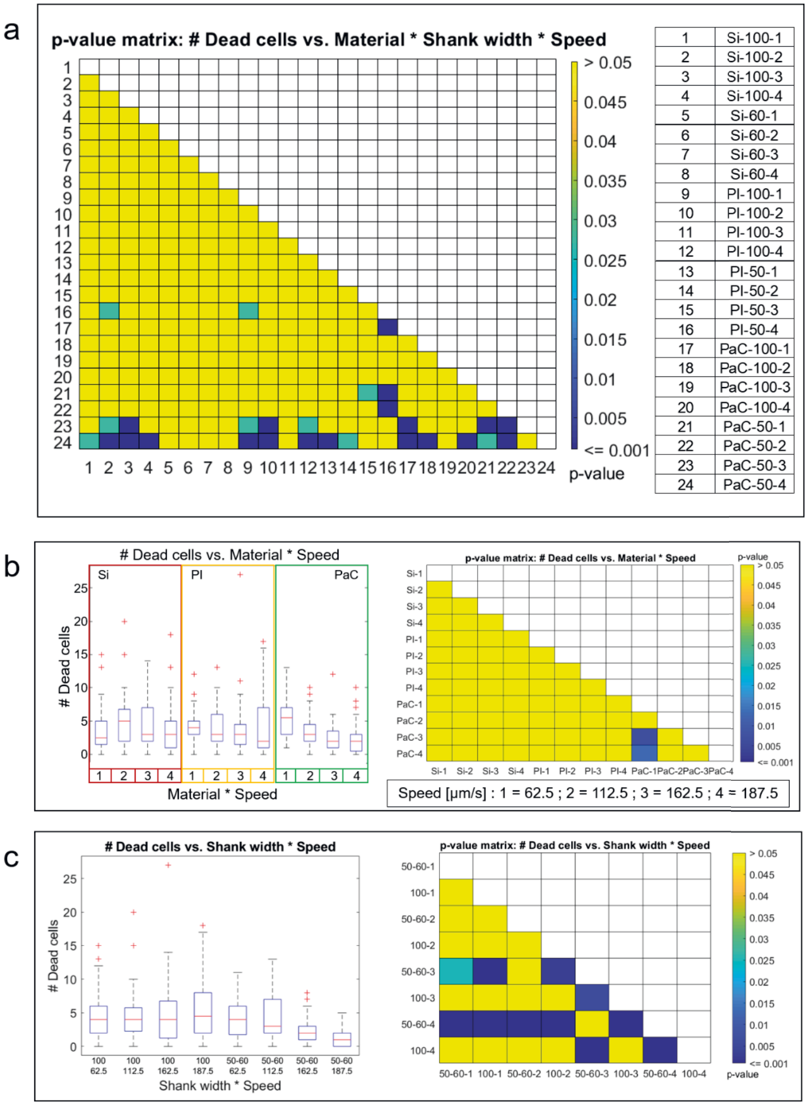

1	Si-100-1
2	Si-100-2
3	Si-100-3
4	Si-100-4
5	Si-60-1
6	Si-60-2
7	Si-60-3
8	Si-60-4
9	Pl-100-1
10	Pl-100-2
11	Pl-100-3
12	Pl-100-4
13	Pl-50-1
14	Pl-50-2
15	Pl-50-3
16	Pl-50-4
17	PaC-100-1
18	PaC-100-2
19	PaC-100-3
20	PaC-100-4
21	PaC-50-1
22	PaC-50-2
23	PaC-50-3
24	PaC-50-4

Figure A.11. 3. Effects of acute intraretinal insertions on the count of dead cells. a) P-value matrix showing the combined effect of the main substrate material, shank width, and insertion speed. The insertion conditions are coded with numbers according to Material – Shank width – Insertion speed as mapped by the table at the right. Likewise, each insertion speed is numbered as follows: 1 = 62.5 µm/s, 2 = 112.5 µm/s, 3 = 162.5 µm/s, and 4 = 187.5 µm/s. b-c) Boxplot comparisons with the corresponding p-value matrix for the combined effect of (b) main substrate material and insertion speed and (c) shank width and insertion speed. P-value matrices were obtained after performing post-hoc pairwise comparisons using non-parametric bootstrap t-tests and Bonferroni correction. P-values showing no statistical significance are colored light yellow ($p > 0.05$), and significant differences ($p \leq 0.05$) are colored following the color code at the right.

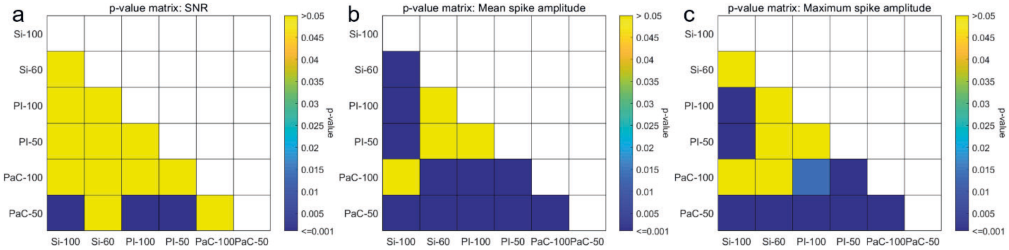

Figure A.11. 4. Significant differences of the recording quality among BiMEA probes. P-value matrices corresponding to pairwise comparisons of a) the signal to noise ratio (SNR), b) the mean spike amplitude (SPK), and c) the maximum spike amplitude (MSPK) of action potentials recorded by electrodes (N = 966) of successfully inserted shanks. Significant differences were established among BiMEA probes grouped by main substrate material (Si, PI, or PaC) and shank width (50, 60, or 100 mm) after computing the p-value of post-hoc pairwise testing using non-parametric bootstrap t-tests and Bonferroni correction.

References

[1] G. J. Tortora and M. T. Nielsen, *Principles of human anatomy*, 11th ed. Hoboken, NJ : Wiley, 2009.

[2] S. R. Flaxman *et al.*, “Global causes of blindness and distance vision impairment 1990–2020: a systematic review and meta-analysis,” *Lancet Glob. Heal.*, vol. 5, no. 12, pp. e1221–e1234, 2017.

[3] D. T. Hartong, E. L. Berson, T. P. Dryja, and C. Hamel, “Retinitis pigmentosa,” *Lancet*, vol. 368, no. 9549, pp. 1795–1809, 2006.

[4] J. O. Mills, A. Jalil, and P. E. Stanga, “Electronic retinal implants and artificial vision: Journey and present,” *Eye*, vol. 31, no. 10, pp. 1383–1398, 2017.

[5] R. Nagaraj, D. R. Bijukumar, B. Mathew, E. A. Scott, and M. T. Mathew, “A review on recent advancements in ophthalmology devices: Currently in market and under clinical trials,” *J. Drug Deliv. Sci. Technol.*, vol. 52, no. February, pp. 334–345, 2019.

[6] S. D. Rathbun *et al.*, “Chapter 1 Restoring Vision to the Blind : The New Age of Implanted Visual Prostheses Recent Advances in Retinal Stimulation : Clinical Applications,” *Transl. Vis. Sci. Technol.*, vol. 3, no. 7, pp. 3–13, 2014.

[7] L. N. Ayton *et al.*, “An update on retinal prostheses,” *Clin. Neurophysiol.*, vol. 131, no. 6, pp. 1383–1398, 2020.

[8] M. S. Humayun *et al.*, “Interim results from the international trial of second sight’s visual prosthesis,” *Ophthalmology*, vol. 119, no. 4, pp. 779–788, 2012.

[9] K. Stingl *et al.*, “Interim results of a multicenter trial with the new electronic subretinal implant alpha AMS in 15 patients blind from inherited retinal degenerations,” *Front. Neurosci.*, vol. 11, no. AUG, pp. 1–11, 2017.

[10] P. Walter, “Zukünftige Entwicklungen bei implantierbaren Netzhautprothesen,” *Klin. Monbl. Augenheilkd.*, vol. 233, no. 11, pp. 1238–1243, 2016.

[11] D. L. Cheng, P. B. Greenberg, and D. A. Borton, “Advances in Retinal Prosthetic Research: A Systematic Review of Engineering and Clinical Characteristics of Current Prosthetic Initiatives,” *Curr. Eye Res.*, vol. 42, no. 3, pp. 334–347, 2017.

[12] C. Haselier, S. Biswas, S. Rösch, G. Thumann, F. Müller, and P. Walter, “Correlations between specific patterns of spontaneous activity and stimulation efficiency in degenerated retina,” *PLoS One*, vol. 12, no. 12, pp. 1–16, 2017.

[13] V. Rincón Montes *et al.*, “Toward a Bidirectional Communication Between Retinal Cells and a Prosthetic Device – A Proof of Concept,” *Front. Neurosci.*, vol. 13, no. April, pp. 1–19, 2019.

[14] J. F. Rizzo, J. Wyatt, J. Loewenstein, S. Kelly, and D. Shire, “Methods and Perceptual Thresholds for Short-Term Electrical Stimulation of Human Retina with Microelectrode Arrays,” *Investig. Ophthalmol. Vis. Sci.*, vol. 44, no. 12, pp. 5355–5361, 2003.

[15] A. Stett, A. Mai, and T. Herrmann, “Retinal charge sensitivity and spatial discrimination obtainable by subretinal implants : key lessons learned from isolated chicken retina,” 2007.

[16] A. Jalligampala, S. Sekhar, E. Zrenner, and D. L. Rathbun, “Optimal voltage stimulation parameters for network-mediated responses in wild type and rd10 mouse retinal ganglion cells,” *J. Neural Eng.*, vol. 14, no. 2, p. 26004, 2017.

[17] E. W. Schmid and W. Fink, “Operational design considerations for retinal prostheses,” *IEEE Circuits Syst. Mag.*, vol. 16, no. 3, pp. 31–44, 2016.

[18] D. Ghezzi, “Retinal prostheses: Progress towards the next generation implants,” *Front. Neurosci.*, vol. 9, no. JUL, pp. 1–6, 2015.

[19] D. Palanker, A. Vankov, P. Huie, and S. Baccus, “Design of a high-resolution optoelectronic retinal prosthesis,” *J. Neural Eng.*, vol. 2, no. 1, pp. S105–S120, 2005.

[20] A. Bendali *et al.*, “Synthetic 3D diamond-based electrodes for flexible retinal neuroprostheses: Model, production and in vivo biocompatibility,” *Biomaterials*, vol. 67, pp. 73–83, 2015.

[21] L. Yanovitz, D. Raz-Prag, K.-O. Eden, R. Saini, Y. Hanein, and R. Gefen, “Retinal responses evoked and recorded with 3D electrodes designated for a novel prosthetic device,” *Invest. Ophthalmol. Vis. Sci.*, vol. 55, no. 13, p. 1808, 2014.

[22] P. González Losada *et al.*, “Protuberant Electrode Structures for New Retinal Implants,” *Proceedings*, vol. 1, no. 4, p. 315, 2017.

[23] T. Flores *et al.*, “Optimization of pillar electrodes in subretinal prosthesis for enhanced proximity to target neurons,” *J. Neural Eng.*, vol. 15, no. 3, 2018.

[24] P. Walter, “A Fully Intraocular Approach for a Bi-directional Retinal Prosthesis,” in *Artificial Vision: a clinical guide*, 2016, pp. 151–161.

[25] J. S. Brusius, “3-dimensionale penetrierende Multi-elektrodenarrays zur Stimulation und Ableitung in der Retina,” 2015.

[26] A. C. Patil and N. V. Thakor, “Implantable neurotechnologies: a review of micro- and nanoelectrodes for neural recording,” *Med. Biol. Eng. Comput.*, vol. 54, no. 1, pp. 23–44, 2016.

[27] J. Blumberg and G. Kreiman, “Review series How cortical neurons help us see : visual recognition in the human brain,” vol. 120, no. 9, 2010.

[28] A. London, I. Benhar, and M. Schwartz, “The retina as a window to the brain,” *Nat. Rev. Neurol.*, vol. 9, no. January, 2013.

[29] X. G. Troncoso, S. L. Macknik, and S. Martinez-Conde, “Vision’s First Steps: Anatomy, Physiology, and Perception in the Retina, Lateral Geniculate Nucleus, and Early Visual Cortical Areas,” in *Visual Prosthetics Physiology, Bioengineering, Rehabilitation*, G. Dagnelie, Ed. Springer, 2011, pp. 23–57.

[30] I. Icke, “Eye-diagram.” Wikimedia Commons, 2007.

[31] P. Hartmann, “Retina layers.” Wikimedia Commons, 2013.

[32] V. J. Kefalov, “Rod and Cone Visual Pigments and Phototransduction through Pharmacological , Genetic , and Physiological Approaches *,” vol. 287, no. 3, pp. 1635–1641, 2012.

[33] T. Euler, S. Haverkamp, T. Schubert, and T. Baden, “Retinal bipolar cells : elementary building blocks of vision,” *Nat. Publ. Gr.*, vol. 15, no. 8, pp. 507–519, 2014.

[34] R. H. Masland, “The fundamental plan of the retina,” *Nat. Neurosci.*, vol. 4, no. 9, pp. 877–886, 2001.

[35] J. R. Sanes and R. H. Masland, “The Types of Retinal Ganglion Cells: Current Status and Implications for Neuronal Classification,” *Annu. Rev. Neurosci.*, vol. 38, no. 1, pp. 221–246, 2015.

[36] H. K. Hartline, “Visual Receptors and Retinal Interaction,” *Science (80-.).*, vol. 164, no. 3877, pp. 270–278, 1969.

[37] R. Nelson, “Visual responses of Ganglion cells,” in *Webvision: The Organization of the Retina and Visual System*, H. Kolb, R. Nelson, E. Fernandez, and B. Jose, Eds. Salt Lake City (UT): University of Utah Health Sciences Center, 1995.

[38] J. D. Weiland, S. T. Walston, and M. S. Humayun, “Electrical Stimulation of the Retina to Produce Artificial Vision,” *Proc. Int. Jt. Conf. Neural Networks*, vol. 5, pp. 3100–3102, 2016.

[39] L. J. Frishman and M. H. Wang, “Electroretinogram of Human, Monkey and Mouse,” in *Adler’s Physiology of the Eye*, 11th ed., L. A. Levin, S. F. E. Nilsson, J. Ver Hoeve, and S. M. Wu, Eds. 2011, pp. 480–501.

[40] I. Perlman, “The Electroretinogram (ERG),” in *Webvision: The Organization of the Retina and Visual System*, H. Kolb, R. Nelson, E. Fernandez, and B. Jose, Eds. Salt Lake City (UT): University of Utah Health Sciences Center, 1995.

[41] J. Atorf, “Studying retinal function of mice using full-field electroretinography Jenny Atorf,” Friedrich-Alexander-Universität Erlangen-Nürnberg, 2012.

[42] E. K. de Jong, M. J. Geerlings, and A. I. den Hollander, “Age-related macular degeneration,” in *Genetics and Genomics of Eye Disease Advancing to Precision Medicine*, X. Raymond Gao, Ed. Academic Press, Elsevier Inc., 2019, pp. 155–180.

[43] A. L. Wang, D. K. Knight, T. T. T. Vu, and M. C. Mehta, “Retinitis pigmentosa: Review of current treatment,” *Int. Ophthalmol. Clin.*, vol. 59, no. 1, pp. 263–280, 2019.

[44] K. Kostarelos, M. Vincent, C. Hebert, and J. A. Garrido, “Graphene in the Design and Engineering of Next-Generation Neural Interfaces,” *Adv. Mater.*, vol. 29, no. 42, pp. 1–7, 2017.

[45] G. E. Loeb, “Neural Prosthetics: A Review of Empirical vs. Systems Engineering Strategies,” *Appl. Bionics Biomech.*, vol. 2018, no. Figure 1, 2018.

[46] E. L. So and A. Alwaki, “A guide for cortical electrical stimulation mapping,” *J. Clin. Neurophysiol.*, vol. 35, no. 2, pp. 98–105, 2018.

[47] C. E. Bouton *et al.*, “Restoring cortical control of functional movement in a human with quadriplegia,” *Nature*, vol. 533, no. 7602, pp. 247–250, 2016.

[48] T. M. Herrington, J. J. Cheng, and E. N. Eskandar, “Mechanisms of deep brain stimulation,” *J. Neurophysiol.*, vol. 115, no. 1, pp. 19–38, 2016.

[49] J. S. Perlmutter and J. W. Mink, “Deep Brain Stimulation,” *Annu. Rev. Neurosci.*, vol. 29, pp. 229–257, 2006.

[50] R. L. Johnson and C. G. Wilson, “A review of vagus nerve stimulation as a therapeutic intervention,” *J. Inflamm. Res.*, vol. 11, pp. 203–213, 2018.

[51] A. Kral, M. F. Dorman, and B. S. Wilson, “Neuronal Development of Hearing and Language: Cochlear Implants and Critical Periods,” *Annu. Rev. Neurosci.*, vol. 42, no. 1, pp. 47–65, 2019.

[52] S. De Wachter *et al.*, “New Technologies and Applications in Sacral Neuromodulation: An Update,” *Adv. Ther.*, vol. 37, no. 2, pp. 637–643, 2020.

[53] P. Verrills, C. Sinclair, and A. Barnard, “A review of spinal cord stimulation systems for chronic pain,” *J. Pain Res.*, vol. 9, pp. 481–492, 2016.

[54] I. R. Minev *et al.*, “Electronic dura mater for long-term multimodal neural interfaces,” *Science (80-.).*, vol. 347, no. 6218, pp. 159–163, Jan. 2015.

[55] V. P. Gabel, Ed., *Artificial vision : a clinical guide*. Springer, Cham, 2017.

[56] L. Karumbaiah *et al.*, “Relationship between intracortical electrode design and chronic recording function,” *Biomaterials*, vol. 34, no. 33, pp. 8061–8074, 2013.

[57] S. P. Lacour, G. Courtine, and J. Guck, “Materials and technologies for soft implantable neuroprostheses,” *Nat. Rev. Mater.*, vol. 1, no. 10, 2016.

[58] J. A. Frank, M. J. Antonini, and P. Anikeeva, “Next-generation interfaces for studying

neural function," *Nat. Biotechnol.*, vol. 37, no. 9, pp. 1013–1023, 2019.

[59] K. D. Wise, "Silicon Microsystems for Neuroscience and Neural Prostheses," *IEEE Eng. Med. Biol. Mag.*, vol. 24, no. 5, pp. 22–29, 2005.

[60] R. A. Normann, "Technology Insight: Future neuroprosthetic therapies for disorders of the nervous system," *Nat. Clin. Pract. Neurol.*, vol. 3, no. 8, pp. 444–452, 2007.

[61] B. Ghane-Motlagh and M. Sawan, "A review of Microelectrode Array technologies: Design and implementation challenges," *2013 2nd Int. Conf. Adv. Biomed. Eng. ICABME 2013*, pp. 38–41, 2013.

[62] J. J. Jun *et al.*, "Fully integrated silicon probes for high-density recording of neural activity," *Nature*, vol. 551, no. 7679, pp. 232–236, 2017.

[63] P. R. Patel *et al.*, "Insertion of linear 8.4 μm diameter 16 channel carbon fiber electrode arrays for single unit recordings," *J. Neural Eng.*, vol. 12, no. 4, p. 46009, 2015.

[64] X. Wei *et al.*, "Nanofabricated Ultraflexible Electrode Arrays for High-Density Intracortical Recording," *Adv. Sci.*, vol. 5, no. 6, 2018.

[65] A. Weltman, J. Yoo, and E. Meng, "Flexible, penetrating brain probes enabled by advances in polymer microfabrication," *Micromachines*, vol. 7, no. 10, pp. 1–36, 2016.

[66] B. Rubehn, C. Bosman, R. Oostenveld, P. Fries, and T. Stieglitz, "A MEMS-based flexible multichannel ECoG-electrode array," *J. Neural Eng.*, vol. 6, no. 3, 2009.

[67] K. P. Hoffmann, K. P. Koch, T. Doerge, and S. Micera, "New technologies in manufacturing of different implantable microelectrodes as an interface to the peripheral nervous system," *Proc. First IEEE/RAS-EMBS Int. Conf. Biomed. Robot. Biomechatronics, 2006, BioRob 2006*, vol. 2006, pp. 414–419, 2006.

[68] Z. Xiang *et al.*, "Progress of Flexible Electronics in Neural Interfacing - A Self-Adaptive Non-Invasive Neural Ribbon Electrode for Small Nerves Recording," *Adv. Mater.*, vol. 28, no. 22, pp. 4472–4479, 2016.

[69] T. Stieglitz, M. Schuettler, and K. P. Koch, "Implantable biomedical microsystems for neural prostheses," *IEEE Eng. Med. Biol. Mag.*, vol. 24, no. 5, pp. 58–65, 2005.

[70] M. Kindlundh, P. Norlin, and U. G. Hofmann, "A neural probe process enabling variable electrode configurations," *Sensors Actuators, B Chem.*, vol. 102, no. 1, pp. 51–58, 2004.

[71] E. Zrenner, "Fighting blindness with microelectronics," *Sci. Transl. Med.*, vol. 5, no. 210, pp. 1–7, 2013.

[72] A. Tiwari and R. H. Talwekar, "Journey of Visual Prosthesis with Progressive Development of Electrode Design Techniques and Experience with CMOS Image Sensors: A Review," *IETE J. Res.*, vol. 65, no. 2, pp. 172–200, 2019.

[73] P. M. Lewis, H. M. Ackland, A. J. Lowery, and J. V. Rosenfeld, "Restoration of vision in blind individuals using bionic devices: A review with a focus on cortical visual prostheses," *Brain Res.*, vol. 1595, pp. 51–73, 2015.

[74] S. D. Rathbun *et al.*, "Chapter 1 - Restoring Vision to the Blind: The New Age of Implanted Visual Prostheses," *Transl. Vis. Sci. Technol.*, vol. 3, no. 7, 2014.

[75] M. S. Humayun *et al.*, "Visual perception in a blind subject with a chronic microelectronic retinal prosthesis," *Vision Res.*, vol. 43, no. 24, pp. 2573–2581, 2003.

[76] L. Ferlauto *et al.*, "Design and validation of a foldable and photovoltaic wide-field epiretinal prosthesis," *Nat. Commun.*, vol. 9, no. 1, pp. 1–15, 2018.

[77] P. Stalmans, "Safety and performance clinical trial of the NR600 retinal implant in end-stage inherited outer retinal degenerative diseases," *Artificial Vision 2019 : The International Symposium on Visual Prosthetics*. Aachen, 2019.

[78] G. Roessler *et al.*, “Implantation and Explantation of a Wireless Epiretinal Retina Implant Device : Observations during the EPIRET3 Prospective Clinical Trial,” *Invest. Ophthalmol. Vis. Sci.*, vol. 50, no. 6, pp. 3003–3008, 2009.

[79] D. L. Cheng, P. B. Greenberg, and D. A. Borton, “Advances in Retinal Prosthetic Research: A Systematic Review of Engineering and Clinical Characteristics of Current Prosthetic Initiatives,” *Curr. Eye Res.*, vol. 42, no. 3, pp. 334–347, 2017.

[80] L. N. Ayton *et al.*, “First-in-human trial of a novel suprachoroidal retinal prosthesis,” *PLoS One*, vol. 9, no. 12, pp. 1–26, 2014.

[81] T. Fujikado *et al.*, “Testing of semichronically implanted retinal prosthesis by suprachoroidal-transretinal stimulation in patients with retinitis pigmentosa,” *Investig. Ophthalmol. Vis. Sci.*, vol. 52, no. 7, pp. 4726–4733, 2011.

[82] C. Veraart *et al.*, “Visual sensations produced by optic nerve stimulation using an implanted self-sizing spiral cuff electrode,” *Brain Res.*, vol. 813, no. 1, pp. 181–186, 1998.

[83] M. E. Brelén, V. Vince, B. Gérard, C. Veraart, and J. Delbeke, “Measurement of evoked potentials after electrical stimulation of the human optic nerve,” *Investig. Ophthalmol. Vis. Sci.*, vol. 51, no. 10, pp. 5351–5355, 2010.

[84] Y. Lu, Y. Yan, X. Chai, Q. Ren, Y. Chen, and L. Li, “Electrical stimulation with a penetrating optic nerve electrode array elicits visuotopic cortical responses in cats,” *J. Neural Eng.*, vol. 10, no. 3, 2013.

[85] J. S. Pezaris and R. C. Reid, “Demonstration of artificial visual percepts generated through thalamic microstimulation,” *Proc. Natl. Acad. Sci. U. S. A.*, vol. 104, no. 18, pp. 7670–7675, 2007.

[86] G. S. Brindley and W. S. Lewin, “The sensations produced by electrical stimulation of the visual cortex,” *J. Physiol.*, vol. 196, no. 2, pp. 479–493, 1968.

[87] E. M. Schmidt, M. J. Bak, F. T. Hambrecht, C. V. Kufta, D. K. O’Rourke, and P. Vallabhanath, “Feasibility of a visual prosthesis for the blind based on intracortical microstimulation of the visual cortex,” *Brain*, vol. 119, no. 2, pp. 507–522, 1996.

[88] R. M. Mirochnik and J. S. Pezaris, “Contemporary approaches to visual prostheses,” *Mil. Med. Res.*, vol. 6, no. 1, pp. 1–9, 2019.

[89] P. Johns, “Synaptic transmission,” in *Clinical Neuroscience*, London, UK: Elsevier, Churchill Livingstone, 2014, pp. 81–89.

[90] D. Johnston and S. M.-S. Wu, *Foundations of Cellular Neurophysiology*. Cambridge, MA: MIT Press, 1995.

[91] M. Carter and J. Shieh, “Electrophysiology,” in *Guide to Research Techniques in Neuroscience*, 2015, pp. 89–115.

[92] P. Johns, “Electrical signalling in neurons,” in *Clinical Neuroscience*, London, UK: Elsevier, Churchill Livingstone, 2014, pp. 71–80.

[93] “Neurons,” *OpenStax CNX*. [Online]. Available: https://courses.lumenlearning.com/wm-biology2/chapter/neurons/.

[94] C. Watson, M. Kirkcaldie, and G. Paxinos, “Nerve cells and synapses,” in *The Brain*, Academic Press, Elsevier Inc., 2010, pp. 1–10.

[95] D. R. Merrill, M. Bikson, and J. G. R. Jefferys, “Electrical stimulation of excitable tissue: Design of efficacious and safe protocols,” *J. Neurosci. Methods*, vol. 141, no. 2, pp. 171–198, 2005.

[96] P. Massobrio, G. Massobrio, and S. Martinoia, “Interfacing cultured neurons to

microtransducers arrays: A review of the neuro-electronic junction models," *Front. Neurosci.*, vol. 10, no. JUN, pp. 1–13, 2016.

[97] S.Srinivasan and S. Srinivasan, "Electrode / Electrolyte Interfaces : Structure and Kinetics of Charge Transfer," in *Fuel Cells: From Fundamentals to Applications*, 1900, pp. 27–96.

[98] Z. Stojek, "The electrical double layer and its structure," in *Electroanalytical Methods: Guide to Experiments and Applications*, 2010, pp. 3–9.

[99] W. M. Siu and R. S. C. Cobbold, "Basic Properties of the Electrolyte-SiO2-Si System: Physical and Theoretical Aspects," *IEEE Trans. Electron Devices*, vol. 26, no. 11, pp. 1805–1815, 1979.

[100] S. F. Cogan, "Neural Stimulation and Recording Electrodes," *Annu. Rev. Biomed. Eng.*, vol. 10, pp. 275–309, 2008.

[101] S. Resatz and F. Rattay, "A model for the electrically stimulated retina," *Math. Comput. Model. Dyn. Syst.*, vol. 10, no. 2, pp. 93–106, 2004.

[102] D. T. Brocker and W. M. Grill, "Principles of electrical stimulation of neural tissue," in *Handbook of Clinical Neurology*, 1st ed., vol. 116, Elsevier B.V., 2013, pp. 3–18.

[103] M. E. J. Obien, K. Deligkaris, T. Bullmann, D. J. Bakkum, and U. Frey, "Revealing neuronal function through microelectrode array recordings," *Front. Neurosci.*, vol. 9, no. JAN, p. 423, 2015.

[104] R. Weis and P. Fromherz, "Frequency dependent signal transfer in neuron transistors," *Phys. Rev. E - Stat. Physics, Plasmas, Fluids, Relat. Interdiscip. Top.*, vol. 55, no. 1, pp. 877–889, 1997.

[105] M. E. Spira and A. Hai, "Multi-electrode array technologies for neuroscience and cardiology," *Nat. Nanotechnol.*, vol. 8, no. 2, pp. 83–94, 2013.

[106] K. M. Szostak, L. Grand, and T. G. Constandinou, "Neural interfaces for intracortical recording: Requirements, fabrication methods, and characteristics," *Front. Neurosci.*, vol. 11, pp. 1–27, 2017.

[107] A. Campbell and C. Wu, "Chronically Implanted Intracranial Electrodes : Tissue Reaction and Electrical Changes," pp. 1–14, 2018.

[108] A. Campbell and C. Wu, "Chronically Implanted Intracranial Electrodes: Tissue Reaction and Electrical Changes," *Micromachines*, vol. 9, no. 9, p. 430, 2018.

[109] A. Lecomte, E. Descamps, and C. Bergaud, "A review on mechanical considerations for chronically-implanted neural probes," *J. Neural Eng.*, vol. 15, no. 3, pp. 1–21, 2018.

[110] M. Jorfi, J. L. Skousen, C. Weder, and J. R. Capadona, "Progress towards biocompatible intracortical microelectrodes for neural interfacing applications," *J. Neural Eng.*, vol. 12, no. 1, pp. 1–45, 2015.

[111] D. F. Williams, "On the mechanisms of biocompatibility," *Biomaterials*, vol. 29, no. 20, pp. 2941–2953, 2008.

[112] K. Scholten and E. Meng, "Materials for microfabricated implantable devices: a review," *Lab Chip*, vol. 15, no. 22, pp. 4256–4272, Oct. 2015.

[113] P. Moshayedi *et al.*, "The relationship between glial cell mechanosensitivity and foreign body reactions in the central nervous system," *Biomaterials*, vol. 35, no. 13, pp. 3919–3925, 2014.

[114] J. K. Nguyen, D. J. Park, and J. L. Skousen, "Mechanically-compliant intracortical implants reduce the neuroin fl ammatory response," *J. Neural Eng.*, vol. 11, no. 5, pp. 1–15, 2014.

[115] A. Sridharan, S. D. Rajan, and J. Muthuswamy, "Long-term changes in the material

properties of brain tissue at the implant-tissue interface," *J. Neural Eng.*, vol. 10, no. 6, 2013.

[116] J. Muthuswamy, R. Saha, and A. Gilletti, "Tissue micromotion induced stress around brain implants," *2005 3rd IEEE/EMBS Spec. Top. Conf. Microtechnology Med. Biol.*, vol. 2005, no. May, pp. 102–103, 2005.

[117] S. R. Goldstein and M. Salcman, "Mechanical Microelectrodes," *IEEE Trans. Biomed. Eng.*, vol. BME-20, no. 4, pp. 260–269, 1973.

[118] R. Chen, A. Canales, and P. Anikeeva, "Neural recording and modulation technologies," *Nat. Rev. Mater.*, vol. 2, no. 2, pp. 1–16, 2017.

[119] J. Case, L. Chilver, and C. T. F. Ross, *Strength of Materials and Structures*, Fourth. Butterworth-Heinemann, 1999.

[120] L. D. Landau and E. M. Lifshitz, *Theory of Elasticity*, 3rd ed. Elsevier Butterworth Heinemann, 1986.

[121] P. M. N. Shesha and G. S. Suresh, *Textbook of Mechanics of Materials*. New Delhi, 2011.

[122] D. J. Edell, V. Van Toi, V. M. McNeil, and L. D. Clark, "Factors Influencing the Biocompatibility of Insertable Silicon Microshafts in Cerebral Cortex," *IEEE Trans. Biomed. Eng.*, vol. 39, no. 6, pp. 635–643, 1992.

[123] P. Stice, A. Gilletti, A. Panitch, and J. Muthuswamy, "Thin microelectrodes reduce GFAP expression in the implant site in rodent somatosensory cortex," *J. Neural Eng.*, vol. 4, no. 2, pp. 42–53, 2007.

[124] J. Thelin *et al.*, "Implant size and fixation mode strongly influence tissue reactions in the CNS," *PLoS One*, vol. 6, no. 1, pp. 1–10, 2011.

[125] C. S. Bjornsson *et al.*, "Effects of insertion conditions on tissue strain and vascular damage during neuroprosthetic device insertion," *J. Neural Eng.*, vol. 3, no. 3, pp. 196–207, 2006.

[126] J. P. Seymour and D. R. Kipke, "Neural probe design for reduced tissue encapsulation in CNS," *Biomaterials*, vol. 28, no. 25, pp. 3594–3607, 2007.

[127] N. Chen *et al.*, "Neural interfaces engineered via micro- and nanostructured coatings," *Nano Today*, vol. 14, pp. 59–83, 2017.

[128] N. P. Aryan, H. Kaim, and A. Rothermel, *Stimulation and Recording Electrodes for Neural Prostheses*. Springer, 2015.

[129] J. Newman, "Resistance for Flow of Current to a Disk," *J. Electrochem. Soc.*, vol. 113, no. 5, 1966.

[130] J. T. Rubinstein, F. A. Spelman, M. Soma, and M. F. Suesserman, "Current Density Profiles of Surface Mounted and Recessed Electrodes for Neural Prostheses," *IEEE Trans. Biomed. Eng.*, vol. BME-34, no. 11, pp. 864–875, 1987.

[131] G. E. Loeb, R. A. Peck, and J. Martyniuk, "Toward the ultimate metal electrode," *J. Neurosci. Methods*, vol. 63, pp. 175–183, 1995.

[132] K. D. Wise, D. J. Anderson, J. F. Hetke, D. R. Kipke, and K. Najafi, "Wireless implantable microsystems: High-density electronic interfaces to the nervous system," *Proc. IEEE*, vol. 92, no. 1, pp. 76–97, 2004.

[133] P. K. Campbell, K. E. Jones, R. J. Huber, K. W. Horch, and R. A. Normann, "A Silicon-Based, Three-Dimensional Neural Interface: Manufacturing Processes for an Intracortical Electrode Array," *IEEE Trans. Biomed. Eng.*, vol. 38, no. 8, pp. 758–768, 1991.

[134] E. Meng, "Microfabrication Methods and Processes for BioMEMS," in *Biomedical Microsystems*, C. Press, Ed. Taylor & Francis Group, 2010.

[135] C. Hassler, T. Boretius, and T. Stieglitz, “Polymers for neural implants,” *J. Polym. Sci. Part B Polym. Phys.*, vol. 49, no. 1, pp. 18–33, 2011.

[136] B. J. Kim and E. Meng, “Review of polymer MEMS micromachining,” *J. Micromechanics Microengineering*, vol. 26, no. 1, p. 13001, 2015.

[137] T. Tsuchiya, “Tensile testing of silicon thin films,” *Fatigue Fract. Eng. Mater. Struct.*, vol. 28, no. 8, pp. 665–674, 2005.

[138] B. Rubehn and T. Stieglitz, “In vitro evaluation of the long-term stability of polyimide as a material for neural implants,” *Biomaterials*, vol. 31, no. 13, pp. 3449–3458, 2010.

[139] “PDS 2010 LABCOTER^{TM} 2 Parylene Deposition System Operator’s Manual.” Specialty Coating Systems (SCS).

[140] S. F. Cogan *et al.*, “Sputtered iridium oxide films for neural stimulation electrodes,” *J. Biomed. Mater. Res. - Part B Appl. Biomater.*, vol. 89, no. 2, pp. 353–361, 2008.

[141] R. J. Jensen and J. F. R. Iii, “Activation of ganglion cells in wild-type and rd1 mouse retinas with monophasic and biphasic current pulses,” 2009.

[142] M. Mahadevappa, J. D. Weiland, D. Yanai, I. Fine, R. J. Greenberg, and M. S. Humayun, “Perceptual Thresholds and Electrode Impedance in Three Retinal Prosthesis Subjects,” *IEEE Trans. Neural Syst. Rehabil. Eng.*, vol. 13, no. 2, pp. 201–206, 2005.

[143] E. Slavcheva, R. Vitushinsky, W. Mokwa, and U. Schnakenberg, “Sputtered Iridium Oxide Films as Charge Injection Material for Functional Electrostimulation,” *J. Electrochem. Soc.*, vol. 151, no. 7, p. E226, 2004.

[144] A. Van Ooyen, G. Topalov, G. Ganske, W. Mokwa, and U. Schnakenberg, “Iridium oxide deposited by pulsed dc-sputtering for stimulation electrodes,” 2009.

[145] M. Ganji, A. Tanaka, V. Gilja, E. Halgren, and S. A. Dayeh, “Scaling Effects on the Electrochemical Stimulation Performance of Au , Pt , and PEDOT : PSS Electrocorticography Arrays,” *Adv. Funct. Mater.*, vol. 27, no. 42, 2017.

[146] J. Pas *et al.*, “A bilayered PVA/PLGA-bioresorbable shuttle to improve the implantation of flexible neural probes,” *J. Neural Eng.*, vol. 15, no. 6, 2018.

[147] A. Williamson *et al.*, “Localized Neuron Stimulation with Organic Electrochemical Transistors on Delaminating Depth Probes,” *Adv. Mater.*, vol. 27, no. 30, pp. 4405–4410, 2015.

[148] Y. Liang, “Interdigitated Organic Electrochemical Transistors for Biosensing,” RWTH Aachen University, 2019.

[149] Y. H. Kim, G. H. Kim, A. Y. Kim, Y. H. Han, M. A. Chung, and S. D. Jung, “In vitro extracellular recording and stimulation performance of nanoporous gold-modified multi-electrode arrays,” *J. Neural Eng.*, vol. 12, no. 6, 2015.

[150] H. Zhang, J. Shih, J. Zhu, and N. A. Kotov, “Layered nanocomposites from gold nanoparticles for neural prosthetic devices,” *Nano Lett.*, vol. 12, no. 7, pp. 3391–3398, 2012.

[151] S. Park, Y. J. Song, H. Boo, and T. D. Chung, “Nanoporous Pt microelectrode for neural stimulation and recording: In vitro characterization,” *J. Phys. Chem. C*, vol. 114, no. 19, pp. 8721–8726, 2010.

[152] M. Rivas, “Iridium Oxide (IrO2) as a Top Electrode for Ferroelectric Micro-Electro-Mechanical Systems (MEMS) Devices for Radiation Rich Environments,” University of Connecticut, 2018.

[153] Z. J. Du, X. Luo, C. L. Weaver, and X. T. Cui, “Poly(3,4-ethylenedioxythiophene)-ionic liquid coating improves neural recording and stimulation functionality of MEAs,” *J.*

Mater. Chem. C, vol. 3, no. 25, pp. 6515–6524, 2015.

[154] S. Venkatraman *et al.*, “In vitro and in vivo evaluation of PEDOT microelectrodes for neural stimulation and recording,” *IEEE Trans. Neural Syst. Rehabil. Eng.*, vol. 19, no. 3, pp. 307–316, 2011.

[155] E. K. Brunton *et al.*, “In vivo comparison of the charge densities required to evoke motor responses using novel annular penetrating microelectrodes,” *Front. Neuroeng.*, vol. 8, no. MAY, pp. 1–11, 2015.

[156] V. Maybeck, J. Schnitker, W. Li, M. Heuschkel, and A. Offenhäusser, “An evaluation of extracellular MEA vs optogenetic stimulation of cortical neurons,” *Biomed. Phys. Eng. Express*, vol. 2, no. 5, pp. 1–9, 2016.

[157] P. Horowitz and W. Hill, *The Art of Electronics*, Third. New York: Cambridge University Press.

[158] V. Rincón Montes *et al.*, “Development and in vitro validation of flexible intraretinal probes,” *Sci. Rep.*, vol. 10, no. 19836, pp. 1–14, 2020.

[159] S. Johnson and P. Rabinovitch, “Ex-vivo imaging of excised tissue using vital dyes and confocal microscopy,” *Curr. Protoc. Cytom.*, vol. 61, no. 1, pp. 9.39.1-9.39.18, 2013.

[160] J. Schindelin *et al.*, “Fiji: An open-source platform for biological-image analysis,” *Nat. Methods*, vol. 9, no. 7, pp. 676–682, 2012.

[161] A. K. Dwivedi, I. Mallawaarachchi, and L. A. Alvarado, “Analysis of small sample size studies using nonparametric bootstrap test with pooled resampling method,” *Stat. Med.*, vol. 36, no. 14, pp. 2187–2205, 2017.

[162] R. Heil, M. Schloesser, A. Offenhäusser, S. v. Waasen, and M. Schieck, “Automated electrical stimulation and recording for retina implant research by LabVIEW configured standalone data acquisition device,” in *SICE Annual Conference 2014*, 2014, pp. 1662–1667.

[163] C. Dysli, V. Enzmann, R. Sznitman, and M. S. Zinkernagel, “Quantitative Analysis of Mouse Retinal Layers Using Automated Segmentation of Spectral Domain Optical Coherence Tomography Images,” *Transl. Vis. Sci. Technol.*, vol. 4, no. 4, pp. 1–13, 2015.

[164] R. Q. Quiroga, “Unsupervised spike detection and sorting Problem : detect and separate spikes,” *Neural Comput.*, vol. 16, pp. 1661–1687, 2004.

[165] R. Segev, J. Goodhouse, J. Puchalla, and M. J. Berry, “Recording spikes from a large fraction of the ganglion cells in a retinal patch,” *Nat. Neurosci.*, vol. 7, no. 10, pp. 1154–1161, 2004.

[166] S. Biswas, C. Haselier, A. Mataruga, G. Thumann, P. Walter, and F. Müller, “Pharmacological analysis of intrinsic neuronal oscillations in rd10 retina,” *PLoS One*, vol. 9, no. 6, pp. 1–13, 2014.

[167] Y. S. Goo *et al.*, “Spontaneous oscillatory rhythm in retinal activities of two retinal degeneration (rd1 and rd10) mice,” *Korean J. Physiol. Pharmacol.*, vol. 15, no. 6, pp. 415–422, 2011.

[168] S. F. Stasheff, M. Shankar, and M. P. Andrews, “Developmental time course distinguishes changes in spontaneous and light-evoked retinal ganglion cell activity in rd1 and rd10 mice,” *J. Neurophysiol.*, vol. 105, no. 6, pp. 3002–3009, 2011.

[169] S. A. Jae, K. N. Ahn, J. Y. Kim, J. H. Seo, H. K. Kim, and Y. S. Goo, “Electrophysiological and histologic evaluation of the time course of retinal degeneration in the rd10 mouse model of retinitis pigmentosa,” *Korean J. Physiol. Pharmacol.*, vol. 17, no. 3, pp. 229–235, 2013.

[170] K. S. Worthington *et al.*, “Mechanical properties of murine and porcine ocular tissues in compression,” *Exp. Eye Res.*, vol. 121, pp. 194–199, 2014.

[171] E. Vecino, F. D. Rodriguez, N. Ruzafa, X. Pereiro, and S. C. Sharma, “Glia-neuron interactions in the mammalian retina,” *Prog. Retin. Eye Res.*, vol. 51, pp. 1–40, 2016.

[172] R. De Hoz *et al.*, “Retinal Macroglial Responses in Health and Disease,” *Biomed Res. Int.*, vol. 2016, 2016.

[173] Y. Lu *et al.*, “Reactive glial cells: increased stiffness correlates with increased intermediate filament expression,” *FASEB J.*, vol. 25, no. 2, pp. 624–631, 2011.

[174] B. Wang and J. D. Weiland, “Resistivity profiles of wild-type, rd1, and rd10 mouse retina,” *Proc. Annu. Int. Conf. IEEE Eng. Med. Biol. Soc. EMBS*, vol. 2015-Novem, pp. 1650–1653, 2015.

[175] A. Corna, T. Herrmann, and G. Zeck, “Electrode-size dependent thresholds in subretinal neuroprosthetic stimulation,” *J. Neural Eng.*, vol. 15, no. 4, 2018.

[176] Y. S. Goo, J. H. Ye, S. Lee, and Y. Nam, “Retinal ganglion cell responses to voltage and current stimulation in wild-type and rd1 mouse retinas,” 2011.

[177] F. Gekeler and A. Stett, “Subretinal electrical stimulation of the rabbit retina with acutely implanted electrode arrays,” pp. 587–596, 2004.

[178] D. H. Szarowski, M. D. Andersen, S. Retterer, A. J. Spence, and M. Isaacson, “B rain responses to micro-machined silicon devices,” vol. 983, pp. 23–35, 2003.

[179] D. Boinagrov, S. Pangratz-Fuehrer, G. Goetz, and D. Palanker, “Selectivity of direct and network-mediated stimulation of the retinal ganglion cells with epi-, sub- and intraretinal electrodes,” *J. Neural Eng.*, vol. 11, no. 2, 2014.

[180] J. D. Weiland *et al.*, “A comparison of retinal prosthesis electrode array substrate materials,” *Proc. 31st Annu. Int. Conf. IEEE Eng. Med. Biol. Soc. Eng. Futur. Biomed. EMBC 2009*, pp. 4140–4143, 2009.

[181] M. E. Pennesi *et al.*, “Long-term characterization of retinal degeneration in rd1 and rd10 mice using spectral domain optical coherence tomography,” *Investig. Ophthalmol. Vis. Sci.*, vol. 53, no. 8, pp. 4644–4656, 2012.

[182] Y. Li, Y. Zhang, S. Chen, G. Vernon, W. T. Wong, and H. Qian, “Light-dependent OCT structure changes in photoreceptor degenerative rd 10 mouse retina,” *Investig. Ophthalmol. Vis. Sci.*, vol. 59, no. 2, pp. 1084–1094, 2018.

[183] D. Kireev, “Graphene Devices for Extracellular Measurements,” RWTH Aachen University, 2017.

[184] R. Fröhlich, A. Rpzany, J. Riedmüller, A. Bolz, and M. Schaldach, “Electroactive coating of stimulating electrodes,” *J. Mater. Sci. Mater. Med.*, vol. 7, pp. 393–397, 1996.

[185] E. Slavcheva, R. Vitushinsky, W. Mokwa, and U. Schnakenberg, “Sputtered Iridium Oxide Films as Charge Injection Material for Functional Electrostimulation,” pp. 226–237, 2004.

[186] S. C. Mailley, M. Hyland, P. Mailley, J. M. Mclaughlin, and E. T. Mcadams, “Electrochemical and structural characterizations of electrodeposited iridium oxide thin-film electrodes applied to neurostimulating electrical signal,” *Mater. Sci. Eng. C*, vol. 21, no. 1–2, pp. 167–175, 2002.

[187] S. F. Cogan, P. R. Troyk, J. Ehrlich, C. M. Gasbarro, and T. D. Plante, “The influence of electrolyte composition on the in vitro charge-injection limits of activated iridium oxide (AIROF) stimulation electrodes,” *J. Neural Eng.*, vol. 4, pp. 79–86, 2007.

[188] Y. Jung, J. Lee, and Y. Tak, “Electrochromic Mechanism of IrO2 Prepared by Pulsed

Anodic Electrodeposition," *Electrochem. Solid-State Lett.*, vol. 7, no. 2, pp. 5–8, 2004.

[189] K. Yamanaka, "Anodically electrodeposited iridium oxide films (AEIROF) from alkaline solutions for electrochromic display devices," *Jpn. J. Appl. Phys.*, vol. 28, no. 4 R, pp. 632–637, 1989.

[190] S. Hackwood, W. C. Dautremont-Smith, G. Beni, L. M. Schiavone, and J. L. Shay, "Volume Changes Induced by the Electrochromic Process in Sputtered Iridium Oxide Films," *J. Electrochem. Soc.*, vol. 128, no. 6, pp. 1212–1214, 1981.

[191] E. Slavcheva, U. Schnakenberg, and W. Mokwa, "Deposition of sputtered iridium oxide — Influence of oxygen flow in the reactor on the film properties," *APSUSC*, vol. 253, no. 4, pp. 1964–1969, 2006.

[192] J. Ortigoza-Diaz *et al.*, "Techniques and considerations in the microfabrication of parylene c microelectromechanical systems," *Micromachines*, vol. 9, no. 9, 2018.

[193] C. Koch and T. J. Rinke, *Photolithography: Basics of Microstructuring*. Microchemicals, 2017.

[194] S. F. Cogan, T. D. Plante, and J. Ehrlich, "Sputtered indium oxide films (SIROFs) for low-impedance neural stimulation and recording electrodes," *Annu. Int. Conf. IEEE Eng. Med. Biol. - Proc.*, vol. 26 VI, pp. 4153–4156, 2004.

[195] S. Negi, R. Bhandari, and F. Solzbacher, "Morphology and Electrochemical Properties of Activated and Sputtered Iridium Oxide Films for Functional Electrostimulation," *J. Sens. Technol.*, vol. 02, no. 03, pp. 138–147, 2012.

[196] S. Negi, R. Bhandari, L. Rieth, and F. Solzbacher, " In vitro comparison of sputtered iridium oxide and platinum-coated neural implantable microelectrode arrays ," *Biomed. Mater.*, vol. 5, no. 1, p. 015007, 2010.

[197] S. Gawad *et al.*, "Substrate arrays of iridium oxide microelectrodes for in vitro neuronal interfacing," *Front. Neuroeng.*, vol. 2, no. JAN, pp. 1–7, 2009.

[198] S. Eick *et al.*, "Iridium oxide microelectrode arrays for in vitro stimulation of individual rat neurons from dissociated cultures," *Front. Neuroeng.*, vol. 2, no. NOV, pp. 1–12, 2009.

[199] A. Ghazavi, J. Maeng, M. Black, S. Salvi, and S. F. Cogan, "Electrochemical characteristics of ultramicro-dimensioned SIROF electrodes for neural stimulation and recording," *J. Neural Eng.*, vol. 17, no. 1, pp. 1–14, 2020.

[200] G. Dijk, H. J. Ruigrok, and R. P. O. Connor, "Influence of PEDOT : PSS Coating Thickness on the Performance of Stimulation Electrodes," *Adv. Mater. Interfaces*, vol. 2000675, pp. 1–9, 2020.

[201] M. Ganji, A. T. Elthakeb, A. Tanaka, V. Gilja, E. Halgren, and S. A. Dayeh, "Scaling Effects on the Electrochemical Performance of poly(3,4-ethylenedioxythiophene (PEDOT), Au, and Pt for Electrocorticography Recording," *Adv. Funct. Mater.*, vol. 27, no. 42, pp. 1–12, 2017.

[202] J. Heinze, "Ultramicroelectrodes-a New Dimension in Electrochemistry?," *Angew. Chem., Int. Ed. Engl*, vol. 30, no. 2, pp. 170–171, 1991.

[203] J. Heinze, "Ultramicroelectrodes in Electrochemistry," *Angew. Chem., Int. Ed. Engl*, vol. 32, no. 9, pp. 1268–1288, 1993.

[204] R. M. Wightman, "Microvoltammetric Electrodes," *Anal. Chem.*, vol. 53, no. 9, pp. 1125A-1134A, 1981.

[205] S. Zhang, P. Kumar, A. S. Nouas, L. Fontaine, H. Tang, and F. Cicoira, "Solvent-induced changes in PEDOT:PSS films for organic electrochemical transistors," *APL Mater.*, vol. 3,

no. 1, pp. 1–8, 2015.
[206] P. J. Rousche, D. S. Pellinen, D. P. Pivin, J. C. Williams, R. J. Vetter, and D. R. Kipke, “Flexible polyimide-based intracortical electrode arrays with bioactive capability,” *IEEE Trans. Biomed. Eng.*, vol. 48, no. 3, pp. 361–370, 2001.
[207] B. K. Sarkar, *Strength of Materials*. Tata McGraw-Hill Education, 2003.
[208] A. Mata, A. J. Fleischman, and S. Roy, “Characterization of polydimethylsiloxane (PDMS) properties for biomedical micro/nanosystems.,” *Biomed. Microdevices*, vol. 7, no. 4, pp. 281–293, 2005.
[209] A. A. Zakhidov *et al.*, “Orthogonal processing: A new strategy for organic electronics,” *Chem. Sci.*, vol. 2, no. 6, pp. 1178–1182, 2011.
[210] K. Chen and J. D. Weiland, “Anisotropic and inhomogeneous mechanical characteristics of the retina,” *J. Biomech.*, vol. 43, no. 7, pp. 1417–1421, 2010.
[211] Y. Qu *et al.*, “Quantified elasticity mapping of retinal layers using synchronized acoustic radiation force optical coherence elastography,” vol. 9, no. 9, pp. 4054–4063, 2018.
[212] S. Song, N. M. Le, Z. Huang, T. Shen, and R. K. Wang, “Quantitative shear-wave optical coherence elastography with a programmable phased array ultrasound as the wave source,” *Opt. Lett.*, vol. 40, no. 21, pp. 5007–5010, 2015.
[213] Y. He *et al.*, “Confocal Shear Wave Acoustic Radiation Force Optical Coherence Elastography for Imaging and Quantification of theIn Vivo Posterior Eye,” *IEEE J. Sel. Top. Quantum Electron.*, vol. 25, no. 1, 2019.
[214] K. T. Brown and T. N. Wiesel, “Analysis of the intraretinal electroretinogram in the intact cat eye,” *J. Physiol.*, vol. 158, no. 2, pp. 229–256, 1961.
[215] T. Tomita and A. Funaishi, “Studies on Intraretinal Action Potential With Low-Resistance Microelectrode,” *J Neurophysiol.*, vol. 15, no. 1, pp. 75–84, 1952.
[216] T. D. Y. Kozai and A. L. Vazquez, “Photoelectric artefact from optogenetics and imaging on microelectrodes and bioelectronics: new challenges and opportunities,” *J. Mater. Chem. B*, vol. 3, no. 25, pp. 4965–4978, 2015.
[217] Z. Hu, P. R. Troyk, T. P. Brawn, D. Margoliash, and S. F. Cogan, “In Vitro and In Vivo Charge Capacity of AIROF Microelectrodes,” in *2006 International Conference of the IEEE Engineering in Medicine and Biology Society*, 2006, pp. 886–889.
[218] S. F. Cogan, “In vivo and In vitro Differences in the Charge-injection and Electrochemical Properties of Iridium Oxide Electrodes,” in *2006 International Conference of the IEEE Engineering in Medicine and Biology Society*, 2006, pp. 882–885.
[219] F. Rattay, “The basic mechanism for the electrical stimulation of the nervous system,” *Neuroscience*, vol. 89, no. 2, pp. 335–346, 1999.
[220] F. Rattay, “On the upper threshold phenomenon of extracellular neural stimulation,” *J. Neurophysiol.*, vol. 112, no. 10, pp. 2664–2665, 2014.
[221] D. Boinagrov, S. Pangratz-Fuehrer, B. Suh, K. Mathieson, N. Naik, and D. Palanker, “Upper threshold of extracellular neural stimulation,” *J. Neurophysiol.*, vol. 108, no. 12, pp. 3233–3238, 2012.
[222] A. Barriga-Rivera *et al.*, “High-amplitude electrical stimulation can reduce elicited neuronal activity in visual prosthesis,” *Sci. Rep.*, vol. 7, no. May 2016, pp. 1–13, 2017.
[223] M. Abramian, N. H. Lovell, J. W. Morley, G. J. Suaning, and S. Dokos, “Activation and inhibition of retinal ganglion cells in response to epiretinal electrical stimulation: A computational modelling study,” *J. Neural Eng.*, vol. 12, no. 1, pp. 1–17, 2014.
[224] S. M. N. Woolley and J. H. Casseday, “Response Properties of Single Neurons in the

Zebra Finch Auditory Midbrain: Response Patterns, Frequency Coding, Intensity Coding, and Spike Latencies," *J. Neurophysiol.*, vol. 91, no. 1, pp. 136–151, 2004.
[225] W. Jensen, K. Yoshida, and U. G. Hofmann, "In-vivo implant mechanics of flexible, silicon-based ACREO microelectrode arrays in rat cerebral cortex," *IEEE Trans. Biomed. Eng.*, vol. 53, no. 5, pp. 934–940, 2006.
[226] N. H. Hosseini, R. Hoffmann, S. Kisban, T. Stieglitz, O. Paul, and P. Ruther, "Comparative study on the insertion behavior of cerebral microprobes," *Annu. Int. Conf. IEEE Eng. Med. Biol. - Proc.*, no. c, pp. 4711–4714, 2007.
[227] H. C. Lee *et al.*, "Histological evaluation of flexible neural implants; Flexibility limit for reducing the tissue response?," *J. Neural Eng.*, vol. 14, no. 3, pp. 1–12, 2017.
[228] B. J. Kim *et al.*, "3D Parylene sheath neural probe for chronic recordings," *J. Neural Eng.*, vol. 10, no. 4, pp. 1–16, 2013.
[229] H. S. Sohal *et al.*, "The sinusoidal probe: A new approach to improve electrode longevity," *Front. Neuroeng.*, vol. 7, no. APR, pp. 1–14, 2014.
[230] F. Wu, L. W. Tien, F. Chen, J. D. Berke, D. L. Kaplan, and E. Yoon, "Silk-backed structural optimization of high-density flexible intracortical neural probes," *J. Microelectromechanical Syst.*, vol. 24, no. 1, pp. 62–69, 2015.
[231] S. F. Cogan, "Neural Stimulation and Recording Electrodes," 2008.
[232] C. W. Chang and J. C. Chiou, "Development of a three dimensional neural sensing device by a stacking method," *Sensors*, vol. 10, no. 5, pp. 4238–4252, 2010.
[233] N. Goshi *et al.*, "Glassy carbon MEMS for novel origami-styled 3D integrated intracortical and epicortical neural probes," *J. Micromechanics Microengineering*, vol. 28, no. 6, pp. 1–12, 2018.
[234] S. Takeuchi, T. Suzuki, K. Mabuchi, and H. Fujita, "3D flexible multichannel neural probe array," *J. Micromechanics Microengineering*, vol. 14, no. 1, pp. 104–107, 2004.
[235] C. L. Schepens, "Clinical and research aspects of subtotal open-sky vitrectomy. XXXVII Edward Jackson Memorial Lecture," *Am. J. Ophthalmol.*, vol. 91, no. 2, pp. 143–171, 1981.
[236] J. Sambrook, T. Maniatis, and D. W. Russell, *Molecular cloning 3: a laboratory manual*, Third. Cold-Spring-Harbor, NY : Cold Spring Harbor Laboratory Press, 2001.
[237] I. Levental *et al.*, "A simple indentation device for measuring micrometer-scale tissue stiffness," *J. Phys. Condens. Matter*, vol. 22, no. 19, pp. 1–9, 2010.

List of publications and contributions in conferences

Peer-reviewed publications

- **Rincón Montes, V**., Gehlen, J., Ingebrandt, S., Mokwa, W., Walter, P., Müller, F., and Offenhäusser, A., "Development and in vitro validation of flexible intraretinal probes," submitted for publication in Scientific Reports, 2020.
- **Rincón Montes, V.**, Gehlen, J., Lück, S., Mokwa, W., Müller, F., Walter, P., and Offenhäusser, A. (2019). "Toward a Bidirectional Communication Between Retinal Cells and a Prosthetic Device – A Proof of Concept". *Frontiers in Neuroscience*, 13. doi: 10.3389/fnins.2019.00367
- Kireev, D., **Rincón Montes, V**., Stevanovic, J., Srikantharajah, K., and Offenhäusser, A. (2019). "N3-MEA Probes: Scooping Neuronal Networks". *Frontiers in Neuroscience*, 13. doi: 10.3389/fnins.2019.00320
- Kireev, D., Shokoohimehr, P., Ernst, M., **Rincón Montes, V**., Srikantharajah, K., Maybeck, V., Wolfrum, B., and Offenhäusser, A. (2018). "Fabrication of Ultrathin and Flexible Graphene-Based Devices for in Vivo Neuroprosthetics". *MRS Advances*, 3(29), 1621–1627. doi:10.1557/adv.2018.94

Contributions in conferences

- **Rincón Montes, V.**, Gehlen, Srikantharajah, K., Müller, F., Offenhäusser, A. (2019). "Polymer-based penetrating probes for retinal applications" (oral presentation). Conference abstract in *Artificial Vision 2019* in Aachen, Germany, 2019. German Medical Science. doi: 10.3205/19artvis19
- **Rincón Montes, V.**, "Current testing procedures and requirements for stability of neural implants" (oral presentation). *Summer School "Bioelectronics: from in vitro to in vivo applications"* in Hirschegg, Austria, 2019.
- **Rincón Montes, V**., Srikantharajah, K., Kireev, and Offenhäusser, A., "Silicon and polymer-based penetrating probes for retinal applications" (oral presentation). *6th International Winter School on Bioelectronics (BioEl 2019)* in Kirchberg, Austria, 2019.
- **Rincón Montes, V**., Srikantharajah, K., Kireev, D., Lange, J. and Offenhäusser, A. (2019). "From stiff silicon to compliant retinal and cortical multisite penetrating implants" (poster). Conference Abstract in *MEA Meeting 2018 |11th International Meeting on Substrate Integrated Microelectrode Arrays* in Reutlingen, Germany, 2018. Frontiers in Cellular Neuroscience. doi: 10.3389/conf.fncel.2018.38.00072
- **Rincón Montes, V.**, Gehlen, J., Lück, S., Mokwa, W., Müller, F., Walter, P., Offenhäusser, A., "Towards a bidirectional communication for retinal implants" (poster). *Gordon Research Conference on Neuroelectronic Interfaces* in Galveston, United States, 2018.
- **Rincón Montes, V.**, "Retinal Implants" (oral presentation). *International Workshop on "Neuroelectronics" ICS-8* in Hirschegg, Austria, 2018.
- **Rincón Montes, V.**, Gehlen, J., Lück, S., Mokwa, W., Müller, F., Walter, P., Offenhäusser, A. (2017). "Retinal recordings with penetrating multielectrode arrays" (oral presentation). Conference abstract in *Artificial Vision 2017* in Aachen, Germany, 2017. German Medical Science. doi: 10.3205/17artvis19
- **Rincón Montes, V.**, Kireev, D., Ernst, M., Walter, P., and Offenhäusser, A., "Flexible and bidirectional 3D penetrating retinal implant" (poster). *BROWN-EPFL-ETHZ joint Summer School on Neurophysiology for Neural and Biomedical Engineering (NNBE 2017)* in Zermatt, Switzerland, 2017.

Band / Volume 53
Operando X-ray photoemission electron microscopy (XPEEM) investigations of resistive switching metal-insulator-metal devices
C. J. Schmitz (2017), IX, 153 pp
ISBN: 978-3-95806-283-2

Band / Volume 54
Optimization of powder and ceramic processing, electrical characterization and defect chemistry in the system $Yb_xCa_{1-x}MnO_3$
M. Rahmani (2018), XIV, 164 pp
ISBN: 978-3-95806-323-5

Band / Volume 55
Organic-Metal Hybrid Interfaces at the Mesoscopic Scale
G. Zamborlini (2018), xi, 133 pp
ISBN: 978-3-95806-328-0

Band / Volume 56
Configurable frequency synthesizer for large scale physics experiments
N. Parkalian (2019), xxi, 114 pp
ISBN: 978-3-95806-393-8

Band / Volume 57
Resistive switching phenomena in stacks of binary transition metal oxides grown by atomic layer deposition
H. Zhang (2019), ix, 196 pp
ISBN: 978-3-95806-399-0

Band / Volume 58
Element-Selective Investigation of Femtosecond Spin Dynamics in Ni_xPd_{1-x} Magnetic Alloys using Extreme Ultraviolet Radiation
S. Gang (2019), 93, xx pp
ISBN: 978-3-95806-411-9

Band / Volume 59
Defect engineering in oxide thin films
F. V. E. Hensling (2019), 10, 164 pp
ISBN: 978-3-95806-424-9

Band / Volume 60
Chemical control of the electrical surface properties of *n*-doped transition metal oxides
M. Andrä (2019), X, 150, XXXVIII pp
ISBN: 978-3-95806-448-5

Band / Volume 61
Digital Signal Processing and Mixed Signal Control of Receiver Circuitry for Large-Scale Particle Detectors
P. Muralidharan (2020), xv, 109 pp
ISBN: 978-3-95806-489-8

Band / Volume 62
Development of Electromagnetic Induction Measurement and Inversion Methods for Soil Electrical Conductivity Investigations
X. Tan (2020), ix, 124 pp
ISBN: 978-3-95806-490-4

Band / Volume 63
Novel System Approach for a mm-range Precision Indoor Positioning System
R. Xiong (2020), xi, 144 pp
ISBN: 978-3-95806-517-8

Band / Volume 64
Quantitative investigation of group III-nitride interfaces by a combination of scanning tunneling microscopy and off-axis electron holography
Y. Wang (2021), 102 pp
ISBN: 978-3-95806-534-5

Band / Volume 65
Scalable Control Electronics for a Spin Based Quantum Computer
L. Geck (2021), xiv, 114, xv-xxxiii
ISBN: 978-3-95806-540-6

Band / Volume 66
DNA-capped silver nanoparticles for stochastic nanoparticle impact electrochemistry
L. Nörbel (2021), VI, 142 pp
ISBN: 978-3-95806-541-3

Band / Volume 67
Development, characterization, and application of intraretinal implants
V. Rincón Montes (2021), XII, 173 pp
ISBN: 978-3-95806-553-6

Weitere ***Schriften des Verlags im Forschungszentrum Jülich*** unter
http://wwwzb1.fz-juelich.de/verlagextern1/index.asp

Information
Band / Volume 67
ISBN 978-3-95806-553-6

Mitglied der Helmholtz-Gemeinschaft

JÜLICH
Forschungszentrum